Theoretical and Experimental Investigation of Hall Thruster Miniaturization

Noah Z. Warner and Manuel Martínez-Sánchez

May 2007   SSL # 18-07

Theoretical and Experimental Investigation
of Hall Thruster Miniaturization

by

Noah Zachary Warner

S.B., Aeronautics and Astronautics, Massachusetts Institute of Technology, 2001
S.M., Aeronautics and Astronautics, Massachusetts Institute of Technology, 2003

SUBMITTED TO THE DEPARTMENT OF AERONAUTICS AND ASTRONAUTICS
IN PARTIAL FULFILLMENT OF THE REQUIREMENTS FOR THE DEGREE OF

DOCTOR OF PHILOSOPHY
AT THE
MASSACHUSETTS INSTITUTE OF TECHNOLOGY

JUNE 2007

Signature of Author . . . .
Department of Aeronautics and Astronautics
May 25, 2007

Certified by . . . .
Manuel Martínez-Sánchez
Professor of Aeronautics and Astronautics
Thesis Supervisor

Certified by . . . .
Jack Kerrebrock
Professor Emeritus of Aeronautics and Astronautics

Certified by . . . .
Oleg Batishchev
Principal Research Scientist in Aeronautics and Astronautics

Certified by . . . .
Vladimir Hruby
President, Busek Company, Inc.

Accepted by . . . .
Jaime Peraire
Professor of Aeronautics and Astronautics
Chair, Committee on Graduate Students

Theoretical and Experimental Investigation
of Hall Thruster Miniaturization

by

Noah Zachary Warner

Submitted to the Department of Aeronautics and Astronautics
on May 25, 2007 in partial fulfillment of the
requirements for the degree of
Doctor of Philosophy in Aeronautics and Astronautics
in the field of Space Propulsion

ABSTRACT

Interest in small-scale space propulsion continues to grow with the increasing number of small satellite missions, particularly in the area of formation flight. Miniaturized Hall thrusters have been identified as a candidate for lightweight, high specific impulse propulsion systems that can extend mission lifetime and payload capability.

A set of scaling laws was developed that allows the dimensions and operating parameters of a miniaturized Hall thruster to be determined from an existing, technologically mature baseline design. The scaling analysis preserves the dominant plasma processes that determine thruster performance including ionization, electron confinement and recombination losses. These scaling laws were applied to the design of a 9mm diameter, nominally 200W thruster based on the Russian D-55 anode layer Hall thruster. The Miniature Hall Thruster (MHT-9) design was further refined using magnetostatic and steady-state thermal finite element modeling techniques. Performance testing was conducted over a wide range of input powers from 20-500W with voltages between 100-300V and propellant flow rates of 0.3-1.0mg/s. Measured thrust was 1-18mN with a maximum thrust efficiency of 34% and specific impulse of 2000s. Significant erosion of thruster surfaces was observed due to the high plasma density required to maintain collisional mean free paths.

Although the thrust efficiency was significantly lower than predicted by scaling laws, the MHT-9 is the best performing subcentimeter diameter Hall thruster built to date. A dimensionless performance analysis has shown that while the magnetic confinement ratio was successfully scaled, the thruster did not maintain the desired Knudsen number because of plasma heating. These trends were confirmed using a computational simulation. An analytical model of electron temperature predicts that, due to a larger relative exposed wall area, the peak temperature inside the MHT-9 is higher than that of the D-55, resulting in greater ion losses and beam divergence. The inability to maintain geometric similarity was a result of the inherent challenges of maintaining magnetic field shape and strength at

small scale, and this difficulty is identified as the fundamental limitation of Hall thruster miniaturization.

Thesis Supervisor: Manuel Martínez-Sánchez
Title: Professor of Aeronautics and Astronautics

ACKNOWLEDGMENTS

First and foremost, I would like to thank my research advisor and mentor, Professor Manuel Martínez-Sánchez. When I entered MIT almost ten years ago as an undergraduate, the first class I enrolled in was a freshman seminar entitled "What's in a Spacecraft?" Professor Martínez-Sánchez was the instructor and has served as my advisor ever since. He has taught me how to be a scientist and shown me that a curious nature can lead to great discovery. I have truly appreciated his mentorship and friendship.

I would like to thank my doctoral committee for their encouragement and support. Professor Jack Kerrebrock brought the grounding and fundamental insight that is needed for every good research project. Dr. Oleg Batishchev's knowledge of plasma physics and his warmhearted nature were very helpful. Dr. Vlad Hruby's academic and financial contributions were absolutely critical to the success of this project, and I will always be grateful for his support and encouragement.

I would also like to thank my thesis readers, Professor Paulo Lozano and Dr. James Szabo. Paulo has helped me with various research projects since I was an undergraduate, and his contributions to this project were invaluable, particularly in the early design phase. He has also been a good friend for many years. James has taught me a great deal about how to successfully mix the worlds of theory and experiments, and I enjoyed the camaraderie we shared while working together at Busek. I would also like to thank Dr. Ray Sedwick who served as a surrogate advisor to me, offering both mentorship and financial support.

There are several other folks at Busek who deserve my appreciation. Bruce Pote provided many insightful comments during the early design phase of the MHT-9 and has always been very supportive of my work. Larry Byrne was very helpful in setting up the experiments and served as a knowledgeable resource on how to successfully build and operate a low power Hall thruster. I would also like to thank Chaz Freeman and George Kolencik for their assistance with various aspects of the experimental work.

I would like to acknowledge the support of the National Defense Science and Engineering Graduate Fellowship Program which is operated out of the Department of Defense. This program allowed me to pursue my own interests when otherwise not financially feasible.

There are too many friends that I have made during my time at MIT to thank them all here. My fellow graduate students in both the Space Propulsion Laboratory and the Space Systems Laboratory have been a wonderful resource both academically and socially. In particular, I would like to thank Yassir Azziz and Shannon Cheng for their support and friendship over what often seemed like a very long road to the doctorate. We navigated every obstacle together as a team. I am not sure I could have made it this far without them, and I certainly would not have enjoyed it as much as I did.

My family has stood behind me every step of the way through my education and they have always been there to support me when needed. Every success of mine is simply a reflection of their love and their belief in me and my abilities.

I was incredibly fortunate to both meet and marry a beautiful woman during my time at MIT. My wife, Anjli, has always been a calming ocean of love and support, and I could not have done this without her. Not only did she never complain when I was spending late nights in the lab or the office, but she was always ready with a fresh perspective when I found myself in a difficult situation. I cannot thank her enough, but I offer her my sincere gratitude.

NZW

Cambridge
May, 2007

TABLE OF CONTENTS

LIST OF FIGURES

LIST OF TABLES

NOMENCLATURE

A_e	thruster exit area [m^2]
A_h	hole area [m^2]
A_w	discharge chamber wall area [m^2]
B	magnetic induction [T]
B_r	remanence [T]
c	ion exhaust speed [m/s]
c_e	electron thermal speed [m/s]
$\bar{c}_e$	mean electron thermal speed [m/s]
c_n	neutral thermal speed [m/s]
D	thruster mid-channel diameter [m]
$D_\perp$	perpendicular diffusion coefficient [m^2/s]
e	electron charge [C]
E_e	electron energy [J]
E_{ew}	electron wall energy [J]
E	electric field [V/m]
E_z	axial electric field [V/m]
h_c	interfacial conductance [W/m^2-K]
h_e	electron enthalpy [J]
H	magnetic intensity [A/m]
H_c	coercivity [A/m]
I_a	electron current to anode [A]
I_b	beam current [A]
I_{bs}	backstreaming electron current [A]
I_c	coil current [A]
I_d	discharge current [A]
I_{sp}	specific impulse [s]
I_w	wall current [A]
j	current density [A/m^2]
j_e	electron current density [A/m^2]
k	Boltzmann constant [J/K]
k_e	plasma thermal conductivity [W/m-K]
k_L	effective thermal conductivity of layer [W/m-K]
k_w	thermal conductivity of thruster wall [W/m-K]

Kn	Knudsen number
l	channel length [m]
L	characteristic length [m]
L_a	ionization layer thickness [m]
L_c	channel length [m]
m_e	electron mass [kg]
m_i	ion mass [kg]
m_n	neutral mass
$\dot{m}$	mass flow rate [kg/s]
$\dot{m}_a$	anode propellant flow rate [kg/s]
$\dot{m}_c$	cathode propellant flow rate [kg/s]
M_i	ion mach number
M_n	neutral mach number
n_e	electron number density [1/m^3]
n_i	ion number density [1/m^3]
n_n	neutral number density [1/m^3]
n_∞	quiescent plasma density [1/m^3]
P_c	chamber pressure [Pa]
P_d	discharge power [W]
P_e	electron pressure [Pa]
P_{ea}	electron anode power [W]
P_{ep}	electron plume power [W]
P_{ip}	ion plume power [W]
P_{ew}	electron wall power [W]
P_{iw}	ion wall power [W]
P_j	jet kinetic power [W]
P_n	neutral pressure [Pa]
P_r	power lost to wall recombination [W]
P_{rad}	radiated power [W]
P_w	wall heating power [W]
q	particle charge [C]
Q	heat transfer [W]
R	specific gas constant [J/kg-K]
R_c	coil resistance [Ω]
R_i	volumetric ionization rate [m^3/s]
R_L	Larmor radius [m]
R_t	thermal contact resistance [K/W]

R_1	channel inner radius [m]
R_2	channel outer radius [m]
S	magnetic shunt length [m]
t_{ie}	electron time between ionizing collisions [s]
t_{re}	electron residence time [s]
t_{in}	neutral time between ionizing collisions [s]
t_{rn}	neutral residence time [s]
T	thrust [N]
T_c	chamber temperature [K]
T_e	electron temperature [K]
T_{ea}	electron temperature near anode [K]
T_{ep}	electron plume temperature [K]
T_H	Hiperco core temperature [K]
T_i	ion temperature [K]
T_{ip}	ion plume temperature [K]
T_m	magnet temperature [K]
T_n	neutral temperature [K]
T_w	thruster wall temperature [K]
v_B	Bohm velocity [m/s]
v_D	diamagnetic drift velocity [m/s]
v_e	electron velocity [m/s]
$v_{e/z}$	axial electron velocity [m/s]
$v_{\overline{E}\times\overline{B}}$	$\overline{E}\times\overline{B}$ drift velocity [m/s]
v_n	neutral velocity [m/s]
$v_\perp$	perpendicular electron velocity [m/s]
V_d	discharge voltage [V]
V_i	ionization potential [V]
α_w	ratio of wall current to beam current
β	Hall parameter
β_a	anomalous Hall parameter
Γ_i	ion flux to chamber walls [$1/m^2s$]
γ	specific heat ratio
ε_0	permittivity of free space [F/m]
η	overall efficiency
η_a	acceleration efficiency
η_b	beam efficiency
η_q	charge efficiency

η_t	thrust (anode) efficiency
η_u	propellent utilization efficiency
λ	mean free path [m]
λ_{ni}	neutral mean free path for ionizing collisions [m]
λ_d	Debye length [m]
λ_{ei}	electron mean free path for ionizing collisions [m]
μ_0	permeability of free space [H/m]
$\mu_\perp$	perpendicular mobility [Cs/kg]
ν_a	anomalous electron collision frequency [1/s]
ν_c	classical electron collision frequency [1/s]
ν_{ei}	electron collision frequency for ionization [1/s]
ν_{ni}	neutral collision frequency for ionization [1/s]
ν_s	collision frequency for scattering [1/s]
σ_i	cross-section for ionization [m^2]
σ_p	plasma electrical conductivity [S/m]
σ_s	cross-section for scattering [m^2]
ϕ	potential [V]
ϕ_{na}	near anode sheath potential [V]
ϕ_{nc}	near cathode potential difference [V]
ϕ_p	plasma potential [V]
ϕ_s	sheath potential [V]
ϕ_w	wall potential [V]
ψ	ratio of excitation energy to ionization energy
ω_c	electron gyrofrequency [1/s]

Chapter 1

INTRODUCTION

The field of space propulsion has seen an increased interest in low power electric propulsion that has coincided with the growing number of small satellite applications. Small spacecraft require scaled down propulsion systems that must meet tight constraints on both mass and power while still satisfying requirements for attitude control, stationkeeping and orbit changes. One particularly interesting application for low power electric propulsion is in the area of formation flight. NASA's Terrestrial Planet Finder Interferometer (TPF-I) will use a distributed telescope approach that combines light gathered from several different satellites that fly in formation. The goal of the mission is to search for planets similar to Earth that orbit Sun-like stars and may have environments suited to the development or habitation of life [1]. The formation flying technology will require low power propulsion at two different precision levels of thrust: μN that finely controls relative positioning for interferometry, and mN for rotation, pointing and reconfiguration of the satellite array. It is possible that a low power Hall thruster could meet the requirements of the mN thrust level for such a mission [2]. Unfortunately, NASA recently decided to indefinitely defer the TPF-I mission, but hopefully interest will eventually be renewed as technology development continues.

There are many other applications for low power electric propulsion beyond space based observatories. Technology demonstrations, university experiments, space-based assembly projects and formation flying activities are all areas in which a high specific impulse pro-

pulsion technology with low power consumption could provide a distinct advantage over traditional chemical rockets. The combination of the flight proven heritage of mature kilowatt class Hall thrusters and the growing interest in low power electric propulsion makes the miniaturization of Hall thrusters an important area of research.

1.1 Hall Thrusters

Hall thrusters are versatile electric propulsion devices with moderate efficiency and high specific impulse. Thrust efficiencies can easily exceed 50%, and specific impulses are typically between 1200-3500s [3-5]. This specific impulse range, as well as the ability to throttle the specific impulse, has been identified by NASA as very appealing for both stationkeeping and orbital transfer missions to the near planets [6]. Hall thrusters adjust their thrust and specific impulse by varying the acceleration voltage and propellant flow rate. This capability makes them ideal for missions where different types of maneuvers require different levels of thrust and specific impulse. For example, in a mission to Mars there will be a long period of low thrust during transfer from geocentric orbit to areocentric orbit where fuel economy is most important. As a spacecraft approaches Mars, a relatively rapid deceleration is necessary for Mars capture, and a high thrust maneuver will be desired. A single Hall thruster could perform both types of maneuvers in a single mission. The thrust output and power requirement of Hall thrusters varies widely with size, ranging from subcentimeter diameter thrusters powered by 50W capable of thrusts on the order of 1mN to thrusters with diameters close to 0.5m powered with 70-100kW providing 3N of thrust or more [7-8].

1.1.1 Description

The Hall thruster geometry typically consists of an axisymmetric, annular discharge chamber with an interior metallic anode and an externally mounted cathode. Propellant is injected at the anode and enters the discharge chamber at low velocity. An axial electric field is established between the positively charged anode inside the thruster and the negatively charged electron cloud produced outside the discharge channel by the cathode. A
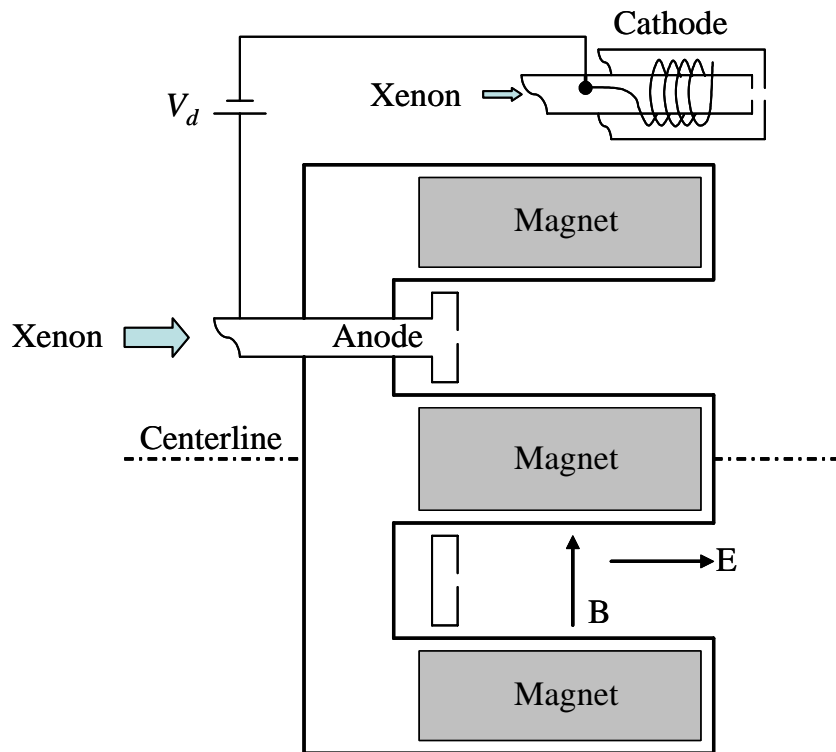
Figure 1.1 Diagram showing a Hall thruster in cross section. Propellant (typically xenon) is injected at the anode and the cathode. A potential difference is applied between the anode and cathode that establishes the axial electric field. A radial magnetic field is created by either electromagnets or permanent magnets placed along the centerline and around the outside of the channel.

nominally radial magnetic field is created by either permanent magnets or electromagnets placed around the annular channel and along the thruster centerline. This radial magnetic field is one of the distinguishing features of Hall thrusters. A cross sectional diagram of a Hall thruster is presented in Figure 1.1.

The magnetic field inside the channel is strong enough to reduce the electron Larmor radius to a small value in comparison to the width of the discharge channel. The electrons are effectively trapped in azimuthal $\overline{E}\times\overline{B}$ drifts around the annular channel as they slowly diffuse across the magnetic field towards the anode through scattering collisions. The azimuthal drift current of electrons is referred to as the Hall current. These trapped electrons serve several purposes. First, they promote ionization by increasing collisionality. An

electron-neutral, or less frequently an electron-ion, collision produces an ion and an additional electron. The ion is accelerated out of the thruster by the axial electric field, and the new electron produced in ionization is trapped by the magnetic field and promotes further ionization. Secondly, the trapped electrons transmit thrust to the thruster body through a magnetic pressure force exerted on the magnets. As the electrons are electrostatically drawn towards the anode and gain velocity, they are quickly deflected and accelerated azimuthally by the strong magnetic field. The electrons transfer their axial momentum to the magnets of the thruster through the magnetic field by creating a magnetic pressure force. It should be noted that although the magnetic field is an essential component for promoting ionization in the Hall thruster, it is considered an electrostatic thruster. This is because ions are accelerated electrostatically and are virtually unaffected by the magnetic field since their Larmor radius is generally larger than the thruster size. The magnetic field is used only to confine electrons and transmit thrust from the plasma to the magnets via the magnetic field. The magnetic field is not used to expel charged particles as in an electromagnetic thruster.

Electrons originating at the cathode are supplied to the discharge plasma for ionization, but also play an important role in keeping the plume downstream of the thruster quasi-neutral. The ions accelerated out of the thruster can cause hazardous spacecraft charging unless their current is balanced by an equivalent current of electrons injected into the beam. These cathode electrons also help to maintain the axial electric field used to accelerate ions out of the thruster.

The most common propellant used in Hall thrusters is xenon. Other propellants have been experimented with, including argon, krypton, bismuth and mixtures of air resembling the upper level Earth atmosphere. Xenon is typically selected for several reasons, but most of them are related to its high atomic weight. The heavy Xe mass minimizes loss factors for a given specific impulse. If the overall efficiency of the thruster is determined by the kinetic energy of the exhaust and a lost energy factor represented by a total loss potential, ϕ_L, then the efficiency can be written as,

$$\eta = \frac{\frac{1}{2}m_i c^2}{\frac{1}{2}m_i c^2 + e\phi_L} = \frac{c^2}{c^2 + \frac{2e\phi_L}{m_i}}. \tag{1.1}$$

The efficiency will increase with the atomic mass of the propellant because it reduces the effects of the loss factor. Xenon ions are only very weakly affected by the thruster's magnetic field because of their large inertia, unlike the electrons which are easily trapped in Larmor gyrations and $\overline{E} \times \overline{B}$ drifts. This allows the heavy ions to be efficiently accelerated out of the thruster with little deflection from the magnetic field. If the ions were significantly lighter, their curved exit trajectories would represent losses in thruster efficiency due to poor thrust vectoring. The noble gases are generally good candidates for propellants because they are chemically inert and safe to handle, gaseous at room temperature and they ionize easily. There is a correlation between atomic mass and the cross section for ionization amongst the noble gases such that heavier elements have a larger cross section. Xenon consequentially has the lowest ionization energy amongst the noble gases, with the exception of radon which is radioactive.

1.1.2 Advantages

Hall thrusters have several advantages over other space propulsion systems that make them attractive options for integration with spacecraft. Their high specific impulse relative to chemical rockets allows for either significant weight savings in propellant or extended mission lifetimes. Hall thrusters are often referred to as "gridless" versions of the ion engine. Although ion engines are functionally similar to Hall thrusters, they require precise alignment and careful production of delicate acceleration grids. Hall thrusters are relatively easy to build and assemble because of their simple annular geometry and use of commonly available materials. Ion engines operate in a space charge limited regime because they accelerate only ions out of the discharge chamber through the grids. The current density is therefore limited by the Child-Langmuir law for the particular grid spacing. Hall thrusters maintain quasi-neutrality and thus are not charge density limited. They are

also relatively simple to operate and easily throttled by adjusting the discharge voltage and mass flow rate.

1.1.3 Issues

Despite their numerous advantages, several barriers remain to the full acceptance of Hall thrusters within the aerospace community. The main factor limiting the lifetime of Hall thrusters is erosion of the inner channel walls. Impingement from high velocity ions can sputter material from the channel walls, changing the wall geometry over time. Eventually the erosion of the channel exposes the magnetic poles and thruster performance declines rapidly. However, advancements in Hall thruster lifetime are being made continually, with the most mature thrusters currently operating for more than 9000 hours before failure [9].

Another important issue for spacecraft designers is the effect of the charged plume emanating from the thruster exit. Spacecraft charging from backstreaming electrons and slow moving charge-exchange ions can be damaging to delicate spacecraft surfaces such as solar arrays and communications antennas. Deposited layers of sputtered material can form on various spacecraft surfaces, altering their thermal or optical properties. The plume radiation can also interfere with optical and communications instruments. Careful placement and pointing of the propulsion system is required, and accurate modeling of the thruster's plume can provide important information for making these decisions.

The problem of plume contamination is not particular to Hall thrusters. However, Hall thrusters have a distinctively wider plume divergence angle compared to ion engines making spacecraft integration more problematic. This is because of the inherently higher electron temperature in Hall thrusters due to only one voltage being used for both ionization and acceleration. Ion engines separate these two processes which allows them to be optimized independently.

1.1.4 Wall Material and Geometry Variations

Hall thrusters can be classified into several categories based on their physical and operational differences. The major distinctions are usually made by differences in channel wall material and channel length. Ceramic walled thrusters typically use a discharge channel lined with boron nitride. These thrusters often have an anode that is set deep in the annulus and a magnetic field profile such that the strength of the radial field increases from the anode towards the channel opening, and peaks near the exit plane. These thrusters are often referred to as the "SPT" variety, which is a name that comes from the Russian acronym for Stationary Plasma Thruster. They are also sometimes called Magnetic Layer Thrusters (MLT), although that name is not as prevalent. A more recently developed type of ceramic walled Hall thruster patented by the Busek Company utilizes a much shorter channel length and an innovative anode geometry [10-11].

Another important classification is the metallic walled thruster which usually has an anode that protrudes further, almost all the way to the exit plane. The discharge channel is axially shorter, and the overall diameter is typically smaller at an equivalent power level as compared to a ceramic walled thruster. The intent of this technology was to push the plasma out of the channel in order to reduce erosion of the channel wall material that protects the magnetic poles. These thrusters are usually referred to as the "TAL" variety, a name that comes from the Russian acronym for Thruster with Anode Layer. The ionization region in a TAL thruster is much thinner than for an SPT and sits much closer to the anode [12]. Figure 1.2 shows cross sectional views of two Hall thruster types, highlighting the major differences. Although the names and acronyms for these two Hall thruster variants are based more in history than in function, they are well accepted in the field and will likely continue to be used.

The majority of the initial development work for Hall thrusters took place in the former Soviet Union, although the early design ideas actually originated in the United States and the USSR almost simultaneously [12]. The US eventually halted work on Hall thrusters in favor of ion engines, while the USSR pursued the opposite course of action. The SPT is

the most well known and flight proven Hall thruster technology to date. It was developed at the Kurchatov Institute of Atomic Energy (KIAE), and later at the Fakel Design Bureau (FDB), under the leadership of Morozov in the 1960s. Over 150 SPT thrusters have been used aboard spacecraft to date. The TAL was originally developed at the Central Scientific Research Institute of Machine Building (TsNIIMASH), under the leadership of Zharinov, for high power missions where it was intended to be the primary propulsion unit for interplanetary probes. Upon realizing that this objective was not near term, the design was refocused on stationkeeping functions. The first flight of a TAL thruster was actually aboard a US military satellite. Several companies in both Europe and the United States have begun to produce Hall thrusters as well, with most of the new designs based on the ceramic walled style of thruster. For example, a low power Hall thruster built by Busek, the BHT-200, recently became the first Hall thruster designed and fabricated in the United States to operate in space.
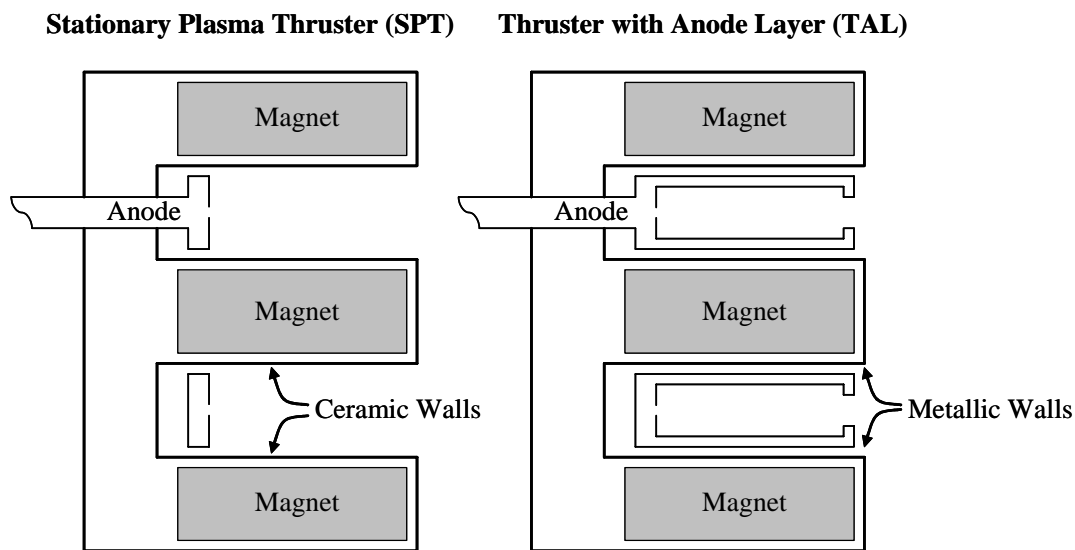
Figure 1.2   Two variants of the Hall thruster shown in cross section. The SPT has a ceramic lined discharge channel and the anode is set deep inside the channel. The TAL has conducting channel walls and a protruded anode.

1.2 Previous Work

A brief literature review is presented here on the development of low power Hall thrusters as well as work in the area of scaling theory focused on reducing thruster size. This review focuses on thrusters with midchannel diameters less than 30mm and does not include efforts to operate larger thrusters at low power by reducing the propellant flow rate, discharge voltage or by operating in pulsed modes.

1.2.1 Low Power Hall Thrusters

Low power Hall thrusters have been under development since the 1990s by many different research teams [13-25]. Performance amongst the thrusters produced varies widely, with efficiencies ranging from 6-45%, and specific impulses from 850-1850s. Presumably, many of these thrusters were designed by scaling down larger, well optimized devices and it is likely that the scaling methods used vary just as widely as the performance. Unfortunately, there has been relatively little publication about the methods used for experimental scaling. This is discussed further in the following section. The majority of the low power Hall thruster designs published thus far have utilized ceramic discharge chamber walls, with two notable exceptions which will be discussed first.

A previous effort at MIT by Khayms produced a 50W thruster with a metallic discharge chamber and a channel diameter of 3.7mm [13-15]. The thruster was actually scaled down from an SPT-100 thruster but then converted to a metallic walled thruster in order to avoid the need for very thin ceramic exit rings. Although the thruster performance (T=1.8mN, η_t=6%, I_{sp}=865s) was significantly lower than expected, several important lessons were learned about small scale Hall thruster design. The low performance was attributed to errors in magnetic circuit design, mechanical assembly and manufacturing. The error in the design of the magnetic circuit was actually discovered by Szabo during simulation of the miniature Hall thruster [26]. Szabo's simulation predicted that a corrected design would double the thrust efficiency. Khayms concluded that there were no obvious funda-

mental limits to building a Hall thruster at the 50W power level, but that the 3.7mm diameter thruster may have been near the lower bound of adequate manufacturability.

Another low power metallic walled thruster, the T-27 (also sometimes referred to as the D-27), was developed at TsNIIMASH [19]. The T-27 refers to the laboratory version, while the D-27 is considered the flight model. This thruster was likely based on the larger D-55, as it has a very similar geometry with an inner magnetic coil and three outer coils arranged in a triangular shape. The T-27 achieved efficiencies between 23-44% over a power range of 100-300W, with the specific impulse ranging from 850-1650s. The TsNIIMASH team recognized the difficulties in maintaining the magnetic field topology and thruster lifetime at small scale, but considered the T-27 a success that indicated the lower bound of effective operation for TALs had not yet been reached at a channel diameter of 27mm.

There have been many low power ceramic thrusters designed and built in recent years. The first of these was likely the SPT-30, built at KIAE in Russia. A laboratory version of this 30mm (outer channel) diameter thruster was tested at what was then the NASA Lewis Research Center (since renamed the Glenn Research Center at Lewis Field) in 1998 [21]. The SPT-30 was targeted as a 200W thruster and was measured to have an anode efficiency of 32% with a specific impulse of 1170s. The lifetime of this thruster has been estimated at approximately 600hrs [28]. KIAE later built the SPT-25, a 25mm (outer channel) diameter thruster that runs on 100-200W of power and performs similarly to the SPT-30 with an efficiency approximately 5% lower [22].

A precursor to the SPT-30 and SPT-25 was described as early as 1995 by Guerrini et al [23-24]. An SPT-20 type thruster with glass chamber walls was built with a 20mm outer channel diameter and 15mm midchannel diameter. Although the thrust efficiency reported was only 10%, the highest discharge voltage tested was only 160V. It is likely that performance would be improved at higher potentials.

Shortly thereafter in 1999, the US based Busek Company, Inc. published results on its 200W thruster, the BHT-200 [16, 70, 73]. This commercially available thruster has a

21mm midchannel diameter and performs at a thrust efficiency of 44% and specific impulse of 1390s. The BHT-200 recently became the first US built Hall thruster to operate in space when it was launched on the Air Force Research Laboratory's TacSat-2 satellite.

Other notable ceramic walled Hall thrusters include the Italian HT-100 and the Russian KM-20. The Italian thruster is a commercial development by Alta with a power target of 100W and a diameter of 29mm. At power levels just over 100W, this thruster operates at a thrust efficiency of 30%. The KM-20 was built at the Keldysh Research Center and is the smallest of the ceramic walled annular thrusters, with a 20mm outer diameter and a 16mm midchannel diameter. This thruster utilizes an advanced magnetic field configuration, given its small size, that includes magnetic shunting to reduce the field strength near the anode while keeping the exit plane field strong. At 210W, this thruster operates at $\eta_t=39\%$ and $I_{sp}=1850s$ [20]. These performance characteristics are particularly impressive given the small diameter of the thruster.

It is widely believed that scaled down Hall thrusters suffer from higher erosion rates because of the increased plasma density required to maintain good collisionality, and the generally higher area to volume ratio. A thruster built at the Princeton Plasma Physics Laboratory abandons the traditional annular shape in favor of a cylindrical geometry to reduce the wall area exposed to the plasma and potentially reduce erosion. They have also incorporated a novel magnetic geometry with a cusped field to utilize the magnetic bottling effect in order to keep the plasma from reaching the walls. The performance of this thruster has been shown to be comparable to that of annular geometries. A 26mm diameter version and its annular counterpart were tested over the range of 50-300W, resulting in thrust efficiencies between 15-32% [17].

Researchers at Stanford have also pursued novel configurations in order to reduce the overall thruster size. An annular 3.5mm midchannel diameter thruster was built without an internal anode. This microthruster utilizes a permanent magnet within an iron magnetic circuit, direct Xe injection into the channel, and coatings of alumina and diamond on the

face of the thruster. Over the power range of 10-40W, the thruster was measured to have 0.6-1.6mN of thrust for a η_t=10-15% and an I_{sp}=300-850s [25]. Although the measured performance was poor compared to the thrusters mentioned previously, it is impressive given the very small size and low power requirement. The efficiency measured is more than twice that measured by Khayms with a similarly sized thruster (D=3.7mm). However, as was previously mentioned, there was a significant design error discovered by Szabo in the magnetic circuit of Khayms' thruster.

1.2.2 Scaling Theory

The inherently competitive nature of thruster development has precluded extensive publication of design methodologies and techniques. It is likely that at least basic work in scaling theory has been performed by all of the teams developing small diameter thrusters. The groups with academic affiliations have done the majority of the theory publishing, with several notable efforts coming from Russia, Europe and the United States.

Khayms and Martínez-Sánchez first published work on a generalized scaling theory for Hall thrusters in 1996 [27]. Their method attempts to maintain efficiency and specific impulse by preserving dimensionless ratios that characterize the important plasma processes related to ionization and electron confinement. This is often referred to as "ideal scaling." The propellant flow rate is scaled in proportion with the characteristic thruster dimension, while the magnetic field strength is scaled inversely with size. The theory predicts that power should scale with flow rate and plasma density scales inversely with length. It is also shown that electron temperature will be a scaling constant if all of the important dimensionless ratios are preserved. Khayms' experimental results using ideal scaling were somewhat inconclusive as manufacturing problems obscured the comparison to theory [13-15].

Scaling theory as applied to the design of the SPT-80, and discussed in the context of the SPT-25 and SPT-30, was published in a paper by Kim et al [28]. The method addresses collisionality, acceleration layer thickness and the inherent challenges of building mag-

netic circuits at small scale. The scaling ideas are similar to those of Khayms, but there are additional constants involved that are likely determined empirically and remain undisclosed. However, the work does agree with Khayms' conclusions that flow rate should scale with thruster size (and an unidentified constant), and magnetic field must increase as the thruster size is reduced (again, with an unidentified constant).

Ahedo and Gallardo outline the critical technical constraints in scaling as well as the potential drawbacks to building a small Hall thruster [29]. They also introduce a radial scaling model that relaxes the requirement to maintain efficiency as a trade-off for improved lifetime and lower thruster temperatures. It is suggested that this may be the approach employed in the SPT scaling efforts. The radial method is used to make a preliminary design effort of a 45W Hall thruster, but no experimental evaluation of the theory was performed.

Andrenucci et al have published a set of two companion papers that tackle the scaling problem using a set of analytical models that are grouped into a system of linear homogeneous equations [30-31]. The first paper in the series demonstrates that this method can be used for a variety of plasma based propulsion devices by basing the model on a generalized Lorentz force that includes pressure forces and collisional effects. The second paper focus solely on the Hall thruster, and looks at the issue of down scaling with particular interest. The model is also refined to include more dimensional characteristics of the Hall thruster geometry, with a focus on ceramic walled thrusters. The model is then used to predict performance of various geometries and power levels, and compared to a large database of experimental data taken on SPT thrusters. The agreement between the model and the experimental data is very good. The predicted trends are similar to those predicted by other models: scaling to larger sizes presents no obvious challenges, but decreasing the size appears to have some fundamental limits that are governed by lifetime and the ability to reproduce the magnetic and physical geometry accurately.

Andrenucci's model deserves credit for tackling the scaling problem with more fidelity than previous attempts and for its comparison to such a large database of measured performance. The model also shows a flexibility that allows the different submodels that predict the plasma behavior to be easily updated or adjusted. This model was likely used in the design of the Alta HT-100, a nominally 100W ceramic walled Hall thruster that utilizes a permanent magnet to provide the majority of the field strength in combination with a small tuning coil [18].

1.3 Motivation

With the recent launch of the BHT-200 aboard the TacSat-2 satellite, it is clear that the interest in low mass, low power Hall thruster systems that began in the 1990s continues today. As small satellites are developed in the near future for distributed spacecraft systems, formation flight projects and technology experiments, Hall thrusters will be a compelling propulsion option. The number of low power Hall thrusters under development in industry and academia continues to grow with the interest in the field, but there have been few efforts to push the channel diameter of thrusters below a centimeter because of concerns about poor performance and lifetime.

Khayms' research at MIT concluded that the poor performance of the 50W miniature Hall thruster was due to manufacturing difficulties imposed by the very small diameter (D=3.7mm). He also hypothesized that the center stem of the magnetic circuit might have been overheating and losing permeability during thruster operation. However, Khayms did not believe that the poor performance was an intrinsic limitation of the small size, despite the inherent manufacturing challenges. It was therefore decided that a second effort at building a very small scale Hall thruster would be a worthy undertaking in order to test the ideal scaling concepts and explore the underlying physics associated with Hall thruster miniaturization.

1.4 Research Objectives

The objectives for this research are twofold. The primary objective is to increase the understanding of the important physical processes controlling the performance of a Hall thruster as it is scaled to small size. The secondary objective is to design, build and test a small scale Hall thruster to test the ideal scaling theory originally developed by Khayms and Martínez-Sánchez, and further refined in the following chapter. The thruster is intended to be a laboratory version that will facilitate the primary objective of better understanding the plasma and thruster properties that determine thrust efficiency and specific impulse. If fundamental limitations exist that limit the performance at small scale, they should be identified and explained if possible.

1.5 Thesis Outline

The thesis is presented in a roughly chronological order that corresponds to how the research progressed. Chapter 2 derives the ideal scaling theory that was used as the starting point for the design of a miniaturized 200W Hall thruster. Although this theory was originally developed by Khayms and Martínez-Sánchez, it has been refined and tailored to be more specific to Hall thrusters. Chapter 3 details the design process used in developing the MHT-9 Hall thruster. It begins with the output from the ideal scaling theory and explains the design of various components of the thruster including the magnetic circuit, the anode and flow system, as well as heat rejection techniques. Chapter 4 presents the experimental testing of the MHT-9, including both checkout tests and performance measurements. Observations about thruster erosion and lifetime are included as well. Chapter 5 examines the thruster performance in the context of the ideal scaling theory and compares the MHT-9 to other low power Hall thrusters. Several models are described that facilitate an understanding of the key factors affecting performance at small scale and an estimate of the miniaturization penalty is made. The models described include a model of electron temperature and a dimensionless performance assessment. A particle-in-cell sim-

ulation is used to confirm trends and conclusions. Finally, Chapter 6 summarizes the accomplishments and contributions of this research, and recommends future work.

Chapter 2

IDEAL SCALING OF HALL THRUSTERS

Hall thruster scaling methods attempt to relate physical dimensions and operating parameters to the processes of plasma generation, confinement and acceleration. Several different methodologies have been developed previously to both predict how plasma properties vary with changes in thruster size and to identify important design guidelines for maintaining high performance at low power levels [13-15, 27-31]. However, the majority of the published scaling methods are either very complex or require intricate knowledge of the baseline thruster to be scaled. The goal of this research is to investigate the more basic principles that control the physics of Hall thruster scaling and to identify the most important parameters that can be controlled by the designer, as well as those factors that may inherently limit performance at small size.

Before designing the miniaturized Hall thruster, a set of scaling laws was developed to determine the basic thruster dimensions and operating conditions with the goal of maintaining thruster efficiency and specific impulse. It has been assumed at the outset that the current 1kW class of mature Hall thruster technology has been sufficiently optimized such that matching this level of performance at low power would be both an ambitious and challenging task. The scaling theory presented below was used to provide a starting point from which more detailed engineering methods were utilized to fully develop the thruster design.

2.1 Ideal Scaling Theory

Empirical evidence points to the fact that thruster power and size are strongly correlated. Higher power thrusters tend to be larger to accommodate higher propellant flow rates, higher discharge voltages and currents, and larger total heat loads. It seems that there must be a mathematical relationship between nominal operating power and size, but it is not evident a priori what the proper characteristic dimension is, nor is its relation to required input power apparent.

If a characteristic length for the thruster could be identified and its relationship to nominal thruster power determined, this would allow a designer to select an appropriate power level for a thruster and calculate the important dimensions using a known device as a baseline. There are several obvious candidates for the characteristic length including thruster diameter, channel width and channel length. However, there is no obvious reason to choose any one of these dimensions over another without a more careful analysis of the important processes that determine thruster behavior and performance. To the extent that the geometrical shape of the thruster affects performance, it could be the case that all of the major dimensions (or their ratios) are important. If any one dimension is selected to be the only significant scaling length, it must be shown that shape does not matter for scaling.

The plasma processes considered while developing the scaling rules include propellant ionization, electron confinement and power lost due to ion-electron recombination at chamber walls. Each of these important processes is addressed in the following sections, as well as a discussion regarding the optimal magnetic field condition. The hypothesis going forward is simply that if the important plasma processes are scaled so as to be similar in the baseline and the scaled down thruster, then the high performance of kilowatt class thrusters will be maintained when scaled to lower powers and smaller dimensions. This approach is often referred to as "ideal scaling."

Figure 2.1 shows an axisymmetric cross sectional schematic with the important thruster dimensions used during the scaling analysis. The midchannel diameter, *D*, inner channel
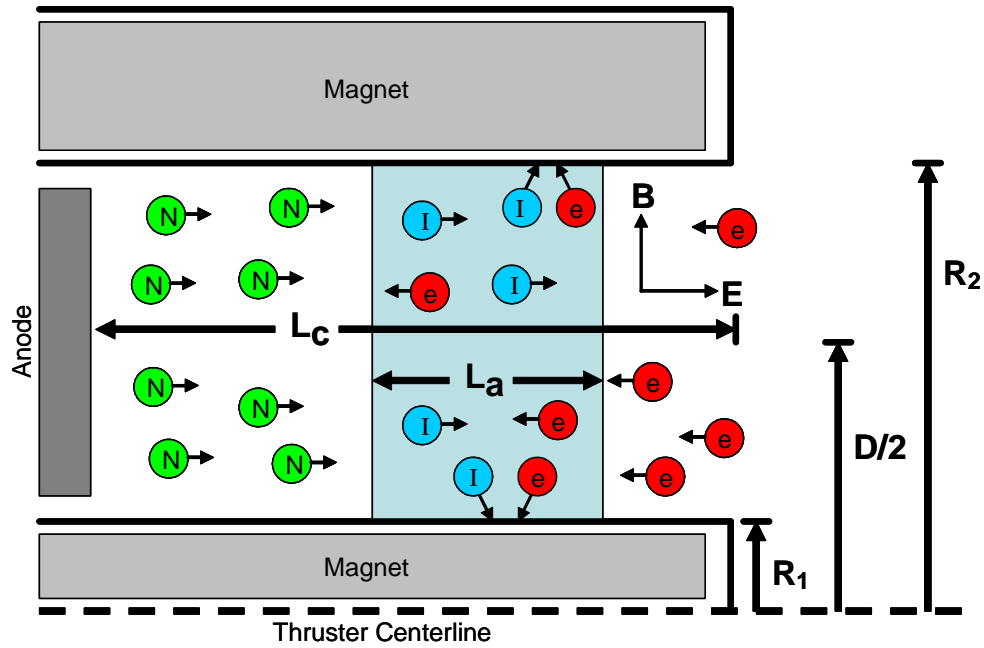
Figure 2.1   This schematic shows the important thruster dimensions considered in developing the scaling methodology.

radius, R_1, and outer channel radius, R_2, are the important radial dimensions. The channel length, L_c, and the ionization layer thickness, L_a, are the critical axial dimensions.

2.1.1 Propellant Ionization

In order to preserve the high utilization efficiency of mature Hall thruster technology, the neutral xenon atoms in the propellant flow must experience a similar number of ionizing collisions inside both the baseline thruster and the scaled down version. Hall thrusters have a thin ionization layer near the channel exit where neutral xenon atoms collide with magnetically confined, high-temperature electrons. The thickness of this layer, L_a, is the characteristic length over which neutrals must be ionized. Another way to consider the scaling requirement for neutral ionization is that the ratio of the residence time of a neutral inside the ionization layer to the time between ionizing collisions must be preserved. The residence time of a neutral in the layer, t_{rn}, is simply the length of the layer divided by the neutral velocity,

$$t_{rn} = \frac{L_a}{c_n}. \tag{2.1}$$

The time between ionizing collisions for a neutral, t_{in}, is the inverse of the ionization collision frequency for neutrals, ν_{ni}, expressed as,

$$t_{in} = \frac{1}{\nu_{ni}} = \frac{1}{n_e c_e \sigma_i}, \tag{2.2}$$

where it is noted that the relative velocity between neutrals and electrons is approximately equal to the electron thermal velocity since $c_e \gg c_n$. These two characteristic times for any well designed thruster with high utilization efficiency should be roughly equal, and their ratio will be unity. This is because the length of the ionization layer is defined by the transition from a purely neutral flow to an ion beam, meaning that a neutral should experience an average of one ionizing collision as it crosses through the layer. Thus, the scaling requirement for the ionization of neutrals becomes,

$$\frac{t_{rn}}{t_{in}} = \frac{L_a n_e c_e \sigma_i}{c_n} \approx 1. \tag{2.3}$$

Assuming that the electron and neutral temperatures are scaling invariants, their thermal velocities and the ionization cross section will be constant. This means that the thickness of the ionization layer and the plasma density will scale inversely. This is not a particularly useful scaling relationship for thruster design, but it can be used as an expression for the ionization layer thickness at a given plasma density.

Scaling of the Ionization Layer Thickness

The electron density is a function of the mass flow rate per unit area, but it can also be expressed as a function of power via the thrust efficiency. The thrust efficiency, η_t, is defined in terms of thrust, flow rate and discharge power as,

$$\eta_t = \frac{T^2}{2\dot{m}P_d}, \tag{2.4}$$

where the thrust can also be written as the product of the propellant flow rate and the effective exhaust velocity,

$$T = \dot{m}c. \tag{2.5}$$

The mass flow at the downstream edge of the ionization layer will be almost completely ionized for a thruster with high utilization efficiency ($\eta_u \approx 1$). Thus, the propellant flow rate can be approximated as,

$$\dot{m} \approx m_i n_e v_B A_e, \tag{2.6}$$

where it is noted that the plasma is quasineutral, meaning that $n_e = n_i$, and the Bohm velocity, v_B, is the ion speed of sound. If it is also noted that the effective exhaust velocity is related to the discharge potential through energy conservation as,

$$eV_d = \frac{1}{2}m_i c^2, \tag{2.7}$$

then Equations 2.4-2.7 can be combined to express the discharge power approximately as,

$$P_d \approx \frac{1}{2\eta_t}\dot{m}c^2 \approx \frac{1}{2\eta_t}m_i n_e v_B A_e c^2 \approx \frac{1}{\eta_t}n_e v_B A_e eV_d. \tag{2.8}$$

Equation 2.8 can be used to express the electron number density as a function of the power per unit area and the thrust efficiency,

$$n_e \approx \frac{\eta_t(P_d/A_e)}{v_B eV_d}. \tag{2.9}$$

This estimate of electron density can be used in Equation 2.3 to write the thickness of the ionization layer as,

$$L_a \approx \frac{c_n}{c_e n_e \sigma_i} \approx \frac{ec_n v_B V_d}{c_e \sigma_i \eta_t(P_d/A_e)}. \tag{2.10}$$

The three velocities (c_n, c_e, v_B) and the ionization cross-section, σ_i, all depend on species temperatures (electron and neutral). If the temperatures and discharge voltage are constant in scaling, and if efficiency is preserved, the ionization layer thickness will scale as,

$$L_a \propto \frac{A_e}{P_d}. \tag{2.11}$$

2.1.2 Confinement of Electrons

Electron confinement is intricately linked to the ionization process. In order to maintain a high propellant utilization in the miniaturized thruster, the electrons must be similarly confined as in the baseline thruster. If the electrons are considered in the same way as the neutrals, then it can be argued that the high energy electrons that enter the discharge chamber must be confined long enough to ionize the passing neutrals. The residence time of electrons in the ionization layer, t_{re}, is simply the length of the layer, L_a, divided by the axial speed of electrons as they diffuse towards the anode, $v_{e|z}$. It is critical that the ratio of this residence time to the time between ionizing collisions, t_{ie}, be maintained in scaling or increased if possible. The time between ionizing collisions for electrons is simply the inverse of their ionization collision frequency, ν_{ei}. Thus, the time ratio is written as,

$$\frac{t_{re}}{t_{ie}} = \frac{L_a \nu_{ei}}{v_{e|z}}. \tag{2.12}$$

This time ratio for electrons is not unity as it was for the neutrals, but to first order it is the number of ionizations performed by each backstreaming electron. It would therefore be approximately equal to the ratio of V_d/V_i', where V_i' is the effective ionization potential of xenon.

The ionization collision frequency for electrons can be written as a product of the neutral density, the mean cross-section for ionization, and the electron thermal velocity,

$$\nu_{ei} = n_n \sigma_i c_e. \tag{2.13}$$

A plausible assumption can be made that the cross-field electron diffusion in the ionization layer is dominated by collisions because the plasma turbulence responsible for anomalous diffusion is suppressed by the drift shear in that region. The axial electron velocity can thus be written using the classical equation for electron diffusion across a magnetic field. The perpendicular velocity for a charged particle moving across a magnetic field is generally expressed as,

$$\bar{v}_\perp = \pm\mu_\perp \bar{E} - D_\perp \frac{\overline{\nabla} n_e}{n_e} + \frac{\bar{v}_{\bar{E} \times \bar{B}} + \bar{v}_D}{1 + (\nu_s / \omega_c)^2}. \tag{2.14}$$

The perpendicular mobility can be expressed in terms of the Hall parameter, β, and the electron collision frequency for scattering, ν_s,

$$\mu_\perp = \frac{e}{m_e \nu_s}\left(\frac{1}{1 + \beta^2}\right). \tag{2.15}$$

The perpendicular diffusion coefficient is similarly expressed in terms of the electron temperature, T_e,

$$D_\perp = \frac{kT_e}{m_e \nu_s}\left(\frac{1}{1 + \beta^2}\right). \tag{2.16}$$

The last term in Equation 2.14 contains the $\bar{E} \times \bar{B}$ and diamagnetic drift velocities. In the case of a Hall thruster, it can be assumed that these terms only affect electron motion in the azimuthal direction and therefore can be ignored for the purposes of evaluating the axial electron velocity. The remaining two terms are due to the axial electric field and the pressure gradient. The electric field term can be written approximately as,

$$\mu_\perp E_z \approx \frac{e}{m_e \nu_s}\left(\frac{1}{1 + \beta^2}\right)\frac{\Delta\phi}{L_a}, \tag{2.17}$$

where the axial electric field has been estimated using the potential drop across the ionization layer, $\Delta\phi$. The pressure gradient term can be expressed as,

$$D_\perp \frac{\overline{\nabla} n_e}{n_e} = \frac{kT_e}{n_e m_e \nu_s} \left(\frac{1}{1 + \beta^2} \right) \frac{\partial n_e}{\partial z}, \tag{2.18}$$

where it is noted that the electron pressure gradient of interest is in the axial direction. Both of these terms can be further simplified by noting that the Hall parameter, the ratio of the electron gyrofrequency to the scattering frequency, inside a Hall thruster is typically much greater than unity,

$$\beta = \frac{\omega_c}{\nu_s} \gg 1. \tag{2.19}$$

The electron gyrofrequency is defined as,

$$\omega_c = \frac{eB}{m_e}, \tag{2.20}$$

which can be used to show that the electric field term scales as,

$$\mu_\perp E_z \approx \left(\frac{m_e \nu_s}{eB^2} \right) \frac{\Delta\phi}{L_a} \propto \frac{\nu_s}{B^2 L_a} \propto \frac{n_n}{B^2 L_a}. \tag{2.21}$$

It has been assumed that the potential drop in the ionization layer, $\Delta\phi$, will be a scaling constant so long as the electron temperature is also constant. It is also noted that the electron scattering frequency scales with the neutral density for constant electron temperature since,

$$\nu_s = n_n c_e \sigma_s. \tag{2.22}$$

It can be shown that the diffusion term scales in a similar way to the electric field term,

$$D_\perp \frac{\overline{\nabla} n_e}{n_e} \approx \frac{kT_e m_e \nu_s}{n_e e^2 B^2} \frac{\partial n_e}{\partial z} \propto \frac{\nu_s}{B^2 L_a} \propto \frac{n_n}{B^2 L_a}, \tag{2.23}$$

by noting that the density gradient in the ionization layer can be approximated as,

$$\frac{\partial n_e}{\partial z} \approx \frac{n_e}{L_a}. \tag{2.24}$$

This is because the flow is nearly fully ionized between the upstream and downstream edges of the layer. Since the diffusion and electric field terms scale similarly, one of them can be ignored for scaling purposes. The axial electron velocity can therefore be written as being proportional to the product of the perpendicular electron mobility and the axial electric field,

$$v_{e|z} \propto \mu_\perp E_z. \tag{2.25}$$

Turning to the ions for a moment, the ion acceleration out of the channel is similar to a presheath process whereby ions are accelerated towards an attracting wall by the potential gradient that provides the required sheath entry (sonic) velocity. An approximate energy balance for ions in the ionization layer exists such that the potential drop within the layer, $\Delta\phi$, accelerates the ions to the sonic point at the exit of the layer (typically close to the channel exit plane). At this point they are traveling at the ion speed of sound, known as the Bohm velocity, v_B. Figure 2.2 shows a sketch of the basic plasma structure in the discharge channel to help illustrate this point. The energy balance for ions in the layer can be written approximately as,

$$e\Delta\phi \approx \frac{1}{2} m_i v_B^2, \tag{2.26}$$

where the Bohm velocity is defined as,

$$v_B = \sqrt{\frac{kT_e}{m_i}}. \tag{2.27}$$
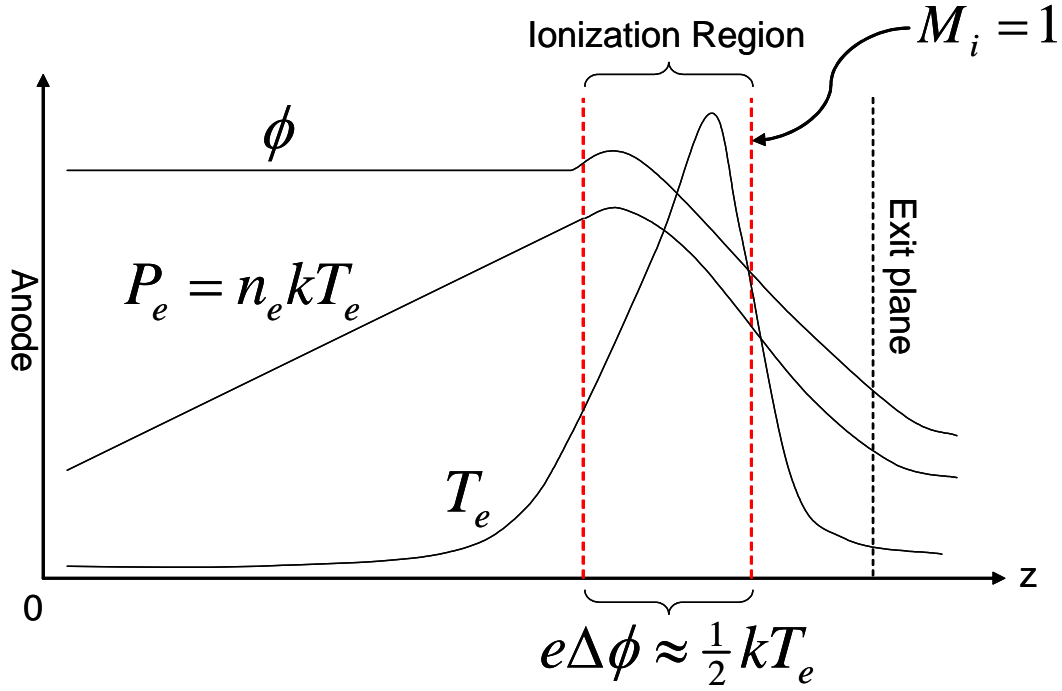
Figure 2.2 Basic axial structure of the plasma inside a Hall thruster. The potential drop in the ionization layer is approximately equal to half the electron temperature (in eV), and the ions leave the ionization region at the ion sonic velocity ($M_i = 1$).

Combining Equations 2.26-2.27, it can be shown that energy balance in the layer is such that the potential drop can be written as,

$$e\phi \approx \frac{1}{2}kT_e.$$

(2.28)

The axial electric field in the ionization layer region can therefore be approximated using the fact that the potential drop in the layer is of the order of kT_e/e, and the layer thickness was previously defined as L_a. Thus, the electric field term is approximately,

$$E_z \approx \frac{kT_e}{eL_a}.$$

(2.29)

Assuming $\beta \gg 1$, the axial diffusion speed for electrons (Equation 2.25) can now be shown to scale as,

$$v_{e|z} \propto \mu_{\perp} E_z = \frac{\nu_s k T_e}{m_e \omega_c^2 L_a}. \tag{2.30}$$

This expression can now be used with Equation 2.13 to show that the electron time ratio in Equation 2.12 scales as,

$$\frac{t_{re}}{t_{ie}} \propto \left(\frac{m_e L_a^2 \omega_c^2}{k T_e} \right) \left(\frac{n_n \sigma_i c_e}{\nu_s} \right). \tag{2.31}$$

This time ratio can be further simplified by noting that the electron thermal velocity is,

$$c_e = \sqrt{\frac{2 k T_e}{m_e}} \approx \sqrt{\frac{k T_e}{m_e}}, \tag{2.32}$$

and the electron Larmor radius can be expressed as,

$$R_L = \frac{m_e v_{\perp}}{eB} \approx \frac{m_e c_e}{eB} \approx \frac{c_e}{\omega_c}. \tag{2.33}$$

If the definition of the cross section for electron scattering, as shown in Equation 2.22, is also substituted into Equation 2.31, then it can be shown that the time ratio scales as,

$$\frac{t_r}{t_i} \propto \left(\frac{L_a}{R_L} \right)^2 \frac{\sigma_i}{\sigma_s}. \tag{2.34}$$

The ratio of cross sections will be a scaling constant since electron temperature has been assumed to be constant. The Larmor radius is the radius of gyration of a charged particle about a magnetic field line. It is strictly defined using the perpendicular velocity of the particle because the magnetic field cannot produce a force along the direction of the field lines. In making the simplification shown in Equation 2.33, it has been assumed that the electrons are sufficiently thermalized such that the perpendicular electron velocity is of the same order as the electron thermal velocity.

It can be seen from Equation 2.34 that in order to maintain the ratio of electron residence time to ionization time, the Larmor radius and ionization layer thickness must scale together. The Larmor radius is a parameter that can be partially controlled by the thruster designer through the magnetic field strength and the electron thermal velocity (via the discharge potential), but the ionization layer thickness is a property seemingly set by the plasma. However, this conclusion forms a scaling requirement,

$$R_L \propto L_a, \tag{2.35}$$

which will be useful once the power lost to wall recombination has been considered. If the expression for the ionization layer thickness shown in Equation 2.11 is utilized, this scaling requirement can be rewritten in terms of the thruster power and exit area as,

$$R_L \propto \frac{A_e}{P_d}. \tag{2.36}$$

2.1.3 Power Lost to Discharge Chamber Walls

The dominant power loss in Hall thrusters occurs through the recombination of ions and electrons at the discharge chamber wall surfaces. In scaling down a kilowatt class thruster to a low power device, it is important that the fraction of power lost to ion recombination does not increase. The ratio of the power lost by wall recombination to useful jet power must be preserved. This loss ratio is written simply as,

$$\frac{P_r}{P_j} = \frac{\Gamma_i A_w e V_i}{\frac{1}{2}\dot{m}c^2}, \tag{2.37}$$

where Γ_i is the ion flux to the thruster walls and V_i is the ionization energy. Kinetic energy lost in the wall sheath by electrons and ions is not considered because it depends only on electron temperature, which has been assumed constant in scaling. The ion flux to the walls is determined by the ion density and the Bohm velocity (defined in Equation 2.27) as,

$$\Gamma_i = 0.61 n_i v_B, \tag{2.38}$$

where the coefficient comes from the Boltzmann equation. The most difficult part of evaluating the power loss ratio in Equation 2.37 is determining the appropriate wall area, A_w, for ion losses. The wall area (including inner and outer wall surfaces) can be written generally as,

$$A_w = 2\pi D L_L, \tag{2.39}$$

where D is the thruster diameter and L_L is the effective channel length for ion losses. An axisymmetric geometry has been assumed, however the πD term could easily be replaced with a more general perimeter variable to allow for non-circular channel shapes. The power loss ratio can now be expressed solely in terms of thruster dimensions and the loss length since the recombination power depends on the exposed area of the channel walls, and the jet power can be written as a function of the exit area. Equation 2.37 can therefore be expanded as,

$$\frac{P_r}{P_j} \approx \frac{0.61 n_i v_B A_w e V_i}{\frac{1}{2} m_i n_i v_B A_e c^2} \approx \frac{0.61 n_i v_B 2\pi (R_1 + R_2) L_L e V_i}{\frac{1}{2} m_i n_i v_B \pi (R_2^2 - R_1^2) c^2}, \tag{2.40}$$

where it is noted that for a circular channel symmetric about the midchannel line,

$$D = R_1 + R_2. \tag{2.41}$$

It has been assumed that the propellant flow is almost fully ionized (high utilization efficiency). If the discharge voltage is kept constant in scaling, the exit velocity term can be ignored since it can be defined as,

$$c = \sqrt{\frac{2 q V_d}{m_i}}. \tag{2.42}$$

The remaining terms important for scaling show that the power loss ratio in Equation 2.40 scales as the wall area ratio, A_w/A_e, which can be simplified to a length ratio as,

$$\frac{P_r}{P_j} \propto \frac{L_L}{R_2 - R_1}. \tag{2.43}$$

As with the argument based on electron residence time, the scaling rule for power loss shows that a physical dimension that can be controlled during design, $R_2 - R_1$, must scale with a plasma parameter that is not easily predetermined, L_L.

If it is assumed that the majority of the ion-electron wall recombination occurs in the ionization layer, one possible choice for the loss length could be the thickness of the ionization layer, $L_L \approx L_a$. The ionization layer thickness would then have to scale with the thruster channel width in order to preserve the ratio of power lost by ion recombination to jet power (Equation 2.43). If this argument is now combined with the results of the scaling arguments based on electron residence time in Equations 2.35-2.36, an important conclusion can be drawn: the gap width and the Larmor radius must scale with each other and the ionization layer thickness (which scales as the inverse of the power per unit area).

$$R_2 - R_1 \propto R_L \propto L_a \propto \frac{A_e}{P_d} \tag{2.44}$$

Another possible choice for the ion loss length is the entire length of the thruster channel, $L_L \approx L_c$. This may be a more reasonable assumption in light of the experimental results from this research that show significant wall erosion for a miniaturized thruster over the whole channel length (see Section 4.7). This choice would be further strengthened if the ionization layer were very thin, meaning that $L_a \ll R_2 - R_1$, because it is likely that the ion losses would spill out beyond the layer even if they were peaked in that region. This would lead to the conclusion (using Equation 2.43) that the shape factor, $L_c/(R_2 - R_1)$, must be preserved in order to properly scale the recombination power loss ratio,

$$\frac{P_r}{P_j} \propto \frac{L_c}{R_2 - R_1}. \tag{2.45}$$

In this case the Larmor radius is not related to the channel width, but only to the power per unit area as shown in Equation 2.36.

2.1.4 Optimal Magnetic Field

Hall thrusters that use electromagnets to create the radial magnetic field are operated by adjusting the coil current until a minimum discharge current is found. This condition corresponds to the maximum thrust efficiency. The magnetic tuning process is a way of minimizing the electron diffusion rate towards the anode. As Figure 2.2 shows, the electron density decreases linearly from the ionization region to the anode. If the electron diffusion rate towards the anode is decreased by increasing the magnetic field strength, the slope of this line will increase. The thruster discharge will go unstable if the anode becomes starved of electrons, thus a maximum magnetic field exists where the electron density goes to zero near the anode. This field strength is likely very close to the optimal magnetic field condition.

The axial electron diffusion in this upstream region will dominated by Bohm diffusion. A diffusion equation can be written for the axial transport in this region using Fick's Law. The product of the anomalous diffusivity and the electron density gradient will be equal to the ion/electron production rate in the ionization layer,

$$D_a \frac{\partial n_e}{\partial z} \approx D_a \frac{n_e - n_{ea}}{L_c} \approx \frac{\dot{m}_i}{m_i A_e}, \tag{2.46}$$

where n_e is the electron density in the ionization layer and n_{ea} is the electron density near the anode. The entire channel length is used to approximate the electron density gradient since the ionization region typically occurs near the channel exit. The anomalous diffusivity, D_a, is expressed as,

$$D_a = \frac{kT_e}{eB\beta_a}, \tag{2.47}$$

where the anomalous Hall parameter, β_a, is approximately 16 for Bohm diffusion. The diffusion equation can thus be written as,

$$\left(\frac{kT_e}{eB\beta_a}\right)\frac{n_e - n_{ea}}{L_c} \approx n_e v_B . \tag{2.48}$$

If the optimal magnetic field condition occurs near $n_{ea} \approx 0$, then the optimal magnetic field will be determined approximately by,

$$B \approx \frac{kT_e}{e\beta_a L_c v_B} . \tag{2.49}$$

Assuming the electron temperature and the anomalous Hall parameter are scaling invariants, an important scaling relationship emerges. The optimal magnetic field will scale inversely with the full channel length,

$$B \propto \frac{1}{L_c} . \tag{2.50}$$

This scaling criterion allows the discrepancy regarding the ion-electron recombination loss length, L_L, to be resolved. In the case that $L_L \approx L_a$, Equation 2.44 showed that the ionization layer thickness was inversely related to the magnetic field strength through the Larmor radius,

$$L_a \propto R_L \propto \frac{1}{B} . \tag{2.51}$$

Combining Equations 2.50-2.51, it must be the case that these two lengths scale together,

$$L_c \propto L_a . \tag{2.52}$$

As a check on the form of the optimal magnetic field strength derived in Equation 2.49, it is a valuable exercise to make an estimate for an existing thruster configuration. If the definition of the Bohm velocity in Equation 2.27 is used in combination with an assumption

of high propellent utilization, the form for the optimal magnetic field in Equation 2.49 can be rewritten in terms of the mass flow rate and the discharge current as,

$$B \approx \frac{\dot{m} v_B}{\beta_a L_c I_d}.$$
(2.53)

The Russian built D-55 anode layer Hall thruster operates at a discharge current of 4.1A for a mass flow rate of 4.5mg/s and discharge voltage of 300V. If the electron temperature is estimated to be 35eV and the channel length is approximately 4mm, then for $\beta_a = 64$ the optimal magnetic field strength is 217G. The magnetic field strength near the anode was measured experimentally to be between 215-230G, indicating a good match.

2.1.5 Thruster Power and Perimeter

The conclusion about channel length scaling allows the thruster power and perimeter to be related. It is assumed for this discussion that the thruster to be scaled has a circular discharge chamber (perimeter$\approx \pi D$), but the analysis is valid for any closed drift geometry. If Equation 2.44 is combined with the $L_c \propto L_a$ result, several useful scaling relationships can be expressed simultaneously as,

$$R_2 - R_1 \propto R_L \propto \frac{1}{B} \propto L_c \propto L_a \propto \frac{A_e}{P_d}.$$
(2.54)

The exit area term can be expanded and the gap width terms cancelled,

$$R_2 - R_1 \propto \frac{A_e}{P_d} \propto \frac{D(R_2 - R_1)}{P_d},$$
(2.55)

to show that the power and diameter will scale together,

$$P_d \propto D.$$
(2.56)

Using Equation 2.8, which shows that $P_d \propto \dot{m}$, it can be concluded that the mass flow rate will also scale with thruster power and diameter,

$$P_d \propto D \propto \dot{m} . \tag{2.57}$$

2.1.6 Cross Sectional Dimensions and Magnetic Field Strength

Although it has been concluded that the thruster diameter (or perimeter) must scale with the discharge power and the mass flow rate, the cross sectional geometry is undetermined. However, it has been shown that the shape of the azimuthal cross section, that is a section in a plane containing the longitudinal axis, must be preserved and its size is related to the magnetic field strength. The channel width, channel length and magnetic field were related in Equation 2.54 as,

$$R_2 - R_1 \propto L_c \propto \frac{1}{B} . \tag{2.58}$$

Thus, the shape factor ratio of channel length to width must be preserved, and the magnetic field strength must scale inversely with their absolute values. However, because the cross sectional geometry can be independently chosen from the thruster diameter, this implies that non-circular geometries should also preserve the scaling properties. The "racetrack" style thruster introduced by Busek is one such example [32].

The conclusion that diameter and cross sectional geometry can be scaled separately highlights a potential design trade-off that could be used to optimize a low power thruster design. Using Equation 2.6, the plasma density near the exit plane will scale as,

$$n_e = \frac{\dot{m}\eta_u}{m_i v_B A_e} = \frac{\dot{m}\eta_u}{m_i v_B \pi D (R_2 - R_1)} \propto \frac{1}{R_2 - R_1} \propto \frac{1}{L_c} . \tag{2.59}$$

By noting that $D \propto \dot{m}$, propellant utilization is preserved, and the Bohm velocity is invariant as long as electron temperature is constant, the electron density is shown to scale inversely with the channel width (and length since they scale together). Photographic scaling of a thruster would imply that all dimensions should be scaled equally, and thus plasma density would scale inversely with the overall thruster size. However, Equation 2.59 suggests that a design trade could be made where the channel width and length are

scaled less strongly than diameter, reducing the plasma density in the thruster (compared to purely photographic scaling). This could potentially reduce the erosion of thruster walls and add lifetime to the device.

An additional benefit of scaling down the channel width and length less than the diameter (for a given target power) is that the required magnetic field is reduced (Equation 2.58). However, the larger channel width increases the distance between the magnetic poles and thus field losses are greater. It is unclear how strongly this will affect the design of the magnetic circuit. The challenge in executing this trade-off is that if the channel is expanded about the midchannel diameter, the center stem becomes increasingly smaller. This may result in overheating of the center stem if the cross sectional area for heat conduction is reduced too much, causing magnetic saturation of the center pole.

2.1.7 Summary of Ideal Scaling Analysis

The major results of the scaling arguments are summarized in the following two equations. Equation 2.60 shows that the discharge power and propellant flow rate will scale with the mid-channel diameter, or more generally with the perimeter. As previously mentioned, the gap width and channel length are not strictly required to be scaled with the diameter, but they are inversely related to both the required magnetic field and the resulting plasma density.

$$P_d \ , \dot{m} \propto D \tag{2.60}$$

$$n_e \ , n_i \ , B \propto \frac{1}{R_2 - R_1} \propto \frac{1}{L_c} \tag{2.61}$$

These two equations can be used to form the starting point of the design of a miniaturized version of a selected baseline thruster. As noted in the previous section, because the diameter (or more generally the perimeter) is not linked to the cross sectional dimensions, there is a trade-off that can be executed to optimize thruster lifetime. Figure 2.3 summarizes the path taken to arrive at the conclusions in Equations 2.60-2.61.
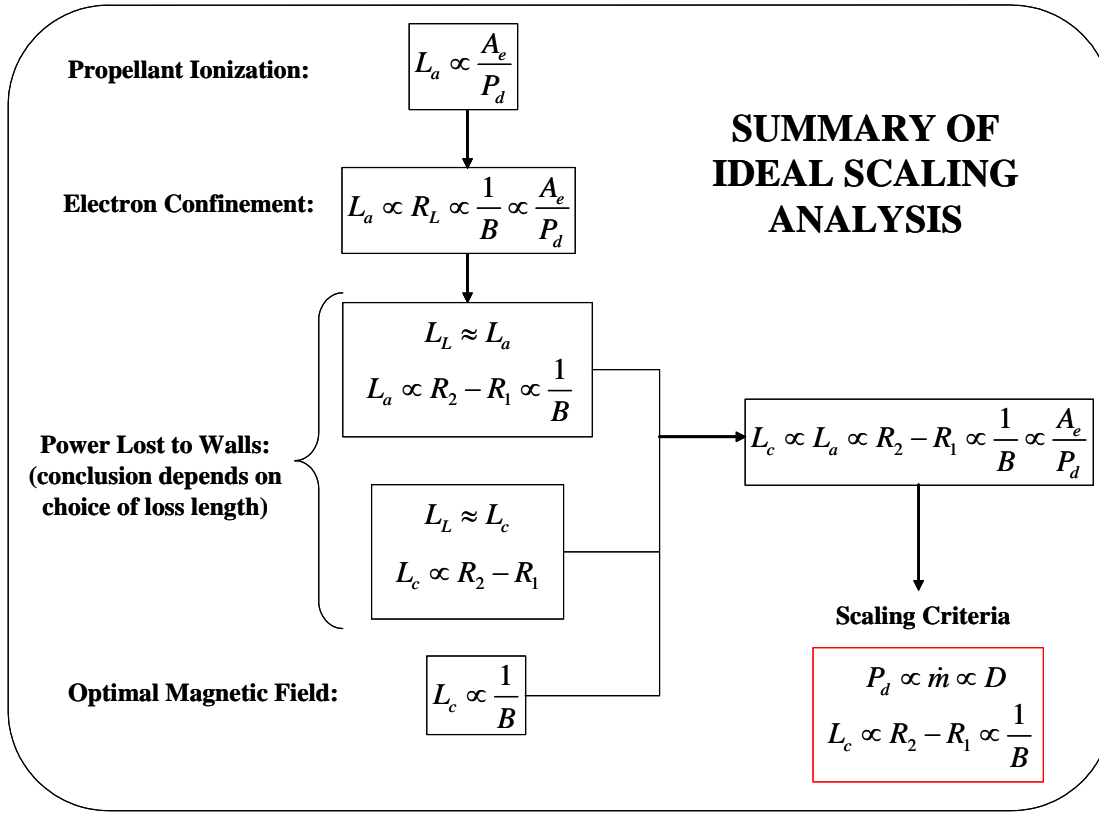
Figure 2.3   Summary of the ideal scaling theory.

2.1.8 Important Assumptions

Two critical temperature invariance assumptions have been made during the course of the ideal scaling analysis. It is worth pointing out these assumptions so that they can be examined once the scaling theory is tested experimentally.

Electron Temperature

The assumption of constant electron temperature with scaling can be checked using an argument originally formulated by Khayms and Martínez-Sánchez [27]. If elastic losses and energy radiation are ignored, the electron energy equation can be written in terms of the electron current density, $\bar{j}_e$, the electron enthalpy, h_e and the thermal conductivity of the plasma, k_e. The energy equation is expressed as,

$$\nabla \cdot \left(- \frac{\bar{\bar{j}}_e}{e} h_e - k_e \nabla T_e \right) = \bar{E} \cdot \bar{j}_e . \tag{2.62}$$

The enthalpy term includes thermal energy, ionization energy and kinetic energy of the electrons. It will be constant in scaling if the electron temperature is also constant. The Wiedemann-Franz law states that the ratio of thermal conductivity to the electrical conductivity of a metal is proportional to the temperature. A plasma can be assumed to be similar to a metal, in that both transport of charge and transport of heat are due to electrons, where the constant of proportionality is simply k/e^2. Therefore, the ratio of plasma thermal conductivity to plasma electrical conductivity, σ_p, can be written as,

$$\frac{k_e}{\sigma_p} = \frac{k}{e^2} T_e . \tag{2.63}$$

The electrical conductivity (which depends most strongly on electron temperature) and electron temperature are assumed to be constant with scaling, thus the thermal conductivity will be constant as well. It can therefore be shown that each term in the electron energy equation will scale as $1/L^2$, where L is a characteristic length over which the electric field acts on the electrons. Energy conservation will only be satisfied at all scales if the electron temperature does not depend on scale.

Neutral Temperature

The neutral propellant flow interacts with thruster surfaces and is assumed to be accommodated at the thruster wall temperature through collisions. Thus, the assumption of constant neutral temperature with scaling can be checked by examining the effect of plasma heating on thruster temperature. The heat flux into thruster surfaces, Q, can be written as,

$$Q = \frac{P_r}{A_w} = \frac{k_w}{L}(T_w - T_0) . \tag{2.64}$$

This heat flux into the thruster surfaces is determined by the ion-electron recombination power, P_r, per unit of wall area, A_w. This should scale with the material conductivity, k_w,

and the temperature difference between the thruster walls and a reference temperature that the thruster conducts to, T_0, but inversely with the characteristic length of the thruster, L. Each term in this equation should scale as $1/L$ if materials of similar conductivity are used since $A_w \approx L^2$ and $P_r \approx L$. Thus, the resulting wall temperature and neutral temperature should be invariant with scaling.

2.2 Summary of Adopted Scaling Method

Turning from general considerations to the particular thruster design used in this research, two assumptions involving thruster dimensions were made early in the design phase before the link between channel length and ionization layer thickness was discovered. First, previous research has shown that small changes in channel length ($\Delta L_c \leq 4$mm), the axial distance between the downstream tip of the anode and the thruster exit plane, have very little affect on performance [33-35]. It was therefore assumed during the design phase that overall channel length was not an important factor for performance. The ionization layer thickness was considered to be the dominant characteristic length in the axial direction because it directly influences total ionization volume. Because this length could not be directly controlled with confidence, and because the actual channel length of the D-55 was unknown, the channel length was not perfectly scaled during the design process. The channel length of the miniaturized thruster was selected more for magnetic concerns than for preserving recombination losses. However, the results of the experimental portion of this research point to the fact that channel length is likely an important factor for erosion and thruster lifetime, and may in fact be significant for performance. In particular, the violation of $L_c/R_2 - R_1$ shape similarity appears to lead to T_e not being conserved, with rippling consequences for the rest of the scaling arguments.

Secondly, a choice was made to scale channel width by the same factor as channel diameter. This was not strictly necessary but it implies that photographic scaling is an optimal assumption, or at least worth testing experimentally. Thus, the governing scaling relationships used in the design of the scaled down thruster for this research were,

$$P_d \propto \dot{m} \propto D \propto R_2 - R_1 \propto \frac{1}{B}. \tag{2.65}$$

2.3 Baseline Thruster Selection

2.3.1 Baseline Thruster Candidates

The candidates for the baseline thruster included both ceramic and metallic walled Hall thrusters. The most well known versions of each type are the Fakel SPT-100 (ceramic) and the TsNIIMASH D-55 (metallic), both originally developed in the former Soviet Union. The model numbers indicate the diameter of each thruster in millimeters, with the SPT-100 being almost twice the size of the D-55. Both thrusters are technically mature and have been flown in space aboard Earth orbiting satellites [9]. The D-55 was the first Hall thruster flown on a U.S. satellite, and the SPT-100 is currently being licensed for use on geostationary communications satellites made by Space Systems Loral [36-37].

2.3.2 Considerations for Scaling

The size difference between the SPT-100 and the D-55 is an important consideration because both of these thrusters are nominally 1.35kW thrusters with almost identical performance. Since the power and diameter will be scaled together, for a given power level the metallic version would be almost half the size of the ceramic version. This makes the design and construction of a metallic walled thruster more challenging for a desired power level of the subscale version. Conversely, it is easier to work with metals than ceramics at the millimeter scale level because thin ceramics have a tendency to crack when subjected to the large heat loads found in a plasma thruster. Both thrusters have been studied extensively and there are plenty of data on each model, but the SPT-100 has certainly received more attention due to its wealth of flight experience [9].

The majority of the low-power Hall thruster research over the past decade has focused on ceramic thrusters. This is most likely because of the popularity and wide-ranging acceptance of the SPT models, but it could also be motivated by the greater secondary electron

emission of ceramic walls. This allows the plasma to operate at a lower average electron temperature, thereby decreasing the energy of ions impacting walls. This is thought to be helpful for thruster lifetime because lower energy ion flux will erode less material from the ceramic lined channel. Electron temperature also plays a role in beam divergence, as the strength of the sheath can affect the radial acceleration of ions leaving the thruster. However, the proponents of metallic walled thrusters have long extolled its more protruded anode structure, claiming that it reduces wall erosion by actually pushing the plasma acceleration process out of the thruster channel [34]. Accelerated wear tests performed at JPL during the early 1990s seem to support the idea that the D-55 may have a lifetime advantage over the SPT-100 [38]. Lifetime is of particular concern when considering a scaling scenario in which plasma density scales inversely with thruster dimensions since erosion rates are directly proportional to density.

2.3.3 Final Selection

The D-55 was selected as the thruster from which to base the design of the miniaturized Hall thruster for several reasons. The potential for lower erosion and the ease of working with metals in the fabrication process were the most notable technical factors. The opportunity to contribute to an area of research not so well explored (low-power metallic walled thrusters) and the inherent tendency towards smaller size with metallic walled thrusters were equally motivating factors. The selection of the D-55 fits the twofold objective of this thesis: to understand the underlying physics of Hall thruster scaling and to push the envelope of miniaturization in plasma propulsion.

2.4 Scaling Results

Table 2.1 shows the results of the adopted scaling arguments as applied to the design of the miniature thruster based on the TsNIIMASH D-55. A target nominal power level of 200W was selected for the scaling. This power level represents a slightly less challenging level of miniaturization when compared to the previous work by Khayms, but still repre-

sents an opportunity to design and build one of the smallest Hall thrusters in the world to date [13-15].

In keeping with the Russian tradition of naming thrusters using their channel diameter, the scaled down thruster will be referred to as the Miniature Hall Thruster, or MHT-9 (this abbreviation can also be conveniently considered as the MIT Hall Thruster). Data used for scaling the D-55 were taken from two separate sources. A very thorough set of performance measurements were completed by Sankovic, Haag and Manzella at the NASA Lewis Research Center [39]. Although the D-55 is commonly referred to as a 1.35kW thruster, this is the total system power including the electromagnets and cathode. The data point used for scaling was from a discharge power of 1.24kW because this condition was identified as "nominal" by Sankovic, Haag and Manzella.

The magnetic field strength and gap width numbers were taken from a paper by Marrese et al [40]. Detailed engineering drawings for the D-55 were not publicly available, so the gap width used for scaling was the total radial width of the anode, not the width of the entire discharge channel. This width for the D-55 was 15mm, as shown in Marrese's paper. The magnet currents used for the magnetic field topology data taken by Marrese et al were not published, but it has been assumed that the nominal condition was used (as identified by Sankovic, Haag and Manzella).

These scaling results represent the starting point of the design for the MHT-9 and are estimates of the dimensions and operating parameters that will theoretically provide for similar performance between the D-55 and the miniaturized thruster. The full scale design process included the use of more detailed engineering tools and analysis to produce an optimized design solution. In developing the MHT-9, every effort was made to allow the design to remain flexible and provide room to push the experiments in different directions. Although the ideal scaling analysis is for a single point design, Hall thrusters can be operated over a wide range of operating conditions. It is the variation of these operating condi-

tions and the resulting performance that will shed light on the ability of this analysis to determine the optimal design point.

TABLE 2.1   Hall Thruster Scaling Results

Scaling Parameter	D-55	MHT-9
Scaling Factor	1.0	6.2
Discharge Power (W)	1239	200
Discharge Voltage (V)	300	300
Discharge Current (A)	4.10	0.67
Thruster Diameter (mm)	55.0	8.9
Channel Width[a] (mm)	15.0	2.4
Magnetic Field Strength (G)	223	1378
Propellant Flow Rate (mg/s)	4.52	0.73
Thrust (mN)	79.2	12.8[b]
Specific Impulse (s)[c]	1786	1786[b]
Efficiency[d]	0.56	0.56[b]

a. Channel width numbers are actually for anode width.

b. Performance predicted by ideal scaling arguments.

c. Specific impulse numbers do not include cathode flow.

d. Efficiency numbers are for "anode efficiency" and therefore do not include cathode flow, cathode power or magnet power.

Chapter 3

DESIGN OF THE MHT-9

The MHT-9 design process began with the outputs of the ideal scaling arguments presented in Chapter 2. A target power level of 200W was selected with the D-55 as the baseline thruster to be scaled down. Scaling arguments determined the midchannel diameter and the nominal flow rate. The channel width was scaled by the same factor as the diameter and this then set the required magnetic field strength. Once the starting point for the design had been identified, an initial magnetic circuit was designed using finite element methods. A propellant feed system and anode were then designed, as well as supporting structure for electrical isolation. Finally, a finite element thermal model was developed to provide insight on heat rejection pathways and internal thruster temperatures. Although this model has only limited accuracy, it proved valuable for material selection and allowed useful design iteration to be performed between the magnetic circuit design, propellant delivery system and the supporting structure used for heat rejection. The design process is summarized below.

Thruster Design Process

1. Select a technologically mature baseline thruster.
2. Select a target nominal power level for the scaled down thruster.
3. Use ideal scaling relationships to determine approximate dimensions and operating conditions from the baseline thruster.
4. Design an initial magnetic circuit using a magnetostatic finite element model.

5. Design an initial anode and propellent distribution system to ensure flow uniformity and electrical isolation.

6. Develop a finite element thermal model to evaluate the design with respect to the thermal constraints. Adjust dimensions, select materials, add heat sinks and thermal barriers where necessary.

7. Iterate on the design by repeating steps 4-6.

The details of this design process as applied to the MHT-9 are described in the sections that follow, but this process could theoretically be applied to any thruster scaled (up or down) from a baseline design. Steps 1-3 were covered by the ideal scaling treatment discussed in Chapter 2. This chapter will address steps 4-7 and present the final thruster design. Although the steps were performed in the order above, they will be presented in a format that allows the thruster components to be built up one by one to a full design drawing before concluding with thermal modeling of the entire structure.

3.1 Magnetic Circuit

3.1.1 Field Requirements

The scaling arguments showed that the thruster required an approximately 0.14T radial field strength near the tip of the anode, based on the D-55 magnetic field measurements taken by Marrese [40]. Several additional requirements were laid out for the magnetic circuit. The materials were required to withstand high temperatures due to plasma heating of the thruster without demagnetization or total loss of permeability. The field lines must be as parallel as possible to the anode face in order to slow electrons and prevent high electron back-streaming currents. The circuit could not be allowed to magnetically saturate near the critical gap region, close to the tip of the anode and exit plane of the thruster, because this would cause field line distortion.

Previous work at MIT showed that using permanent magnets that are brittle and chip easily can lead to contamination of the channel with small magnetic debris [15]. This type of material can get lodged into tight crevices and cause electrical shorts between the anode

and low potential surfaces. If permanent magnets were to be used, they would need to be encapsulated in a metallic coating as a preventive measure. Finally, although tuning capability of the field strength (as with electromagnets) was not prescribed as a formal requirement, it would be beneficial for finding the optimum field condition for each thruster operating point. Tuning capability also allows for a greater exploration of the performance map, which is useful for validation and refinement of the overall scaling theory.

3.1.2 Components and Configuration

Electromagnetic Coils

The D-55 magnetic circuit uses four electromagnets in a configuration that places three coils in triangle around the outside of the channel and one in the center stem [38-39]. Ideal scaling arguments require that the magnetic field strength increase inversely with the thruster size, thus the high field strength needed at small scale would require a high amp-turn coil. Ampere's law applied to an electromagnetic coil shows that the magnetic field produced within the coil is,

$$B = \frac{\mu_c N I_c}{L_c},$$ (3.1)

where μ_c is the core permeability, N is the number of turns in the coil, I_c is the coil current and L_c is the length of the coil. Figure 3.1 shows a diagram of an electromagnet in cross section. If the length of the coil scales as the characteristic length of the thruster, L, and it is recalled that the ideal scaling analysis showed that the magnetic field must scale inversely with the thruster size ($B \propto 1/L$), the coil current then scales as,

$$I_c \propto \frac{BL}{N} \propto \frac{1}{N}.$$ (3.2)

Alternatively, it can be said that the product NI_c is a scaling constant. The resistance of the coil depends on the wire resistivity, ρ, the length of the wire, L_w, and the cross sectional area of the wire, A_w. The length of the coil wire will scale as the product of the number of
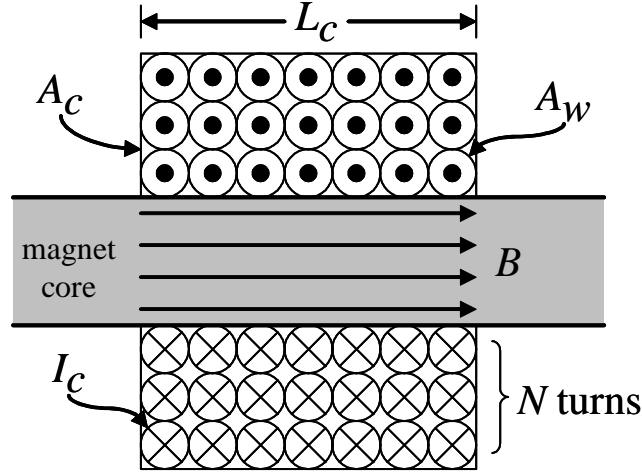
Figure 3.1 Cross sectional view of an electromagnet with N turns within an
area A_c. The wire carries a current I_c with cross sectional area A_w.

turns and the characteristic length of the thruster, NL, since the length of one coil loop depends on the core diameter (which should scale as L). Thus, the coil resistance, R_c, scales as,

$$R_c = \frac{\rho L_w}{A_w} \propto \frac{NL}{A_w}. \tag{3.3}$$

The power dissipated by a coil is determined by the current and resistance. Using Equations 3.2-3.3, the coil power scales as,

$$P_{coil} = I_c^2 R_c \propto \left(\frac{1}{N}\right)^2 \frac{NL}{A_w} \propto \frac{L}{NA_w}. \tag{3.4}$$

The number of turns that can fit within the cross sectional area of the coil will scale as the ratio of the area available for the coil to the cross sectional area of the wire,

$$N \propto \frac{A_c}{A_w}, \tag{3.5}$$

and this can be used in Equation 3.4 to show that the coil power scales as,

$$P_{coil} \propto \frac{L}{A_c} \propto \frac{1}{L}.$$
(3.6)

It is noted that the cross sectional area available for the coil within the thruster scales as the characteristic length squared ($A_c \propto L^2$). Thus, using magnetic coils at small sizes eventually becomes impossible because of the increasing heat flux dissipated by such a coil. Excessive heating of a coil can electrically short the magnet wire insulation, and also reduce the permeability of the magnetic core material used to shape the field lines. The scaling relation in Equation 3.6 indicates that the nominal D-55 coil power of 43.5W would require 270W in the scaled down MHT-9 thruster.

It was decided that magnetic coils would be cast aside in favor of permanent magnets to provide the majority of the required field strength. However, trim coils were considered for field tuning purposes. A secondary motivation for the decision to use a permanent magnet system was that it provided a chance to expand the experience in the field using permanent magnets in Hall thrusters, which looks to be a growing trend [13-15, 25, 41].

Permanent Magnets

The use of permanent magnets circumvents the issue of increased ohmic heat dissipation of electromagnetic coils at small scale. However, permanent magnets bring their own unique complications as well. Using permanent magnets leaves no option for shutting down the field in the thruster. In theory this could present a problem for thruster startup when the field is strong and the electron density is low, making it difficult to initiate the ionization cascade process. As with coils, permanent magnets are also subject to temperature constraints. Permanent magnets typically experience a reversible loss of field strength with increasing temperature until the operating temperature limit is reached, beyond which irreversible damage will begin to occur. The Curie point is defined as the point where the magnet has been completely demagnetized. The high permeability materials used for the circuit core, typically iron based alloys, also lose permeability as their temperature is increased and must be monitored for field saturation.

Permanent magnets also present a problem from a spacecraft integration perspective. Although the ions in the thruster are generally considered to be unmagnetized, they do leave the thruster with a small azimuthal velocity. This ion angular momentum will induce a small torque on the spacecraft that must be absorbed by momentum wheels and eventually taken out of the system through propulsion. Electromagnets provide the option of reversing the field direction (radially positive or negative) to induce a torque in the opposite direction and remove the angular momentum without a special maneuver to do so. Permanent magnets obviously do not have the option of reversing their field direction once placed aboard a spacecraft. One potential solution to this problem would be to use pairs of thrusters with opposing magnetic field directions. In the laboratory this is not an important issue, but it is an important consideration for the long term future of the technology.

Configuration Concepts

The scaled down thruster uses a permanent magnet made from a high temperature grade of samarium cobalt (SmCo). The particular magnetic material selection is discussed in detail in the following section. Several concepts for the magnetic circuit configuration were explored in the early stages of the design. Figure 3.2 highlights three of these initial ideas.

All three of the initial magnetic circuit concepts shown utilize a permanent magnet (or several) to drive the majority of the field strength in the thruster, but they also incorporate trim coils to make adjustments to the field shape and strength. Figure 3.2 shows the permanent magnets in red, the soft magnetic material (iron) in grey and the trim coils in blue. All of the permanent magnets are magnetized in the axial direction.

Concept A utilizes several SmCo rods placed around the outside of the discharge channel. Large field strength tuning could be achieved by varying the number of rods and small strength adjustments could be done through the use of coils wrapped around each of the rods. This concept was rejected because it was difficult to produce a strong enough field

Concept A: SmCo Rods with
Individual Coils (not shown)
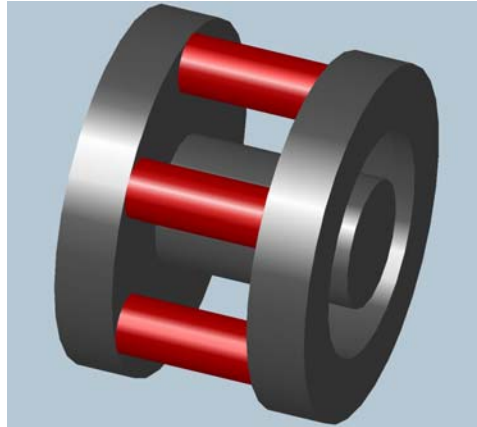
Concept B: Cylindrical SmCo Magnet
with Center Stem Coil
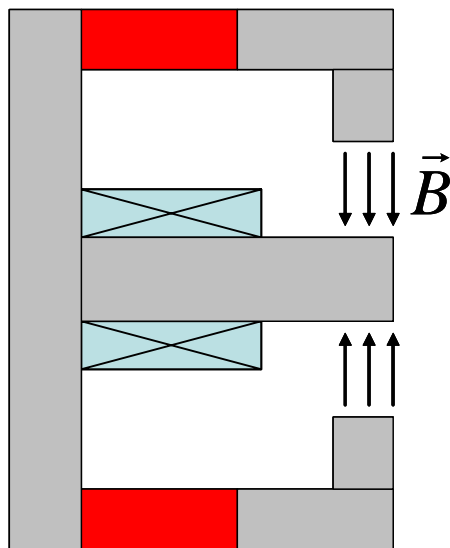
Concept C: Cylindrical SmCo Magnet
with Opposing Concentric Coils
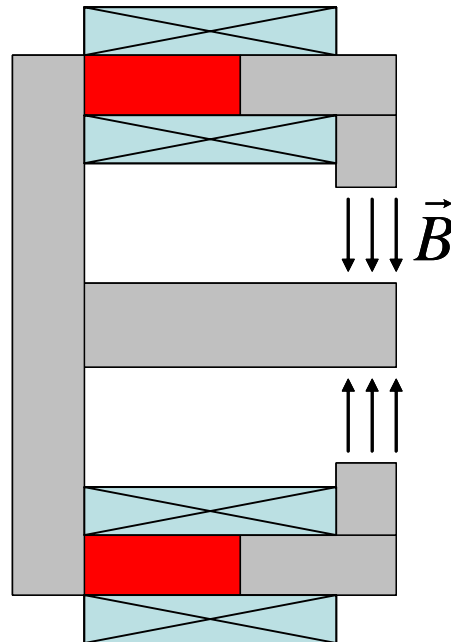
Figure 3.2   Three different initial magnetic circuit concepts.

with only the rods. The size of the rods approached the one piece cylindrical shape shown
in the other two concepts to overcome the flux leakage between the magnets.

Concepts B and C both employ a cylindrically shaped magnet and at least one trim coil.
They are shown in cross-section in Figure 3.2. The permanent magnet supplies the

required field strength in both configurations, and the coil adjusts the field strength up or down by passing current through the coil(s). Concept B is very effective magnetically because the coil is positioned along the centerstem and adjusts the field directly with little leakage. However, the centerstem region is the most critical thermally as it is forced to accept and conduct large heat loads from the plasma. This heat load could potentially melt the coil insulation and cause a short. High temperatures can also reduce the permeability of the centerstem, reducing the effectiveness of the coil (and the permanent magnet).

Concept C utilizes two concentric coils that pass current in opposing directions. This idea was originally conceived as a way to reduce the thermal load on the coils by placing them further out in the radial direction. Although this concept is novel and effective in theory, it is difficult to implement in this geometry because the coils must operate partially around the SmCo magnet. The magnet has a low permeability (relative to iron) and therefore greater field leakage reduces the effectiveness of the trim coils in this region.

Concepts B and C were eventually both rejected because of thermal concerns. The predicted temperatures along the magnet and iron exceeded 240°C, the operational limit of polyimide magnet wire insulation. Details about the thermal model that enabled this decision are provided in Section 3.4. The cylindrical permanent magnet was retained in the final design because it easily provided the required field strength. However, a different concept was needed for field tuning.

Final Configuration

Figure 3.3 shows the final configuration of the magnetic circuit for the MHT-9 and Figure 3.4 shows a plot of the magnetic flux lines. The cylindrically shaped SmCo magnet (shown in red) has an inner diameter of 17mm and an outer diameter of 25mm. The magnet is 5mm long and is magnetized in the axial direction. The magnetic core material (shown in grey) is made of Hiperco 50A, an iron cobalt alloy. The particular magnetic material selections are discussed more in the following section. Field strength tuning is accomplished through the use of a magnetic shunt. The SmCo magnet is oversized to pro-

vide a stronger field than the required 0.14T. In order to reduce the field strength, a magnetic steel ring is slid over the outside diameter of the magnet. By using rings of different sizes, more or less field strength can be siphoned off the circuit, allowing the strength in the discharge chamber to be adjusted. This tuning system is described more in Section 3.1.5, and a schematic of the circuit with the shunt is shown in Figure 3.12.

Figure 3.3 Cross sectional view of the MHT-9 magnetic circuit configuration. The permanent magnet is shown in red, and the core material is in grey.
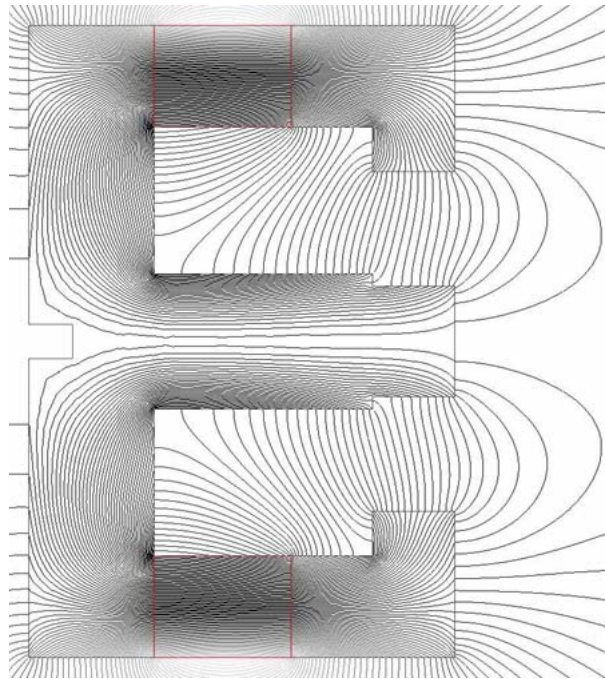
Figure 3.4 Cross sectional plot of magnetic flux lines for the MHT-9 magnetic circuit operating at a magnet temperature of 400°C.

The tip of the center stem in the circuit is reduced in diameter to allow room for a guard ring. The field lines produced by the circuit, pictured in Figure 3.4, show that they are nearly radial in the exit plane region. This slows the diffusion of electrons into the channel towards the anode. By placing the SmCo magnet far from the discharge region (near the exit plane), the field leakage is increased but this also reduces the temperature in the magnet and allows for greater field tuning capability.

3.1.3 Magnetic Material Selection

Simple Circuit Model

The idealized model of a magnetic circuit using a permanent magnet can lend some insight into material selection and circuit design. The typical "c-core" circuit geometry is pictured in Figure 3.5, with the magnetic field of a permanent magnet (B_m) driving the field in a vacuum gap (B_g), connected by a core material of high permeability.
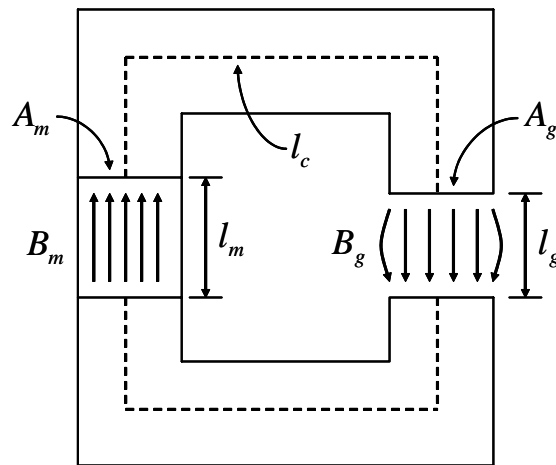
Figure 3.5 Cross sectional diagram of a typical magnetic circuit with a permanent magnet driving the field in a vacuum gap for a "c-core" style geometry.

Simple analysis of this circuit can be performed if it is assumed that the core material has infinite permeability, there are no field leakages and field fringing is negligible. It should be noted that this type of analysis is most useful for understanding the trends and qualitative requirements for material selection and component sizing. In reality, leakage fields and fringing are significant and can result in serious under prediction of the required magnet size. Finite element methods are required to get an accurate picture of the behavior of even the simplest magnetic circuits, unless cumbersome empirical methods are used to estimate the fringing and leakage factors.

The circuit above, and all magnetostatic circuits for that matter, are governed by two of Maxwell's equations. Their differential forms in a vacuum are shown below.

$$\overline{\nabla} \cdot \overline{B} = 0 \tag{3.7}$$

$$\overline{\nabla} \times \overline{H} = \overline{j} + \varepsilon_0 \frac{\partial \overline{E}}{\partial t} \tag{3.8}$$

The right hand side of Equation 3.8 includes the terms relating to magnetic fields produced by currents in the plasma and displacement currents. Both of these terms are negligible relative to the applied magnetic field and can be ignored. Equation 3.8 can thus be rewritten as,

$$\overline{\nabla} \times \overline{H} = 0. \tag{3.9}$$

In magnetic circuit analysis, the integral forms of these equations are more useful. They can be used to compare magnetic fluxes in different parts of the circuit and write conservation equations for the magnetic intensity.

$$\iint \overline{B} \cdot \overline{dA} = 0 \tag{3.10}$$

$$\oint \overline{H} \cdot \overline{dl} = 0 \tag{3.11}$$

If Equation 3.10 is applied to a closed surface that encompasses the boundary between the core material and the vacuum gap (or the boundary between the core material and the magnet), a flux conservation equation results. Magnetic flux through the circuit is conserved as the area and medium change,

$$B_g A_g = B_m A_m = B_c A_c. \tag{3.12}$$

When Equation 3.11 is applied around the loop passing through circuit, shown as a dashed line in Figure 3.5, another conservation equation results,

$$H_c l_c + H_m l_m + H_g l_g = 0. \tag{3.13}$$

With the earlier assumption of infinite core permeability ($\mu_c \approx \infty$), the first term in Equation 3.13 can be ignored (since $B_c = \mu_c H_c$). This equation can also be expressed in terms of the field and vacuum permeability within the gap,

$$H_m = -\frac{B_g l_g}{\mu_0 l_m}.$$

(3.14)

The permanent magnet in the c-core circuit can be modeled as having a linear normal demagnetization curve, as shown by the black dashed line in Figure 3.6. The "normal" curve (solid black) is the curve associated with operation of the magnet within a circuit that has a gap in it for useful work, whereas the "intrinsic" curve (solid green) applies to the more theoretical case where the magnet is operated in a completely closed circuit [42]. The linear approximation to the normal curve is very accurate for the "rare earth" permanent magnet materials, which include SmCo [43]. The red dashed line represents the load line for the circuit and it has a slope of $B_m / \mu_0 H_m$. The load line is a characteristic of the geometry of the circuit only and indicates where on the demagnetization curve the magnet is operating. The load line can be expressed as a function of dimensional properties only when written as,

$$\frac{B_m}{\mu_0 H_m} = -\frac{A_g l_m}{A_m l_g}.$$

(3.15)

It is generally considered good practice to operate the circuit with the load line "above the knee" so that small changes in the forcing field (H_m) do not rapidly demagnetize the circuit. The linear approximation to the normal curve can be written in terms of the particular magnetic material's coercivity (H_c), remanence (B_r), and its operating point on the demagnetization curve (H_m, B_m),

$$B_m = \frac{B_r}{|H_c|} H_m + B_r.$$

(3.16)
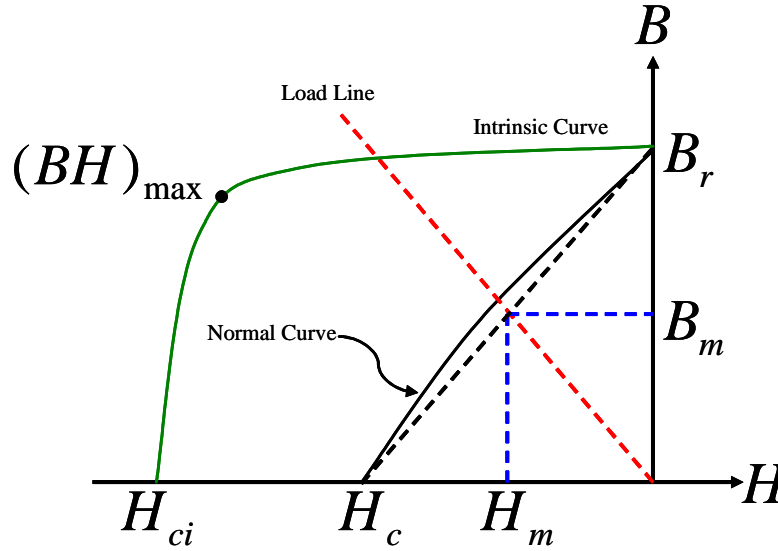
Figure 3.6 Demagnetization curves for a permanent magnet with a linear approximation to the normal curve.

If Equations 3.12 and 3.14 are combined with Equation 3.16, an expression for the field within the gap can be found that illustrates the important trends in the design of the c-core circuit,

$$B_g = \frac{B_r}{\frac{A_g}{A_m} + \frac{B_r}{\mu_0 |H_c|} \frac{l_g}{l_m}}.$$ (3.17)

There are several important lessons to be learned from this equation that provide qualitative input for the design of the magnetic circuit:

1. It is important to select a permanent magnet material with high B_r and H_c in order to meet the high field requirement in the gap as the thruster is scaled to small size.

2. Increasing the magnet to gap area ratio, A_m/A_g, will increase the field strength in the gap.

3. Increasing the magnet to gap length ratio, l_m/l_g, will increase the field strength in the gap.

These lessons helped guide the material selection and the geometry adjustments as the magnetic circuit was designed. The material trade-offs are discussed in the following section. The geometry of the circuit was designed using finite element methods in Ansoft's Maxwell software. Most of the analysis was conducted in axisymmetric coordinates because the circuit design is almost perfectly symmetric. A few three dimensional models were constructed to show that the minor azimuthal asymmetries due to bolt holes in the base of the centerstem were not significant in determining the field strength in the exit plane region. Parametric studies were conducted to optimize the geometry of the magnetic circuit and evaluate the effects of temperature and shunting on field strength.

Permanent Magnet Material Selection

Several magnetic materials were considered for the main driving magnet including Alnico, NdFeB and SmCo. Table 3.1 shows typical properties of each of these materials [42]. The product of *BH* is typically used to evaluate the maximum magnetic energy that can be extracted from a magnetic material and it represents the point on the intrinsic demagnetization curve furthest from the origin.

Alnico magnets were originally developed in the 1940's and are an alloy of aluminum, nickel, cobalt and iron. They can be either cast from a molten alloy or they can be sintered from a very fine powder. Alnico magnets can operate at very high temperatures but are relatively easy to demagnetize because of their low coercivity. Neodymium iron boride (NdFeB) magnets became commercially available more recently in the 1980's. These magnets are formed by a sintering and pressing process or they can be bonded with plastic binders. NdFeB magnets have the highest possible magnetic energy of the three candidates but their high temperature performance is very poor [42].

Samarium cobalt was selected for its high operating temperature and Curie point, large residual field strength (remanence) and its strong resistance to demagnetization (high coercivity). The particular grade of SmCo used in the MHT-9 is the EEC-16-T550, made by the Electron Energy Corporation using their proprietary thermal stabilization process to

TABLE 3.1 Typical Properties of Permanent Magnet Materials Considered for the MHT-9

	B_r (Gauss)	H_c (Oersteds)	Maximum BH (MGOe)	Maximum Operating Temperature (°C)	Curie Point (°C)
Alnico	8200	1650	5.3	550	890
NdFeB	13,500	11,000	44	150	310
SmCo	10,500	9,000	26	300[a]	825

a. This value is typical, but a proprietary grade made by the Electron Energy Corporation can have operating temperatures up to 550°C.
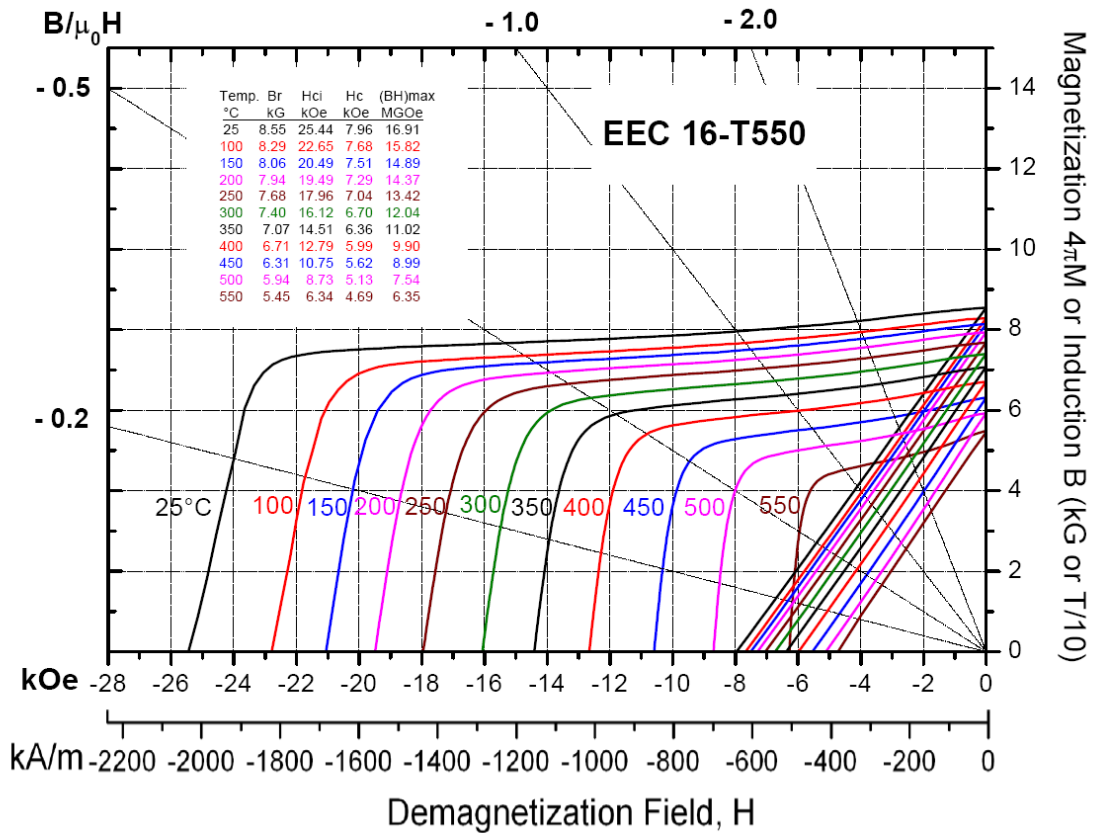
Figure 3.7 Demagnetization curve for the samarium cobalt material used in the MHT-9 as it varies with temperature [45]. The intrinsic curves have a square-like shape while the normal curves are nearly straight lines with positive slope. Load line values are shown in black starting from the origin with negative slope. These material data were used to model the MHT-9 permanent magnet in finite element simulations of the magnetic circuit. The variation of the field output with temperature was included in the model. The MHT-9 magnet operates at a load line of -3.14 at a temperature of 300°C.

increase the useful operating temperature limit to 550°C [44]. Traditional SmCo magnet grades typically begin to permanently demagnetize in the 300-350°C temperature range. The demagnetization curve for EEC-16-T550 is shown in Figure 3.7. The variation of the curve with temperature shows how the performance of the magnet decreases as it is heated. These data were used to model the MHT-9 magnetic circuit at many different magnet operating temperatures to ensure that the field requirement in the thruster could be met at the temperatures predicted by the thermal model. The EEC-16-T550 material was conservatively modeled with a remanence (B_r) of five percent less than the values in the published chart shown in Figure 3.7. This is because the magnet was thermally stabilized at a very high temperature to ensure continuous operation above 500°C [44].

This material selection for the permanent magnet is a good middle-ground magnetically and a cautious choice thermally. It allows for a margin of safety in the thermal model so that it can be assured not to permanently demagnetize due to plasma heating of the thruster. The MHT-9 magnet is also coated with a thin layer of nickel to prevent chipping and crumbling.

Core Material Selection

Two different materials were considered for the core pieces of the magnetic circuit: Hiperco 50A and 1018 cold rolled steel. Hiperco and 1018 steel are very similar magnetically, but Hiperco has a slightly higher saturation field strength, B_s, maximum permeability and Curie point. Hiperco is an iron cobalt vanadium alloy used for magnetic cores and also in strip form for aircraft generators and motors. The 1018 grade of steel is referred to as "low-carbon" steel and is often used as an inexpensive material for magnetic cores. The two materials are compared in Table 3.2. Figure 3.8 shows part of the magnetization curves for both materials. The Hiperco 50A data in this plot are for a bar with the standard heat treatment for the material [46]. The steel data are for untreated material [43].

The plot in Figure 3.8 shows that the maximum permeability ($\mu_c=B/H$) of Hiperco is higher than that of steel, meaning that Hiperco is more easily magnetized than steel. Both

TABLE 3.2 Comparison of Soft Magnetic Core Materials

Core Material	B_s (T)	Curie Point (°C)	Thermal Conductivity (W/m-K)
1018 Steel	2.1	760	51.9
Hiperco 50A	2.4	940	29.8
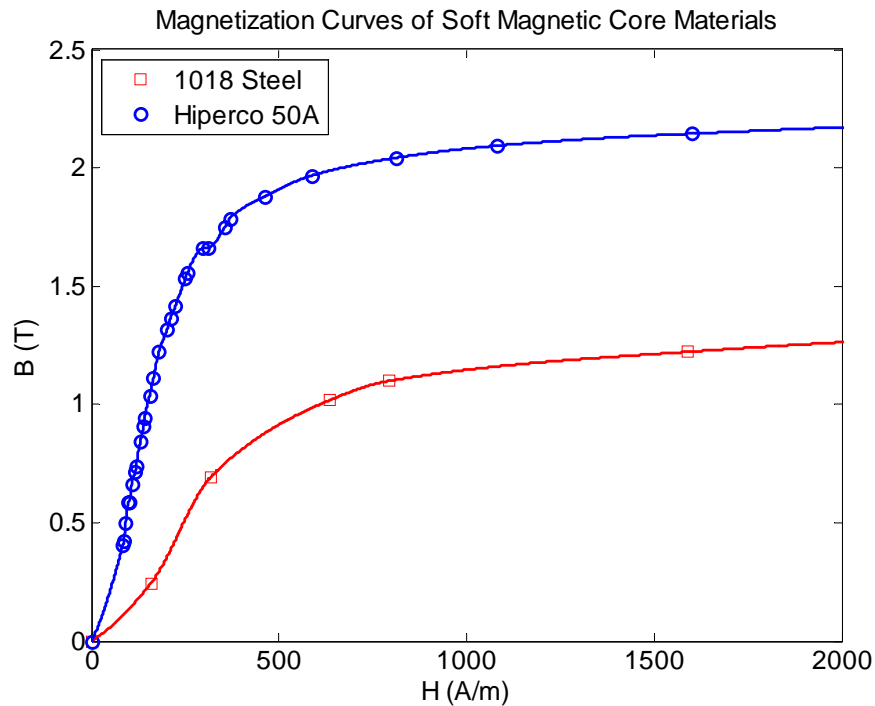
Figure 3.8 Magnetization curves for 1018 cold rolled steel and Hiperco 50A [43, 46]. All data taken at room temperature.

materials enter the saturation portion of their magnetization curves at roughly 500A/m, but Hiperco has a much higher saturation level than low-carbon steel. However, complete saturation of the magnetic core is a situation that should be avoided since it distorts the field shape and increases field line leakage.

Although it exhibits superior magnetic properties, Hiperco has a lower thermal conductivity than steel. If the core material is an important component of the heat rejection pathway, this can actually lead to higher temperatures in the pole regions near the plasma discharge. If the permeability of the core material decreases with increasing temperature (usually the

case), then this could potentially negate any magnetic advantages if a Hiperco core were forced to operate at a higher temperature than a core made from steel.

A literature search for the behavior of soft magnetic materials subjected to DC magnetic fields at high temperature was made in order to model the decline in permeability as the core material heats up from plasma contact. However, very little research in this area was discovered. A 1967 NASA report on magnetic materials showed magnetization curves for Hiperco 50 laminations (0.004in and 0.008in thick) at temperatures up to 1400°F [47]. The 0.004in. lamination plot from this report is shown as Figure 3.9. The saturation field strength for both thicknesses dropped from 2.4T to 1.8T when raising the temperature of the lamination from room temperature to 1400°F (760°C). Although the shapes of the magnetization curves for the two different thicknesses were different, their saturation levels matched and were used as a reference in studying the saturation of the MHT-9 magnetic circuit. Unfortunately, there was no research located on the changes in permeability or saturation field strength of low-carbon steel as its temperature is increased.
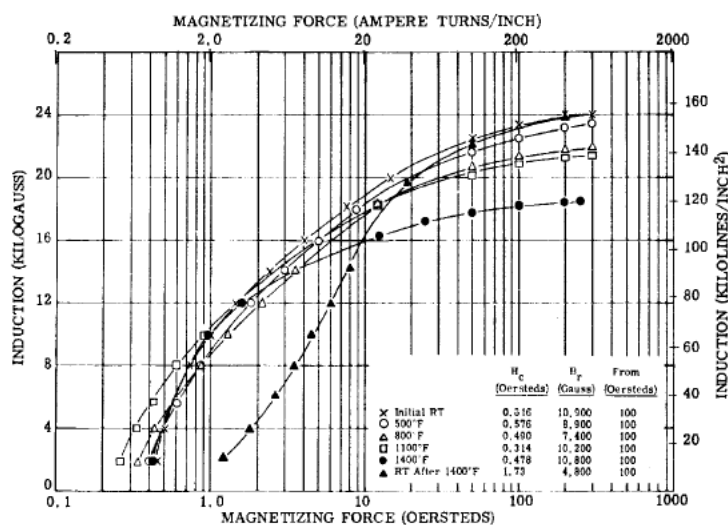
Figure 129. - Direct-current magnetization curves for Hiperco 50 alloy 0.004-inch laminations. Test atmosphere, air to 800° F and argon above 800° F; interlaminar insulation, aluminum orthophosphate.

Figure 3.9 Plot from 1967 NASA report on magnetic materials showing variation of the Hiperco magnetization curve with increasing temperature [47].

The thermal model described in Section 3.4 predicted that the permanent magnet will operate in a temperature range of 310-451°C. The reduction in field strength with increasing temperature of the permanent magnet has been included in the finite element magneto-static modeling. The magnetization curve used for the core material was from room temperature data because a reliable magnetization curve shape at higher temperatures was not found in the literature search. Figure 3.10 shows a plot of the magnetic field strength in the circuit with the magnet operating at 400°C. The scale in the plot is set such that red coloring indicates a field strength of at least 2.1T.
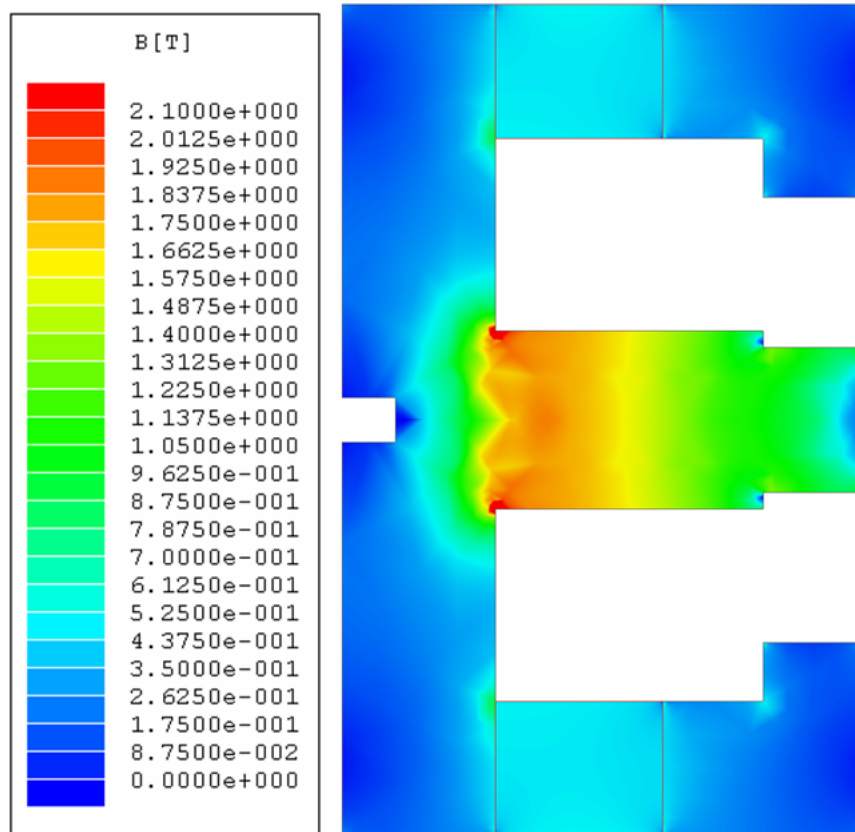
Figure 3.10 Plot of the magnetic field strength within the MHT-9 magnetic circuit when the SmCo permanent magnet is operating at 400°C. The plot is in units of Tesla.

According to the NASA report previously mentioned, Hiperco saturates at 2.1T when operating at a temperature of 1100°F (593°C). Thermal modeling has predicted that the average temperature in the core material will be 594°C or less. Figure 3.10 indicates that saturation should not occur anywhere in the circuit when operating at a magnet temperature of 400°C, but it also shows that the base of the center stem is the region most likely to saturate. The peak temperature of the core material was predicted to be between 600-874°C and occur near the tip of the center pole. At these temperatures, Hiperco should saturate at about 1.8T and Figure 3.10 shows that these field strengths only occur near the base of the center pole, where the predicted temperature is closer to 500°C. Thus, a Hiperco center pole should not saturate according to the magnetic and thermal models.

Hiperco 50A was chosen over the 1018 steel for the soft magnetic core material in the circuit because of its high Curie point. Although Hiperco only offers a slight advantage in magnetic flux over low-carbon steels, it has a Curie point of 940°C whereas the low-carbon steels have a Curie point of approximately 760°C. It is important to note that the Hiperco will likely run hotter because of its lower thermal conductivity, but thermal and magnetic models have shown that field saturation will likely be avoided. A literature search has provided some knowledge about the behavior of Hiperco at high temperature, but the behavior of low-carbon steel remains unknown. However, low-carbon steel was selected for the magnetic shunt rings that slide over the permanent magnet to adjust the field strength in the thruster because it is easier to machine in thin pieces.

Stainless Steel

The outer cover for the MHT-9 was made from 316 stainless steel. This alloy was selected over the more popular 304 stainless steel because it has a lower relative permeability (μ_c/μ_0). When cold worked, 304 can have a relative permeability above two, whereas the relative permeability for 316 stays very close to one even with excessive work [48].

3.1.4 Anode Tip Placement

Engineering drawings with detailed dimensions of the D-55 were not available for study. It has been estimated that the channel length of the D-55, the distance between the downstream tip of the anode and the thruster exit plane, is approximately 1-4mm. The MHT-9 was designed to be able to accommodate different channel lengths by adjusting the anode tip position through variation of the thickness of the insulating ceramic at the base of the anode (see Figure 3.11). The axial length of the focusing pole is 3mm, and was made intentionally long to accommodate repositioning of the anode tip. An initial position for the anode tip relative to the exit plane was determined from the magnetic field strength requirement. Figure 3.11 shows a plot of the average radial magnetic field at different axial positions within the thruster, representing different possible anode tip locations. This plot shows how the average field strength at each axial position varies with the temperature of the permanent magnet. The radial magnetic field is averaged across each of the red radial lines for the different z positions, as pictured in the graphic. Although the graphic obscures two of the radial lines, they are all the same length. The anode is pictured with the tip at the $z=-1$mm position as an example.

The plot in Figure 3.11 shows that in order to meet the 0.14T field requirement at the tip of the anode (shown as a dashed red line), the tip must be placed at the exit plane ($z=0$mm) or even further upstream ($z=-1$mm or $z=-2$mm). If the operating temperature of the SmCo magnet should reach 400°C, the exit plane position will not meet the requirement. For the initial construction, the anode was positioned with the anode tip 1mm upstream of the exit plane ($z=-1$mm). This choice was intended to minimize wall loses while still meeting the field requirement, assuming the magnet temperature remains below 500°C. The $z=-2$mm position does not offer much extra field strength but would double the exposed channel area and potentially increase wall losses.
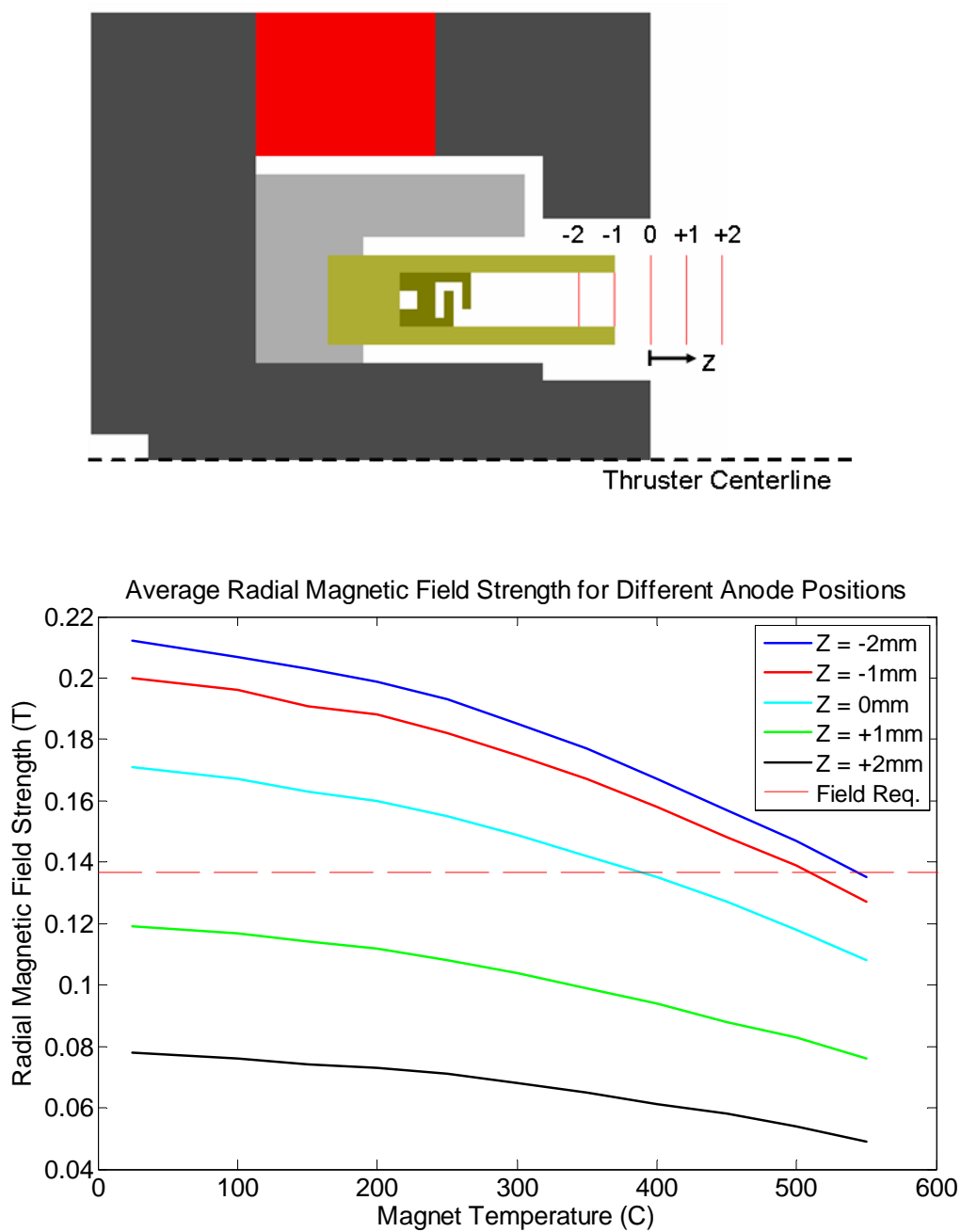
Figure 3.11 The graphic at the top shows the top half of a cross section of the MHT-9 magnetic circuit. There are red radial lines at five possible anode tip positions. The anode is pictured in gold, held in place by a ceramic insulator (shown in light grey). The plot shows the average radial magnetic field at each of the axial positions, as well as the variation of the field strength with magnet temperature.

3.1.5 Magnetic Field Tuning

Electromagnets have the advantage of being able to adjust the field strength and shape through variations in the magnet current. Permanent magnets cannot be changed during operation as easily, but shunts can be inserted between firings to allow for coarse tuning of the field strength. However, the use of shunts only allows the field to be reduced; additional permanent magnet material would be required to increase the field strength. The MHT-9 permanent magnet has been oversized to allow for some variation of the field strength both above and below the field requirement determined from the ideal scaling theory. The field in the circuit is reduced from the initial strength using thin rings of low-carbon steel as magnetic shunts.

Figure 3.12 shows the location of the shunt and the direction of measurement for the shunt length, S. The shunt is a cylinder that slides over the magnetic circuit and is made from 1018 steel. The shunt is 1mm thick and can be made in different lengths to vary the field strength in the thruster exit region. Longer shunt lengths result in lower field strengths. Figure 3.13 shows an example of a plot of the flux lines in the magnetic circuit when operating with a 5.6mm long shunt and a magnet temperature of 200°C. The plot can be qualitatively compared to Figure 3.4 to see that the shunt does not distort the field shape near the exit plane of the thruster.

Figure 3.14 shows the variation of the average radial magnetic field strength at the tip of the anode (positioned at $z=-1$mm) for various shunt lengths and magnet operating temperatures. This figure is a powerful tool for both estimating and selecting the field strength within the thruster. For a given magnet operating temperature estimate, a shunt length can be selected to choose a field strength at, above or below the ideal scaling field requirement. This shunt is then inserted into the thruster for operation. The required nominal magnetic field strength (as calculated with the ideal scaling theory) is shown in Figure 3.14 as a dashed red line.

Magnetic Field Shunt
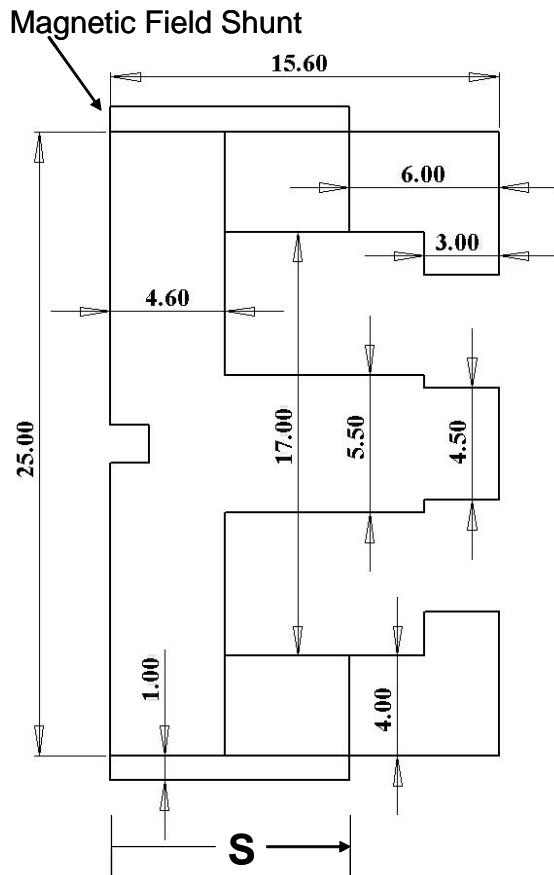
Figure 3.12 This schematic shows the position of the shunt used to tune the magnetic field strength in the MHT-9. The shunt shown in this drawing is 9.6mm in length. All dimensions shown are in millimeters.
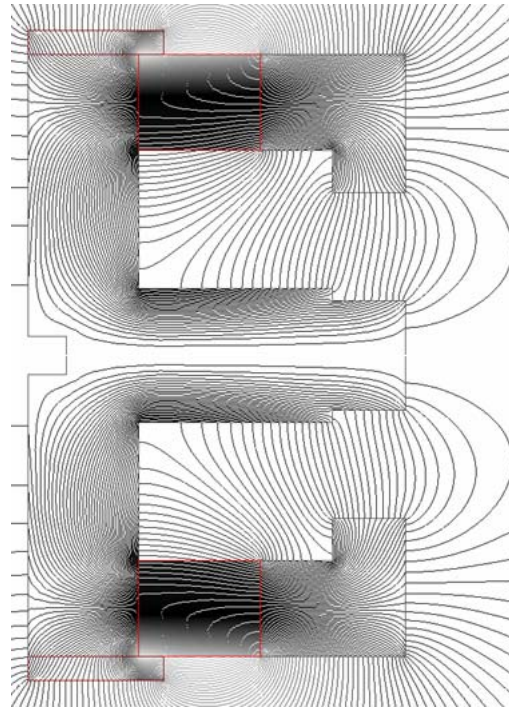
Figure 3.13 This is a cross-sectional plot of the flux lines in the MHT-9 magnetic circuit when using a 5.6mm long magnetic shunt and a magnet operating temperature of 200°C.

The field tuning capability with the shunt depends on the magnet operating temperature, with lower temperatures allowing for greater tuning because the permanent magnet energy output is higher. For example, a magnet temperature of 400°C allows for tuning of only 8% above the ideal scaling requirement (0.1368T), but at 200°C this increases to over 28%. Figure 3.15 shows the variation of tuning capability of the magnetic circuit with magnet operating temperature. The tuning capability is calculated from the finite element results at the maximum field strength with no shunt. The difference between this field strength and the field requirement (0.1368T) was then plotted as a percentage of the field
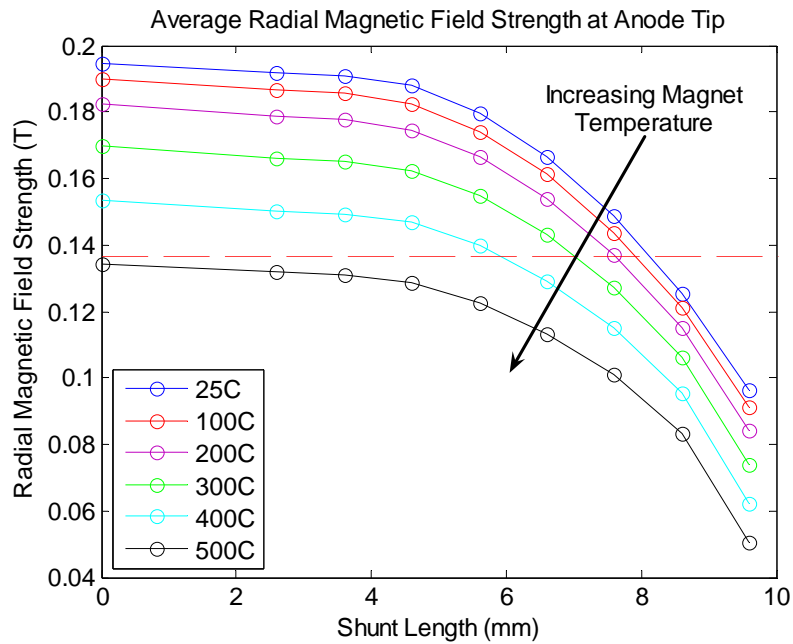
Figure 3.14 This plot illustrates the tuning capability of the MHT-9 magnetic circuit. The average radial magnetic field strength at the anode tip is shown as it varies with shunt length and magnet operating temperature. This graph can be used as a tool for estimating and selecting the field strength within the thruster.
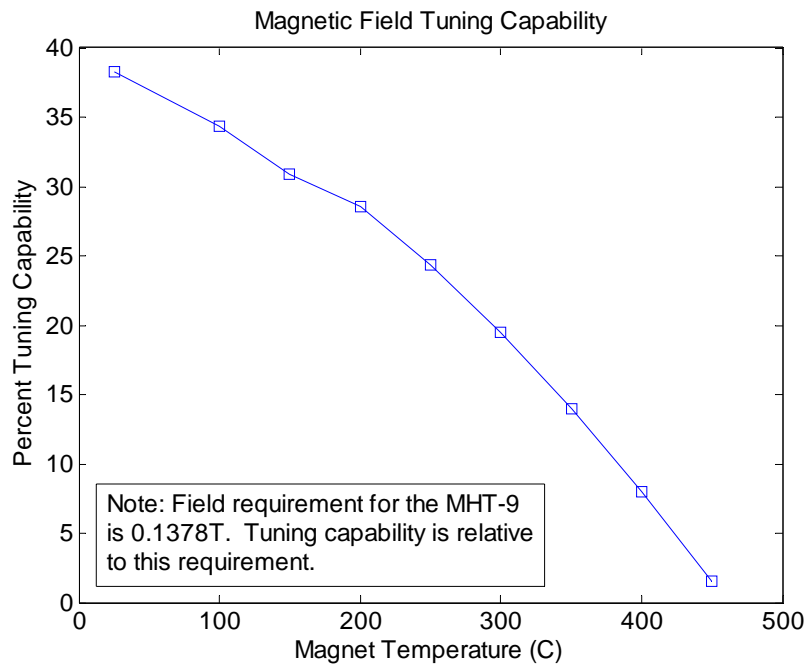
Figure 3.15 This plot shows the tuning capability of the MHT-9 magnetic circuit as a percentage of the field requirement determined by scaling. As the magnet temperature increases, the tuning capability is reduced.

requirement. As the magnet heats up and provides a lower field strength, there is a smaller difference available between the maximum output and the field requirement for adjustment with shunts.

3.2 Anode and Propellant Flow Design

The anode in a Hall thruster serves several important functions. It is the positive potential source for the plasma current, drawing a high energy flux from incoming electrons, and some ions. It usually also functions as the propellant distributor and must ensure azimuthal uniformity of the neutral flow. In order to achieve high propellant utilization, the distributor must also slow the axial speed of the flow and allow the neutrals a long enough residence time in the channel to ionize.

3.2.1 Flow Distribution

The MHT-9 anode is made of tantalum (Ta) and consists of a deep channel with an internal manifold and two baffles press fit into the channel. The manifold distributes the propellant azimuthally by using a set of equally spaced holes. These holes were sized to provide choke points for the flow based on estimates of temperature and pressure for the nominal flow rate of 0.74mg/s. The two baffles further improve azimuthal flow distribution and slow the axial speed of neutrals by blocking a 45° expansion cone from each of the holes in the manifold. The 45° expansion of a sonic, circular free jet has been shown to be a good approximation for both laminar and turbulent flow [49]. A cross-section of the MHT-9 anode configuration is shown in Figure 3.16. The governing choked flow equation for n holes of area A_h is shown in Equation 3.18.

$$nA_h = c_d \frac{\dot{m}_a c^*}{P_c} = c_d \frac{\dot{m}_a}{P_c} \sqrt{\frac{RT_c}{\gamma}} \left(\frac{\gamma+1}{2}\right)^{\frac{\gamma+1}{2(\gamma-1)}} \tag{3.18}$$

The pressure in the chamber of the manifold, P_c, was estimated to be 10torr. The temperature of the flow, T_c, was estimated to be 1300K. The discharge coefficient, c_d, for a sharp,

Anode Cup Cross Section
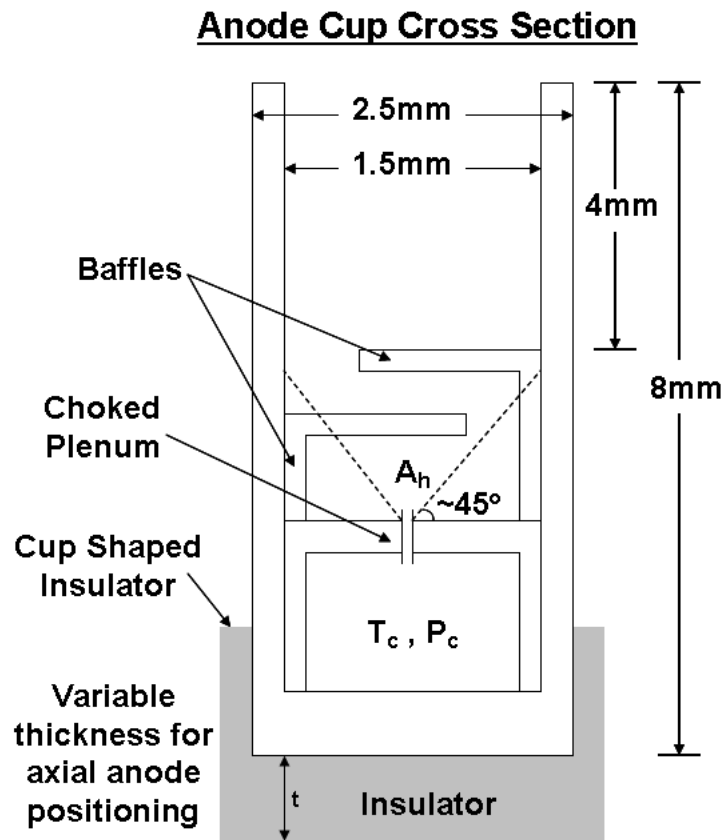
Figure 3.16 Cross sectional schematic of the MHT-9 anode design. There are eight choke points in the manifold and two baffles to ensure azimuthal uniformity of the flow. This diagram is not to scale.

small diameter injector is approximately 0.65 [50]. The discharge coefficient for this case was estimated to be about 0.5. For a xenon mass flow rate of 0.74mg/s, an estimate of the hole diameter can be calculated for different numbers of injection points in the manifold, as shown in Table 3.3. The eight hole configuration was selected because drill bits with a 0.13mm diameter were available for purchase and using smaller drill sizes seemed prohibitive from a manufacturing perspective.

TABLE 3.3   Estimates of Manifold Injection Hole Diameter

Number of Injection Points	Hole diameter (mm)
6	0.152
8	0.132
10	0.118

3.2.2 Manufacturing

The MHT-9 anode was made from several different pieces that were eventually press fit and/or welded together. The previous effort at MIT to build a 50W Hall thruster used only press fits to link the pieces of the anode together and connect it to the propellant flow lines [13-15]. The use of press fits instead of leak proof welds and fittings may have led to propellant leakage, which would help to explain the low utilization efficiencies measured during the previous experiments.

The annulus/cup shaped portion of the anode flow distributor was milled out from a single piece of tantalum. The plenum piece with the eight choke point manifold holes, as well as the two baffles, were made separately and then press fit into the cup shaped annulus. There may have been leakage points within the plenum and baffle system due to the use of a press fit, but based on erosion profiles on the guard rings it qualitatively appears that the flow was well distributed azimuthally. A cross-sectional schematic is shown to scale in Figure 3.17.

The anode assembly is pictured in Figure 3.18. The anode cup had four holes drilled into the bottom face. One hole was a 1mm diameter through hole and carried the propellant into the plenum. A 2in long tantalum pipe with an outer diameter of 2mm and an inner diameter of 1mm was slip fit into a 1mm deep counterbore and then electron beam welded at the junction in order to ensure a leak free connection. The other three holes in the base of the anode annulus cup were not through holes, but rather 1mm deep with 2mm diameter. In each of these holes, short tantalum rods were slip fit inside and tack welded in place. These rods are 2mm in diameter and threaded at the other ends so that they could secure
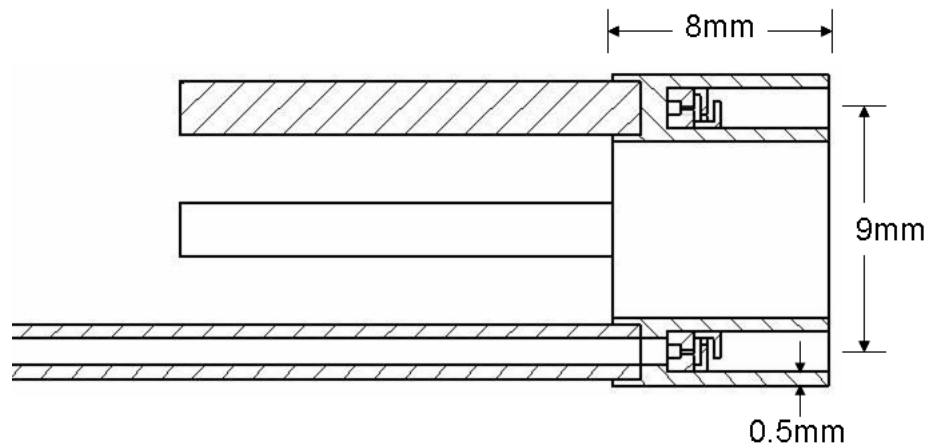
Figure 3.17 Cross sectional view of the MHT-9 anode assembly. This drawing is shown to scale and includes the entire sectional view (not just the section plane). The propellant inlet tube extends further to the left than pictured.
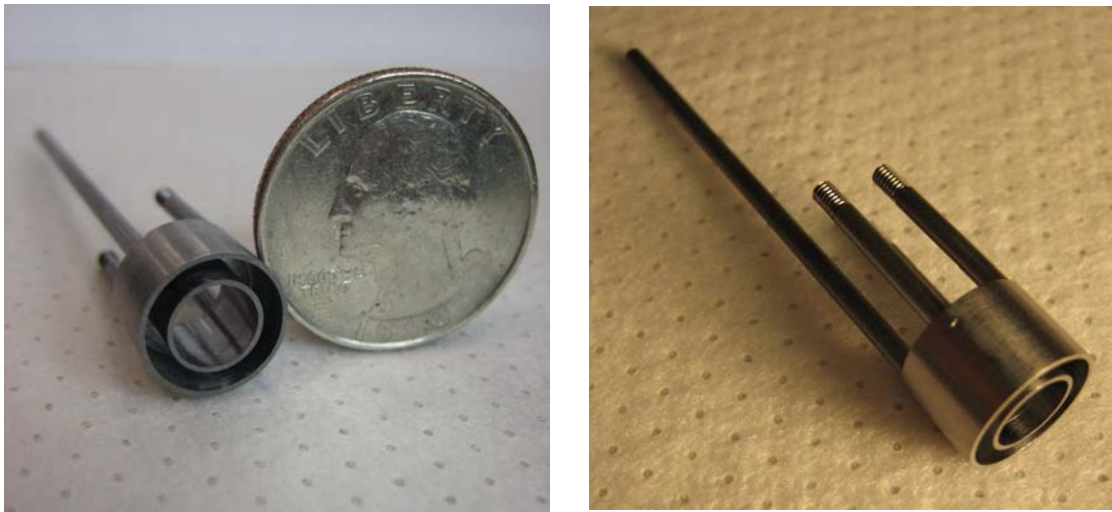
Figure 3.18 The MHT-9 anode is shown in two separate images to give an idea of its scale and shape. The entire anode is made of tantalum, including the long propellant flow tube and three posts that stick out of the back. The photograph on the right shows that the tips of the three short posts are threaded so that the anode can be secured tightly to insulators inside the body of the thruster.

the anode tightly in place. In retrospect, it would have been better to press fit these small rods in place instead of tack welding them. The tack welds broke eventually and the rods had to be pressed back into place.

3.2.3 Material Selection

Previous research indicated that the anode material should be able to withstand high temperatures and heat loads from the plasma. When building the 50W miniature Hall thruster at MIT, Khayms originally used platinum as the anode material (melting point of 1769°C) but found that, "excessive arcing and exposure to high temperatures have damaged the anode tip over the course of the first few hours of operation" [15]. This eventually led to Khayms selecting molybdenum for the second generation anode. Several materials were considered for the MHT-9 anode, as shown in Table 3.4. All of these refractory metals have very high melting points.

TABLE 3.4 Thermal Properties of Materials Considered for the MHT-9 Anode

Material	Melting Point (°C)	Thermal Conductivity (W/m-K)	Specific Heat (J/kg-K)	Coefficient of Thermal Expansion (μm/m-°C)
Molybdenum	2617	138	255	6.5
Tantalum	2996	54.4	153	7.0
Tungsten	3370	163.3	134	4.4
Rhenium	3180	39.6	138	6.7

Khayms' anode relied on press fits for flow connections and thus weldability was not a concern. However, the MHT-9 anode relies on a welded connection between the flow input tube and the anode cup annulus. This rules out molybdenum and tungsten because they tend to be too brittle to allow a welded joint to survive handling stresses. Rhenium was a potential candidate for welding but was found to be extremely expensive. Tantalum can be electron beam welded with relative ease and was therefore selected for the MHT-9 anode.
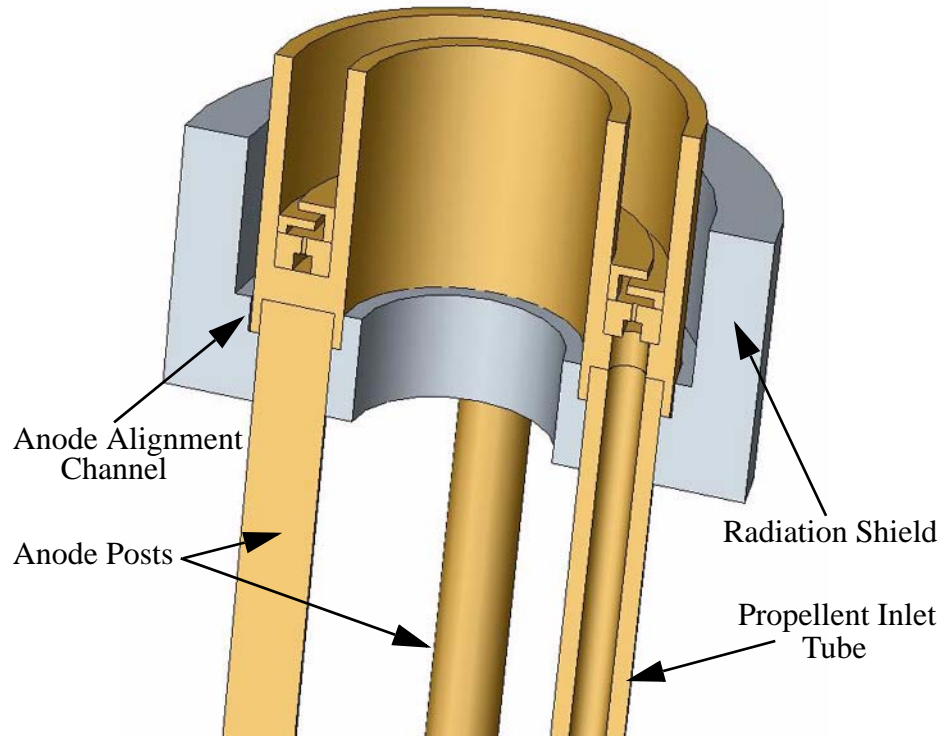
Figure 3.19 This is a cross sectional view of a three dimensional solid model of the MHT-9 anode assembly. It is shown sitting in the channel of the boron nitride insulator.

3.2.4 Insulation and Alignment

The anode must remain electrically isolated from the thruster body, which is typically kept at cathode potential. This requires that the anode be secured to the thruster body using high temperature ceramics. Boron nitride is a ceramic insulator commonly used in Hall thrusters because it can withstand high temperatures and thermal cycling; it has a low coefficient of thermal expansion and it is easily machined. The Saint-Gobain AX05 grade of boron nitride was selected for the MHT-9 insulating pieces. It can withstand temperatures up to 2000°C and has a relatively high thermal conductivity for an insulating material (70-130W/m-K at room temperature, depending on the direction). This high thermal conductivity is important because it provides a conduction path for heat to move from the high temperature anode to the copper heat sinks built into the thruster body.

Khayms pointed out the sensitivity of a miniature TAL Hall thruster to misalignment of the anode and the possibility of reduced performance when the anode face is no longer parallel to magnetic field lines [15]. In order to ensure alignment of the MHT-9 anode with the centerline of the thruster, a boron nitride insulator was built with a channel for the anode to be seated into. This channel provides a short interior wall along which the inside wall of the anode cup annulus can be closely fit. The outer wall of the insulator's channel has a diameter slightly larger than that of the anode outer wall to allow room for thermal expansion. This is important because both the predicted temperature and the coefficient of thermal expansion of the tantalum anode are larger than that of the boron nitride insulator. In addition to the alignment channel, the boron nitride insulator also has a high outer wall that prevents direct radiation of heat from the high temperature anode to the permanent magnet. A cross-sectional view of the MHT-9 anode seated in the insulator channel is shown using the engineering model of the thruster in Figure 3.19.

3.3 Complete Design

Two different cross sectional drawings of the MHT-9 are shown in Figures 3.20-3.21. Figure 3.20 was chosen at an angle that does not include the posts or propellant tube connected to the anode. This view is a simple surface view and shows only the plane of the sectional cut. All of the relevant components of the thruster are labeled. The mid-channel diameter is 9mm. The entire anode assembly and guard rings are made of tantalum. The copper heat sink is threaded onto the Hiperco focusing pole to ensure good thermal contact, and the entire thruster is mounted to a copper plate. Figure 3.21 is shown at an azimuthal angle that includes the extended features of the anode assembly. This is a full sectional view of the three dimensional model and shows the entire thruster from the cross-sectional plane. Propellant enters the anode through a single tantalum tube and is then distributed by the manifold and baffle system previously described. The short posts connected to anode cup are threaded at their tips and secured to insulators using small 2mm nuts. This view also shows the thruster with the version of the heat sink that allows a magnetic shunt to be inserted. A 5.6mm long shunt and the accompanying 4mm long cop-

per ring are displayed in this view as well. This copper ring simply fills the rest of the gap in the heat sink that allows up to a 9.6mm long shunt to be placed around the magnetic circuit.

Figure 3.22 shows a three dimensional model of the thruster with a cutaway section view. In this view you can see that there are boron nitride sleeves around the propellant inlet tube and posts connected to anode so that the high potential anode surfaces are not directly exposed to the cathode potential thruster body at any point. Figure 3.23 is a cross sectional view shown to scale with the major dimensions labeled in millimeters. Figure 3.24 shows several pictures of the MHT-9 mounted to an aluminum stand with a Busek built hollow cathode.

3.3.1 Propellant Connection and Isolation

Inside the thruster, the anode assembly is connected only to the insulating pieces of boron nitride in order to maintain the potential difference between the anode and the rest of the thruster body. The anode is also electrically isolated from the vacuum tank propellant feed line through the use of a cryogenic break that has a ceramic cylinder brazed between two stainless steel tubes. This cryogenic break functions as an inexpensive propellant isolator and is connected to the anode propellant inlet tube via a Swagelok union. Figure 3.25 shows these flow connections in a side view of the region behind the thruster. The pieces connected to the anode on the downstream side of the isolator are all at high potential, and therefore they must be shielded from the very mobile electrons that exist in the background plasma that fills the vacuum tank.

The Debye length, λ_D, for the background plasma surrounding the thruster can be estimated as,

$$\lambda_D = \sqrt{\frac{\varepsilon_0 k T_e}{e^2 n_e}}.$$
(3.19)

Copper Mounting Plate

Stainless Steel Outer Cover

Copper Heat Sink

Hiperco Focusing Pole

Tantalum Anode

Tantalum Guard Rings

Boron Nitride Insulator

SmCo Magnet

Hiperco Center Stem

Boron Nitride Insulator

Magnetic Shunt

Copper Ring

Boron Nitride Sleeve
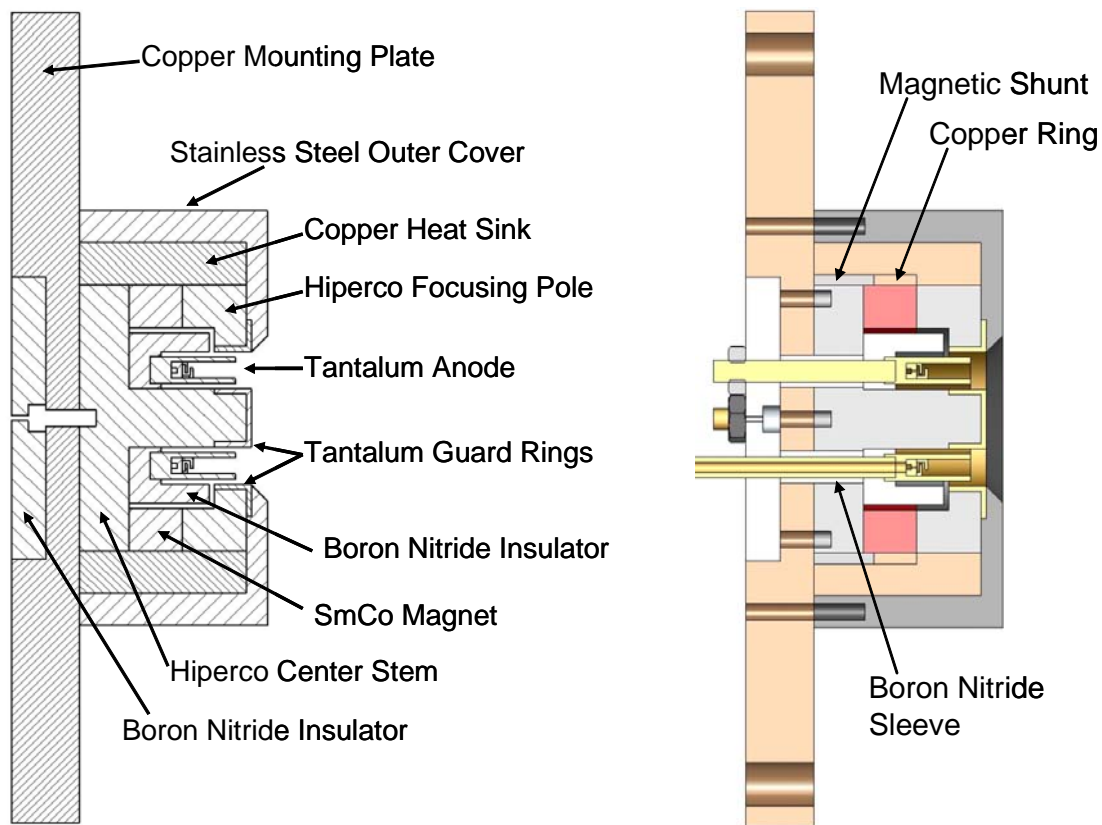
Figure 3.20   LEFT: Cross sectional drawing of the MHT-9. This is a surface view at an angle that does not contain the propellant flow tube or the posts connected to the anode. This view is shown to scale.

Figure 3.21   RIGHT: This full cross sectional view of the solid model is in a plane that includes the propellant tube and anode posts. This view is shown to scale and includes the boron nitride sleeves, as well as a view of the thruster with a 5.6mm shunt in place. Next to the shunt is a copper ring that fills the rest of the gap within the version of the heat sink used with shunts.
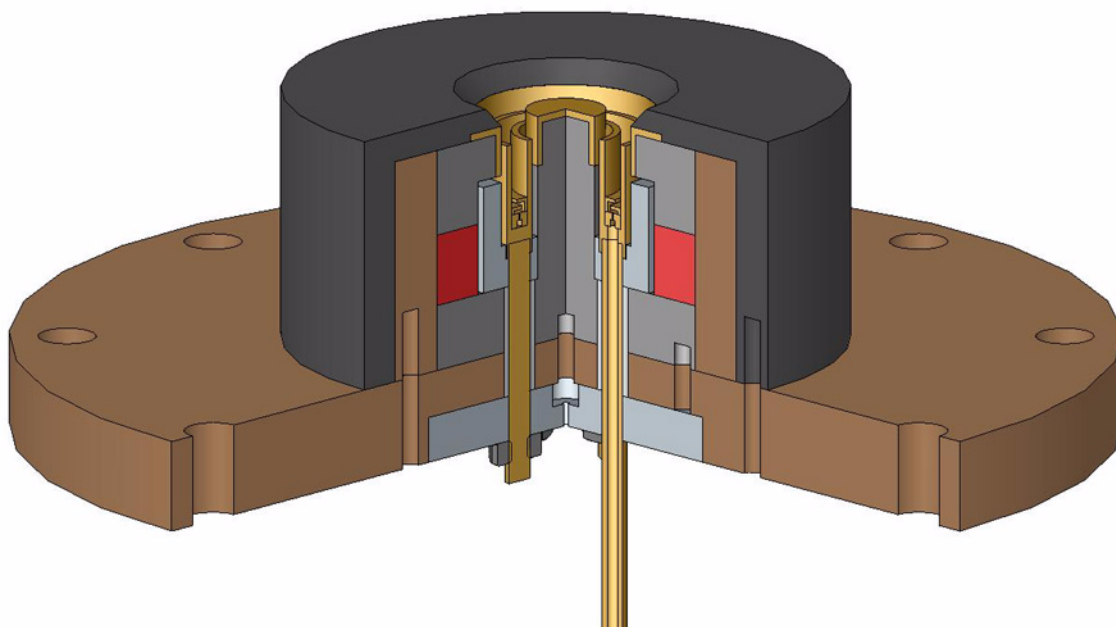
Figure 3.22   This cutaway view of the MHT-9 three dimensional solid model shows all of the main components of the thruster. The tantalum anode assembly and guard rings are shown in gold. The permanent magnet is pictured in red, Hiperco core pieces are grey, boron nitride insulators are light grey, outer steel cover is dark grey and the copper heat sinks are pictured in brown. This view of the thruster is shown without a shunt or assembly screws in place.
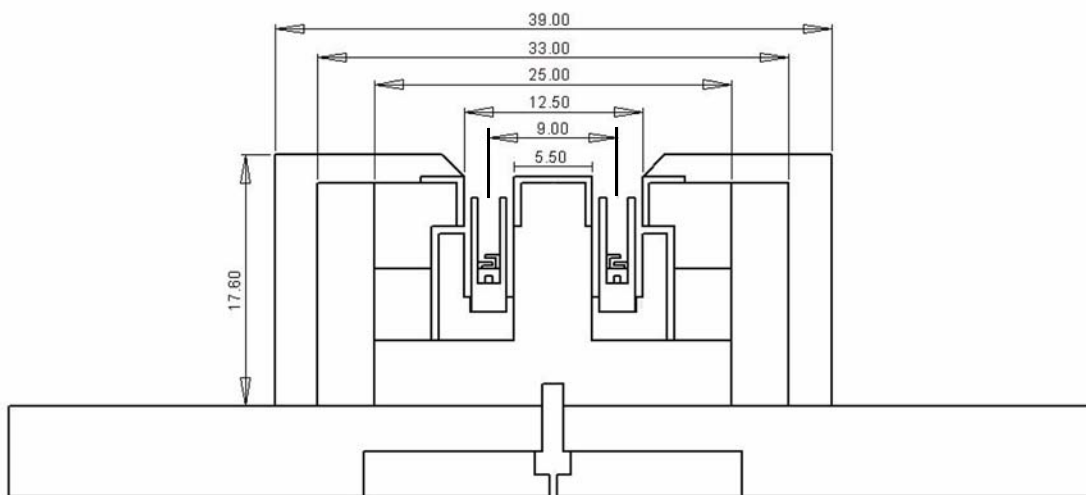
Figure 3.23   MHT-9 cross sectional drawing with major dimensions in mm.
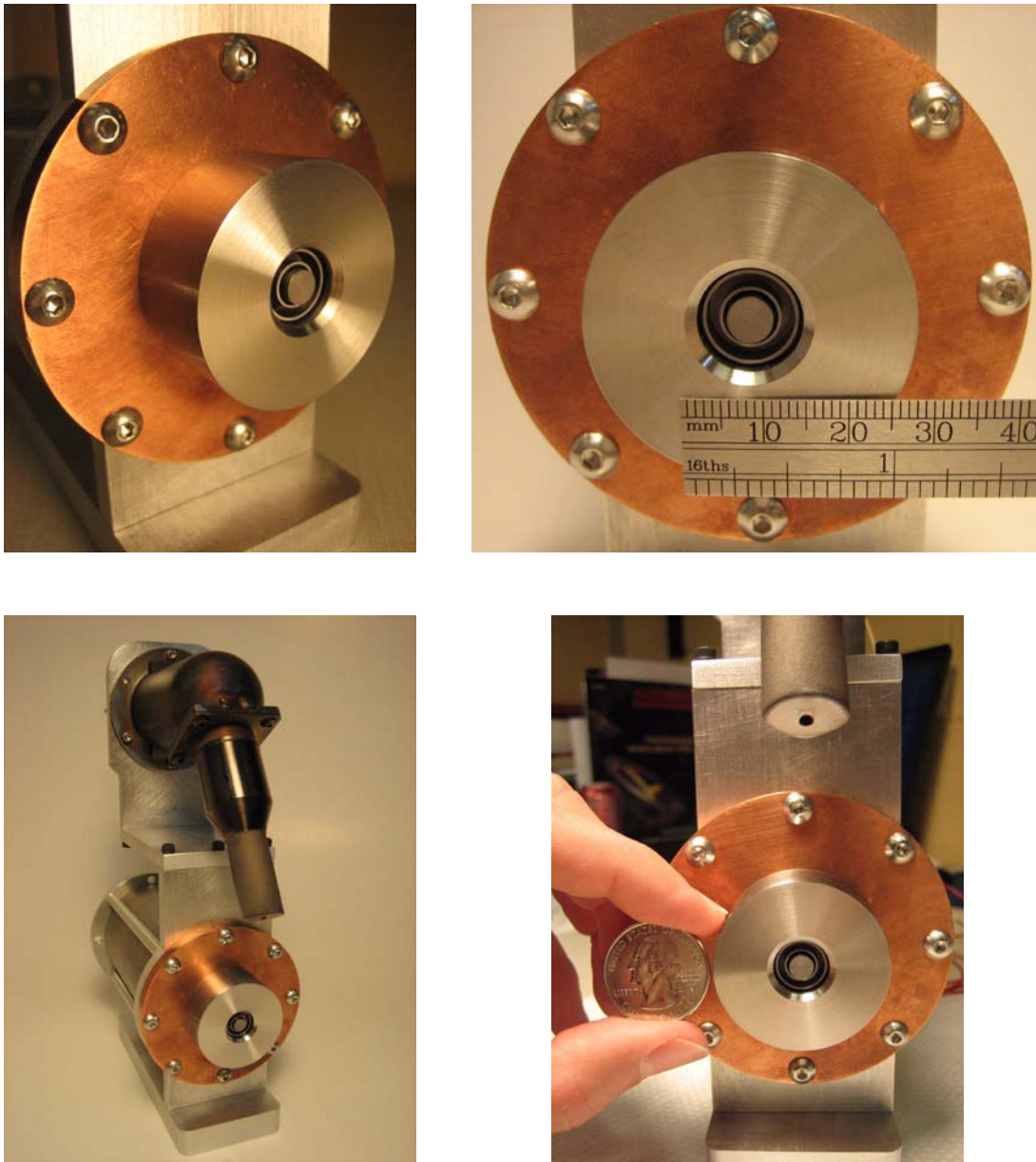
Figure 3.24   Pictures of the MHT-9 fully assembled. The thruster is mounted to an aluminum stand with a hollow cathode built by the Busek Company, Inc.

Propellant
Isolator

Anode Propellant
Inlet Tube

MHT-9

Propellant
Flow Line
Connection
(Swagelok)

Swagelok
Union
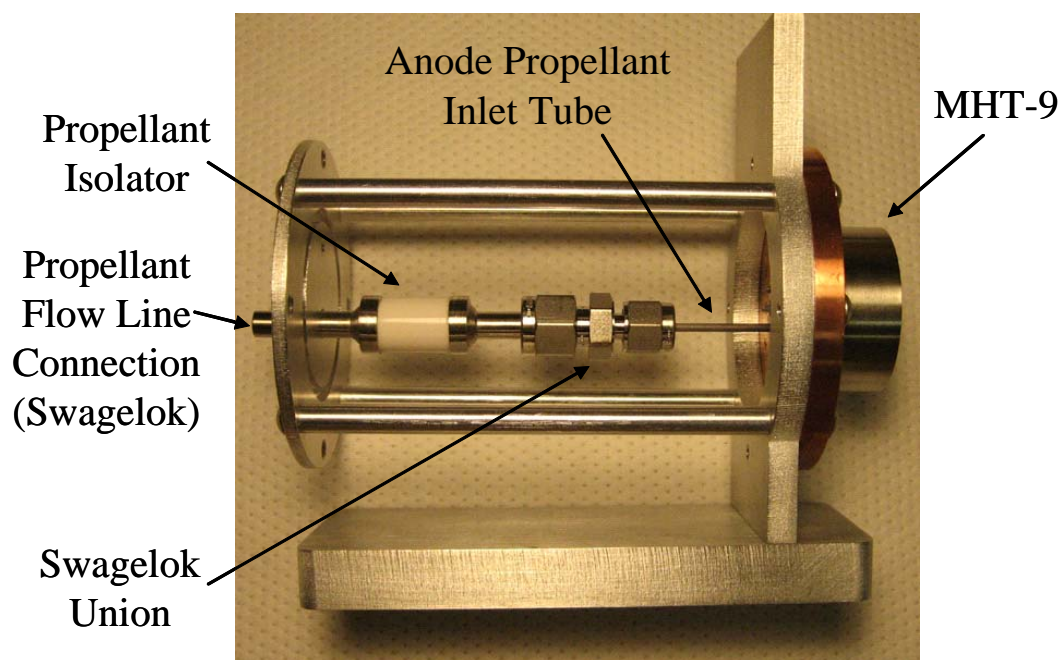
Figure 3.25   Internal side view of MHT-9 flow connections.
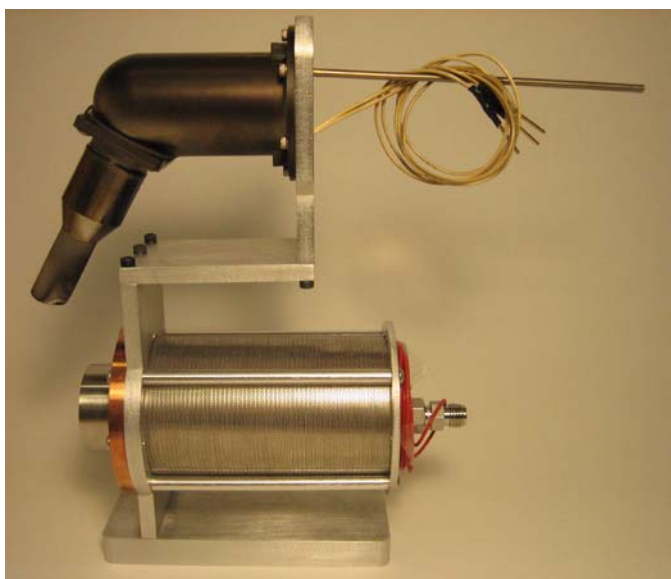
Figure 3.26   Side view of the MHT-9 fully assembled and mounted to the aluminum frame. This frame also holds the cathode as well as the isolation and shielding components for the anode potential components in the back of the thruster.
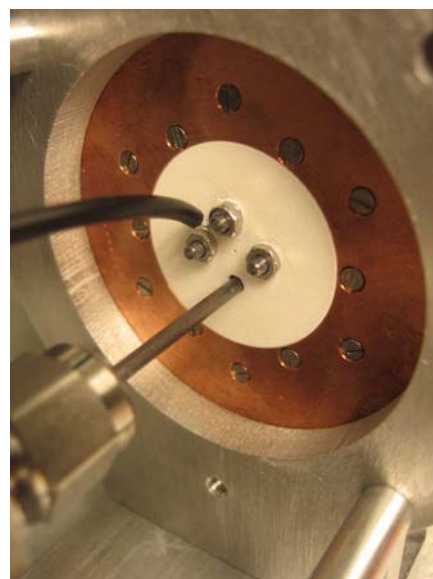
Figure 3.27   The electrical connection for the MHT-9 anode (the shielding screen and alumina tube have been removed for this view).

Plume data for the BHT-200 thruster taken at MIT by Azziz show that the electron density at 90° off the thruster centerline and 25cm from the thruster exit plane is approximately $1.5 \times 10^{15} \text{m}^{-3}$, while the electron temperature is 1.2eV [51]. The actual density behind the thruster exit plane is likely lower by an order of magnitude or more. The BHT-200 is a relatively small 200W thruster with ceramic walls, and likely has a plume signature similar to that of the MHT-9. These plasma properties taken by Azziz indicate a Debye length in the range of 0.2-0.7mm. Plasma shielding occurs through a sheath at surfaces that typically has a thickness of 4-5 Debye lengths. In order to properly shield the anode potential surfaces behind the thruster where flow connections are made, the hole size of the shielding should be on the order of a Debye length or preferably smaller.

The flow connections behind the MHT-9 were protected from the plasma background in the tank by covering them with both an alumina cylinder and a stainless steel screen. The stainless steel screen was perforated with holes of diameter 0.5mm. This double layer of protection ensured that stray current was not drawn to the anode behind the thruster. The alumina and steel cylinders are concentric, with the steel mesh on the outside as shown in the side view of the thruster presented in Figure 3.26.

3.3.2 Discharge Power Connection

The thruster requires an electrical connection between the anode and an external power supply to establish the discharge potential. In order to make this connection, an insulated wire was attached to one of the anode posts as shown in Figure 3.27. This wire was inserted through a hole in the back of the shielding components that protect the anode potential pieces from the background plasma. The propellant and electrical connections are formed in such a way that they (and their shielding) actually take up much more volume than the thruster itself. This was done as a matter of convenience and to keep the construction simple where possible. All of these connections could be made much smaller and less massive for a flight production thruster.

3.3.3 Arcing

The small dimensions of the MHT-9 make electrical breakdown a concern. The smallest dimension of concern is 0.5mm, the radial distance between the high potential anode and the low potential metallic chamber walls, as shown in Figure 3.28. The Paschen curve for xenon must be consulted to investigate the possibility of an arc discharge occurring between the anode and the thruster body. This curve shows the gas breakdown voltage as a function of the product of the gas pressure and the distance between the electrodes. The Paschen curve for xenon has been determined experimentally by several researchers [52-54]. The experiments used to determine the Paschen curve typically use a parallel plate electrode geometry. Although the geometry of the MHT-9 is more cylindrical, the ratio of the gap dimension to the radius of curvature (d/r_c) at the inside and outside of the anode is 0.17 and 0.08 respectively, thus a parallel plate analogy is likely adequate.
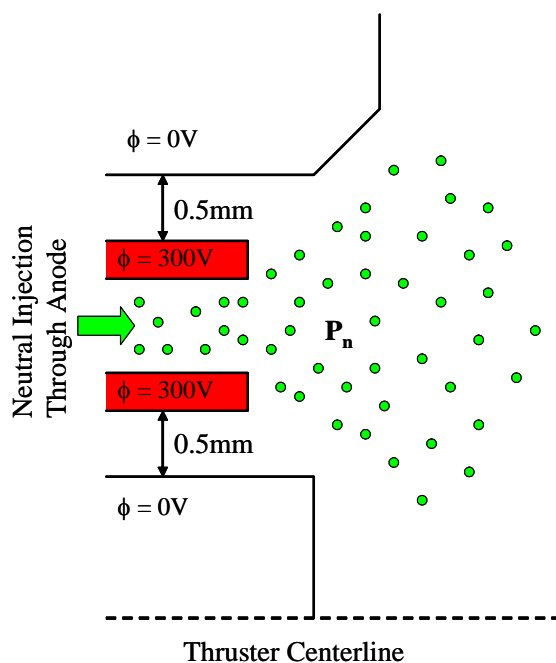
Figure 3.28   Neutral injection in the MHT-9.

A plot of the xenon Paschen curve using two separate experimental results by Kruithof and Schönhuber is shown in Figure 3.29. The two experiments cover different ranges of the pressure-distance product but together form a complete picture of the xenon behavior. The minimum voltage for breakdown at any pressure-distance product was shown to be close to 250V. This means that breakdown could occur in the MHT-9 when operating at the nominal 300V potential difference, if the flow conditions were such that the thruster operated near the minimum in the curve.
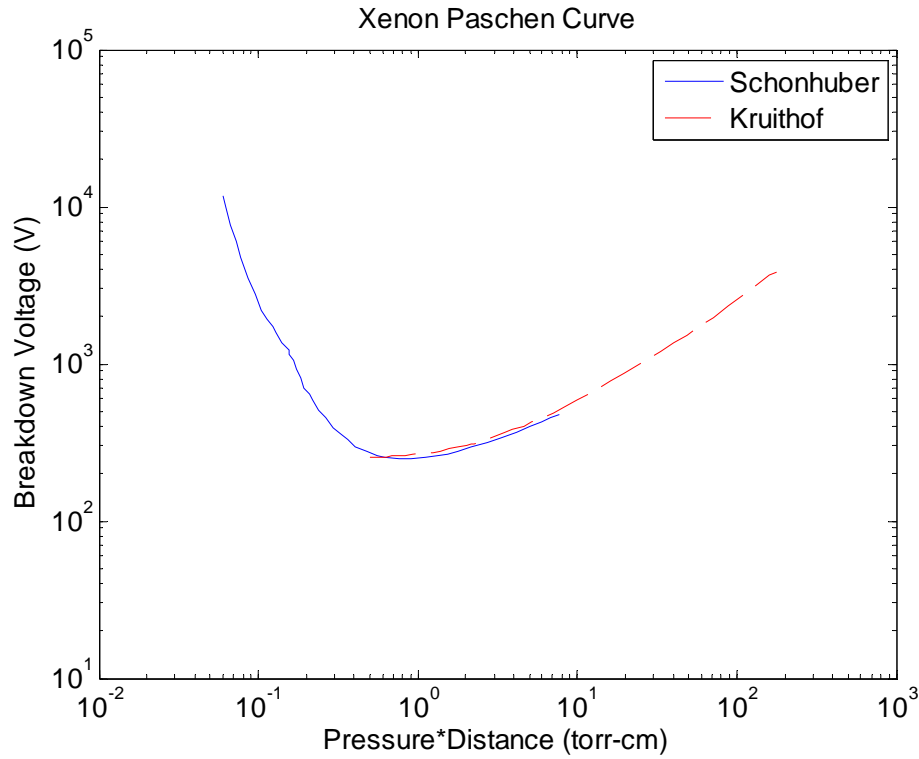
Figure 3.29 The Paschen curve for xenon as determined experimentally by Kruithof and Schonhuber [52-53].

In order to determine the region of interest on the Paschen curve, the neutral pressure inside the MHT-9 must be estimated. The pressure can be expressed simply as,

$$P_n = n_n k T_n.$$

(3.20)

The neutrals exiting the anode will have a temperature similar to that of the anode material because they will make many collisions with the anode walls as they are distributed azimuthally by the plenum and baffles. The neutral number density can be estimated using continuity,

$$\dot{m} = m_n n_n v_n A_e .$$
(3.21)

The neutral velocity in the discharge region is likely near sonic as the flow expands into the low pressure vacuum outside the thruster. If the anode/neutral temperature is approximately 1000°C (1273K), then the xenon neutral sonic velocity would be 367m/s. The exit area of the MHT-9 is approximately 100mm^2, and at the nominal flow rate of 0.74mg/s, the neutral pressure in the discharge region is approximately 0.01torr. For a gap distance of 0.5mm, this gives a pressure-distance product of 5×10^{-4}torr-cm. This conservative estimate is likely higher than the actual neutral pressure in the small 0.5mm gap region between the anode and the thruster chamber walls since most of the flow will exit the thruster directly.

At this pressure-distance product, the Paschen curve shows that an arc will form at voltages much greater than 10,000V, and thus breakdown is not an important concern for the MHT-9. The thruster operates in a region far to the left of the minimum breakdown potential. An arc can form through a distance greater than the smallest gap dimension if that minimizes the energy required, as it would for conditions to the left of the breakdown minimum. However at the estimated pressure in the MHT-9 it would require an arc travelling roughly three orders of magnitude greater distance, or 0.5m to allow breakdown at 300V (the nominal operating voltage of the thruster).

This analysis assumes that there are no features within the thruster that intensify the electric field. If there were particularly rough surfaces or sharp corners that caused the electric field to be locally very high, this could cause breakdown to occur more easily. Given that the margin of safety for breakdown voltage with the above analysis is so great, the corners and surface features are likely not problematic.

The above analysis also assumes that there are no flow leaks in the anode assembly, meaning that the neutrals enter the thruster through the anode annulus. If a flow leak occurred and the majority of the flow entered through the region that forms the gaps between the anode and the thruster walls, this would decrease the flow exit area and thus increase both the neutral density and pressure. The exit area would then be closer to 28mm^2, and the pressure-distance product would be 0.002torr-cm. This condition would still require a potential of greater than 10,000V for breakdown, assuming the trends in the Paschen curve continue to the left of the data shown in Figure 3.29.

3.4 Thermal Modeling

A two-dimensional, steady-state, axisymmetric finite element thermal model was created to evaluate the conduction and radiation of heat through the thruster, and to predict operating temperatures of key components. The model was built using the Maxwell finite element software package. Inputs for the thermal model were determined from estimates of heat deposited to thruster surfaces from electron-ion recombination, electron bombardment of the anode and radiation from excited neutrals. The boundary condition used for the model was a constant temperature along the back of the copper mounting plate shown in Figure 3.20. The initial version of the thermal model used perfect conduction between adjacent thruster components, but the resulting temperatures seemed far too low when considering previous research done on other Hall thrusters at MIT [55]. The thermal contact resistance of interfaces between adjacent conducting components was introduced in order to more accurately model the heat conduction pathways. This improvement increased the predicted temperatures and gave more realistic results. The finite element model also includes radiation of the outer surfaces of the thruster, but unfortunately does not include radiation between model objects within the thruster.

The following sections will discuss the analytical models used to determine the heat inputs for the model, the idea of contact resistance at the interfaces between thruster components

as well as the temperatures and thruster design changes that resulted from use of the thermal model.

3.4.1 Heat Load Estimates

Estimates of the heat fluxes to thruster surfaces from the discharge plasma were used as inputs to the finite element thermal model. These inputs were estimated using a combination of analytical models and a power balance for the thruster. If a control volume is drawn around the thruster system as shown in Figure 3.30, it can be seen that the discharge power supply puts energy into the system while power leaves the system as exhaust energy, radiated heat and conducted heat. A steady state power balance equation can be written that expresses the relationship pictured in the figure as,

$$P_d = P_{exhaust} + P_{radiation} + P_{conduction}. \tag{3.22}$$

This equation can serve as a check on the model to ensure that energy is conserved. However, in order to understand the heat fluxes inside the thruster it is more useful to think in terms of the species involved. Figure 3.31 shows the energy balance from a species perspective. The power put into the thruster through the discharge power supply creates the plasma. This plasma then transmits power to ions and electrons that are ejected into the plume, lost to walls or collected by the anode. Neutrals and ions can enter transitional states where they will be excited and then radiate energy either onto thruster surfaces or into the plume as they return to their original energy state. In the following subsections, this mental model will be used to organize the estimates of power consumption for each of these processes.
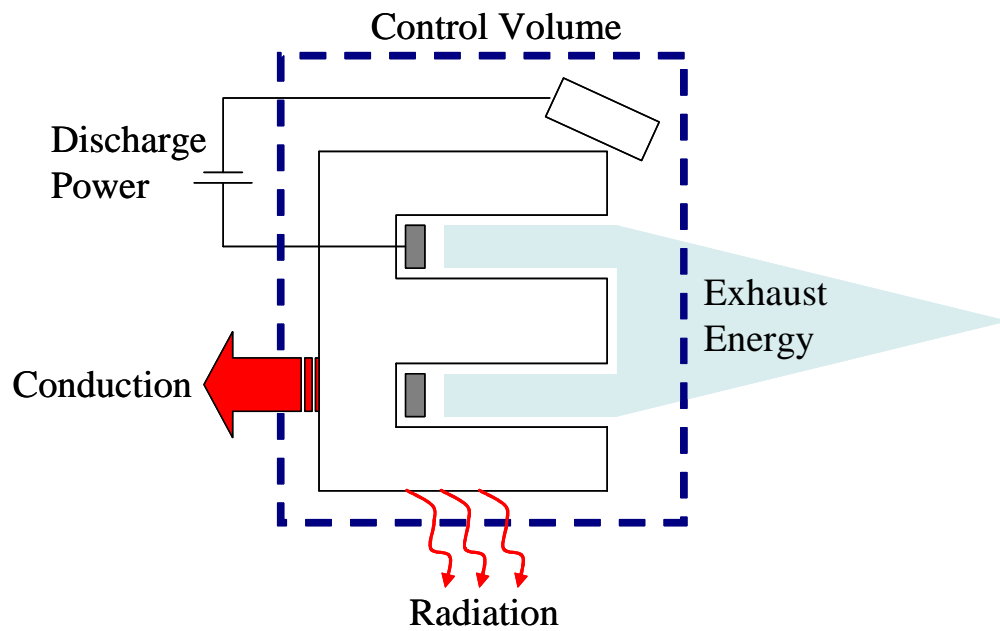
Figure 3.30 This control volume diagram illustrates the power balance used to make estimates of the heat loads inside the MHT-9.
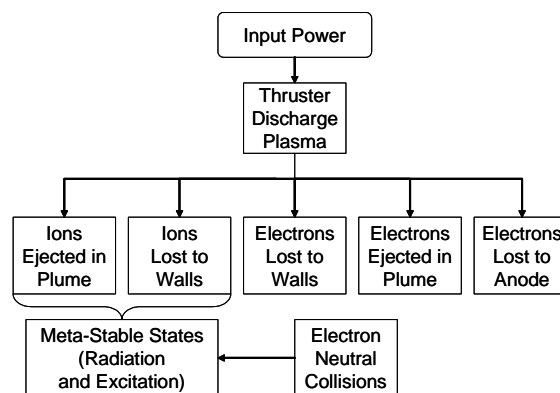
Figure 3.31 The power balance from a species perspective.

Ions in the Plume

The ions created in the discharge plasma are born with a potential close to that of the anode and are then accelerated into the low potential region just outside of the thruster. These ions carry the sum of kinetic energy, thermal energy and the energy spent for ionization. The power expelled from the thruster by these ions, P_{ip}, can be expressed as,

$$P_{ip} = \left[\frac{1}{2} m_i c^2 + \frac{5}{2} k T_{ip} + e V_i \right] \frac{I_b}{e}. \qquad (3.23)$$

In order to arrive at an estimate for this ion plume power, some assumptions must be made. The ion velocity, c, can be estimated using the target specific impulse as indicated by the ideal scaling arguments, or through an assumption about the acceleration efficiency and the operating voltage. The ion temperature in the plume, T_{ip}, is on the order of 1eV or less as indicated by previous experimental research [56]. The ionization energy of xenon, V_i, is 12.1eV. The beam current can be estimated simply as a fraction of the total discharge current. The integrated beam current in the plume is typically at least 70% of the discharge current, meaning that $I_b \approx 0.7 I_d$. This estimate is supported by previous research in 1-D Hall thruster modeling by Ahedo for thrusters with high utilization efficiencies [57]. Another way to make a simple estimate of the beam current is directly from the utilization and flow rate expressed as,

$$I_b = \frac{\dot{m}_a e}{m_i} \eta_u. \qquad (3.24)$$

Experimental results for the MHT-9 and elsewhere by Hofer have shown that Hall thruster utilization efficiencies can exceed 90% [58]. In this regime, the two different methods of determining beam current agree well.

Electrons in the Plume

The electrons that neutralize the plume originate in the cathode and are pushed into the beam by a small potential difference between the cathode and the nearby plasma. This

near cathode potential difference, ϕ_{nc}, is typically on the order of 15-20V and it gives the electrons directed kinetic energy. The electrons also carry thermal energy determined by the electron temperature in the plume, T_{ep}. Thus, the total electron power in the plume, P_{ep}, is simply the sum of this thermal power and the kinetic power,

$$P_{ep} = \left[\frac{5}{2}kT_{ep} + e\phi_{nc}\right]\frac{I_b}{e}. \tag{3.25}$$

The electron temperature in the plume, T_{ep}, is typically on the order of 3eV or less, as observed in experimental results at MIT by Azziz [51].

Ions Lost to Walls

The recombination of ions at wall surfaces within a Hall thruster is the most significant power loss mechanism and a source of direct wall heating. As ions are accelerated by the presheath towards the wall, they reach the edge of the sheath with a kinetic energy determined by the Bohm velocity (Equation 2.27). The ion then falls through the sheath, gaining more kinetic energy. The final energy carried into the wall by an ion is the sum of the ionization energy spent in creating the ion, the thermal energy of the ion, kinetic energy gained in the presheath and the potential energy transferred to the ion by the electric field in the sheath. The ion power collected by the wall, P_{iw}, can thus be expressed as,

$$P_{iw} = \left[eV_i + \frac{5}{2}kT_i + \frac{1}{2}m_i v_B^2 + e(\phi_s - \phi_w)\right]\frac{I_w}{e}. \tag{3.26}$$

Several intermediate estimates must be made in order to arrive at an estimate of the ion power lost to the walls. Simulation results at MIT by Szabo have shown that the ion temperature in the radial and azimuthal directions is on the order of a few electron-Volts [26]. The axial ion temperature is much higher (40-60eV) due to the variation in potential at which ions are created. The azimuthal/radial temperature is the appropriate number to use in Equation 3.26 since the energy of directed motion of the ion is expressed through the sheath effects.

The Bohm velocity requires an estimate of electron temperature. Szabo shows that for a small TAL style thruster, the electron temperature in the discharge region for a thruster operating at 300V is in the range of 25-30eV. The ideal scaling analysis justified the assumption that the electron temperature is a scaling invariant. Szabo's predictions for T_e have been confirmed experimentally on a larger, ceramic walled thruster [55]. The electron temperature was measured inside the BHT-1000, a kilowatt class thruster, by Langmuir probes implanted in the exit rings. Measurements showed a T_e of at least 20eV for a discharge voltage of 300V, and the peak temperature is likely higher as the peak temperature region may have been missed by static axial placement of the probes.
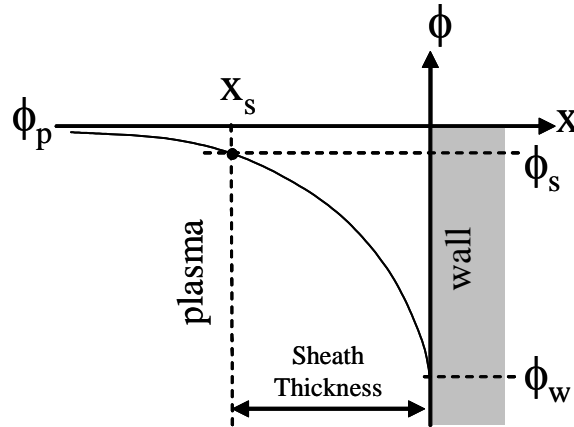
Figure 3.32   The sheath that forms between the bulk plasma and the thruster walls has a thickness of a few Debye lengths.

The potential energy transferred to the ion from the sheath can be estimated using the difference between the sheath potential and the thruster wall potential. Figure 3.32 shows a sketch of the plasma sheath structure near the solid walls of the thruster. The sheath forms in order to repel the fast moving electrons, and serves as a metering device to ensure that no net current is drained from the plasma by the wall. For a plasma with a thin planar sheath and $T_i \ll T_e$, the sheath potential (relative to the plasma potential) is,

$$\phi_s = -\frac{kT_e}{2e}. \tag{3.27}$$

With similar assumptions, the wall potential relative to the plasma potential is,

$$\phi_w = \frac{kT_e}{2e}\left[\ln\left(2\pi\frac{m_e}{m_i}\right) - 1\right]. \tag{3.28}$$

An ion enters the sheath at x_s with the Bohm velocity, and is then accelerated towards the wall with the remaining potential difference, $(\phi_s - \phi_w)$. This potential difference can be written in terms of the previous two equations as,

$$\phi_s - \phi_w = -\frac{kT_e}{2e}\left[\ln\left(2\pi\frac{m_e}{m_i}\right)\right]. \tag{3.29}$$

For a xenon plasma the mass ratio can be calculated to show that the potential difference between the sheath and the wall is roughly five times the electron temperature, where the electron temperature is now in electron-Volts instead of Kelvin.

$$\phi_s - \phi_w \approx 5.27 T_e(eV) \tag{3.30}$$

Thus, for an electron temperature of 25eV, the potential energy transferred to the ion would be about 132eV. The final parameter in Equation 3.26 that must be estimated is the ion current to the wall. When an ion contacts the wall, it recombines with an electron and then bounces back as a neutral xenon atom. This neutral can either be ionized again or drift out of the thruster. For every beam ion that is accelerated out of the channel, there will be some fraction of these ions that have undergone the recombination process at the wall before being ionized again and expelled into the plume. Thus, the wall current can be expressed as a fraction, α_w, of the beam current.

$$I_w = \alpha_w I_b \tag{3.31}$$

Szabo's simulation results have shown that α_w inside a small TAL style Hall thruster is between 25-30% [26]. In order to be conservative about the effectiveness of the MHT-9 to contain plasma, α_w has been estimated at 50%, meaning that one of every two ions in the beam has undergone a recombination power loss.

Electrons Lost to Walls

An equilibrium plasma in contact with a wall with a fully developed sheath will receive an average energy of $2kT_e$ from the repelled species that reach the wall. This is the result of an integral in spherical coordinates of a modified Maxwellian distribution function for the energy received by the wall from the repelled species represented in the loss cone. In this particular case, the repelled species is electrons, and the electron velocity towards the wall, w, is integrated from zero to infinity in the direction of the wall. Figure 3.33 shows a drawing of the electron velocity vector with the important angles used in the energy integral, which can be written as,

$$E_{ew} = \int_0^\infty \int_0^{\frac{\pi}{2}} \int_0^{2\pi} \tilde{f}(w)(w\cos\theta)\left(\frac{1}{2}m_e w^2\right)w^2\sin\theta\, d\chi\, d\theta\, dw . \qquad (3.32)$$

The modified distribution for the electron velocity assumes that far away from the wall the electrons are governed by a normal Maxwellian distribution. The modified distribution takes into account the effect of the retarding potential, ϕ, on the density of electrons,

$$\tilde{f}(w) = n_\infty\left(\frac{m_e}{2\pi kT_e}\right)^{\frac{3}{2}} e^{-\frac{1}{kT_e}\left(\frac{m_e w^2}{2} + e\phi\right)} . \qquad (3.33)$$

The energy received by the wall from electrons, E_{ew}, is the result of the integral shown in Equation 3.32 and is expressed as,

$$E_{ew} = \frac{1}{4}n_\infty \bar{c}_e e^{-\frac{e\phi}{kT_e}}(2kT_e) . \qquad (3.34)$$

The group of terms outside the parentheses determine the flux of electrons that reach the wall. The $2kT_e$ term inside the parentheses is the average energy received by the wall for each electron that arrives. This can be used to estimate the total power received by the thruster walls from electron impact, P_{ew}, written as,

$$P_{ew} = [2kT_e]\frac{I_w}{e}.$$

(3.35)

The electron temperature and wall current can be estimated as discussed in the previous section.
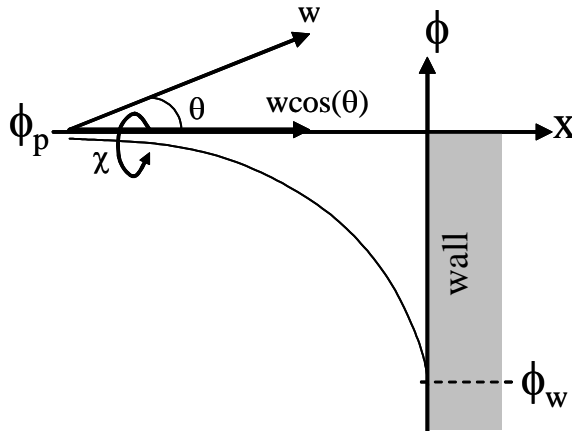
Figure 3.33 Electrons carry an average energy of $2kT_e$ into the wall. The energy flux is calculated using a modified Maxwellian distribution for a repelled species.

Electrons Lost to Anode

The electrons that eventually diffuse to the anode arrive there with a small amount of thermal energy, but they are repelled by the near anode sheath. The 1D simulation results by Ahedo indicate that the near anode sheath potential, ϕ_{na}, is on the order of 4V [57]. Since this process is similar to the electron flow into the sheath on the thruster wall surfaces described by Equations 3.32-3.35, the electron power collected by the anode, P_{ea}, can be estimated as,

$$P_{ea} = [2kT_{ea}]\frac{I_d}{e}.$$ (3.36)

The electron temperature near the anode, T_{ea}, is usually less than the temperature in the ionization region. As electrons surrender energy during the ionization process, they cool and scatter towards the anode through collisions with neutrals. Simulation results indicate a very wide range of temperatures, depending on the structure of the ionization region. Szabo reports temperatures of about 10eV along the outer anode piece and up to 30eV along portions of the inner anode surface near where the peak discharge density also occurs. The range of possible estimates for this parameter is rather large, and the effect is important, so trial and error may be necessary.

Excitation and Radiation

Making estimates of the excited states is both difficult and inexact. It is likely that neutrals (and possibly ions as well) are excited into higher level energy states through collisions with energy transfer that falls just short of ionization. This could happen to neutrals that eventually become ions in the beam or ions that are eventually lost to the thruster walls. When the excited neutrals transition back to the ground state, they will radiate their excess energy. The power radiated and absorbed by the thruster surfaces will contribute to thruster heating. This radiation power, P_{rad}, can be expressed as,

$$P_{rad} = [\psi e V_i]\frac{I_b + I_w}{e}.$$ (3.37)

The coefficient ψ is the ratio of energy spent on excitation to the energy of ionization per ion created within the thruster. An analytical fit by Fife of work done by Dugan and Sovie has shown that for xenon with electron temperatures above the ionization energy (12.1eV), this ratio is approximately 2.2 and does not vary significantly with T_e [59-60]. Thus, for every ion created within the thruster, the total ion production cost is 3.2 times V_i (38.7eV). This total energy cost includes the actual ionization of the neutral, V_i, as well as the energy spent in excitation ($2.2V_i$). Fife also estimates that, "inelastic losses due to elec-

tron-ion collisions are two orders of magnitude smaller than those due to electron-neutral collisions." This would mean that it is safe to ignore the radiation due to excited ions since they consume very little power relative to neutral excitation [59].

As neutrals are excited before being ionized they can also enter metastable states at certain excitation levels. These metastable states last longer than other excitation levels but still shorter than the ground state or full ionization. Experiments by Khakoo et al have determined the twenty lowest excitation levels for xenon, showing that in the threshold energy range of 8.315eV (the lowest excitation level) to 10.593eV, there are two metastable states at 8.315eV and 9.447eV [61-63]. However, the production rates of these metastable states are not well known and likely do not constitute a significant power loss. They are therefore ignored in this analysis.

Some of the radiated energy from excited states will fall on the thruster surfaces and the remainder will leave the thruster. The fraction of the power that reaches the thruster walls can be estimated using simple arguments. If the majority of excitation occurs in a high density region near the exit of the thruster, half of the radiation is likely to leave the thruster and half will be picked up by wall surfaces. If the excitation occurs a little more deeply in the annulus, a ratio of wall area to thruster exit area could be used. Considering both of these methods, the fraction is likely in the range of 0.5-0.8. As a conservative estimate, it will be assumed that half of the radiated power falls on the outer and inner thruster wall surfaces and a quarter of the power is absorbed by the anode surface.

3.4.2 Thermal Contact Resistance

The amount of interfacial conduction between two materials in contact depends on several factors: surface finish and cleanliness, material properties, contact pressure, the interstitial fluid and its pressure, as well as the temperature at the contact surface [64]. Figure 3.34 shows an exaggerated diagram of the heat transfer that occurs between two objects in contact with each other. The materials are not in perfect contact because they have surface roughness. There may be background gas, called the interstitial fluid, trapped inside the

gaps that form between the objects. This fluid conducts heat via convection, and there may also be radiation across these gaps as well. Contact pressure may also vary over the surface, for instance around bolt heads.

Heat Transfer at Surface Boundaries ($T_1 > T_2$)
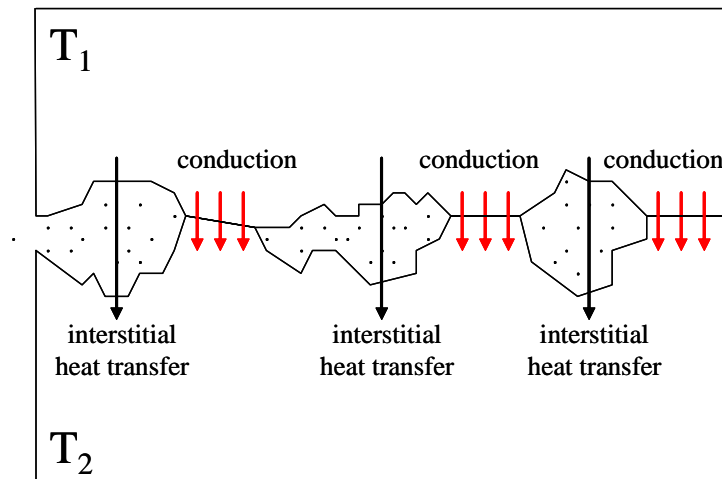
Figure 3.34 Diagram of heat transfer between two objects in contact (adapted from text by Lienhard) [64].

Many thermal models ignore this issue, using perfect thermal contact instead, which results in better heat conduction and lower predicted temperatures. In fact, contact resistance can cause some of the largest temperature gradients in a Hall thruster [65]. A very simple model of this effect was incorporated into the finite element thermal model of the MHT-9 in order to improve temperature prediction accuracy. The thermal contact resistance or its inverse, the interfacial conductance, was estimated for each material interface in the thruster, and applied to a thin artificial layer at the boundary between adjacent materials. The interfacial conductance, h_c, has units of W/m^2-K and acts as an effective conductivity for the boundary between two objects. For a contact region of total area A and temperature differential ΔT, the heat transfer through the interfacial layer can be expressed as,

$$Q \, = \, Ah_c\Delta T \, = \, \frac{\Delta T}{R_t}. \tag{3.38}$$

The thermal contact resistance, R_t, is defined as shown in Equation 3.38 and has units of K/W. Figure 3.35 shows how the contact resistance was implemented within the finite element model. A thin layer of artificial material was placed at the interface boundary of objects within the model. This layer had a thickness of Δx=0.05mm and an effective conductivity, k_L, calculated as,

$$k_L \, = \, h_c\Delta x. \tag{3.39}$$

The values of h_c used to estimate the interfacial conductance between materials were extrapolated from data in the text by Lienhard, which were adapted from other sources [64, 66-67]. Because data on the specific material interfaces in the MHT-9 could not be located, general properties were used as shown in Table 3.5. These values are intended to be accurate for interfaces under vacuum with moderate contact pressure (1-10atm). The interfaces with the boron nitride materials were the only boundaries to use the metal/ceramic values. Although the samarium cobalt magnet has a texture similar to a ceramic material, the magnet is coated with a thin layer of nickel to prevent chipping.

It should be noted that interfacial conductance can be improved with the use of foils inserted between objects that are particularly rough. The foil is intended to fill some of the gaps formed at the contact surface, enhancing the direct conduction component of heat transfer. The foil materials work best when they are soft and have a high thermal conductivity. Common foil material choices are indium and lead [68]. Indium foils were considered for the MHT-9 but initial testing showed that they were not necessary because the thruster did not overheat.
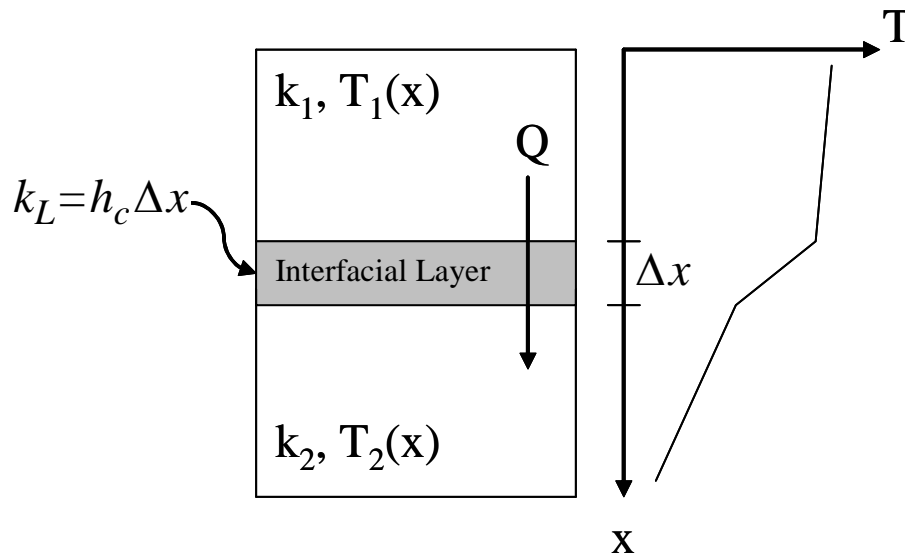
Figure 3.35   Thin layer model for heat transfer at surface boundaries.

TABLE 3.5   Interface Properties Used in the MHT-9 Thermal Model

Material Interface	Interfacial Conductance (W/m²-K)	Thermal Conductivity for $\Delta x = 0.05$mm (W/m-K)
metal/metal	650	0.0325
metal/ceramic	1140	0.057

3.4.3 Finite Element Model

The finite element thermal model was built using the Maxwell software package produced by Ansoft. The model is steady-state, two-dimensional and axisymmetric. The thruster geometry and boundary conditions are specified within the software, along with material properties, so that the problem is fully defined. Boundary conditions can be made for temperature, heat sources and surface radiation. However, radiation between objects within the model is not included. The size of the solution space is set by the user, but is typically ten times larger than the size of the thruster. Meshing is performed automatically and refined after each iteration until the energy error in the solution is reduced below a limit set by the user (typically 0.1% of the total energy in the system). The mesh can be further

refined manually in order to provide greater resolution in a region of interest. This procedure is similar to that used for the finite element magnetostatic model.

Boundary Conditions

Several different boundary conditions were required for each run of the simulation. Figure 3.36 shows a diagram of the top half of the thruster with the location of boundary conditions labeled. Along the back of the copper mounting plate (shown in blue), a temperature boundary condition was set. This temperature was typically set to either 200°C or 300°C. The outer surfaces of the thruster were all set up to radiate to a reference temperature of 25°C, including the mounting plate, the outer cover and the tip of the center stem cap (also referred to as the inner guard ring). The emissivity used for each of these materials are listed in Table 3.6.
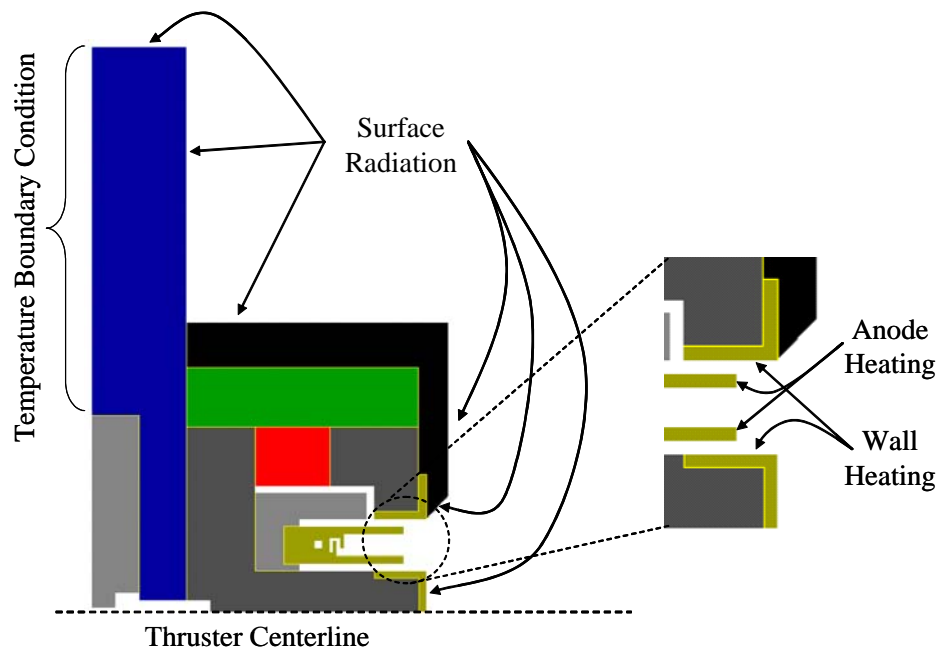
Figure 3.36 Axisymmetric cross sectional diagram of the MHT-9 thermal model with the locations of the boundary conditions identified.

TABLE 3.6   Emissivity Values for the MHT-9 Thermal Model

Thruster Component	Material	Emissivity
Center Stem Cap	Tantalum	0.25
Outer Cover	316 Stainless Steel	0.65
Mounting Plate	Copper (matte finish)	0.22

Heat Sources

In addition to the boundary conditions already mentioned, heat sources were applied to both the anode tip and the discharge chamber walls. The power delivered to the anode was determined by the electrons lost to the anode and radiation from excited neutrals, as previously discussed. The power input to the walls was determined by the ion and electron losses to walls through recombination, as well as radiation from excited neutrals. Both heat sources were applied evenly to their respective surfaces. The wall heating was applied over a channel length of 1.5mm, the distance between the anode tip and the channel exit (axial end of the guard rings).

Material Properties

Steady state thermal models only require thermal conductivities to be specified for materials. These conductivities, along with the model geometry, boundary conditions and heat sources fully define the problem. The conductivities used for the MHT-9 thermal model are shown in Table 3.7. Wherever possible, the conductivities selected were for the elevated temperatures predicted by the thermal model.

TABLE 3.7   Thermal Conductivities of Thruster Materials

Material (Type)	Thermal Conductivity (W/m-K)
Tantalum	58
Hiperco (50A)	29.8
Copper	400
Boron Nitride	71
Samarium Cobalt	23
Stainless Steel (316)	16.3

3.4.4 Model Results

Thermal models were executed with several different inputs and boundary conditions because of the uncertainty in estimating operating parameters before actual test data were available. The calculated model inputs and resulting temperatures output by the finite element model are discussed below.

Heat Load Inputs

The analytical heat load estimates discussed in Section 3.4.1 were calculated for two different scenarios: a high performance case and a low performance case. The high performance case is intended to represent the nominal design conditions with a discharge power of 200W and a discharge current of 0.67A. The low performance case determines the heat loads for a higher than nominal thruster power of 300W and a discharge current of 1A. Both cases assume a 300V discharge voltage, 0.74mg/s propellant flow rate, and the 1786s specific impulse used in the ideal scaling analysis. The high and low performance cases have thrust efficiencies of 57% and 38%, respectively.

Results of the analytical heat load estimates for each case are shown in Figure 3.37 and Figure 3.39. These two figures shown below have the inputs to the analytical equations in the upper left hand box. This includes the assumptions about temperatures and current ratios. These numbers are used to produce the intermediate calculations which determine the energies on a per ion basis, and finally the analytical model outputs in the bottom left. These power estimates are the results of the equations discussed in Section 3.4.1. As a check on the analytical model, the total power produced by the plasma processes should be equal to the thruster discharge power, as shown by the power balance in Equation 3.22.

Once the power estimates have been determined by the analytical equations, they can be appropriately summed to determine where to place the heat loads within the finite element model of the MHT-9. The heating power applied to the wall is the sum of the ion and electron power delivered to the wall, plus half of the total power radiated by excited neutrals. The heating power applied to the tip of the anode is the sum of the power carried to the

anode by the electrons that eventually diffuse across the magnetic field and a quarter of the radiated power from excited neutrals.

Temperature Results

The finite element model calculates steady state temperatures for every point within the thruster. As mentioned in the section on boundary conditions, the simulation was run for two different temperature boundary conditions on the back of the copper mounting plate. The simulation was also run for both the high performance and low performance cases, making for a total of four sets of temperature data. Average and maximum temperatures were calculated for a variety of key thruster components, as shown in Table 3.8.

Figure 3.38 shows a color contour plot of temperature within the thruster for the high performance case with a 200°C boundary condition on the back plate. This case is modeled with a heat input of 40.7W spread evenly on the inner and outer chamber walls, as well as 37.4W spread evenly on the tip of the anode. Figure 3.40 shows a similar temperature plot for a low performance case with a 300°C boundary condition on the back plate. This case applies 61.1W to the thruster walls and 56.1W on the anode. Both of these plots show that the tip of the anode sustains the highest temperature in the thruster. They also indicate that the tip of the center stem is an area of concern for exceeding the Curie point. Furthermore, as the Hiperco core heats up, but before the Curie point is reached, the permeability will slowly decrease and field lines will deform if the material saturates magnetically.

The SmCo permanent magnet can operate continuously at temperatures up to 500°C and for short durations up to 550°C. As Table 3.8 indicates, the predictions for the average magnet temperature are between 310-451°C. Thus, the margin of safety for reversible demagnetization is at least 50°C and likely higher if the worst case scenario does not occur. The Curie point for SmCo is 825°C, so complete demagnetization is very unlikely.

The center stem has a large temperature gradient across it compared to most of the other components in the thruster, as indicated by the roughly 200°C difference between its average and maximum temperature. This is likely due to the close contact with the plasma and

inner guard ring on the hot side, and the copper mounting plate on the cold side. The maximum temperature predicted in the center stem ranges from 600-874°C. This is well below the Hiperco Curie point of 940°C, but as Figure 3.9 indicates, the saturation strength of Hiperco decreases from a nominal 2.4T to 1.8T as the temperature of the material is raised from room temperature to 760°C (1400°F). This makes saturation near the tip of the center stem a concern. The magnetic field strength indicated in Figure 3.10 shows that the tip of the center stem carries a field strength of approximately 1.2T or less (for a permanent magnet temperature of 400°C). The magnetic field plot also shows that the base of the center stem is the region most likely to incur saturation problems due to the high field strength there, but as the plots of temperature indicate, the temperature is much lower there. These opposing trends of high field strength at the base and high temperature at the tip seem to indicate that saturation and field shape deformation are unlikely problems. However, a gradual reduction in permeability with increasing temperature may still have a small effect on the field strength and shape near the thruster exit plane.

The average temperature inside the other core material component, the Hiperco focusing pole that sits on top of the permanent magnet, ranges from 327-474°C. Therefore, this piece should not experience any problems due to overheating.

3.4.5 Design Improvements

Several important design changes resulted from use of the finite element thermal model. As discussed in the description of the design process at the beginning of this chapter, the thermal model was used as a tool to support the mechanical design and material selection, and to serve as a check on the magnetic circuit to ensure that the thruster would not exceed critical temperatures for operation of the magnet and core material. The plots of temperature shown here are for the final geometry of the thruster, but there were several iterations of the design process where the thermal characteristics of the thruster were improved through the use of this model.

The initial design used an insulator across the entire back of the center stem, and the copper mounting plate only connected to the stainless steel outer cover. In order to increase heat conduction away from the center stem, the copper mounting plate was extended all the way across the back of the center stem. The boron nitride insulating sleeves were extended to allow for the high potential anode components to pass through holes in both the base of the center stem and the copper mounting plate.

An additional copper heat sink was added surrounding the temperature sensitive magnetic circuit. It threads onto the Hiperco focusing pole to increase the surface area of conduction and provide good thermal contact. This heat sink is also bolted into the mounting plate so that there is good thermal contact between the two copper pieces. The heat sink is intended to pull heat out of the outer guard ring and focusing pole, but likely does not provide for much thermal relief of the permanent magnet. There is no physical mechanism to ensure good conduction between the magnet and the heat sink. Furthermore, with the heat sink that allows for magnetic shunts to be placed in the thruster, a gap exists along the outside of the permanent magnet to make room for the shunt and copper filler ring. Compare Figure 3.20 and Figure 3.21 to understand the geometry difference between these two versions of the heat sink.

Tantalum guard rings were added near the thruster exit plane to not only reduce erosion of the magnetic pole pieces, but also to provide an additional thermal gradient between the plasma and the magnetic circuit. The outer guard ring is intentionally slip fit (instead of a close fit or press fit) inside the focusing pole to reduce the interfacial conductance between the guard ring and the magnetic circuit. The tantalum can withstand very high temperatures, but the Hiperco focusing pole is temperature sensitive as previously described. The slip fit takes advantage of the thermal contact resistance to increase the temperature difference between the outer guard ring and the focusing pole. The inner guard ring (center stem cap) required a press fit to keep it in place. Using a bolt would have reduced the cross sectional area and increased the chance of magnetic saturation in the center stem.

HIGH PERFORMANCE CASE

ANALYTICAL MODEL INPUTS	
Discharge Power (W)	200
Discharge Voltage (V)	300
Specific Impulse (s)	1786
Beam Current Fraction	0.7
Wall Current Fraction	0.3
Ion Excitation & Radiation Factor	2.2
Ion Plume Temperature (eV)	1
Electron Plume Temperature (eV)	3
Near Cathode Potential Difference (V)	20
Ion Chamber Temperature (eV)	3
Electron Chamber Temperature (eV)	27.5
Near Anode Electron Temperature (eV)	25

INTERMEDIATE CALCULATIONS	
Discharge Current (A)	0.67
Beam Current (A)	0.47
Wall Current (A)	0.14
Sheath Potential Drop (V)	144.9
Ion Exit Velocity (m/s)	17502.8
Bohm Velocity (m/s)	4496
Wall Ion Ionization Energy (J)	1.94E-18
Wall Ion Thermal Energy (J)	1.20E-18
Wall Ion Kinetic Energy (J)	2.20E-18
Wall Ion Potential Energy (J)	2.32E-17

ANALYTICAL MODEL OUTPUTS	
Ion Plume Kinetic Power (W)	97.3
Ion Plume Thermal Power (W)	1.2
Ion Plume Ionization Power (W)	5.6
Electron Plume Thermal Power (W)	3.5
Electron Plume Kinetic Power (W)	9.3
Ion Wall Power (W)	25.0
Electron Wall Power (W)	7.7
Electron Anode Thermal Power (W)	33.3
Radiation from Excited Neutrals (W)	16.1
TOTAL POWER (W)	199.0

FINITE ELEMENT MODEL INPUTS	
Wall Heating Power (W)	40.7
Anode Heating Power (W)	37.4

Figure 3.37 Heat load estimates calculated for the high performance case.
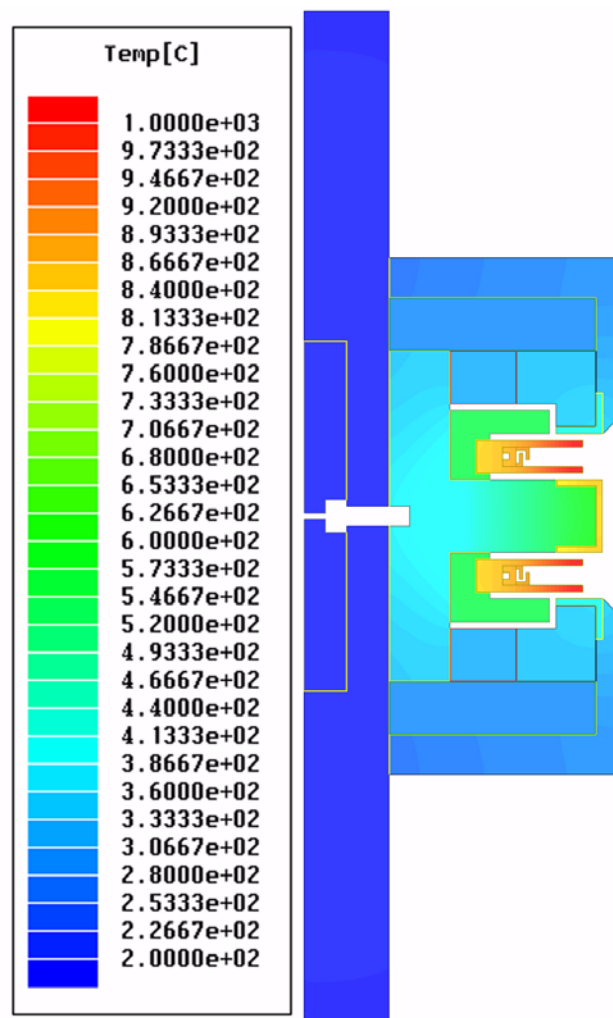
Figure 3.38 Contour plot of temperature within the MHT-9 for the high
performance case with a 200°C temperature boundary condi-
tion along the back of the copper mounting plate.

LOW PERFORMANCE CASE

ANALYTICAL MODEL INPUTS	
Discharge Power (W)	300
Discharge Voltage (V)	300
Specific Impulse (s)	1786
Beam Current Fraction	0.7
Wall Current Fraction	0.3
Ion Excitation & Radiation Factor	2.2
Ion Plume Temperature (eV)	1
Electron Plume Temperature (eV)	3
Near Cathode Potential Difference (V)	20
Ion Chamber Temperature (eV)	3
Electron Chamber Temperature (eV)	27.5
Near Anode Electron Temperature (eV)	25

INTERMEDIATE CALCULATIONS	
Discharge Current (A)	1.00
Beam Current (A)	0.70
Wall Current (A)	0.21
Sheath Potential Drop (V)	144.9
Ion Exit Velocity (m/s)	17502.8
Bohm Velocity (m/s)	4496
Wall Ion Ionization Energy (J)	1.94E-18
Wall Ion Thermal Energy (J)	1.20E-18
Wall Ion Kinetic Energy (J)	2.20E-18
Wall Ion Potential Energy (J)	2.32E-17

ANALYTICAL MODEL OUTPUTS	
Ion Plume Kinetic Power (W)	145.9
Ion Plume Thermal Power (W)	1.8
Ion Plume Ionization Power (W)	8.5
Electron Plume Thermal Power (W)	5.3
Electron Plume Kinetic Power (W)	14.0
Ion Wall Power (W)	37.4
Electron Wall Power (W)	11.6
Electron Anode Thermal Power (W)	50.0
Radiation from Excited Neutrals (W)	24.2
TOTAL POWER (W)	298.6

FINITE ELEMENT MODEL INPUTS	
Wall Heating Power (W)	61.1
Anode Heating Power (W)	56.1

Figure 3.39   Heat load estimates calculated for the low performance case.
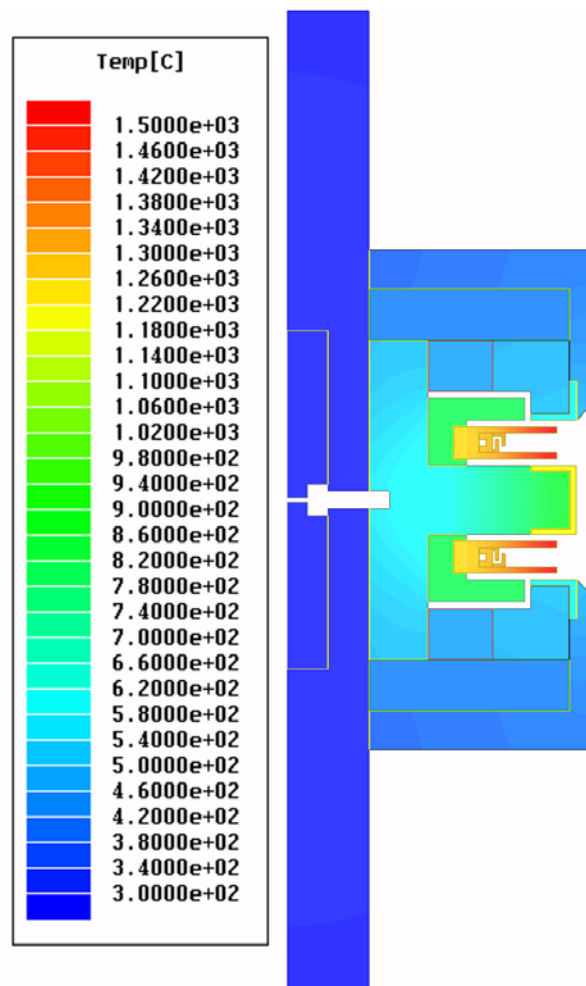
Figure 3.40 Contour plot of temperature within the MHT-9 for the low performance case with a 300°C temperature boundary condition along the back of the copper mounting plate.

TABLE 3.8   Predicted Temperatures in Thruster Components (All Temperatures in Degrees Celsius)

Thruster Component	Data Type	High Performance Case (η_t=57%)		Low Performance Case (η_t=38%)	
Boundary Condition[a]	Constant	200	300	200	300
Permanent Magnet	Average	310	397	366	451
	Maximum	311	399	368	453
Focusing Pole	Average	327	411	392	474
	Maximum	338	422	409	490
Center Stem	Average	405	497	504	594
	Maximum	600	689	789	874
Anode	Average	912	1004	1268	1358
	Maximum	1027	1119	1440	1530
Center Stem Cap (Inner Guard Ring)	Average	860	945	1166	1243
	Maximum	873	958	1184	1262
Outer Guard Ring	Average	437	520	558	637
	Maximum	449	531	575	654

a. The temperature boundary condition was set on the back of the copper mounting plate.

Chapter 4

EXPERIMENTAL TESTING OF THE MHT-9

This chapter describes the experimental setup and the performance testing of the MHT-9 conducted at both the MIT Space Propulsion Laboratory (SPL) and the Busek Company. Data are presented to provide a picture of the full range of operating conditions of the thruster. The analysis of these data, the comparison of the results to design goals and the implications for Hall thruster miniaturization are discussed in the following chapter.

4.1 Experimental Setup

The first two tests of the MHT-9 were conducted at the MIT SPL facility on a fixed shelf setup (no thrust stand). These tests were conducted to make sure the thruster could fire stably over a wide range of operating conditions before conducting full performance measurements at the Busek facility. Four separate tests were conducted at Busek using an inverted pendulum thrust stand designed for the BHT-200 thruster. Over 100 different operating conditions were tested to characterize the MHT-9.

4.1.1 Vacuum Tanks

MIT Facility

The initial two tests of the MHT-9 were conducted in the MIT SPL Astrovac chamber. This chamber is 1.5m in diameter and 1.6m in length. It is equipped with a mechanical pump and two cryopumps capable of a total xenon pumping speed of 7,500L/s. The pres-

sure within the chamber is monitored by a thermocouple gauge at high pressure and a cold cathode gauge at pressures below 10^{-3}torr. The tank is usually equipped with a water cooled target that the thruster can fire towards to reduce sputtering and heating of the tank walls. However, the target was not in place during testing of the MHT-9 because the back window was utilized for spectroscopy measurements related to work by Celik [69]. The tank is pictured in Figure 4.1

Figure 4.1   The MIT Space Propulsion Laboratory Astrovac vacuum facility.

Busek Facility

The Busek T6 vacuum facility was used for performance testing of the MHT-9. The tank is shown in Figure 4.2. It is split into two different sections for experimental setup and pumping. The overall tank length is 3m, with the experimental section having a diameter of 1.8m and a length of 1.8m. The pumping section is 2.4m in diameter and has a length of 1.2m. Pumping is performed by a combination of an oil diffusion pump and four cryopumps. At peak capacity, the combination of the diffusion and cryopumps evacuate

xenon at a rate of 90,000L/s [70]. The interior of the tank surface is cooled with a liquid nitrogen pumped shroud in the experimental section and a target in the pumping section. The pressure inside the tank is monitored using a hot-cathode ionization gauge and corrected for xenon.

Figure 4.2   The Busek T6 vacuum facility.

4.1.2 Thrust Stand

The thrust stand used at Busek during performance testing of the MHT-9 is the inverted pendulum type originally developed by Haag at what was then the NASA Lewis Research Center. The construction and calibration of the thrust stand are similar to those previously documented [71-72]. The thrust stand uses a linear variable differential transformer (LVDT) that measures displacement and produces an output voltage proportional to the thrust. The signal is read into a computer controlled data logger so that the thrust signal can be filtered and monitored. The thrust stand is water cooled and can be calibrated in situ. Inclination of the thrust stand is read with an inclinometer and actively controlled with a leveling motor.

The thrust stand was calibrated with a series of four 0.5g weights at the beginning and end of each test run. The linear fits of the calibration curves before and after each test were averaged to provide the proportionality constant between LVDT output voltage and thrust for each test run. Error in the thrust measurement is primarily due to drift in the thrust stand zero point because of thermal effects. The thruster was shut off several times during performance testing to record the drift of the zero point. Thrust stand measurements were always referenced to the most recent zero point determination. The error in the thrust measurement was determined to be ±0.3mN based on the average drift of the thrust stand zero.

4.1.3 Cathode

A Busek built hollow cathode was used for the MHT-9 test campaign. The cathode is pictured with the MHT-9 thruster in Figure 3.24 and Figure 3.26. The electron emitting element inside the cathode is made of tungsten and impregnated with various oxides to lower the work function. The element is wrapped with a heating coil to allow it to be warmed up before the keeper is turned on for ignition. The keeper power supply provides a potential difference between the tungsten element and the body of the cathode, helping to pull electrons out of the material. This cathode, designated the BHC-1500, is the same cathode used with the BHT-200 thruster and was specifically designed for low power operation. It has an orifice diameter of 3.2mm and can operate on flow rates of 0.1mg/s or less. It requires only 10W for ignition once the electron emitting element has been warmed up. The cathode is self-sustaining, meaning that if the thruster discharge is operating, the cathode heater and keeper power supplies can be turned off [73]. In this self-sustaining mode of operation, the cathode's electron emission process is maintained through the discharge current. However, for the MHT-9 testing the cathode keeper was maintained at 0.5A while the heater was set to 4A. This was in part due to the fact that the cathode used was near end of life and also as an attempt to remove the cathode as a potential source for thruster shut down.

During testing, the cathode was initially started with 2sccm (0.2mg/s) of xenon flow and then reduced to 1sccm (0.1mg/s) for performance testing. The cathode flow rate was held constant at 1sccm for all tests conducted with the MHT-9. The ratio of cathode flow to anode flow ($\dot{m}_c/\dot{m}_a$) for the MHT-9 ranged between 10-33% during testing. This is similar to the ratio used during testing of the D-55 by NASA, where a range of 18-38% was reported [39]. At the MHT-9 nominal anode flow rate of 0.74mg/s, the $\dot{m}_c/\dot{m}_a$ ratio was 13.5%. The D-55 uses a nominal anode flow rate of 4.52mg/s and cathode flow of 1.0mg/s, for a flow ratio of 22.1%. This ratio is important to consider because the cathode typically ejects a mostly neutral flow into the vacuum tank, providing an extra background density of neutral xenon atoms that can potentially be ionized if they drift into the discharge chamber. By ensuring that the cathode flow ratio in the MHT-9 is similar or less than that of the D-55, a fair comparison of performance metrics can be assured (for similar vacuum tank pressures).

4.1.4 Power

The MHT-9 requires three power supplies to operate, less than the 4-5 typically required for a laboratory Hall thruster with electromagnets. The discharge power supply sets up the potential difference between the anode and the cathode, and it controls ion acceleration. The cathode heater power supply warms up the tungsten element before cathode ignition. The cathode keeper power supply pulls electrons off of the element and ejects them out of the cathode orifice into the thruster plasma. Both the heater and the keeper power supplies are grounded to the cathode. Once the cathode is warmed up and operational, and the plasma discharge has been started, the heater and keeper could conceivably be shut off. This would allow the thruster to run on just one power supply. However, this was never attempted during testing of the MHT-9.

For the initial checkout testing at MIT, three separate rack mounted power supplies were used to operate the MHT-9. During the performance measurements at Busek, the thruster was operated using the Busek 600W breadboard power processing unit (PPU) that was

originally developed for the BHT-600 thruster. This PPU requires only one power supply input and provides all necessary separate thruster outputs through DC-DC conversion.

The metallic-walled TAL variety of Hall thrusters are typically operated with the cathode grounded to the thruster body. This means that the metallic guard rings that form the walls near the exit plane are at cathode potential [38]. For in-orbit operations, the entire thruster assembly floats relative to the rest of the spacecraft [36]. This is often simulated in the laboratory environment by insulating the thruster and allowing it to float relative to the tank. However, in testing of the MHT-9 the thruster body and cathode were grounded to each other and the vacuum tank in order to minimize the potential for short circuits. This configuration is shown in the electrical diagram pictured in Figure 4.3. Grounding the cathode and thruster body should not affect performance, and significantly simplifies the test configuration because insulated mounting platforms are not required and propellant isolation can be accomplished within the thruster body.

4.1.5 Propellant

The MHT-9 requires two flow controllers to provide separately metered flow to both the anode and the cathode. Research grade xenon was supplied from a single bottle to two mass flow controllers. In the MIT experimental setup, the two controllers were made by Omega Engineering (model FMA-A2400). These controllers can provide flow rates from 0-10sccm with an accuracy of ±1% of the full scale flow rate (±0.1sccm). The Busek facility uses flow controllers made by Unit Instruments (model 7300). The anode controller can provide up to 50sccm of flow and the cathode controller can provide up to 10sccm. Both controllers are accurate to within ±1% of the full scale flow rate (±0.5sccm for anode; ±0.1sccm for cathode). The Busek setup also uses pressure transducers in the propellant lines, immediately downstream of the mass flow controllers. These are MKS Baratron transducers rated to 100torr, and they allow the pressure in the flow line to be monitored on a continual basis during testing.
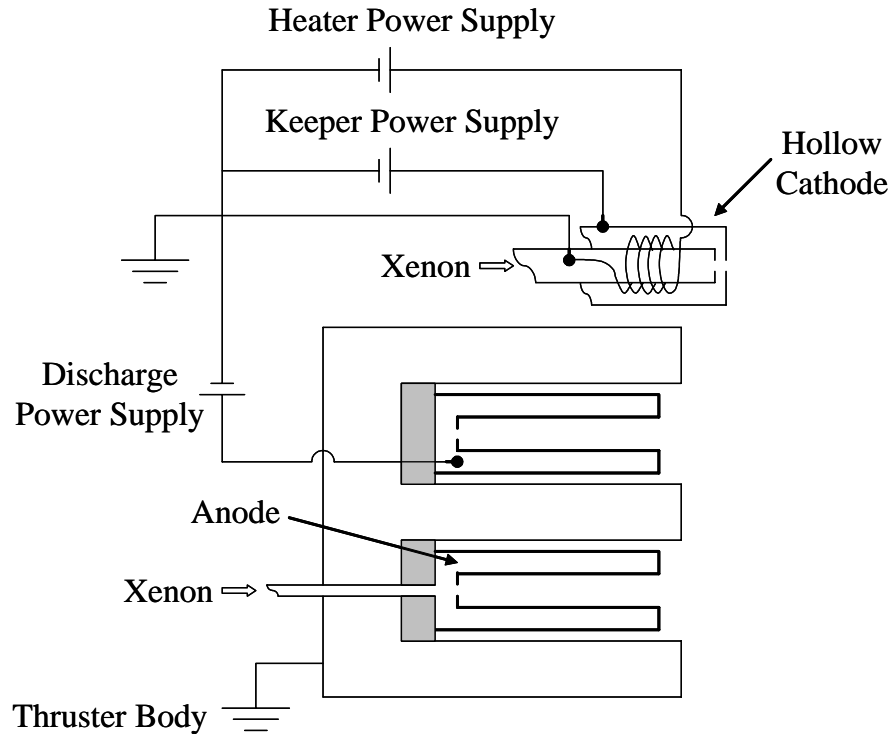
Figure 4.3   Electrical diagram for testing of the MHT-9.

4.1.6 Temperature Measurement

The temperature inside the MHT-9 was monitored using two type-K thermocouples made by Omega Engineering. The thermocouples are insulated and contained within 1/16in diameter stainless steel sheaths but they are ungrounded, meaning that the wires and junction are insulated from the sheath and do not touch at the tip. This causes the thermocouples to have a slightly slower response, but it allows the temperature measurement to be undisturbed by any stray plasma current that intersects the probe sheath. The tips of the thermocouples were inserted into the thruster through two 1/16in diameter holes made through the outer cover and heat sink. One thermocouple was pressed against the permanent magnet while the other was pressed against the outer edge of the center stem base, as shown in Figure 4.4. Holes were made in the shunts and copper filler rings so that the temperatures could be monitored when operating with a shunt as well.
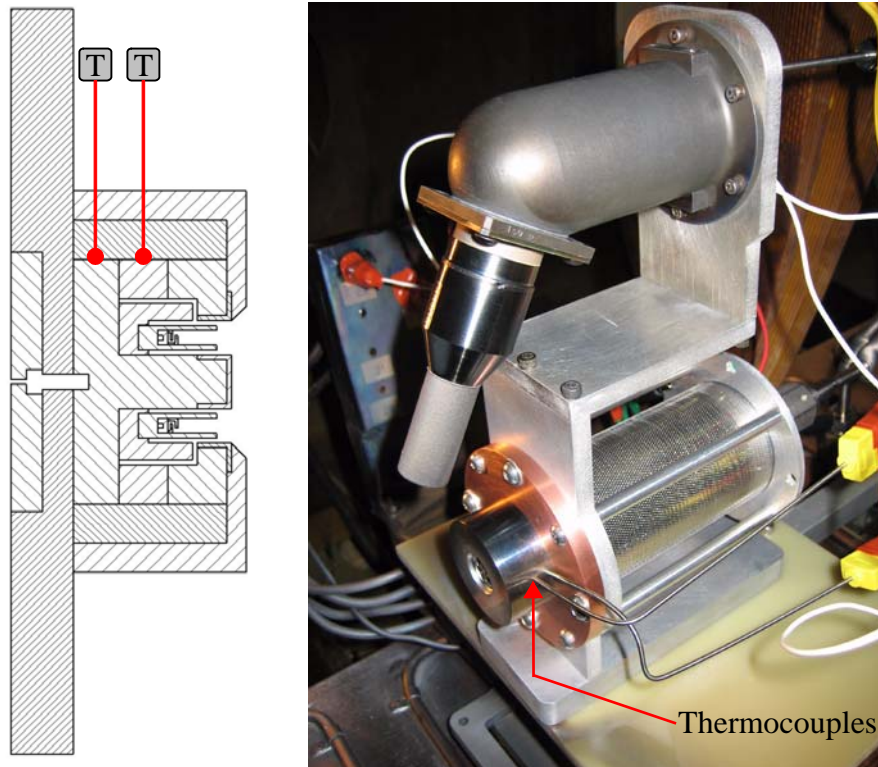
Figure 4.4 Drawing of the MHT-9 showing the location of thermocouples and a picture that shows the thermocouples in place before a test at Busek.

4.1.7 Data Collection

During the verification testing conducted at MIT, data were collected by manually recording values. The performance testing at Busek used a 22-bit Agilent data logger (HP34907A) equipped with a twenty channel multiplexer (HP34901A) that allows all of the relevant data to be stored directly to a computer. The only data recorded manually during the performance testing were tank pressure measurements. All voltages, currents, flow rates, line pressures, thermocouple temperatures, and thrust measurements were recorded automatically every few seconds.

4.2 Thruster Verification

The MHT-9 was test fired on six separate occasions. The first two tests of the MHT-9 were performed at MIT in the Astrovac facility to make sure that the thruster could maintain stable operation. The experimental setup inside the MIT vacuum tank is pictured in Figure 4.5. The first test lasted only a few minutes, with an extremely bright plasma observed at the thruster exit plane as shown in Figure 4.6. Several bright arc flashes were also observed before the anode eventually shorted to the thruster body. The second test was successful, and was voluntarily ended after two hours with the thruster operating stably at many different flow rates and voltages.
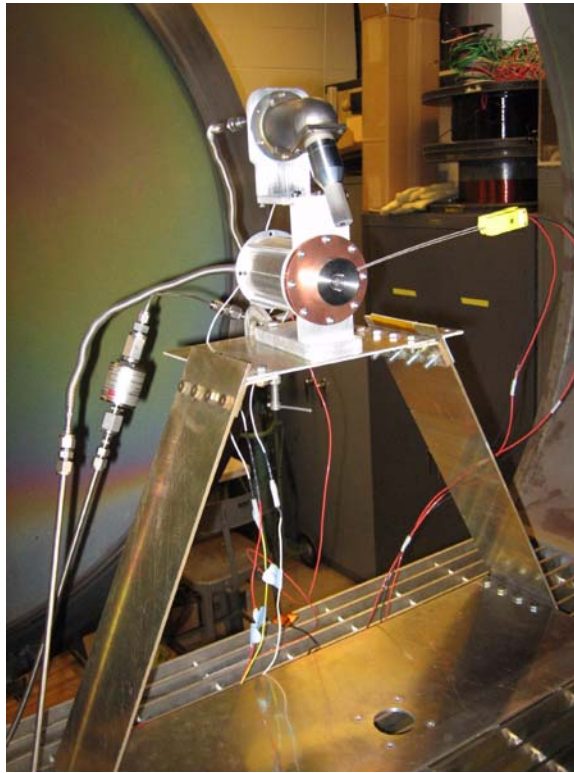
Figure 4.5 Experimental setup inside the MIT vacuum tank.

4.2.1 Verification Test #1

The problems during the first test were likely due to both electrical and flow issues. The cathode was not properly grounded to the thruster body, but instead was floating relative to the thruster and vacuum tank. If the cathode potential floated below the tank potential, as it does in the case of ceramic walled thrusters, the electrons emitted by the cathode would have been attracted to the entire thruster body. When allowed to float, the cathode potential is usually between 15-20V below the ground potential. Thus, the anode would still be the most likely place electrons were accelerated towards, but nearby thruster body surfaces could have drawn excess current from the cathode as well.

The propellant connections along the flow line were suspiciously loose upon examination of the thruster after the test. This may have been because the Swagelok connections were made with teflon ferrules. These ferrules were being used on metal tubing to make disconnection and reassembly easier, but it can be difficult to assure a leak tight connection when swaging dissimilar materials. Thus, there may have been flow leaks both within the enclosed insulating back section of the thruster and outside the thruster at the connection to the tank propellant line.

The brief plasma produced in test #1 was captured in the photo shown in Figure 4.6. The plasma appears almost spherical and very bright. All of the pictures of the MHT-9 show a very bright plasma relative to those of other thrusters, such as the BHT-200. This could be due to the higher plasma density predicted by the scaling analysis. Spectroscopic measurements by Celik also indicate a higher electron temperature than the D-55 thruster [69].

Upon disassembling the thruster after the first test, pitting was observed near the base of the center stem as shown in Figure 4.7. Conductive sputtered material was deposited along the ceramic insulator that sits between the anode and the center stem, and this is likely the source of the short circuit between the anode and thruster body that ended the test. There was some sputtered material observed on the inside wall of the anode as well. One hypothesis for this shorting is that the ceramic insulator built up charge along its surface and

because of the flow leak in the back of the thruster, pressure built up in the gap region. Arcing between the anode and center stem was not likely the cause of the pitting along the center stem surface because of the arguments made in Section 3.3.3, and because the pitting was observed only near the base of the center stem where the ceramic is located (not along the whole length of the center stem). However, if the ceramic built up significant charge, there may have been arcs from it to the center stem that removed material, deposited it back on the insulator and this could have led to the eventual short circuit.

Figure 4.6 The MHT-9 briefly firing during test #1. The plasma is very bright and almost spherical in shape. The large bright circle on the far tank wall is a copper plate reflecting the camera flash. The yellow plastic pieces just above the plasma are thermocouples.
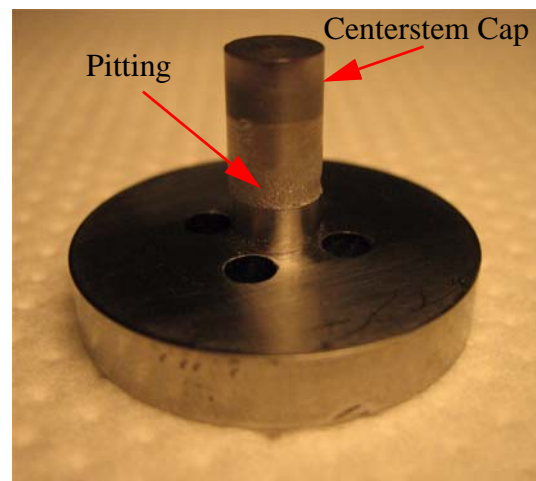
Figure 4.7 Pitting was observed along the base of the center stem after test #1. The pitting begins where the ceramic insulator ends. The end of the center stem is a different color because the tantalum center stem cap is pressed into place.

4.2.2 Verification Test #2

The second test at MIT was conducted with the cathode grounded to the thruster body and the tank. The teflon ferrules were used again with the Swagelok union because of the need for easy disassembly of the thruster. When metal ferrules are used on metal tubing, they

assure a leak tight connection but they cannot be removed. A metal ferrule along the anode feed tube must be cut off in order for the anode to be removed. This tube is welded to the anode cup and is only long enough to tolerate having the ferrule cut off 2-3 times. Thus, the teflon ferrules were given a second chance with extra tightening for the anode tube connection. The tank flow line and the propellant isolator were connected using an Ultra-Torr fitting that utilizes a rubber O-ring seal.

The second test was successful. The thruster ran stably for almost two hours at flow rates between 0.30-0.74mg/s, and discharge voltages from 100-300V. A picture of the thruster firing is shown in Figure 4.8. The plasma has the shape of a conical jet, instead of the more spherical shape observed in test #1. The temperature of the magnet could not be monitored continuously due to a thermocouple grounding problem, but it could be observed when the discharge was turned off. After running the thruster for twenty minutes at the nominal flow rate of 0.74mg/s and a discharge voltage of 300V, the thruster was shut down and the magnet temperature was measured to be 250°C. This temperature was a reassuring result that the magnet was operating well within the 500°C continuous temperature limit.

Preliminary data from test #2 are shown in Figure 4.9. The data show that the thruster discharge current peaks at a voltage of 200V. This voltage point was also observed to have some visible plasma oscillations and flickering. The thruster was expected to operate at a discharge power of 200W at the nominal flow rate of 0.74mg/s and a discharge of voltage of 300V. However, the plot of discharge power shows that this nominal point is about 100W higher than expected.

The pitting of the center stem observed during test #1 was not nearly as severe in test #2. However, there was additional evidence of a flow leak. In the back of the thruster, inside the region insulated with the ceramic tube and stainless steel mesh screen (see Section 3.3.1), there were signs that a plasma had formed. The back of the copper mounting plate had a thin silver colored deposit, which may have been sputtered aluminum from
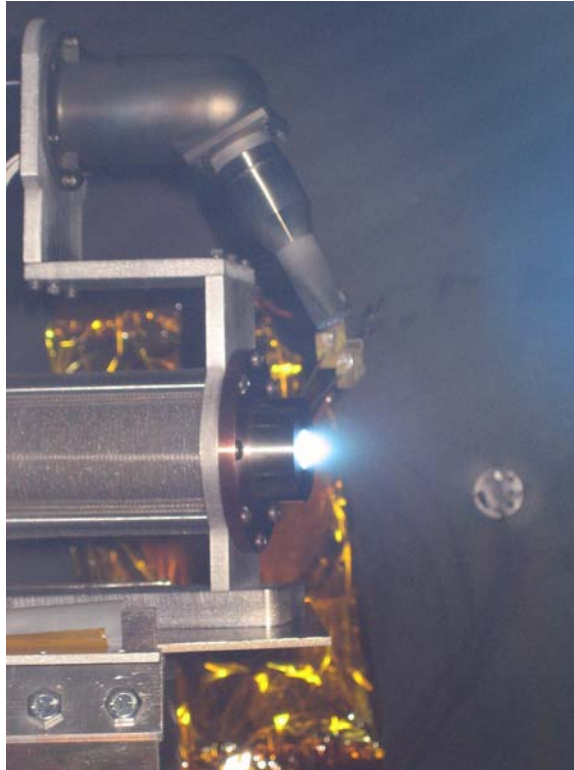
Figure 4.8 This photograph of the MHT-9 firing was taken during test #2. The plume has the shape of a conical jet.
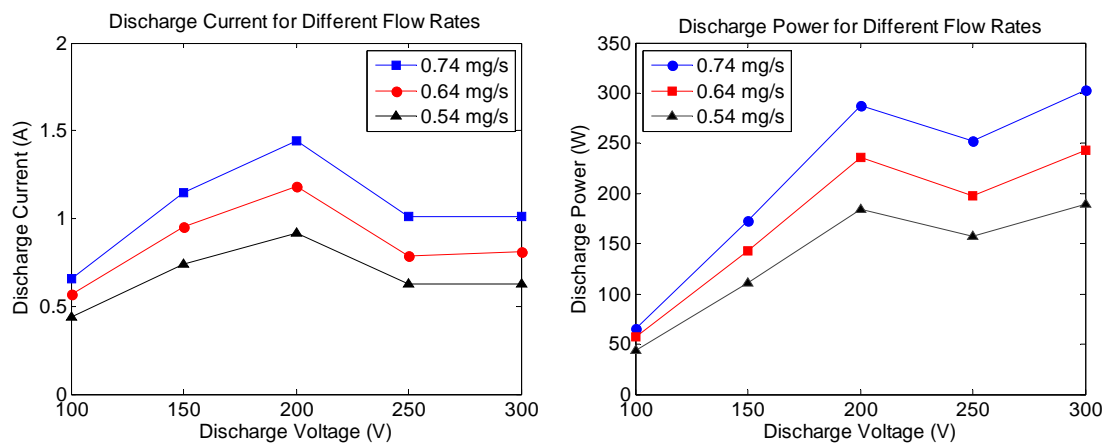
Figure 4.9 Plots of power and discharge current measured as a function of discharge voltage during the thruster verification test #2 at MIT.

the thruster mounting apparatus or steel from the bolts that hold the thruster down to the plate. The back of the copper plate is shown in Figure 4.10 along with the teflon ferrule used between the Swagelok union and the anode tube. The discoloration on the copper plate extends to the inner diameter of the alumina tube that insulates the high potential components from the background plasma. The ferrule looks melted and deformed. Teflon (PTFE) has a melting point of 327°C, but its mechanical properties begin to degrade above 260°C. The figure shows that the ferrule is warped and close inspection showed that bubbles had formed where the ferrule is very thin. It is likely that the temperature of this ferrule was somewhere in the range of 260-327°C. The other teflon ferrule, and the O-ring used in the Ultra-Torr fitting showed similar signs of high temperature wear.
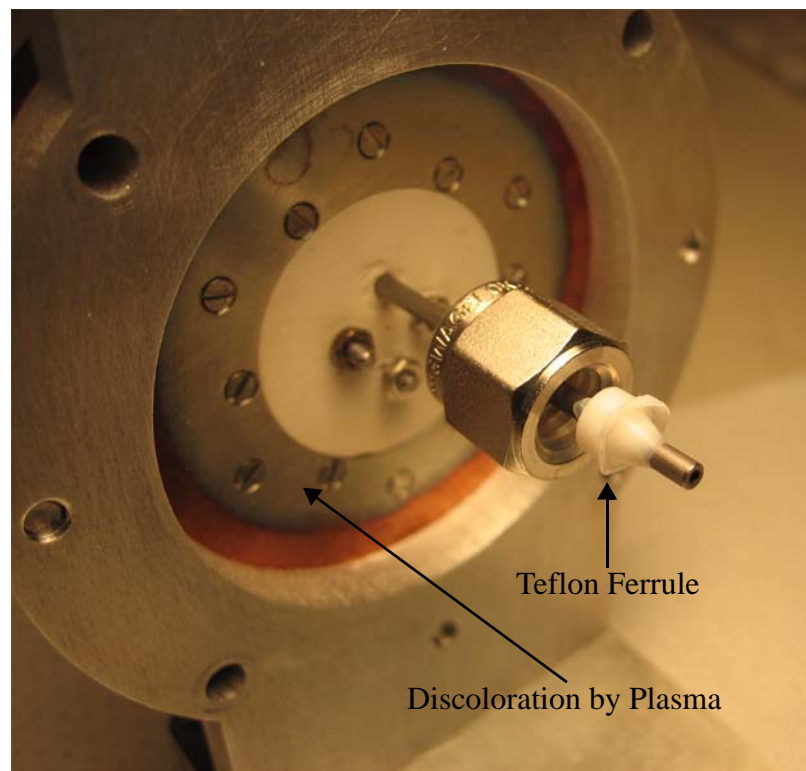
Figure 4.10 The back of the MHT-9 showed evidence of a propellant leak after verification test #2 at MIT. A plasma formed and discolored the copper plate (compare to Figure 3.27). The teflon ferrule melted and deformed.

Given the duration of stable operation and the acceptable temperature range observed at the surface of the permanent magnet, it was decided to move subsequent testing to Busek for performance measurements. However, future tests used all metal ferrules and no further propellant leaks were observed. The center stem was rebuilt after test #2 due to the pitting mentioned previously and because of erosion at the center stem cap (discussed further in Section 4.7). Post-test inspections showed that no further arcing occurred within the thruster and no plasma formed in the flow connection area behind the thruster.

4.3 Performance Test Matrix

The final four tests of the MHT-9 focused on performance testing in the Busek T6 vacuum facility. The test matrix included nine different mass flow rates, five different discharge voltages and three different magnetic shunt lengths. This matrix was nearly full, as shown in Table 4.1. In order to change the magnetic shunt, the thruster must be taken out of the tank and reassembled, forcing a vacuum break. Test #4 was the longest shunt tested and was closest to the design magnetic field strength as determined by the ideal scaling analysis. Tests #5-6 used the same shunt condition but were performed over two separate days, with a vacuum break to inspect the thruster and make adjustments to the thermocouple wiring. Note that in Table 4.1 a Xe flow rate conversion factor of 1mg/s=10.16sccm has been used, as reported by Garner after conversations with the National Institute for Standards and Technology (NIST) [76].

4.4 Performance Test Results

The experimental setup at Busek is pictured in Figure 4.11. A picture of the thruster firing in the Busek vacuum chamber is shown in Figure 4.12. The following sections show the results in graphical form. The full table of performance data can be found in Appendix A. After the cathode had been warmed up and the initial thrust stand calibration taken, the thruster was started and warmed up for 10-15 minutes at a flow rate of 4.0sccm. Data were then taken in order of increasing flow rate starting from 3.0sccm. For each flow rate, volt-

ages were tested in descending order starting from 300V. The thruster temperature and discharge current were allowed to come to steady state when changing to a new flow rate and setting the discharge voltage to 300V. This typically took 5-10 minutes, and then the thruster was run at the voltages between 250-100V for two minutes each. This proved to be enough time for the discharge current to come to steady state. Thrust data were averaged over the last sixty seconds of each data point.

TABLE 4.1 The MHT-9 Performance Test Matrix

Shunt Length (mm)	Voltage (V)	Flow Rate (sccm)								
		3.0	**3.5**	**4.0**	**4.4**	**5.9**	**7.5**	**8.5**	**9.1**	**10.0**
0	300									
	250									
	200			Test #3						
	150									
	100									
5.6	300									
	250									
	200			Test #5-6						
	150									
	100									
6.6	300									
	250									
	200			Test #4						
	150									
	100									
Shunt Length (mm)	Voltage (V)	0.30	0.34	0.39	0.43	0.58	0.74	0.84	0.89	0.98
		Flow Rate (mg/s)								
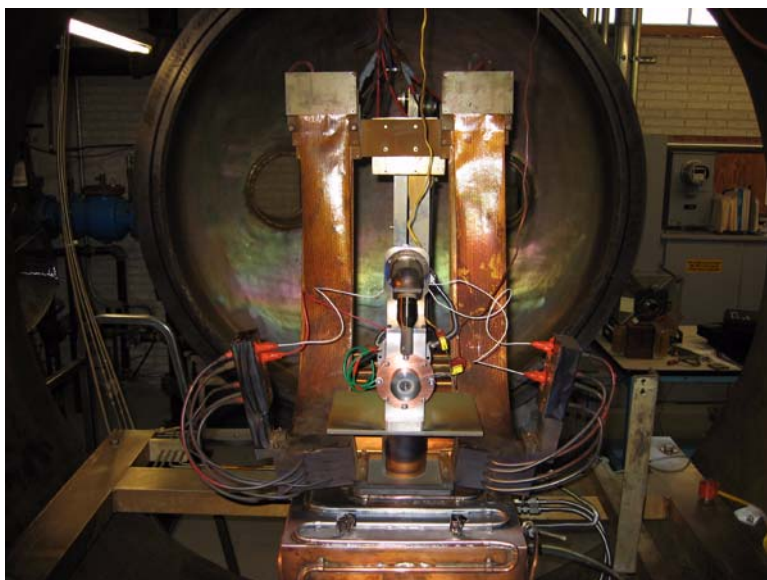
Figure 4.11   Experimental setup inside the Busek T6 vacuum tank.
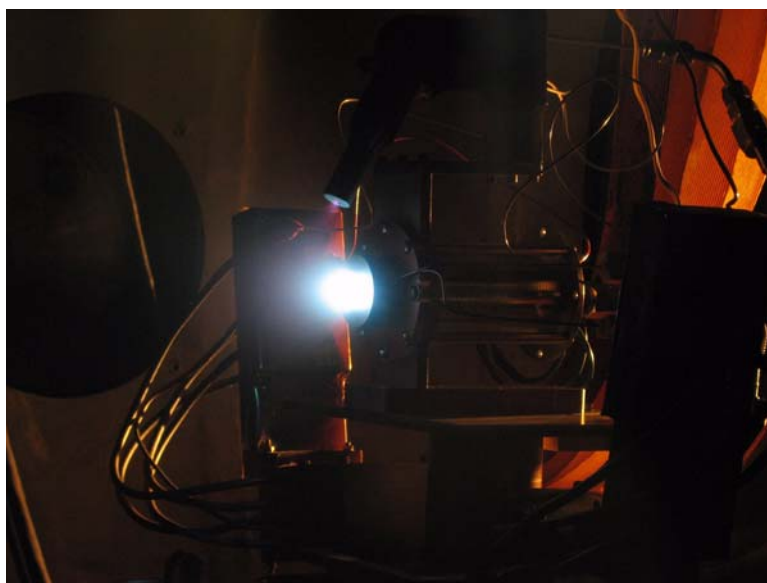
Figure 4.12   The MHT-9 firing inside the Busek T6 vacuum tank.

4.4.1 Discharge Current

The discharge current was monitored during the test and recorded by the data logger. The steady state values of the discharge current are plotted versus the discharge voltage in Figures 4.13-4.15. As was noted during the verification testing at MIT, the current peaks at a discharge voltage of 200V for most of the operating conditions tested. The 200V conditions were observed to have deeper discharge current oscillations than other voltages and noticeable flickering of the plume occurred at times.

The discharge current at the nominal operating condition of 300V and 0.74mg/s was 1.14A when operating with a 6.6mm long magnetic shunt. This shunt length was the magnetic field condition closest to the design field strength as determined by the ideal scaling analysis. The current was 70% higher than the expected nominal value of 0.67A. Over the course of the entire performance test, the discharge current ranged from as low as 0.20A to as high as 1.97A.
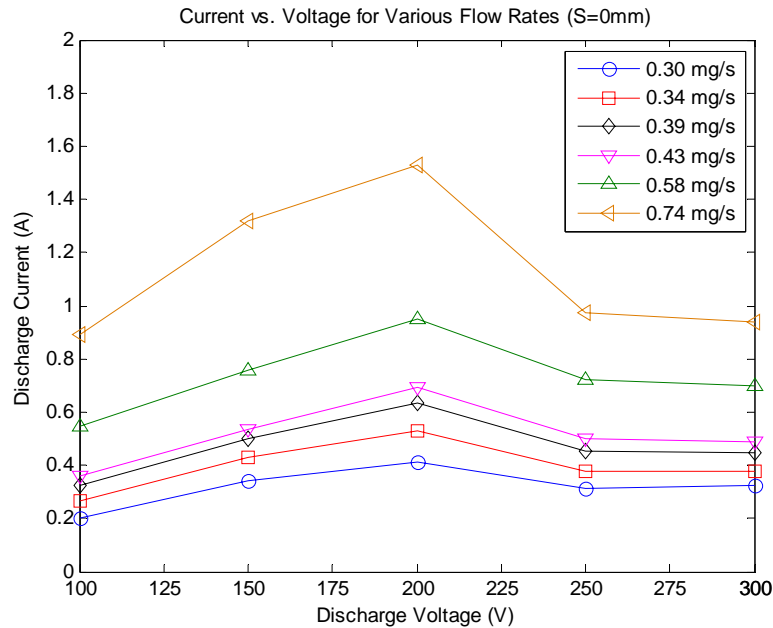
Figure 4.13 Discharge current versus discharge voltage for the MHT-9 operating with no magnetic shunt (*S*=0mm).
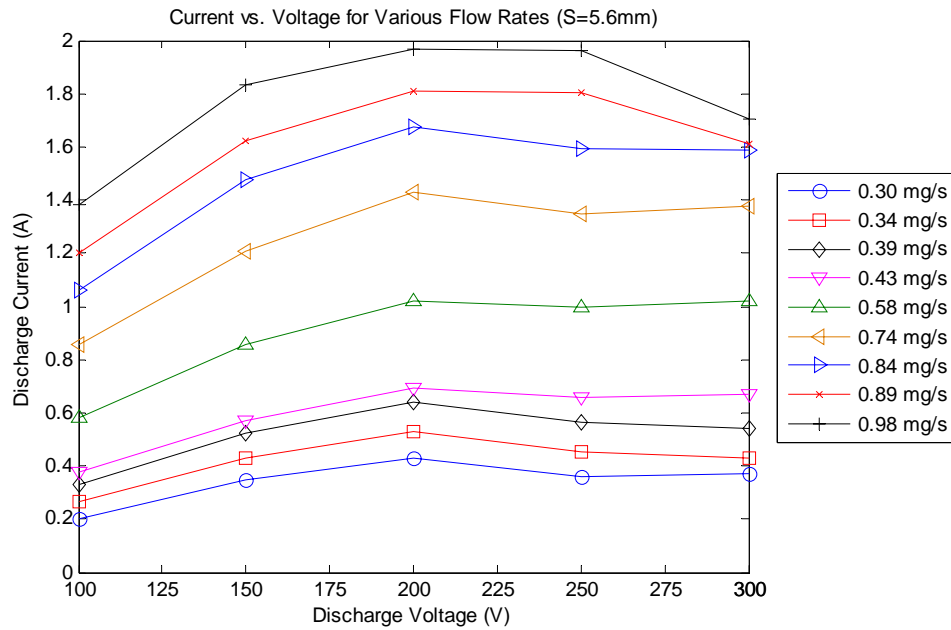
Figure 4.14 Discharge current versus discharge voltage for the MHT-9 operating with a 5.6mm long magnetic shunt (*S*=5.6mm).
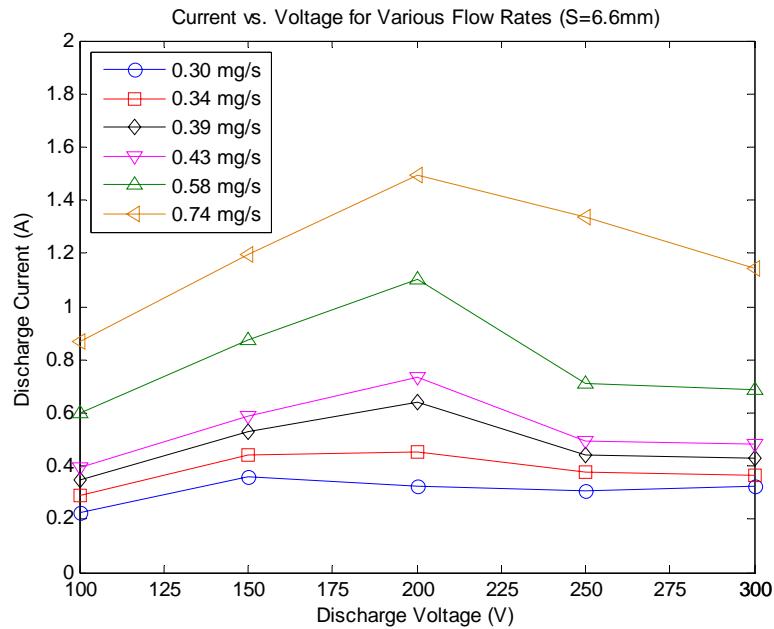
Figure 4.15 Discharge current versus discharge voltage for the MHT-9 operating with a 6.6mm long magnetic shunt (*S*=6.6mm).

4.4.2 Discharge Power

Figures 4.16-4.18 show plots of discharge power versus discharge voltage for all of the operating conditions tested. The trends in discharge power show some similarities to the trends in discharge current. For several of the flow rates tested, the 200V operating condition was a local maximum in discharge power. This is most visible in the case of no magnetic shunt (S=0mm) and the longest shunt tested (S=6.6mm). The 5.6mm shunt conditions showed monotonically increasing power with voltage. For all conditions tested, the power increased monotonically with flow rate.

At the nominal operating point of 0.74mg/s and 300V, the MHT-9 discharge power ranged from 284-418W, depending on the magnetic field strength. The thruster was successfully operated over a very wide power range from as low as 20W to as high as 517W.
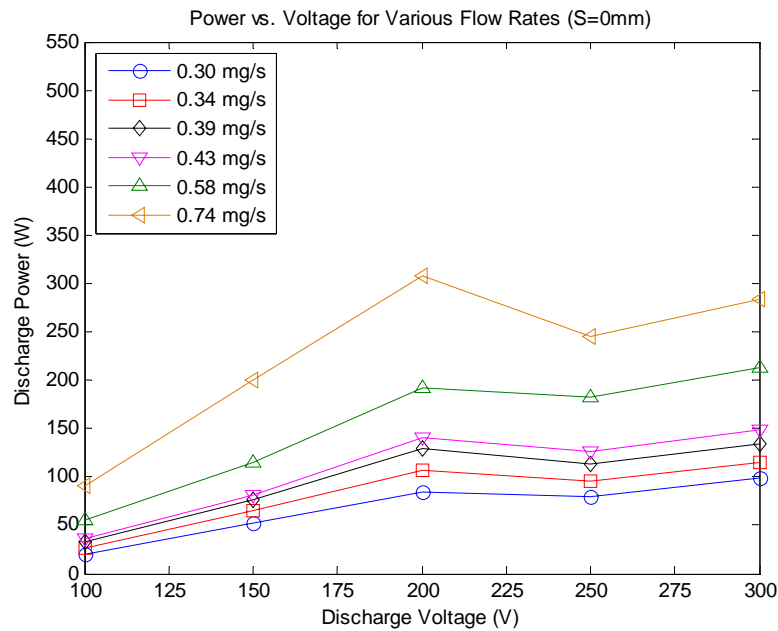
Figure 4.16 Discharge power versus discharge voltage for the MHT-9 operating with no magnetic shunt (S=0mm).
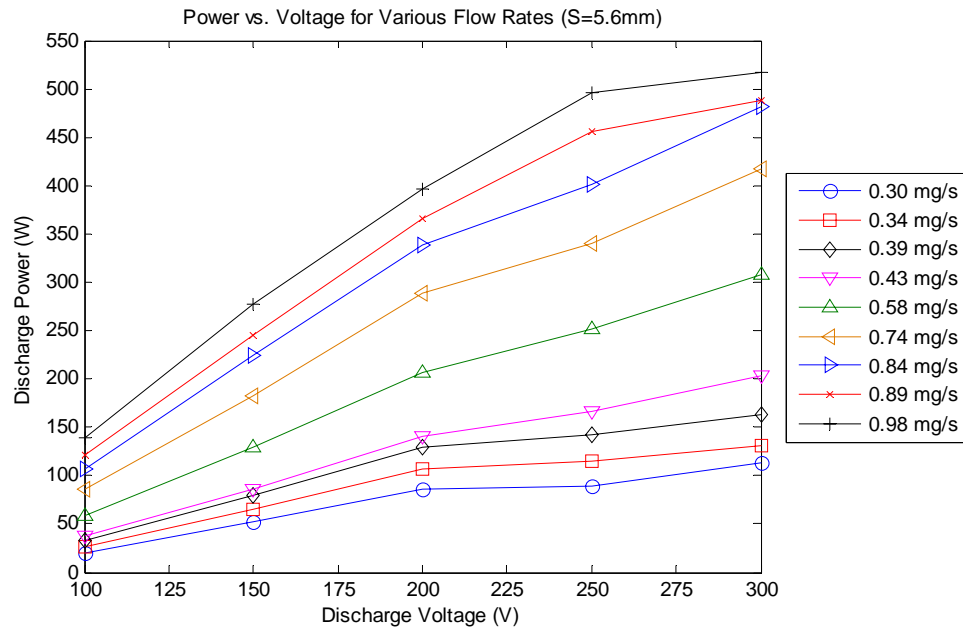
Figure 4.17 Discharge power versus discharge voltage for the MHT-9 operating with a 5.6mm long magnetic shunt (*S*=5.6mm).
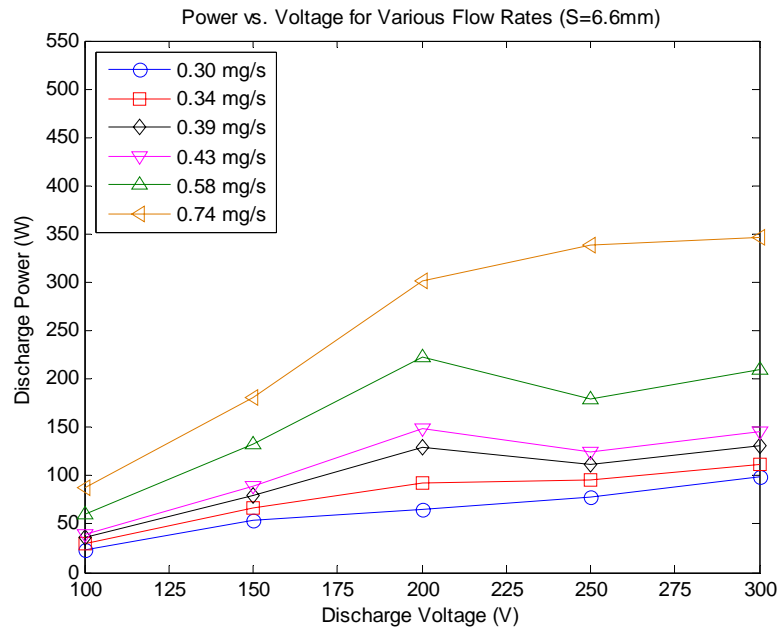
Figure 4.18 Discharge power versus discharge voltage for the MHT-9 operating with a 6.6mm long magnetic shunt (*S*=6.6mm).

4.4.3 Thrust

The measured thrust is plotted against the discharge voltage for various flow rates in Figures 4.19-4.21. Each separate plot is for a different shunt length. The graphs show that thrust increases with both flow rate and discharge voltage. Thrust of the MHT-9 was measured over a very wide range of operating conditions, from as low as 0.5mN at a discharge power of 23W to 17.6mN at a power level of 517W. For the design operating point of 0.74mg/s and 300V, the highest measured thrust was 14.4mN with the 5.6mm long shunt. However, the 6.6mm shunt was closer to the design magnetic field strength and the measured thrust at that point was 12.3mN. The variation of performance with magnetic field is discussed further in Section 4.5. As noted in Section 4.1.2, the overall error in the thrust measurement was estimated to be ±0.3mN.
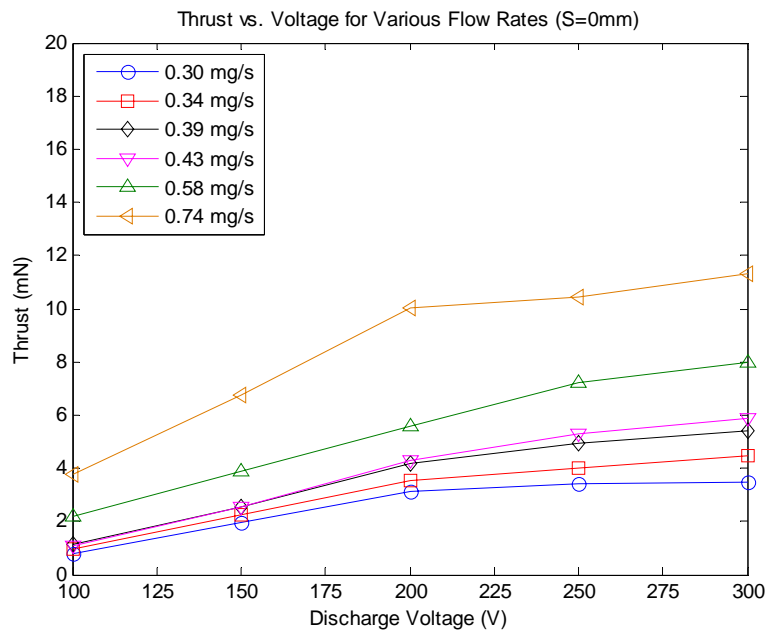
Figure 4.19   Thrust versus discharge voltage for the MHT-9 operating with no magnetic shunt (S=0mm).
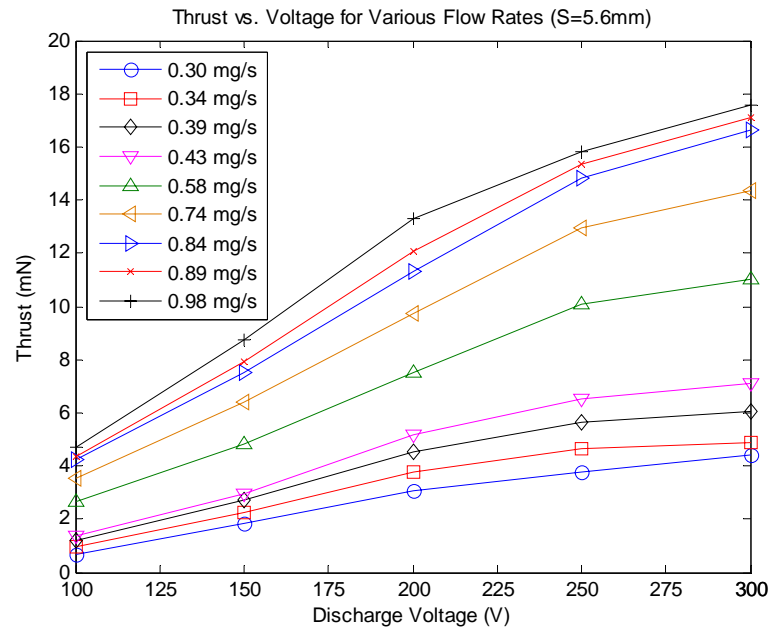
Figure 4.20 Thrust versus discharge voltage for the MHT-9 operating with a 5.6mm long magnetic shunt (S=5.6mm).
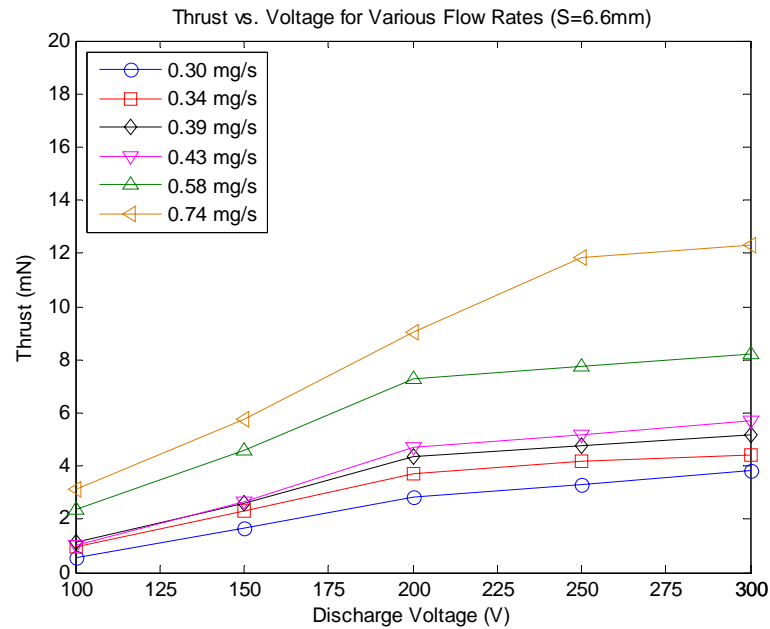
Figure 4.21 Thrust versus discharge voltage for the MHT-9 operating with a 6.6mm long magnetic shunt (S=6.6mm).
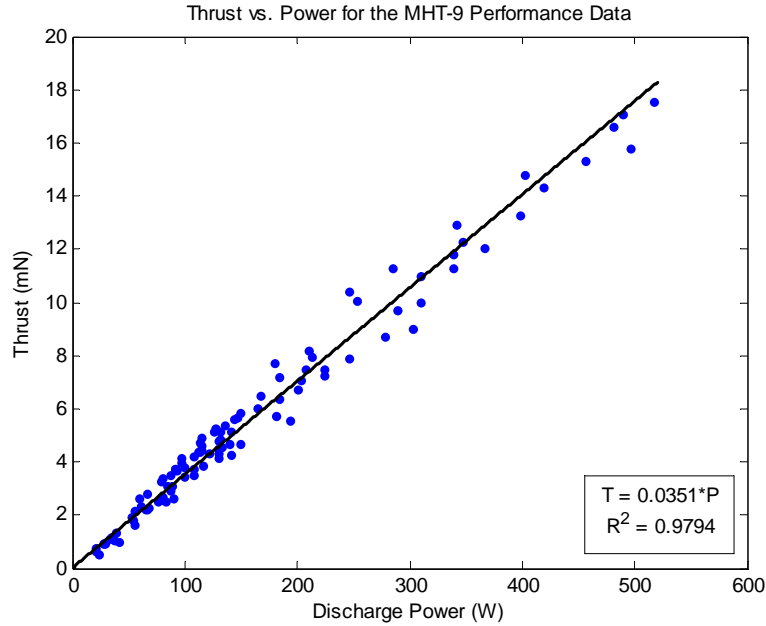
Figure 4.22   Thrust versus power for all of the MHT-9 performance data.

Figure 4.22 shows a plot of thrust versus discharge power for every data point taken during the performance testing (all flow rates, voltages and shunt conditions tested are included). A linear fit to this data was made with an intercept point at the origin. This is a characteristic line for the MHT-9 which gives a picture of overall efficiency for the thruster because it is relatively independent of the operating condition. The slope of this line will be compared to that of the baseline thruster, the D-55, in the following chapter. A greater slope would indicate a thruster with better thrust to power and thus a higher efficiency. This can be seen by rearranging the expression for thrust efficiency in Equation 2.4 to show that the thrust to power ratio can be written as,

$$\frac{T}{P} = \frac{2\eta_t}{c} = \frac{2\eta_t}{gI_{sp}}.$$ (4.1)

Thus a higher thrust to power ratio, or greater slope in Figure 4.22, would indicate a higher thrust efficiency for a given exhaust velocity. Since $I_{sp}=c/g$, it can also be concluded that the ratio of efficiency to specific impulse is relatively constant.

4.4.4 Specific Impulse

The specific impulse was calculated from the thrust measurements and the anode flow rate as shown below. The cathode flow was excluded from the calculation. This is often referred to as the anode specific impulse,

$$I_{sp} = \frac{T}{\dot{m}_a g}.$$ (4.2)

Plots of the anode specific impulse for the three different shunt conditions are shown in Figures 4.23-4.25. The specific impulse increases strongly with discharge voltage but rather gradually with flow rate. The MHT-9 produced a peak specific impulse of 2022s while operating at 300V and 0.84mg/s with a 5.6mm shunt. This was the only shunt condition that showed the specific impulse reaching a peak and leveling off as Hall thrusters typically do with increasing flow rate. The other two shunt conditions (S=0mm, 6.6mm) were not tested at high enough flow rates to observe this asymptotic behavior. At the designed operating point and magnetic field as determined by the ideal scaling theory (300V, 0.74mg/s, S=6.6mm), the specific impulse was 1706s. This is very close to the specific impulse observed in the baseline thruster. As noted in Chapter 2, the D-55 specific impulse was 1786s.

The error bars in the plots of specific impulse show one standard deviation above and below the measurement based on the error estimates for flow rate and thrust. The error analysis is discussed further in Section 4.4.7.

4.4.5 Thrust Efficiency

The thrust efficiency was calculated using the measured thrust, the anode flow rate and the discharge power as shown below. Cathode flow and cathode power were excluded from the calculation. This is sometimes referred to as the anode thrust efficiency,

$$\eta_t = \frac{T^2}{2\dot{m}_a P_d}.$$ (4.3)
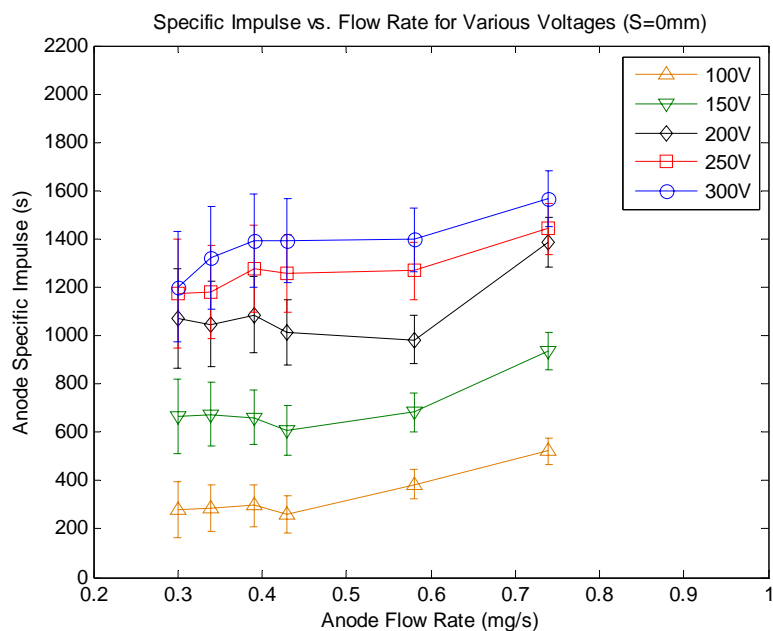
Figure 4.23 Specific impulse versus anode flow rate for the MHT-9 operating with no magnetic shunt (*S*=0mm).
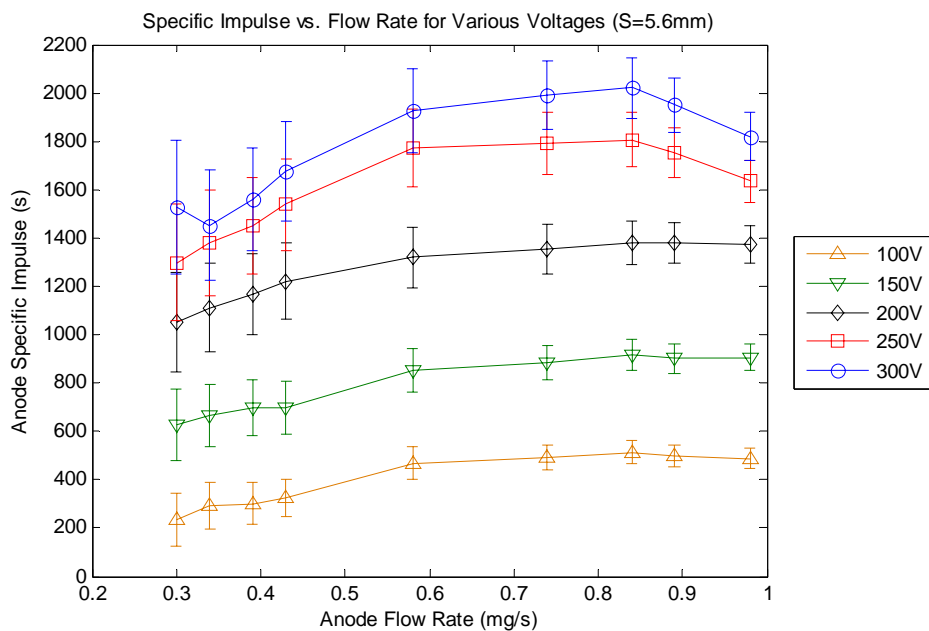
Figure 4.24 Specific impulse versus anode flow rate for the MHT-9 operating with a 5.6mm long magnetic shunt (*S*=5.6mm).
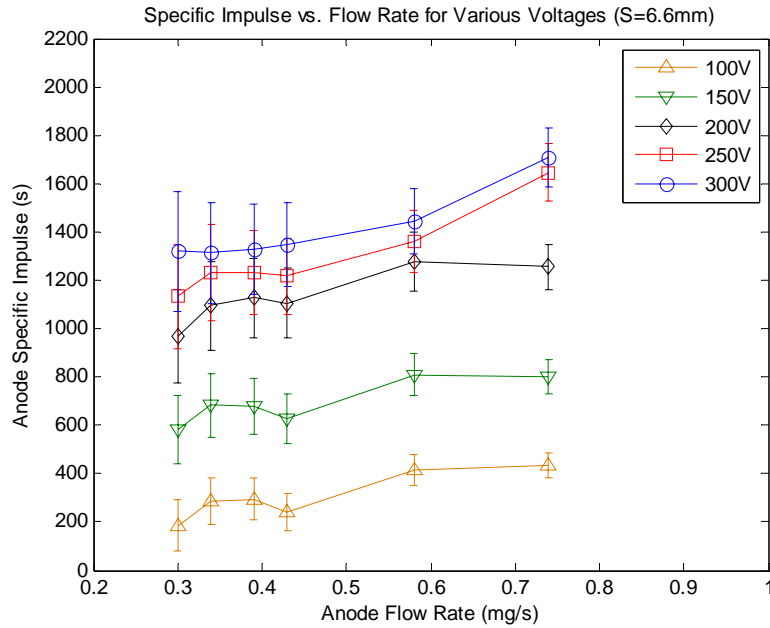
Figure 4.25 Specific impulse versus anode flow rate for the MHT-9 operating with a 6.6mm long magnetic shunt (S=6.6mm).
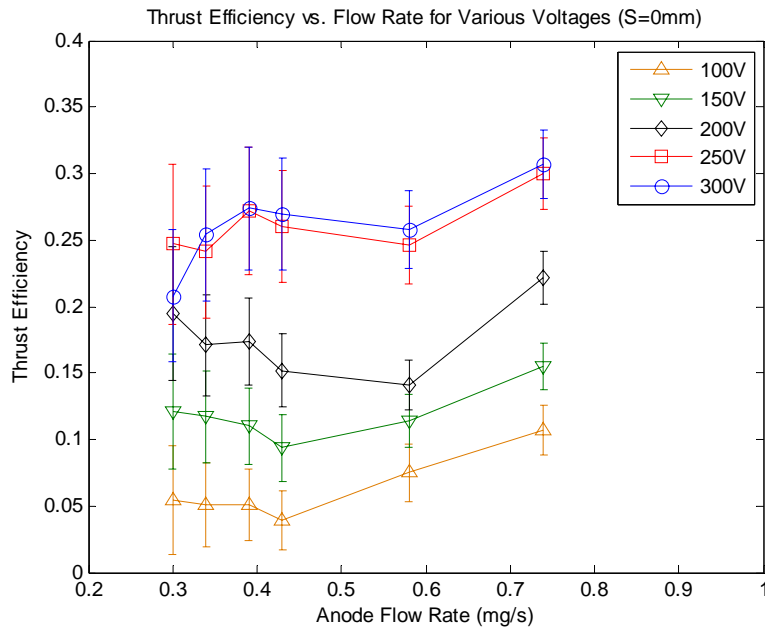
Figure 4.26 Thrust efficiency versus anode flow rate for the MHT-9 operating with no magnetic shunt (S=0mm). Cathode flow was excluded from efficiency calculations.
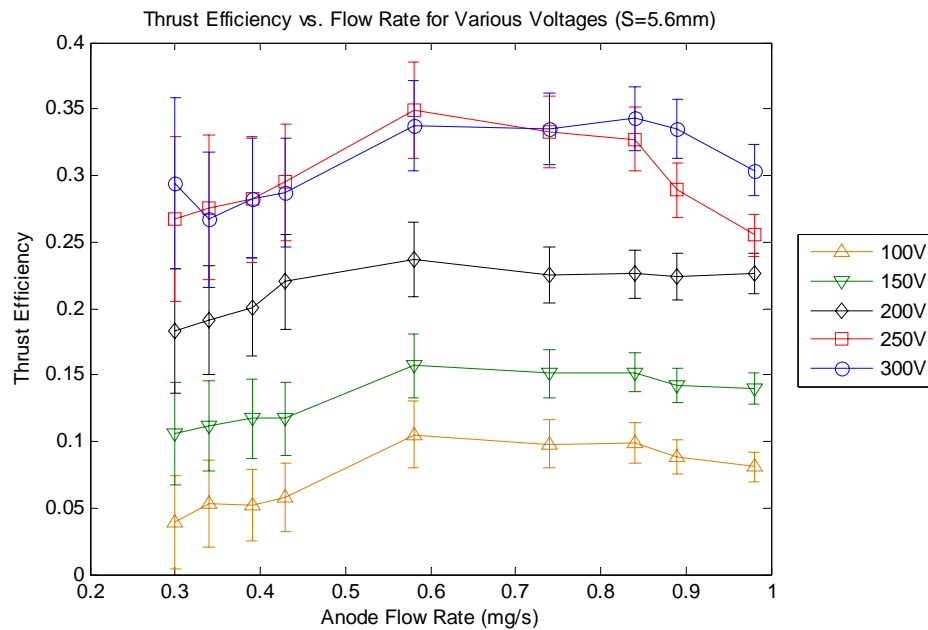
Figure 4.27 Thrust efficiency versus anode flow rate for the MHT-9 operating with a 5.6mm long magnetic shunt (*S*=5.6mm). Cathode flow was excluded from efficiency calculations.
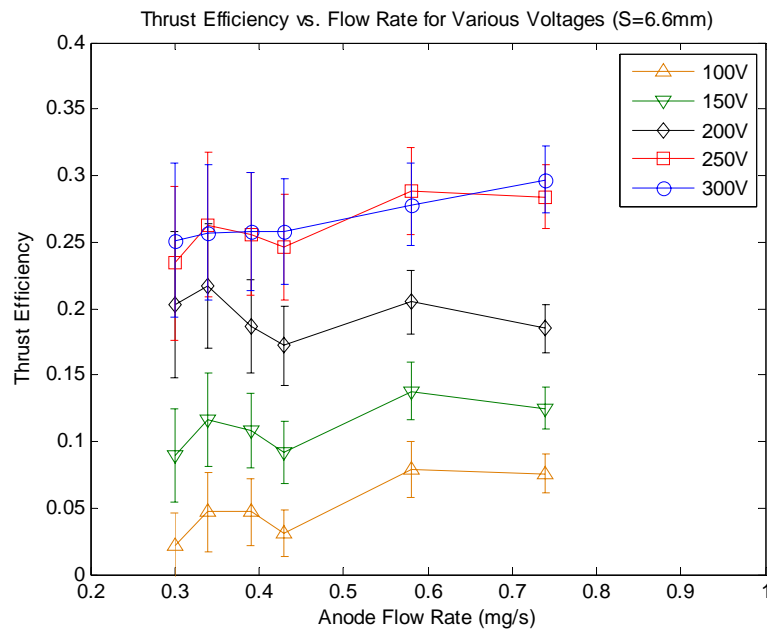
Figure 4.28 Thrust efficiency versus anode flow rate for the MHT-9 operating with a 6.6mm long magnetic shunt (*S*=6.6mm). Cathode flow was excluded from efficiency calculations.
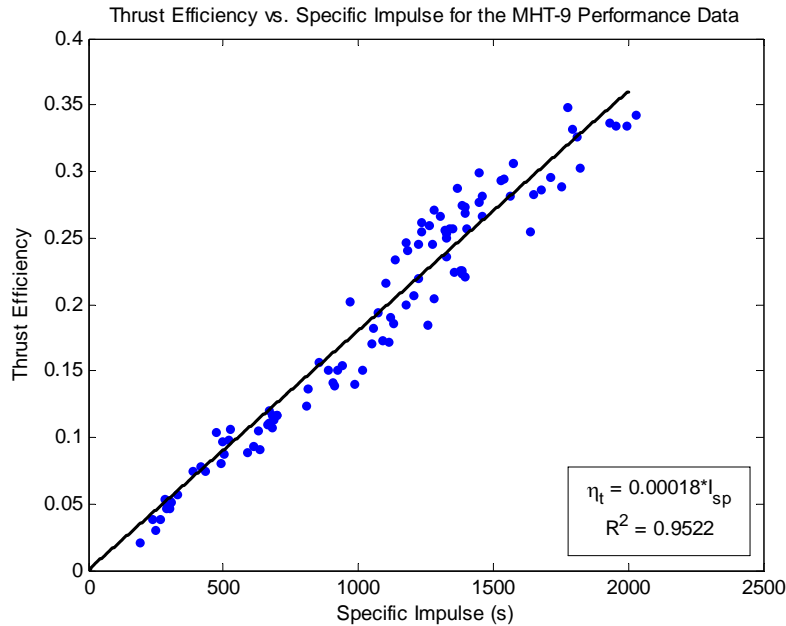
Figure 4.29 Thrust efficiency versus specific impulse for all of the MHT-9 performance data.

The trends in thrust efficiency are similar to those in specific impulse, because as shown in Figure 4.22 these two metrics are incredibly well correlated. In general, the thrust efficiency increases strongly with voltage and gradually with flow rate, reaching a maximum with asymptotic behavior. However, there are some notable exceptions to the trend. The thruster showed very similar efficiencies at 250V and 300V, with almost all of the data taken at these two voltages separated by less than the standard deviation (as determined by the error analysis). At the highest flow rates tested, with the shunt length of 5.6mm, there were decreases in efficiency with flow rate observed at some voltages (see Figure 4.27). This trend was observed in the specific impulse results as well. It is unclear what could be causing these decreases in efficiency. One hypothesis is that the higher flow rates are increasing the plasma density and also the heat delivered to the thruster wall surfaces. This could result in a higher magnet temperature, decreasing the magnetic field strength and increasing ion losses to the wall due to decreased electron confinement. Magnet temperature measurements are discussed further in Section 4.6.

The peak thrust efficiency measured for the MHT-9 was 35% while operating at 250V and 0.58mg/s with a shunt length of 5.6mm. As with the thrust and specific impulse, the efficiency was greatest with the 5.6mm magnetic shunt. At the design condition of 300V and 0.74mg/s with the 6.6mm shunt, the thrust efficiency was 30%. This is much less than the D-55 anode efficiency of 56% (magnet and cathode power excluded), but also significantly more than the 6% measured by Khayms [13, 15, 39]. At the target power level of 200W, efficiencies as high as 29% were observed for the MHT-9.

Figure 4.29 shows a plot of thrust efficiency versus specific impulse for all of the performance data taken with the MHT-9. As shown in Equation 4.1, the slope of the trend line for this data is proportional to the slope of the thrust to power trend line, with the constant of proportionality being $2/g$. It should be noted that thrust efficiency typically asymptotes to a maximum value with increasing specific impulse. If the discharge voltage, and therefore the specific impulse, of the MHT-9 was increased significantly beyond 300V, the linear behavior in Figure 4.29 would likely not continue.

4.4.6 Propellant Utilization

The utilization efficiency, η_u, is a measure of how effectively propellant is ionized. It is one factor of the thrust efficiency as shown below.

$$\eta_t = \eta_a \eta_q \eta_b \eta_u \qquad (4.4)$$

The thrust efficiency is the product of acceleration, charge, beam, and utilization efficiencies. The acceleration efficiency, η_a, is a measure of the ability of the thruster to transfer kinetic energy to the ions. It accounts for performance loss due to divergence of the plume and ions that are not accelerated through the full discharge potential. The charge efficiency, η_q, is a measure of how much energy is wasted producing ions with charge states greater than one (Xe^{++}, Xe^{+++}). Double and triple ions require more energy to produce than multiple single ions, and because they create spread in the ion velocity distribution, energy is lost in thermalization of the exhaust. The beam efficiency, η_b, is a measure of the

inherent Hall thruster inefficiency due to the electron backstreaming current. It is defined as the ratio of the beam current to the discharge current,

$$\eta_b = \frac{I_b}{I_d}.$$ (4.5)

The utilization efficiency, as previously defined in Equation 3.24, is a measure of the efficiency of the ionization process. It is defined as,

$$\eta_u = \frac{I_b m_i}{\dot{m}_a e}.$$ (4.6)

If the acceleration and charge efficiencies are assumed to be near unity ($\eta_a \approx \eta_q \approx 1$), then Equations 4.4-4.6 can be combined to express the beam efficiency as,

$$\eta_b = \sqrt{\eta_t \frac{\dot{m}_a e}{I_d m_i}}.$$ (4.7)

This expression can then be used to write the utilization efficiency directly in terms of measured quantities and constants,

$$\eta_u = \frac{\eta_t}{\eta_b} = \frac{T}{\dot{m}_a \sqrt{\frac{2 V_d e}{m_i}}}.$$ (4.8)

The grouping in Equation 4.8 is particularly interesting because it is actually a thrust ratio. It shows that the utilization efficiency can be estimated using the ratio of measured thrust to the ideal thrust. The ideal thrust assumes that all of the propellant is ionized and that each ion created is accelerated completely axially with the full discharge potential. It should be noted that if the acceleration and charge efficiencies are less than unity, the actual utilization efficiency will be higher than the estimate shown in Equation 4.8 (since the other efficiency components would appear in the denominator). Thus, this estimate for propellant utilization is conservative.
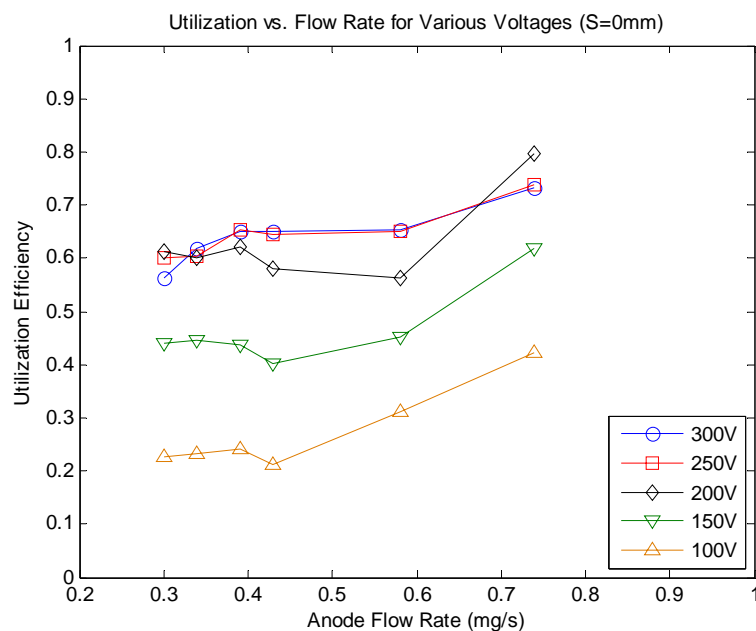
Figure 4.30 Utilization efficiency versus anode flow rate for the MHT-9 operating with no magnetic shunt (*S*=0mm). Cathode flow was excluded from efficiency calculations.
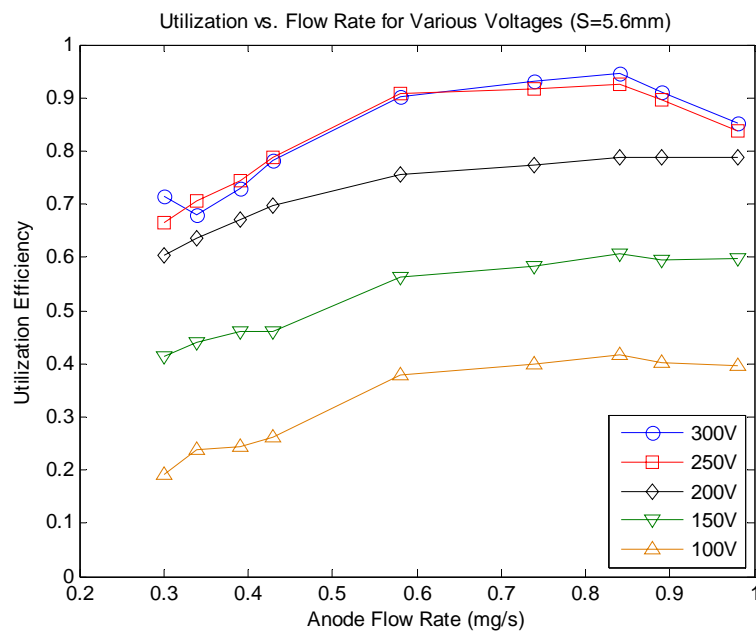
Figure 4.31 Utilization efficiency versus anode flow rate for the MHT-9 operating with a 5.6mm long magnetic shunt (*S*=5.6mm). Cathode flow was excluded from efficiency calculations.
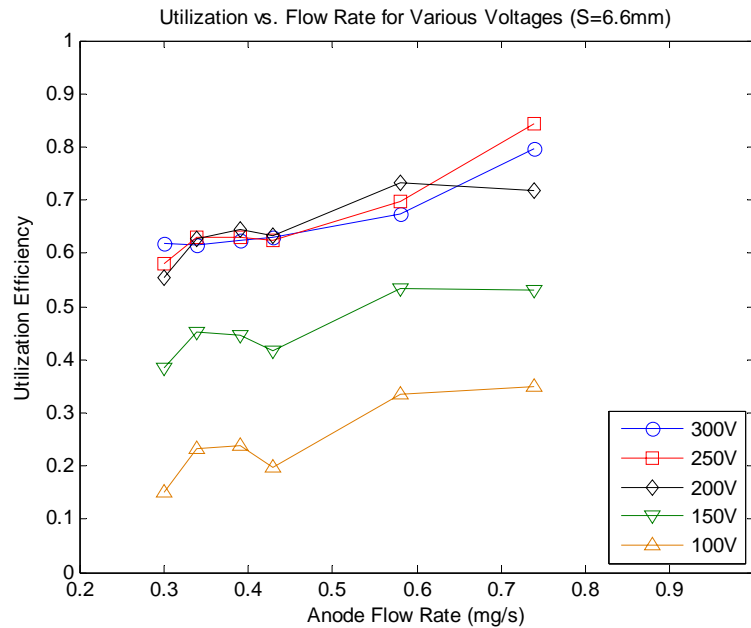
Figure 4.32   Utilization efficiency versus anode flow rate for the MHT-9 operating with a 6.6mm long magnetic shunt (S=6.6mm). Cathode flow was excluded from efficiency calculations.

Figures 4.30-4.32 show estimates of propellant utilization for the MHT-9. Error bars were not included on these plots because the utilization values are simply estimates given the assumptions previously stated. However, the error bars could be calculated in a similar fashion as those for specific impulse (see Section 4.4.7). The trends are similar to those found in the thrust efficiency, where the efficiency generally increases with both flow rate and discharge voltage. The utilization efficiency appears to asymptotically approach maximums with both flow rate and discharge voltage. There are several operating points with utilization efficiencies above 90%, which is typical for well optimized Hall thrusters. The highest estimated utilization efficiency for the MHT-9 was 95% while the thruster was operating at 300V and 0.84mg/s with a shunt length of 5.6mm. At the nominal condition of 300V and 0.74mg/s with a shunt length of 6.6mm, the utilization was only 80%. Although these estimates are on the conservative side, this does indicate that efficiency improvements could be made through better ionization for the designed operating point. However, this data point actually compares well to the baseline thruster. For the D-55

operating conditions described in Section 2.4, the utilization efficiency is 83% when calculated by the same method. This evidence signals that the thrust efficiency differences between the MHT-9 and the baseline thruster are likely due to ion loss mechanisms instead of poor ionization. This is fundamentally different from Khayms' conclusion that the 50W miniature Hall thruster inefficiencies were largely due to poor ionization caused by overheating of the magnetic circuit, manufacturing difficulties and excessive electron leakage to the anode. The peak estimated utilization efficiency for the 50W miniature thruster was only 40% [15].

4.4.7 Error Analysis

The error bars for specific impulse and efficiency were estimated using the standard deviation. For a general performance metric, y, which is some function of measured quantities, $x_1...x_n$, an expression can be written as,

$$y = f(x_1, x_2, ..., x_n),$$ (4.9)

where the error in the performance metric, dy, due to an error in one of the measured quantities, dx_i, is simply,

$$dy|_{x_i} = \frac{\partial f}{\partial x_i} dx_i.$$ (4.10)

Thus, the total error in the performance metric due to all the measured quantities that make up the function, f, would be,

$$dy = \sum_{i=1}^{n} \frac{\partial f}{\partial x_i} dx_i.$$ (4.11)

The variance of the performance metric can be written using a similar expression,

$$\sigma_y^2 = \sum_{i=1}^{n} \left(\frac{\partial f}{\partial x_i}\right)^2 \sigma_i^2,$$ (4.12)

where σ_i is the estimated standard deviation of error in the measured quantity, x_i. It has been assumed that errors are uncorrelated so that the averages of products of errors are zero. The error bars for specific impulse (as defined in Equation 4.2) use the standard deviation, which can be written using the general formula as,

$$\sigma_{I_{sp}} = I_{sp} \sqrt{\left(\frac{\sigma_T}{T}\right)^2 + \left(\frac{\sigma_{\dot{m}_a}}{\dot{m}_a}\right)^2} . \tag{4.13}$$

The standard deviation of the thrust efficiency (as defined in Equation 4.3) is,

$$\sigma_{\eta_t} = \eta_t \sqrt{\left(\frac{2\sigma_T}{T}\right)^2 + \left(\frac{\sigma_{\dot{m}_a}}{\dot{m}_a}\right)^2} . \tag{4.14}$$

Error in the measurement of the discharge voltage and current are much less than 1%, and therefore have been ignored in this analysis. As mentioned in previous sections, the error (standard deviation) for the thrust measurement and the anode flow rate have been estimated as ±0.3mN and 0.05mg/s, respectively.

4.5 Influence of the Magnetic Field

4.5.1 Magnetic Field Sampling

The magnetic field inside the MHT-9 was surveyed with a handheld gaussmeter several times between thruster firings. These tests served only as a check that the magnet was functioning properly and were not meant to be a mapping of the field profile within the channel. The probe size was large relative to the channel dimensions, allowing for only very rough estimates of the true location of the probe. The probe tip was 1.3mm thick and approximately 7mm^2 in cross sectional area. The strength of the radial component of the magnetic field was measured on three separate occasions and compared to results of the Maxwell simulation, as shown in Figure 4.33. The plot shows simulation results at three different axial positions with $z=0$mm being the exit plane of the magnetic circuit, and the

other two positions are inside the channel formed by the circuit. The exact axial position of the probe sampling region is unknown, but it is likely somewhere just inside the channel (-2<z<0mm). Estimates of the radial position are indicated on the plot by the location of each test point. Test A was conducted between the MHT-9 verification tests #1-2. Test B was performed just before the performance testing at Busek commenced, between MHT-9 tests #2-3. The final gaussmeter probe sample, Test C, was conducted between performance tests #4-5.
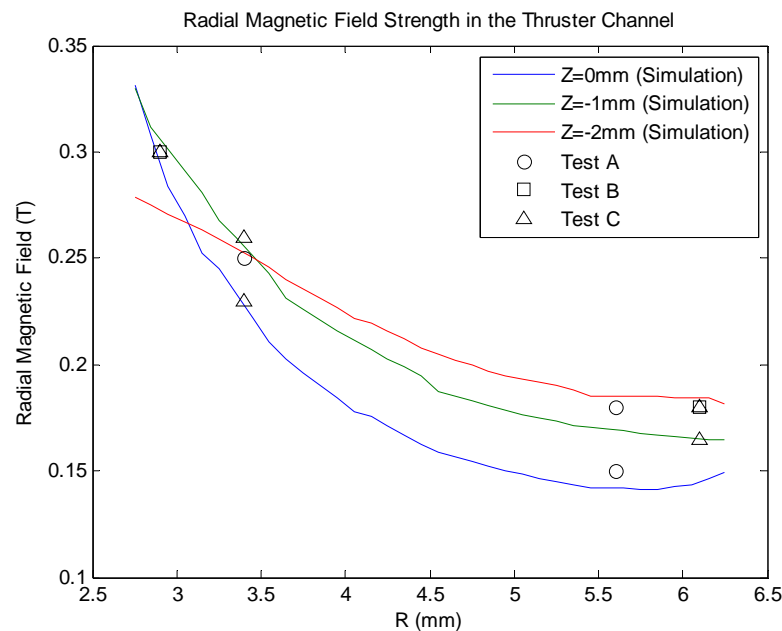
Figure 4.33 Comparison of gaussmeter measurements inside the MHT-9 to results of the Maxwell simulation. Measurements were made with a handheld probe to ensure that the magnet was operating as designed and to ensure it had not undergone any permanent demagnetization. Knowledge of the location of the probe sampling region is inexact but likely in the range of -2<z<0mm with the radial dimension estimated using the probe thickness and placement with respect to the channel walls. The magnetic field was tested on three separate occasions: Test A occurred between MHT-9 tests #1-2, Test B was between tests #2-3, and Test C was between performance tests #4-5. Multiple data points for a single test indicate the range of measurements.

The magnetic field sampling was conducted at room temperature in a benchtop setting (not inside the vacuum tank). The data indicate that the magnet did not experience any permanent demagnetization, and the good correlation with simulation at room temperature suggests that the simulation is likely accurate at higher temperatures as well.

4.5.2 Magnetic Field Interpolation

The plots in the previous sections relate performance parameters for three different magnetic shunts. Although shunt length is the physical mechanism for changing the magnetic field, it is not linearly related to the field strength as shown in Figure 3.14. In order to plot performance parameters versus the actual magnetic field strength inside the thruster, the results of the field simulations presented in Figure 3.14 were interpolated to the magnet temperatures measured inside the thruster during operation. This interpolation process was performed for the three different shunt conditions tested using a cubic spline method. The results are shown in Figure 4.34. The ideal field strength determined by scaling was 0.1378T. At the designed nominal point of 300V and 0.74mg/s, the magnet reached a temperature of 241°C and a resulting (predicted) field strength of 0.1442T with the 6.6mm shunt. This is within 5% of the target field strength.

4.5.3 Effect of Magnetic Field on Thrust Efficiency

Hall thrusters that have electromagnets are typically operated by first setting a voltage and flow rate, and then tuning the coil currents to find the minimum discharge current. This is thought to be the point of highest efficiency. With a thruster that runs on permanent magnets, this process is not as easy. The mechanical adjustment system in the MHT-9 requires the shunts to be changed between tests and the energy output of the magnet is sensitive to temperature, a parameter that cannot be directly controlled. However, simulations can help in estimating the field strength variation with both shunt length and temperature to provide insight on the magnetic tuning of the thruster.
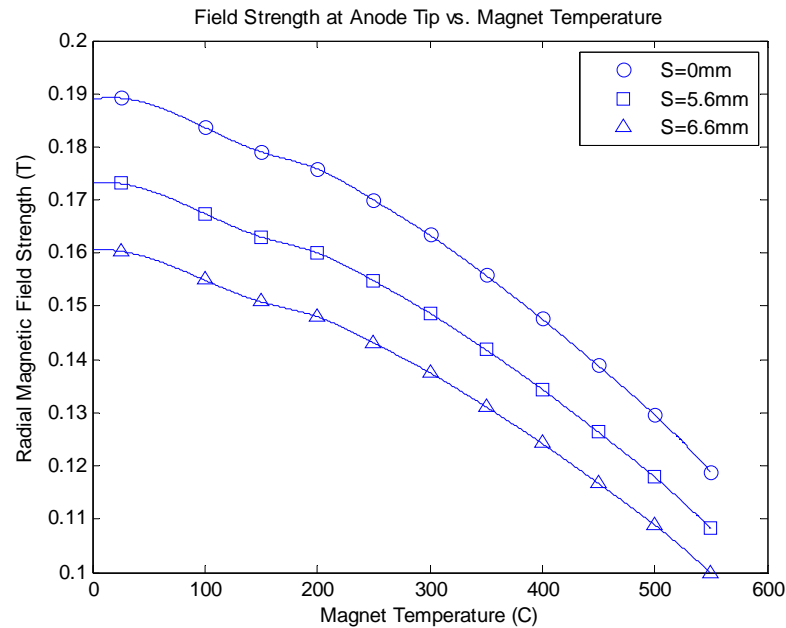
Figure 4.34   Radial magnetic field strength at the anode tip in the MHT-9 versus magnet temperature for the three shunt lengths tested.

Figures 4.35-4.37 plot the thrust (anode) efficiency versus the radial magnetic field strength at the anode tip for various voltages at three different flow rates. These data were taken over the course of the four separate performance tests because they required changing of the magnetic shunt in order to vary the magnetic field strength. The field strength values were determined using measured magnet temperatures and the interpolated magnetostatic simulation results shown in Figure 4.34.

Comparing the plots shows several interesting features. First, the points clustered in the middle of each plot seem to be near a local maximum in thrust efficiency. This suggests that over the course of the performance testing, there indeed was tuning of the magnetic field for best performance. Figure 4.35 indicates the shunt lengths used for each grouping of data points, and this trend holds for the other two plots as well, showing that the maximum measured efficiency was with the 5.6mm long shunt. Secondly, comparison of the three graphs shows that as the flow rate increases, the curves shift to lower magnetic fields. This illustrates the effect of the magnet temperature rising with flow rate and the

resulting drop in magnetic field strength. Finally, for the nominal flow rate (0.74mg/s) and voltage (300V), the thruster achieved a tuning capability of 27%. This is because the measured magnet temperature at this operating point for the highest magnetic field strength was only 212°C, allowing for a field strength of 0.1748T (27% above the field requirement of 0.1378T). This operating temperature was lower than the 310-451°C range predicted by the thermal model.

An examination of the optimal magnetic field scaling analysis in Section 2.1.4 can shed some light on why the thrust efficiency peaked at a higher than expected field strength. The initial target field strength for the MHT-9 was 0.1378T, determined by scaling the D-55 magnetic field inversely with channel width. However, as results in Figures 4.35-4.37 show, the best performance was achieved in the range of 0.1550-0.1650T. According to Equation 2.49, the optimal magnetic field scales as,

$$B \approx \frac{kT_e}{e\beta_a L_c v_B} \propto \frac{T_e}{L_c v_B} \propto \frac{\sqrt{T_e}}{L_c}, \tag{4.15}$$

assuming that the anomalous Hall parameter is constant in scaling. Leaving the effect of channel length, L_c, aside for a moment, an analytical model of electron temperature presented in Section 5.4 predicts that the electron temperature in the MHT-9 was 36% higher than expected because the ratio of wall area to exit area was not maintained in scaling (D-55 T_e=37.1eV, MHT-9 T_e=50.6). Using the scaling shown in Equation 4.15, this would result in the optimal magnetic field being 17% higher, or 0.1610T.

Ideal scaling analysis has shown that the channel width and length should be scaled in the same proportion to preserve performance, meaning that the optimal magnetic field strength should scale inversely with either dimension. However, channel length scaling was not considered for the design of the MHT-9. Therefore, the actual optimal field strength may be lower than 0.1610T since the channel length was likely scaled down less strongly than the channel width. Estimates of this effect are difficult to make because the actual channel length of the D-55 remains unknown.
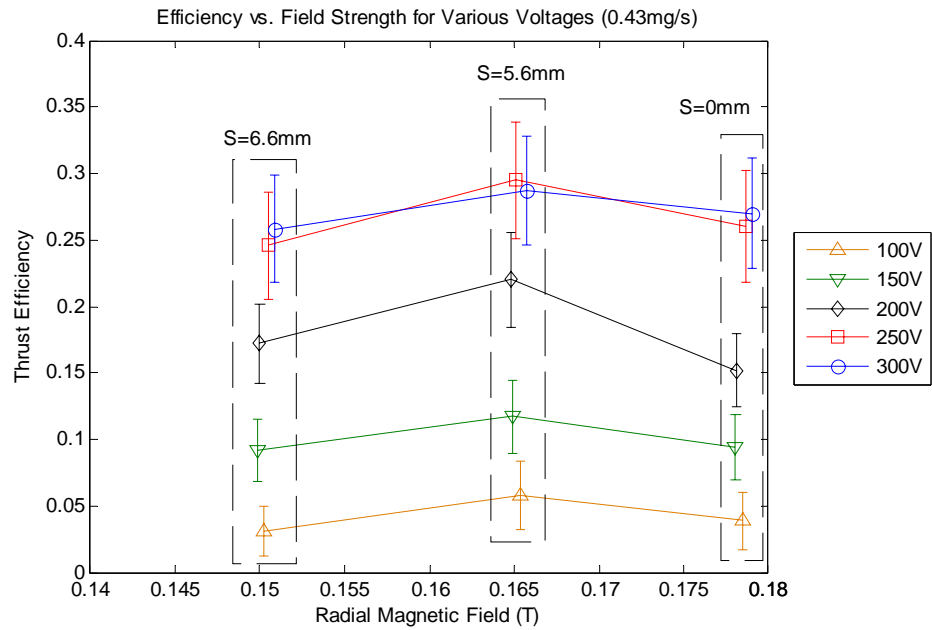
Figure 4.35   Thrust (anode) efficiency versus radial magnetic field for the MHT-9 operating at a flow rate of 0.43mg/s. The dashed boxes indicate which groups of points were taken with each shunt length.
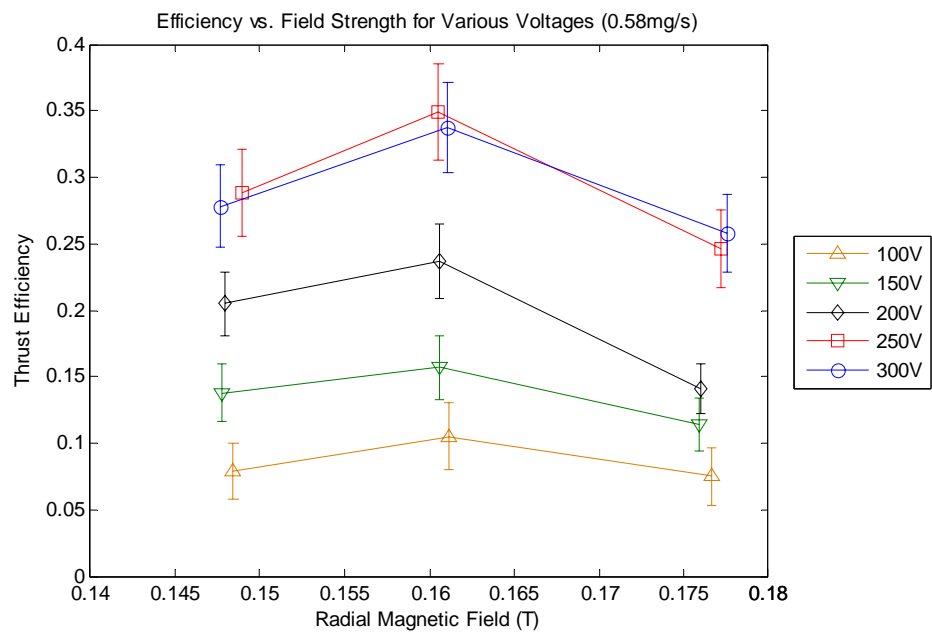
Figure 4.36   Thrust (anode) efficiency versus radial magnetic field for the MHT-9 operating at a flow rate of 0.58mg/s.
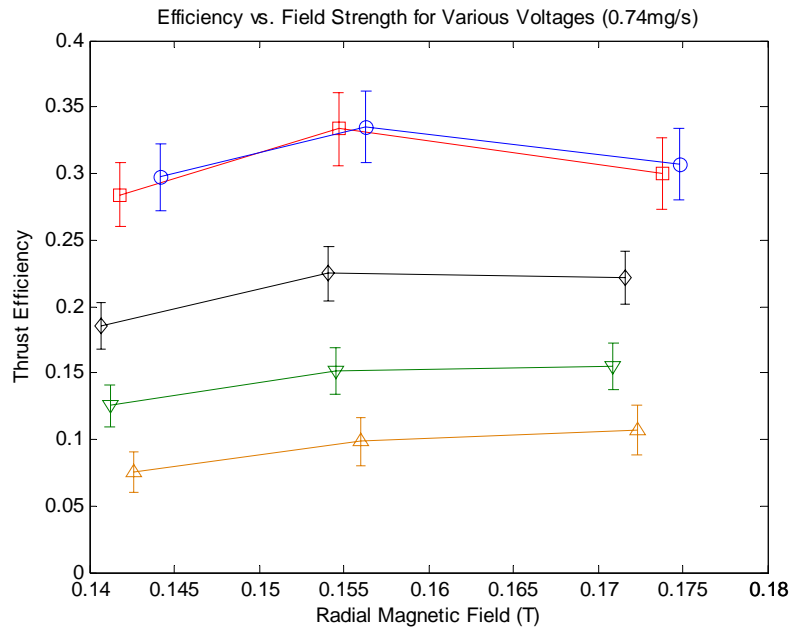
Figure 4.37   Thrust (anode) efficiency versus radial magnetic field for the MHT-9 operating at a flow rate of 0.74mg/s.

4.5.4 Effect of Magnetic Field on Discharge Current

The previous section showed that a local maximum in efficiency was discovered when changing the magnetic field strength between test runs. In thrusters that utilize electromagnets, the field strength with maximum efficiency is usually a local minimum in discharge current. However, this did not prove to be the case with the MHT-9. Figures 4.38-4.39 show plots of discharge current versus magnetic field strength for all the voltages tested at two different flow rates. At discharge voltages of 250-300V, the exact opposite of the anticipated behavior was observed. A local maximum in discharge current occurs for the magnetic field strengths that showed a maximum in thrust efficiency. At voltages of 100-200V, the current remained relatively flat across the different magnetic field strengths. These trends were observed at other flow rates as well.

These data seem to indicate that there is a difference between the behavior of the thruster at 250-300V and the behavior at voltages of 200V and below. This conclusion is supported by the thrust efficiency data shown in Figures 4.35-4.37. The efficiency is relatively con-
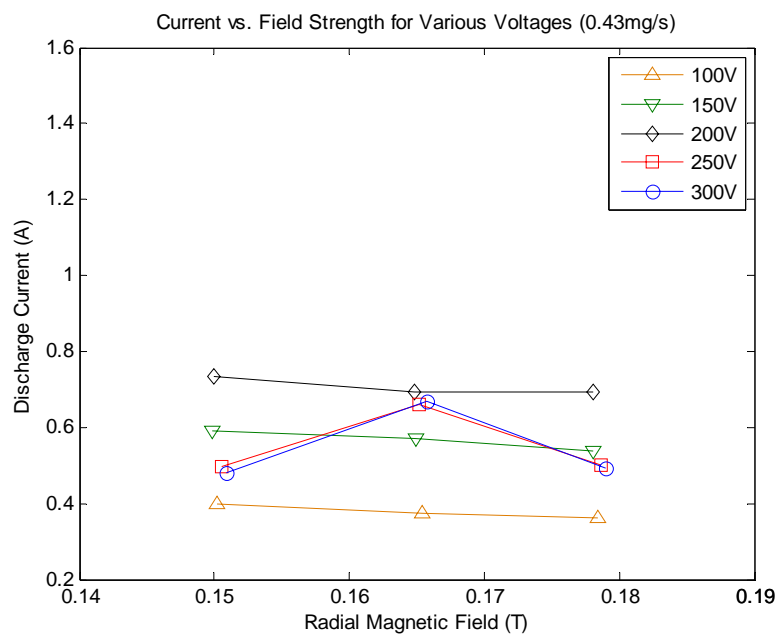
Figure 4.38 Discharge current versus radial magnetic field for the MHT-9 operating at a flow rate of 0.43mg/s.
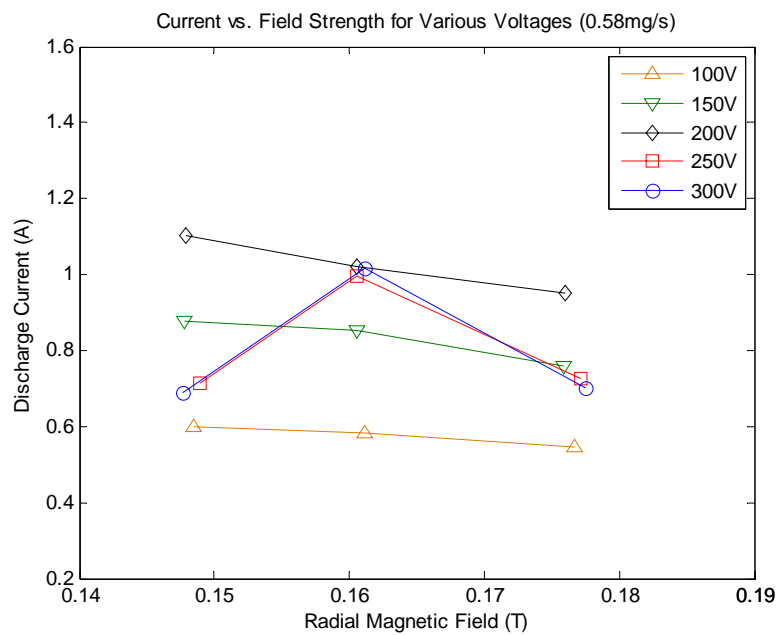
Figure 4.39 Discharge current versus radial magnetic field for the MHT-9 operating at a flow rate of 0.58mg/s.
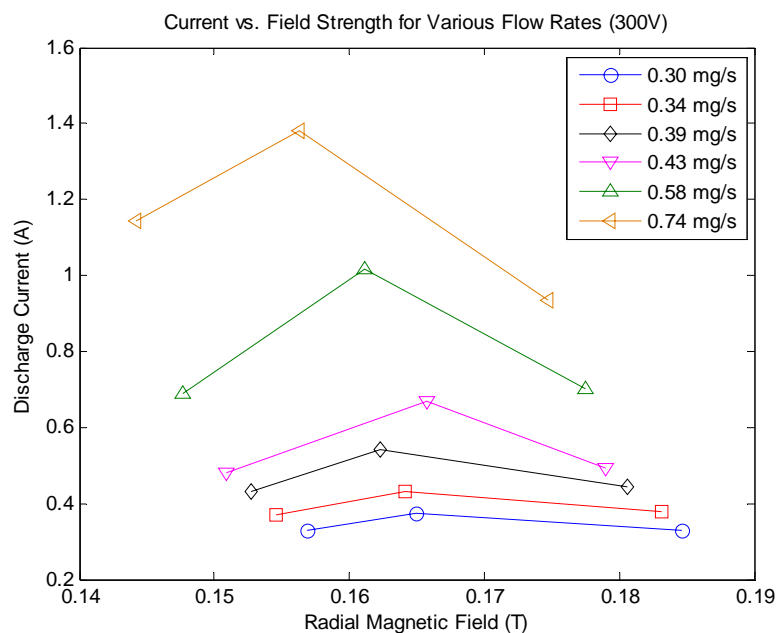
Figure 4.40 Discharge current versus radial magnetic field for the MHT-9 operating at a discharge voltage of 300V.
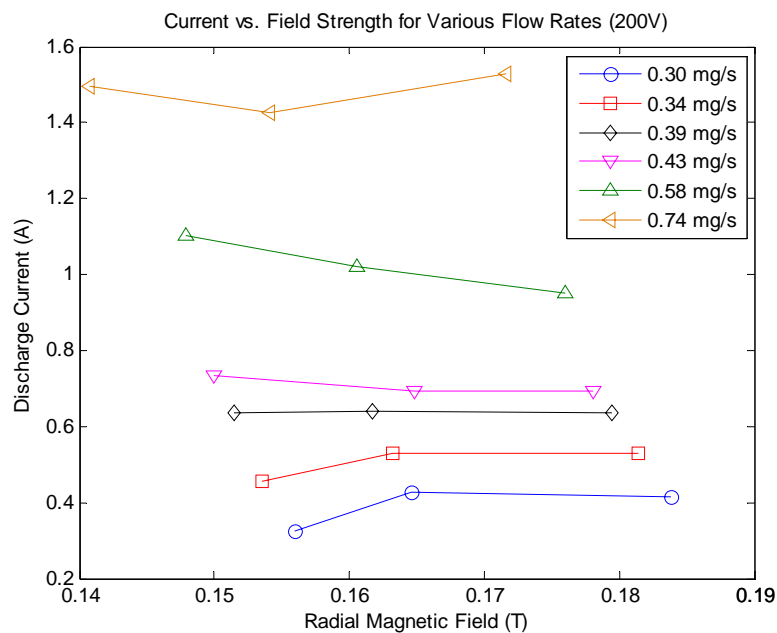
Figure 4.41 Discharge current versus radial magnetic field for the MHT-9 operating at a discharge voltage of 200V.

stant between 250-300V, but begins a sharp decrease at voltages of 200V and below. Looking more closely at the discharge current data, Figures 4.40-4.41 show the difference in behavior of the thruster discharge current at 300V compared to 200V. Figure 4.40 shows that for 300V, a maximum in discharge current was observed at the magnetic field strengths where a maximum in efficiency was observed for all the flow rates tested. This pattern was observed in the 250V data as well. However, Figure 4.41 shows that at 200V the pattern changes. The discharge current is relatively flat for each of the flow rates tested. This behavior was similar to that of the 150V and 100V data as well.

One hypothesis is that the magnetic field condition at the 5.6mm shunt length was the right middle ground for ionization. It was not so high that the field starved the discharge of electron currrent and not so low as to allow the electrons to pass too freely. The propellant utilization would be peaked under these conditions and explain the increased current observed at 250-300V. The lower voltages may have had different trends in current because of increased discharge oscillations and lower electron temperatures that may not have been optimized for the ionization collision cross-section.

4.5.5 Effect of Magnetic Field on Propellant Utilization

Figures 4.42-4.44 show the propellant utilization plotted against the simulated magnetic field strength for three different flow rates. The utilization efficiency is peaked in the same region as the thrust efficiency. This could explain the increased efficiency observed. The peaks are more pronounced at the higher voltages (250-300V) indicating that the effect may be more dominant at these voltages. The lower voltages appear flat on one side or the other of the curve, and this less peaked structure may indicate that other significant effects such as discharge oscillations and low electron temperature (for ionization) may be present.
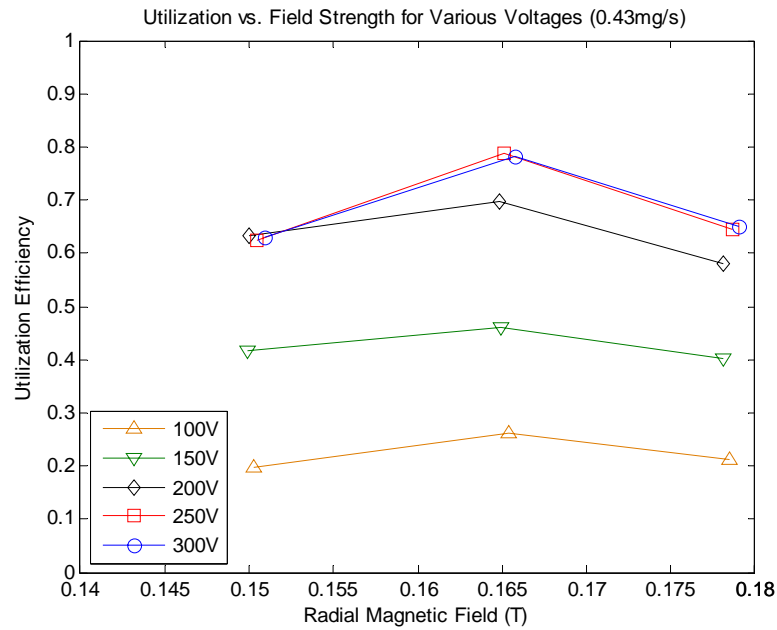
Figure 4.42 Utilization efficiency versus radial magnetic field for the MHT-9 operating at a flow rate of 0.43mg/s.
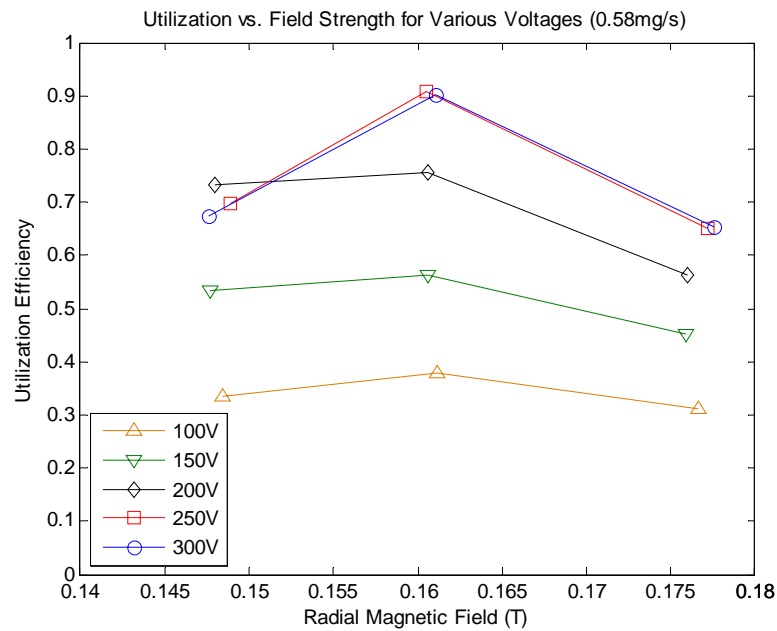
Figure 4.43 Utilization efficiency versus radial magnetic field for the MHT-9 operating at a flow rate of 0.58mg/s.
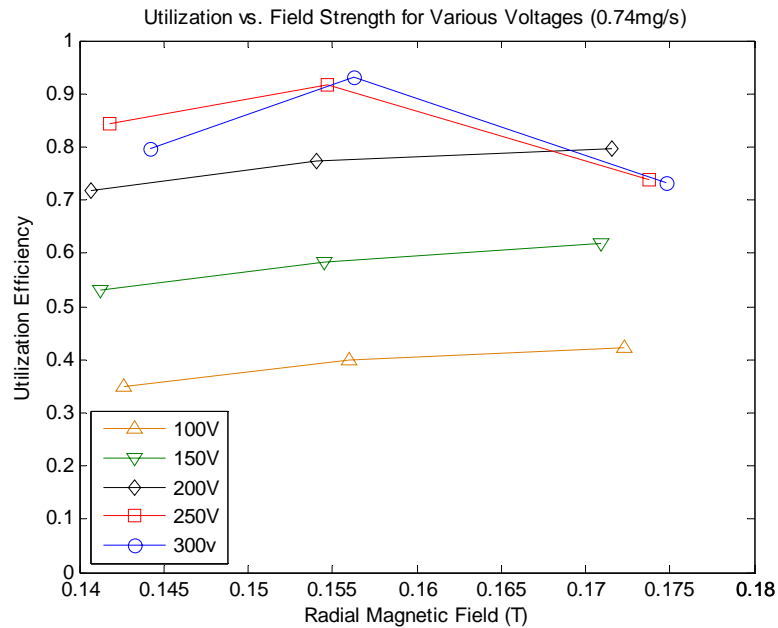
Figure 4.44 Utilization efficiency versus radial magnetic field for the MHT-9 operating at a flow rate of 0.74mg/s.

4.6 Temperature Results

The temperature inside the thruster was monitored to determine if the limits on the permanent magnet had been exceeded. Fortunately, the thermal model described in the previous chapter was indeed conservative and the actual magnet temperature was lower than predicted. At the nominal design condition of 0.74mg/s and 300V, the magnet temperature varied between 212-241°C which was much lower than the predicted range of 310-451°C. The peak temperature measured on the magnet was 364°C while operating at a flow rate of 0.98mg/s. Figure 4.45 shows a plot of the temperature measured on the magnet for different operating conditions with no magnetic shunt. The temperature is higher at the lower voltages which agrees with the trends in power shown in Figure 4.16. The discharge power peaks at 200V and thrust efficiency begins to decrease rapidly from 200V downward, as shown in Figure 4.26. This indicates a relatively high amount of power lost to wall surfaces at the lower voltages, which would likely drive the thruster temperature upward.

As indicated by Figure 4.4, the temperature of both the magnet and adjacent center stem material were monitored during testing of the MHT-9. The two temperatures were always within 12°C of each other, indicating that there was likely very good thermal conductance between the two materials. The contact pressure was likely high and evenly distributed due to their magnetic attraction. This would facilitate heat conduction across the material interface.
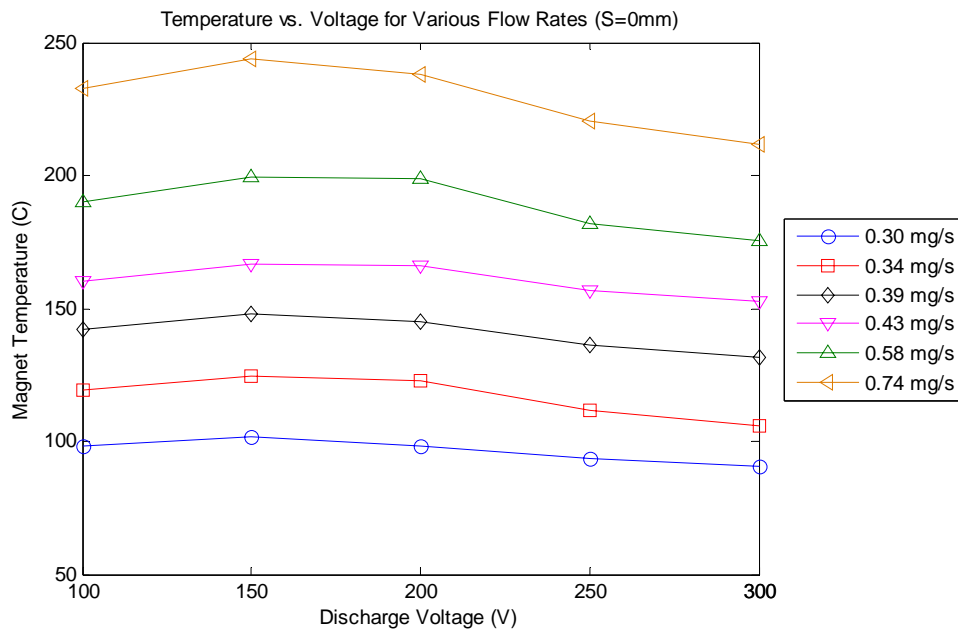
Figure 4.45 Magnet temperature versus discharge voltage for the MHT-9 operating with no magnetic shunt (*S*=0mm).

4.7 Thruster Erosion

Significant erosion was observed at both the inner and outer guard rings after the verification test period at MIT. The outer guard ring had a small chamfer eroded into it at the thruster exit point. The inner guard ring, or center stem cap as it is also called, was completely eroded through at the channel exit and separated into two pieces. The top of the cap ended up as a thin plate with a small hole in the center while the remaining cylinder showed erosion beginning at approximately the axial location of the anode tip and extend-

ing downstream. Figure 4.46 shows both guard rings as they looked after completing both verification tests at MIT for total running time of approximately 120 minutes.

The significant erosion observed on the guard rings prompted several changes to the plan for performance testing at Busek. First, a new center stem, outer guard ring and three center stem caps were manufactured for the thruster. The center stem cap was replaced each time the shunt length was changed (at the beginning of tests #3-5), using three center stem caps in total. The new outer guard ring was not replaced for each test. It survived the first three performance tests at Busek until finally splitting into two pieces during the final run (test #6). Second, the duration of each test was limited to less than two hours. The test procedure was conducted as described at the beginning of Section 4.4. The thruster was allowed to warm up at 300V for each flow rate tested and then successive voltages were tested for at least two minutes each. If a particular data point required more time for the discharge current, thrust or magnet temperature to stabilize, adjustments were made to lengthen the test point as needed.
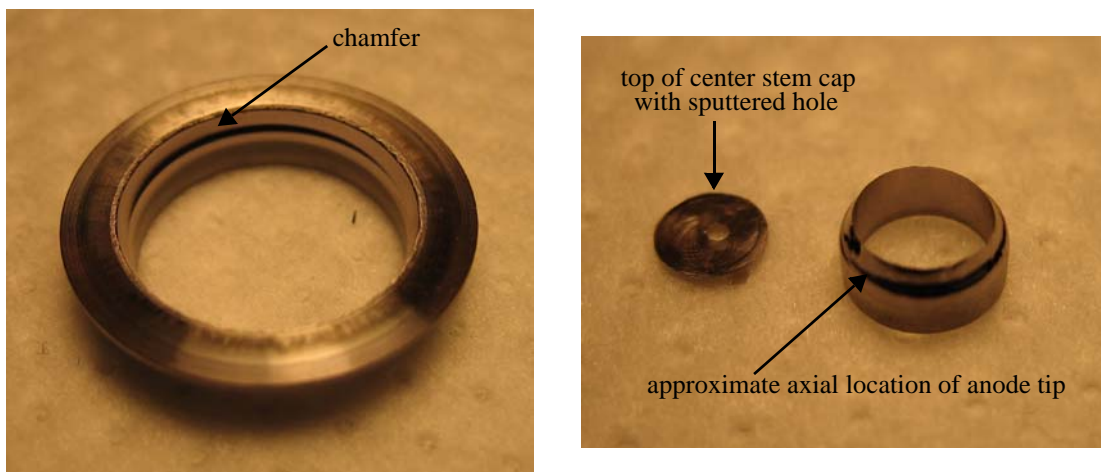
Figure 4.46   Pictures of the MHT-9 guard rings after the two verification tests at MIT. The left image shows the outer guard ring having a chamfer at the thruster exit plane. The right image shows that the center stem cap was actually split into two pieces at the channel exit. The top of the cap had a small hole sputtered from the center. The remaining cylinder showed significant erosion beginning at the axial location of the anode tip.

4.7.1 Guard Ring Material

The outer and inner guard rings were both made of tantalum. As noted before, tantalum has a very high melting temperature and good machinability. However, the D-55 uses graphite for guard rings due to its very low sputter yield. Figure 4.47 shows sputter yields determined by Wehner and Rosenberg (reprinted by Wilson) for various materials bombarded with Xe and Hg ions with energies of 400eV [77]. The data show that under Xe ion impact, the sputter yield of tantalum compares favorably to most other refractory metals. Tantalum has a yield of 0.75 atoms/ion, which is just slightly higher than molybdenum at 0.7 atoms/ion. Tungsten and rhenium have higher yields with both being about 0.9 atoms/ion. However, carbon shows a low sputter rate of approximately 0.1 atoms/ion. This likely forms the justification for the use of graphite in flight versions of the D-55.
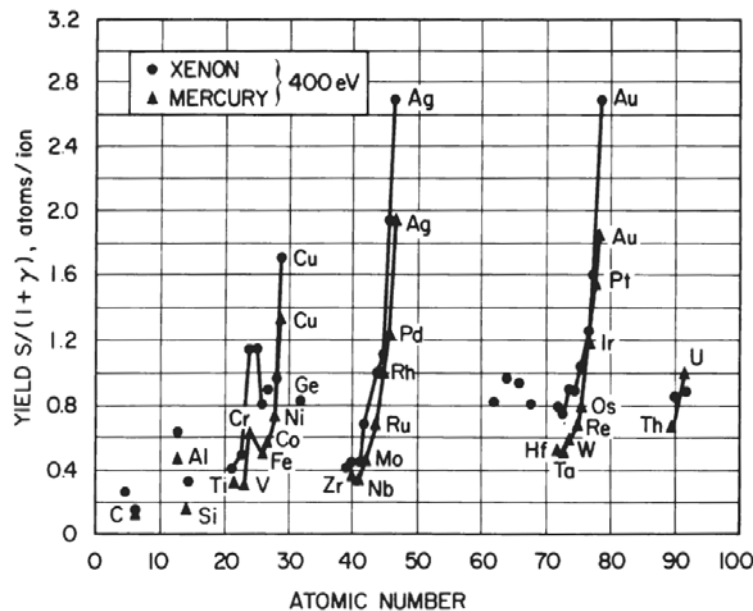
Figure 4.47 Sputter yields for Xe and Hg ions with 400eV of kinetic
energy impacting various materials [77].

4.7.2 Erosion Rate Estimates

Simple estimates of the erosion rate in the MHT-9 were made by measuring the erosion depth using digital calipers. The mass of sputtered material was estimated for some of the guard rings by comparing their mass before and after a test. Figure 4.48 shows the change in profile of the center stem cap as it eroded during each of the test runs. The radial erosion rate of the center stem cap near the exit plane was estimated using the change in diameter at the tip of the cap ($D_1 \Rightarrow D_2$). The axial erosion rate was estimated using the change in height of the cap ($H_1 \Rightarrow H_2$). The results of these esimates for the center stem cap are shown in Table 4.2.
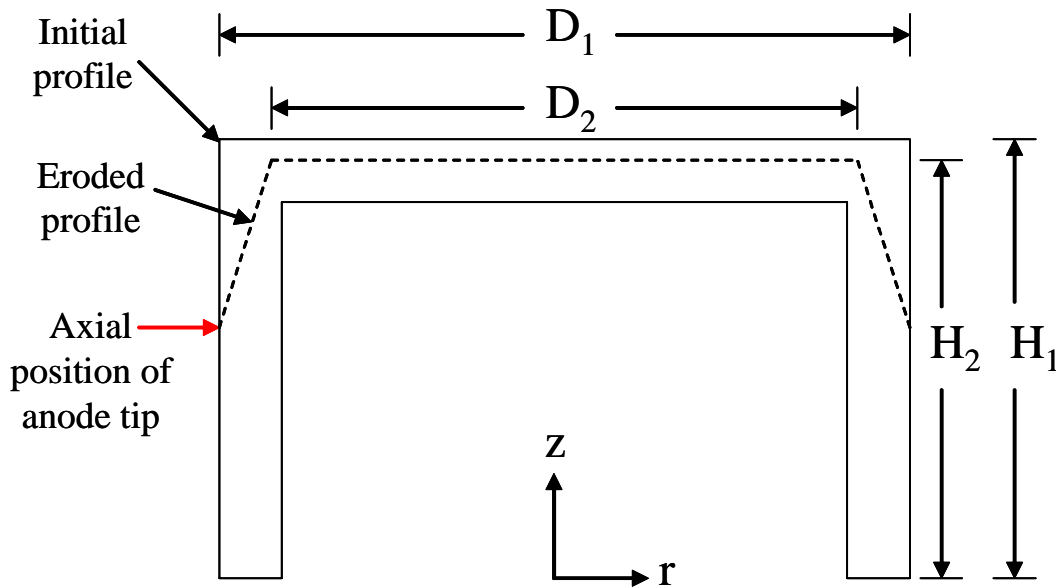
Figure 4.48   Change in profile of center stem cap as it erodes due to ion sputtering. Erosion begins axially at the same position as the tip of the anode.

TABLE 4.2   Erosion Rate Estimates for the Center Stem Cap

Test #	Radial Erosion Rate (mm/hr)	Axial Erosion Rate (mm/hr)	Sputtered Mass (g/hr)
3	0.23	0.10	0.118
4	0.28	0.10	0.117

These estimated erosion rates are very high, especially considering that the thickness of the center stem cap is only 0.5mm. This would mean the minimum lifetime is on the order of 2-5hrs, if the end of life is determined by when the plasma reaches the magnetic material. The thruster would continue to operate beyond this point but performance would begin to decline as the pole pieces were eroded and overheated. These rates are recognized to be maximum erosion rates since they are measured at the thruster exit plane where the density is likely very high. It is also possible that the erosion would slow over time as the ions carved out a natural expansion path. Changing the guard ring material to graphite would likely increase the minimum lifetime by an order of magnitude to 20-50hrs.

The radial expansion rate for the outer guard ring used in tests #3-6 was estimated to be 0.15mm/hr at the thruster exit plane, which is lower than that of the center stem cap. This may be because the plasma density is likely lower at the outside of the channel, allowing the outer guard ring to survive longer than the center stem cap.
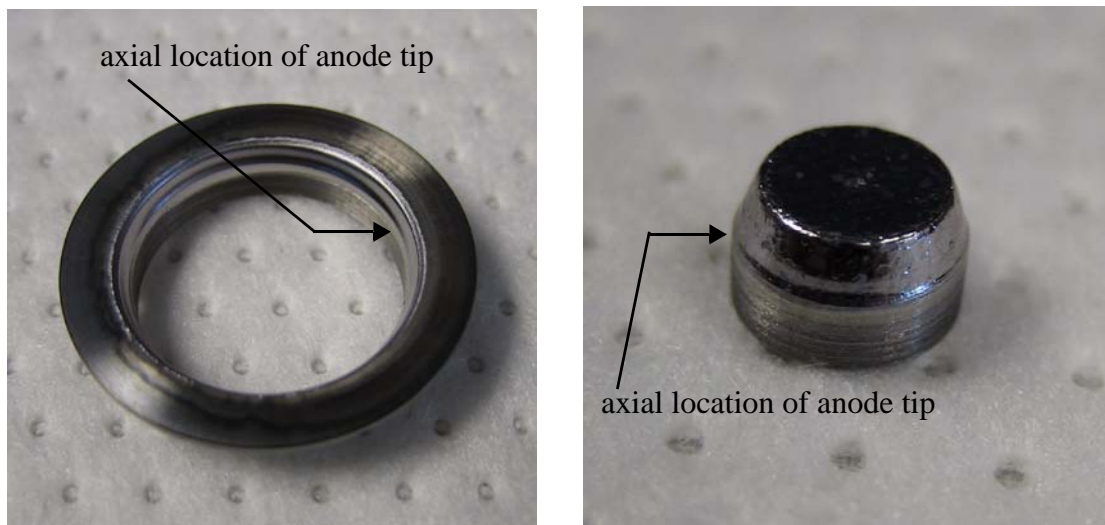
Figure 4.49 Photos of the erosion on the guard rings after performance testing. The left photo of the outer guard ring was taken after 3.4 hours of use. The right photo of the center stem cap was taken after 1.7 hours of use. The erosion very clearly begins where the anode tip is located.

Photos of the guard rings after performance testing at Busek are shown in Figure 4.49. It can be very clearly seen that there is an axial boundary between the eroded portions of the guard rings and the regions that are completely untouched. This position corresponds directly with the axial location of the anode tip. Two possible solutions to the problem of high erosion for the MHT-9 would be to either move the tip of the anode axially downstream or to shorten the center stem slightly. Previous research with the D-55 thruster has shown that extending the anode all the way to the exit plane will not only reduce guard ring erosion, but also has little effect on performance [34]. The cylindrical Hall thruster built at Princeton has shown success using the idea of a short center stem to reduce erosion in a ceramic lined thruster [78].

Chapter 5

PERFORMANCE ANALYSIS AND THRUSTER MODELING

This chapter examines the performance of the MHT-9 in the context of the original objectives: to develop a small scale Hall thruster with performance equivalent to the mature 1kW class technology currently available, and more importantly to understand the physics underlying the scaling process. The performance of the MHT-9 is compared to the initial scaling predictions as well as other low power Hall thrusters found in the literature. A list of possible causes for decreased thruster performance at small size is presented to motivate a discussion of thruster performance through dimensionless parameters. The effect of changes in the discharge chamber geometry on electron temperature are investigated through an analytical model. Finally, a computational model was used to simulate the MHT-9 to shed light on the plasma properties within the thruster as well as performance trends over ranges of operational parameters that could not be examined in the laboratory.

5.1 MHT-9 Performance Evaluation

The performance testing of the MHT-9 was a modest success. Although the thruster did not perform as well as the baseline D-55 thruster, significant improvements were made over the previous effort at MIT. The MHT-9 performance also compared favorably to other low power thrusters considering its very small diameter. This section will compare the performance of the MHT-9 to the initial expectations as well as some of the other low power Hall thrusters built previously.

5.1.1 Ideal Scaling Comparison

The predictions of the ideal scaling theory discussed in Chapter 2 are shown in Table 5.1 alongside the results from performance testing at the nominal conditions. The data point used in the experimental results column was taken with the MHT-9 operating with a 6.6mm long magnetic shunt. This data point was selected because it most closely matched the operating conditions determined by ideal scaling arguments. The table shows that the discharge current and power were much higher than expected, and this significantly reduced the thrust efficiency. The thrust and specific impulse were very close to the predicted values, however there was a 26% deficit in efficiency and a 80s deficit in specific impulse. The 1786s specific impulse and 56% thrust efficiency shown in the predictions represent the performance of the D-55 baseline thruster, which were the goals for the MHT-9 at the outset of the design process.

TABLE 5.1   Comparison of Ideal Scaling Predictions with Experimental Results at the Nominal Operating Condition

	Ideal Scaling Predictions	Experimental Results
Discharge Power (W)	200	347
Discharge Voltage (V)	300	300
Discharge Current (A)	0.67	1.14
Magnetic Field Strength (G)	1378	1442
Propellant Flow Rate (mg/s)	0.73	0.73
Thrust (mN)	12.8	12.3
Specific Impulse (s)[a]	1786	1706
Thrust Efficiency[b]	0.56	0.30

a. Specific impulse numbers do not include cathode flow.

b. Efficiency numbers are for "anode efficiency" and therefore do not include cathode flow or cathode power.

Although the performance did not meet the goals set forth by the ideal scaling theory, there were several data points that had better performance than the nominal conditions. Table 5.2 lists three such data points: the highest efficiency for the target power level of

200W, the highest overall anode efficiency and the highest overall specific impulse. The performance of the 200W data point is actually comparable to the nominal condition, but has a much lower power input. This low flow rate point would be an interesting regime to do further experimental exploration around. The point of highest efficiency also has a lower flow rate and discharge power than the nominal condition, yet better overall performance. The highest specific impulse point measured an impressive 2022s as well as a 34% thrust efficiency at a very high thrust level for such a small diameter thruster.

TABLE 5.2 Selected Experimental Results for the MHT-9

	Highest Performance at 200W	**Highest Thrust Efficiency**	**Highest Specific Impulse**
Discharge Power (W)	203	252	481
Discharge Voltage (V)	300	250	300
Discharge Current (A)	0.67	1.00	1.59
Magnetic Field Strength (G)	1657	1606	1495
Propellant Flow Rate (mg/s)	0.43	0.58	0.84
Thrust (mN)	7.1	10.1	16.6
Specific Impulse (s)[a]	1676	1772	2022
Thrust Efficiency[b]	0.29	0.35	0.34

a. Specific impulse numbers do not include cathode flow.

b. Efficiency numbers are for "anode efficiency" and therefore do not include cathode flow or cathode power.

5.1.2 Low Power Hall Thruster Comparison

The MHT-9 compares favorably to other low power Hall thrusters considering its very small diameter and inability to actively tune the magnetic field with electromagnets. Table 5.3 shows a comparison of several different low power Hall thrusters, including the MHT-9. The data were selected from the literature to be as close as possible to a power level of 200W, with the notable exception of the MIT-50W thruster built by Khayms. The 50W miniature thruster was not designed to operate at power levels that high. The thrust-

ers listed in the comparison include (all thrusters are ceramic walled unless indicated otherwise):

1. MIT-50W: The 50W metallic walled thruster built by Khayms at MIT [13-15].

2. MHT-9: Metallic walled thruster built for this research.

3. KM-20: Built by the Keldysh Research Center in Russia [20].

4. BHT-200: Flight qualified thruster built by the Busek Company, and the first Hall thruster built in the United States operational in space [70, 73].

5. SPT-25: Built by the Fakel Design Bureau in Russia [22].

6. HTX: The annular version of the 2.6cm laboratory model built at the Princeton University Plasma Physics Laboratory [78].

7. T-27: Laboratory version of low power D-55 derivative (metallic walled) thruster built by the Russian Central Research Institute for Machine Building (TsNIIMash) [19].

8. HT-100: Nominally 100W thruster built by the Alta Company in Italy [18]. Utilizes a permanent magnet along with a small trim coil.

TABLE 5.3   Comparison of the MHT-9 to Other Low Power Hall Thrusters

	MIT 50W	MHT-9	KM-20	BHT 200	SPT-25	HTX	T-27	HT-100
Type[a]	M	M	C	C	C	C	M	C
D (mm)	3.7	9	20	21	25	26	27	29
P_d (W)	126	203	210	200	193	200	201	210
V_d (V)	300	300	350	250	224	270	251	n/a
I_d (A)	0.42	0.67	0.6	0.8	0.86	0.74	0.8	n/a
$\dot{m}_a$ (mg/s)	0.21	0.43	0.5	0.94	0.7	0.7	0.7	0.41
T (mN)	1.8	7.1	8.8	12.8	10.2	9.3	9.5	7.4
I_{sp} (s)	865	1676	1850	1390	1300	1350	1430	1850
η_t	0.06	0.29	0.39	0.44	0.32	0.31	0.33	0.32

a. Type indicates ceramic (C) or metal (M) walled discharge chamber.

There does not appear to be a clear trend between size and performance. However, this comparison is somewhat qualitative in that it relies on absolute metrics. Dimensionless metrics allow for a more accurate comparison of different models because they help to remove the effects of using different operating conditions. This idea will be explored further in a later section. The comparison does show that, with the exception of the BHT-200 and the KM-20, the efficiency at the 200W power level is relatively constant across thruster model, type and diameter at roughly 30%. The specific impulse depends on the discharge voltage of the operating point since it directly affects the exit velocity of ions. Thrust and discharge current are well correlated to the propellant flow rate.

5.1.3 Comparison to Baseline Thruster

Section 5.1.1 compared the MHT-9 performance to the baseline thruster at a single point identified in the ideal scaling analysis. A comparison can also be made over varying operating conditions to examine the differences in trends. This is done using dimensionless parameters in a later section to enable a fair comparison of thrusters of such different size, but it is also interesting to look at the trends in thrust for the two thrusters. Figure 5.1 shows a plot of thrust versus power for both the D-55 and the MHT-9. It is clear that a characteristic relationship between thrust and power exists for each thruster. Linear fits are shown that relate the efficiency of each thruster to the ratio of thrust to power for a given exhaust velocity (or specific impulse) as,

$$\frac{T}{P_d} = \frac{2\eta_t}{c}.$$

$$(5.1)$$

The linear approximations show that the D-55 is roughly 1.75 times as efficient as the MHT-9 for a given exhaust velocity, or at a given power the D-55 thrust would be 1.75 times that of the MHT-9. This fits well with the single point comparison shown in Table 5.1 since the specific impulses of the two thrusters are so closely matched.
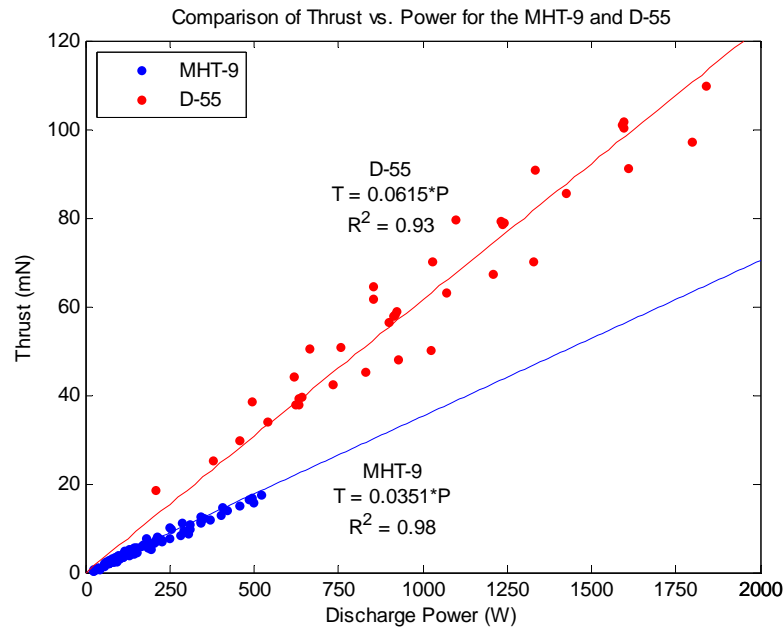
Figure 5.1 Comparison of the thrust to power characteristics for the MHT-9 and D-55.

5.2 Challenges of Building a Miniature Hall Thruster

The lower than expected performance of the MHT-9 raises questions about the ideal scaling theory developed in Chapter 2 and the practical limitations of applying its principles. A list of potential problems was developed to drive the performance analysis. These issues are presented in the following subsections.

5.2.1 Manufacturing

As the size of the thruster is reduced, the difficulty of producing complicated parts and the sensitivity to dimensional tolerances will increase. This can affect the performance of the thruster in a variety of ways. The Hall thruster anode is usually dual purpose, serving as the positive potential point and as a propellant distributor. This generally requires a choked manifold and baffles to ensure the flow is distributed evenly around the annulus, and to slow the axial speed of the flow. These complicated structures proved very difficult to machine in the MHT-9, which used separately produced baffles and a plenum that were

press fit into the anode annulus. At even smaller size, as for the 50W thruster built by Khayms, making just the annulus was a challenge. In that thruster the baffles were just minor features of the annulus, not separately machined pieces, and there was no room for a full fledged plenum. Khayms had serious challenges making leak tight flow connections as well. The MHT-9 was able to use electron beam welding and Swagelok components due to its slightly larger size.

The anode assembly also plays a role in the electron confinement. The magnetic circuit is designed so as to produce radial field lines that are as parallel as possible to the face of the anode. However, tight positioning and alignment tolerances or variabilities in the anode tip surface can cause some lines to directly intersect the anode surface. This creates direct paths for the trapped electrons to be captured by the anode. In order to align the MHT-9 anode properly during assembly, a separate jig piece made of plastic was built to sit between the inner wall of the anode and the center stem while the anode was tightened into position. This was used to further reduce the radial play of the anode inside the insulator that was specifically shaped for alignment purposes. The MHT-9 is shown with the anode alignment cylinder in place in Figure 5.2.

Finally, along with the small anode comes small insulators. These insulators are not necessarily difficult to produce, but they are easily cracked, eroded or coated with sputtered material. Any of these problems can lead to a breakdown of the insulation and shorting of the thruster anode to the low potential body. The boron nitride grade used for highest temperatures also tends to be rather soft, making it difficult to use as an alignment surface.

These manufacturing problems become more challenging as the size of the thruster is reduced. However, determining a quantitative relationship between manufacturability and performance would be difficult and imprecise. The 200W target power level was selected for the MHT-9 in part because it allowed for a thruster diameter that was small and challenging to build, yet more than twice as large as the previous effort at MIT by Khayms. This eased the manufacturing tolerances and allowed for a more reliable construction. The
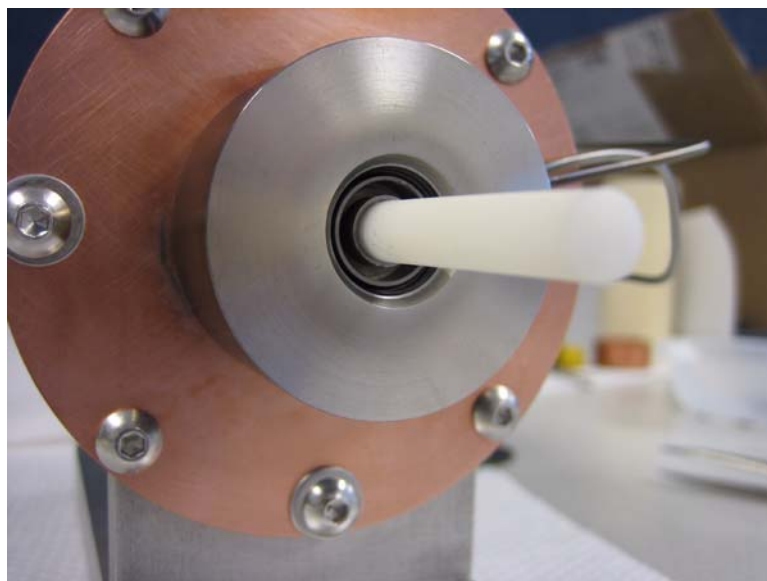
Figure 5.2 MHT-9 shown with plastic anode alignment cylinder in place during assembly. This plastic jig piece kept the anode axially aligned while it was tightened down with screws from the back.

erosion patterns in the MHT-9 were visually observed to be azimuthally uniform, indicating that propellant distribution was even. Measurements of the anode position with digital calipers indicated that the axial position of the anode was within fractions of millimeters, and the use of the alignment cylinder as well as an insulator with an alignment channel added confidence in maintaining radial separation. Therefore, it is unlikely that manufacturing defects played a significant role in the performance deficiencies of the MHT-9.

5.2.2 High Wall Temperature

The neutral propellant that flows into the discharge chamber collides with both the anode surfaces and the channel walls as it moves downstream. When a particle bounces off of a wall, the reflection can be either specular or diffuse. Specular reflection is similar to a hard-sphere interaction, commonly referred to as a "billiard ball" collision, where kinetic energy is conserved and the angle of reflection equals the angle of incidence. Diffuse reflection allows for some energy transfer between the incident particle and the wall surface, and the angle of reflection may be different from the incident angle. In Szabo's sim-

ulation of the 50W miniature Hall thruster, diffuse reflection was used for neutrals with full accommodation at the wall temperature [26]. Szabo quotes the work of Bird, who states that "engineering" surfaces in contact with gases at normal temperatures results in a nearly diffuse reflection process where the particles are accommodated with the wall temperature [79]. Bird also states that outgassed smooth metal surfaces tend to behave differently, but in the MHT-9 it is likely that the anode and channel surfaces are microscopically rough due to the erosion and sputtering processes.

Given the assumption that neutral xenon atoms reflect from thruster surfaces with a thermal energy equivalent to the wall temperature, the neutral density is directly influenced by the thermal state of the thruster. If the wall temperatures inside a miniature thruster are higher than those of the baseline thruster, the neutral population will have a higher temperature. This could lead to a lower density of neutrals in the ionization region and therefore a lower than expected plasma density. Neutral temperature was assumed to be invariant during the ideal scaling discussion of ionization collisions in Chapter 2. However, this assumption rested on the preservation of power loss mechanisms such as ion-electron recombination at wall surfaces. A more careful look at this parameter is warranted given the lower than expected performance of the MHT-9 and the significant erosion of thruster surfaces. Neutral heating is therefore incorporated into the dimensionless performance analysis below via the Knudsen number (Section 5.3.1).

5.2.3 Magnetic Field Strength

The strength of the magnetic field in the MHT-9 was determined using the adopted scaling method described in Chapter 2, where the field was scaled inversely with channel width but not channel length. The field strength was varied between experiments with the use of a magnetic shunt. However, the field strength could only be increased by 27% above the nominal level determined by scaling. Typical electromagnet driven thrusters can vary their field strengths by 100% or more above nominal field strength, allowing for a greater range over which magnetic optimization can be performed. During the testing of the MHT-9, a

local optimum in performance was observed within the range of magnetic fields tested. However, it is possible that a better optimization point exists outside of the range of fields available with the magnetic shunt system. The effects of magnetic field strength are investigated further through the magnetic confinement ratio, R_L/L, in the dimensionless performance analysis section below.

$$D_1 > D_2$$
$$B_1 < B_2$$

Miniature Hall Thruster with
Cylindrical Permanent Magnet

Hall Thruster with Electromagnets
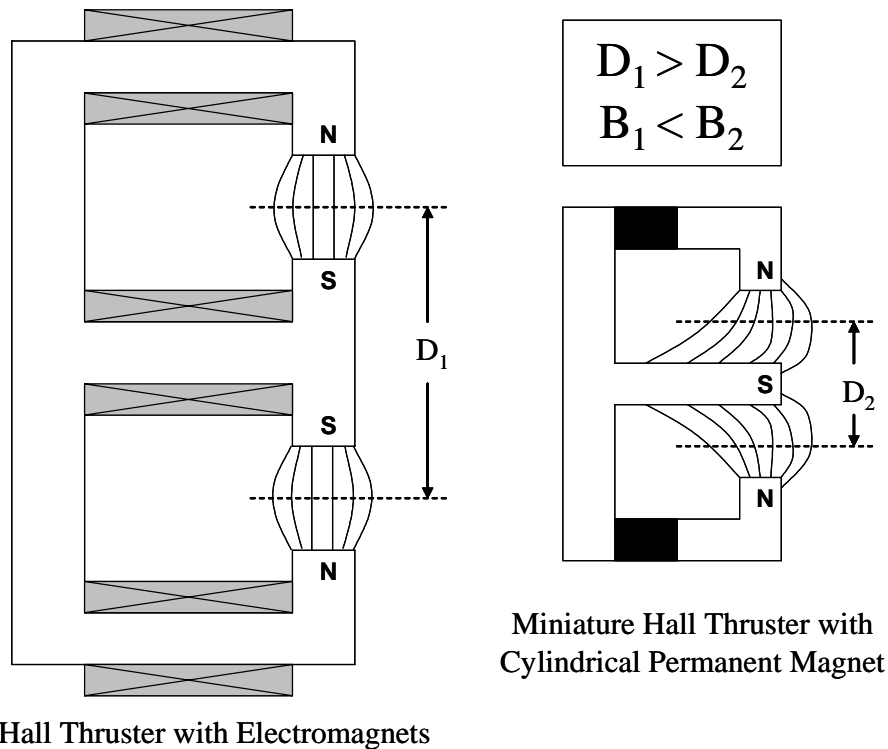
Figure 5.3   This diagram illustrates the qualitative differences in the magnetic field shape of a large Hall thruster that uses electromagnets and a miniature thruster that uses a permanent magnet. It is impossible to maintain the symmetric lens shape of the field at small sizes where distinct inner pole shapes cannot be used.

5.2.4 Magnetic Field Topology

The shape of the magnetic field inside a Hall thruster is typically designed to be symmetric about the midchannel axis with a lens-like profile. In order to create the shape of these field lines, two distinct magnetic pole pieces are required as shown on the left hand side of Figure 5.3. This arrangement allows the field strength to be adjusted through variation of

the coil currents, and by changing the ratio of inner to outer coil current, the field shape can be altered as well. As the midchannel diameter of the thruster is reduced, the volume available for making distinct inner and outer pole pieces is decreased, particularly at the center body. As shown in the ideal scaling analysis, a decrease in diameter also requires an increase in the field strength. This often causes the designer to select a permanent magnet in order to provide the high field strength in a small package that will not produce excessive ohmic heating. In order to avoid saturation of the center pole, the full radial width of the center body must be used for soft magnetic core material as shown on the right hand side in Figure 5.3. This leaves no room to make a separate center pole piece that brings the field lines into a concentrated radial shape. The field lines then begin to flow down the center body, causing a reduction of the field strength at the exit plane as well as a loss in symmetry of the field. By not focusing the field lines strongly into a pole piece, the magnetic bottling effect that helps repel electrons is reduced at the center stem. This also causes field lines to be less parallel to the anode face, making electron leakage to the anode more likely.

Radial inhomogeneity of the magnetic field is inherent to the annular geometry of a Hall thruster. The magnetic flux is generally conserved throughout the circuit, as described by Equation 3.10. Since the cross sectional area of the circuit decreases with radius at the thruster exit plane, the field strength, B, must increase in order to conserve the magnetic flux. However, because the symmetry of the pole shapes about the midchannel line is no longer present in a small diameter thruster, the magnetic field structure across the channel can become severely inhomogeneous and create radial plasma density gradients. These density gradients in turn produce electric fields that could potentially increase plume divergence and thereby reduce thruster performance.

Figures 5.4-5.5 show two different ways of plotting the radial magnetic field strength across the channel of the MHT-9. Both plots show the magnitude of the radial magnetic field. Figure 5.4 shows the field strength for three separate axial positions relative to the channel exit. Figure 5.5 shows a color contour plot of the radial field strength everywhere
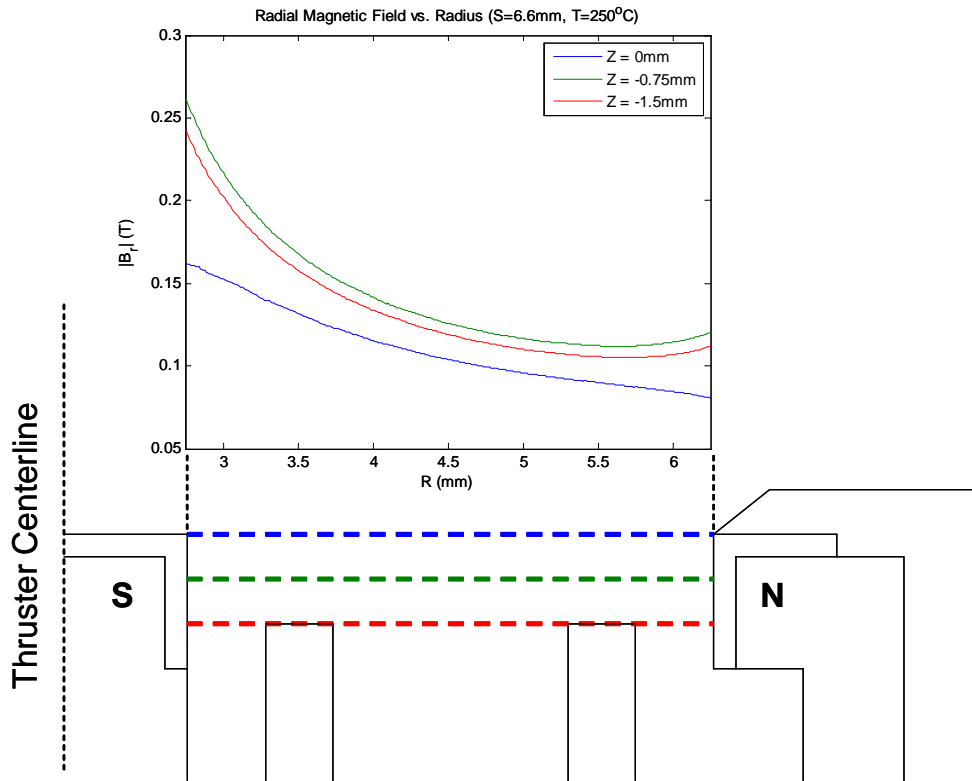
Figure 5.4 This figure shows a plot of the absolute value of the radial magnetic field across the channel relative to the thruster geometry. The radial lines along which the field values are plotted are shown as dashed lines in the geometry. The field strength more than doubles across the channel. These data are taken from a Maxwell simulation performed with a magnetic shunt length of 6.6mm and a magnet temperature of 250°C.

in the region near the channel exit. The two plots clearly indicate that the field strength more than doubles from the outer wall to the inner wall, indicating a strongly inhomogeneous field profile.

There is a strong possibility that the shape of the magnetic field played some role in the performance degradation of the MHT-9. Attempts to quantify the magnetic field topology in ceramic thrusters have been made by Gorshkov et al in two papers published recently [74-75]. Gorshkov quantifies the field topology using a function, F, that is a projection of the magnitude of the magnetic field gradient onto a surface normal to the magnetic field lines. The function is defined as,
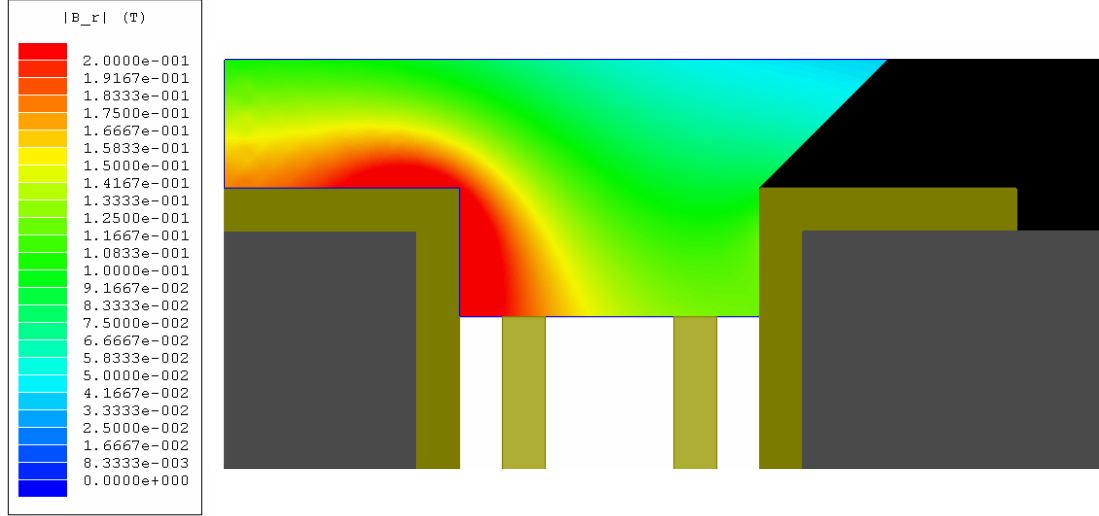
Figure 5.5 Contour plot of absolute value of the radial magnetic field strength in the discharge channel of the MHT-9. This plot is taken from a Maxwell simulation performed with a magnetic shunt length of 6.6mm and a magnet temperature of 250°C.

$$F = \left| \frac{\bar{B} \times \nabla |\bar{B}|}{|\bar{B}|} \right| . \tag{5.2}$$

Gorshkov uses this function in combination with a numerical model and a laboratory thruster built specifically to adjust field shape to show that F can be a good predictor of the location of the ionization region. He argues further that because F finds the location of the maximum gradient of the magnetic field inside the thruster, it should be centered near the exit plane along the channel midline for best performance. This alludes to the long held belief that the optimal configuration of the magnetic field inside a SPT style Hall thruster has a radial magnetic field that is sharply peaked in magnitude at the exit plane. It is unclear if this field profile also applies to the TAL geometry where the anode is much closer to the exit plane. Gorshkov experimentally shows that the measured efficiency of a ceramic walled thruster is highest when the maximum of the F function is located in the center of the channel. A plot of the F function inside the MHT-9 shown in Figure 5.6 indicates that the maximum is nowhere near the center of the channel, but rather clustered near the magnetic poles. The geometry shown by Gorshkov also has maxima located at the
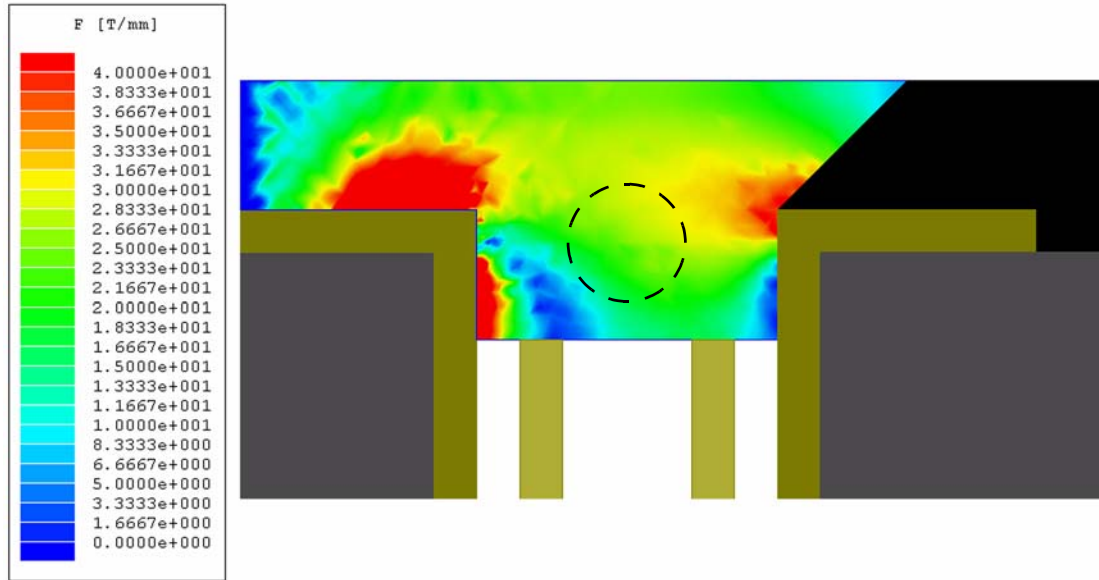
Figure 5.6 Plot of Gorshkov's *F* function inside the channel of the MHT-9 in units of T/mm. This plot shows that there is not a sharp maximum near the center of the discharge chamber, as it would be in a sharply peaked field profile that is symmetric about the channel midline. The dashed circle indicates where Gorshkov argues there ought to be a peak for optimal magnetic field topology. Plot is shown for $S=6.6$mm and $T_m=250°$C.

poles, but a third maximum region is also present in the middle of the thruster channel. There does seem to be a local increase in the middle of the MHT-9 channel, but it is not nearly as apparent as in Gorshkov's plots. This is another indication of the inherent problems with magnetic field topology at small scale.

It should be noted also that Gorshkov and others argue that in order to minimize discharge current oscillations, the magnetic field gradient should be positive between the anode and the exit plane of the thruster. Figure 5.7 shows that this is not the case for the MHT-9. The field geometry is such that the axial profile of the radial magnetic field strength shows a decrease in magnitude from the anode towards the thruster exit plane. Although discharge current oscillations did not prevent stable operation of the thruster, it is possible that they could be further reduced by changing the field geometry such that the peak of the field is closer to the exit plane. However, this can be difficult to accomplish without a clear pole shape on the center body that concentrates the field strength at the exit plane. The peak-to-

peak amplitude of discharge current oscillations in the MHT-9 were typically on the order of 10-35% of the time averaged current at the nominal flow rate. Repeatable discharge current oscillations were observed at some operating conditions, with frequencies between 20-35kHz for the nominal flow rate.
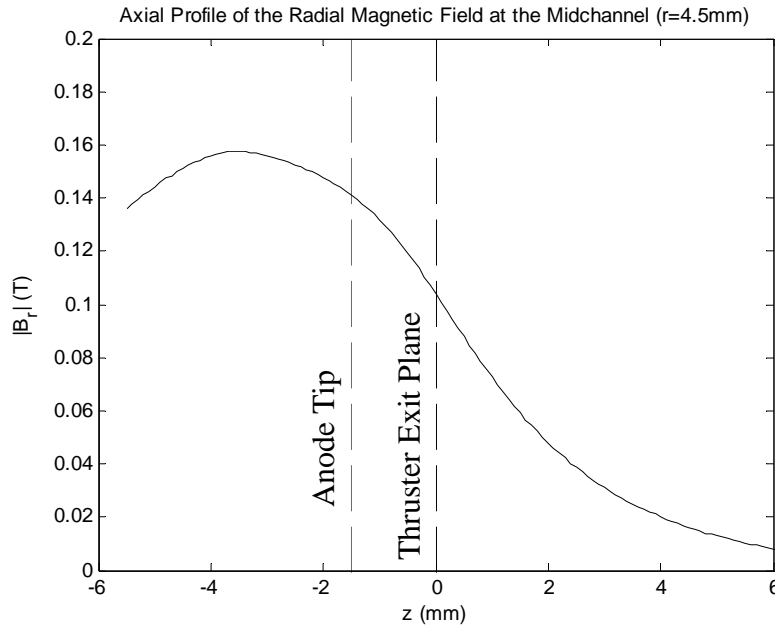
Figure 5.7   Axial profile of the radial magnetic field along the midchannel line.

5.2.5 Relative Sheath Thickness

The size of the sheath near the thruster walls is typically on the order of a few Debye lengths, where the Debye length is defined as in Equation 3.19. According to the ideal scaling analysis, the size of the sheath relative to the channel width will vary as,

$$\frac{\lambda_D}{R_2 - R_1} = \frac{1}{R_2 - R_1}\sqrt{\frac{\varepsilon_0 k T_e}{e^2 n_e}} \propto \frac{1}{\sqrt{R_2 - R_1}}, \tag{5.3}$$

where the electron temperature is a scaling constant. This indicates that the relative sheath thickness could be an issue at very small scale, but an estimate of the Debye length shows

that it is not a concern for the MHT-9. Using very conservative estimates of density and temperature ($n_e=1\times10^{18}\text{m}^{-3}$, $T_e=10\text{eV}$) near the wall, the Debye length is 24μm. If the sheath thickness is five times the Debye length, this is only 3% of the MHT-9 channel width. As simulation results in Section 5.7 indicate, this is a very conservative estimate.

5.3 Dimensionless Performance Analysis

The ideal scaling theory discussed in Chapter 2 was developed using several dimensionless ratios that were intended to capture the ionization, recombination and confinement processes within the discharge chamber. After building and testing the MHT-9, the data suggest that further insights are needed to fully understand the scaling process. This section intends to explore the performance of the MHT-9 using dimensionless parameters in order to make a more accurate comparison between the baseline thruster and the scaled down version in the hopes that this will shed more light on the underlying physics.

5.3.1 Knudsen Number

The Knudsen number, *Kn*, is a dimensionless number defined as the ratio of the mean free path length to a characteristic length scale. It is often used in fluid dynamics to determine if a flow is governed by collisional interactions, and thus well described by a continuum assumption, or if it is a molecular free flow and therefore best modeled statistically. The general form of the Knudsen number is written as,

$$Kn = \frac{\lambda}{L}. \tag{5.4}$$

In the case of a Hall thruster, the Knudsen number can be used to examine the utilization of electrons for ionizing neutrals. The hypothesis is that if the Knudsen number is kept constant in scaling, it would be ensured that a similar number of ionizing electron-neutral collisions would take place in both the baseline and the miniaturized thruster. This is a similar argument to the one used in the scaling treatment of electrons in Chapter 2 (Section 2.1.2).

The mean free path between ionization collisions for an electron, λ_{ei}, is defined as,

$$\lambda_{ei} = \frac{1}{n_n \sigma_i},\tag{5.5}$$

where n_n is the neutral number density and σ_i is the cross section for ionization. This is the average distance an electron will travel along its trajectory between ionizing collisions with neutrals. Electrons move mostly in the radial and azimuthal directions because of the orientation of the electric and magnetic fields, and diffuse more slowly in the axial direction when scattered by collisions. However, it is this axial movement that is important for scaling purposes because in order to ensure a similar number of ionizing collisions for each electron as it passes through the ionization layer, the ratio of this axial movement to a characteristic thruster length must be preserved. Thus, it is useful to define an axial mean free path, Λ_{ei}, that is the product of the axial diffusion velocity of the electron and the time between ionizing collisions,

$$\Lambda_{ei} = v_{e|z} t_{ie}\tag{5.6}$$

The axial diffusion velocity, $v_{e|z}$, was used in the scaling analysis of Chapter 2 to evaluate how the residence time of electrons in the ionization layer scales. It can be argued by continuity that the ion flux into the beam must be similar to the electron flux towards the anode, and therefore the ions and electrons must move with equal velocity because of quasineutrality. This is not strictly true because there are backstreaming electrons as well, but the argument should be a good approximation since the backstreaming to anode current ratio for electrons is typically less than one ($I_{bs}/I_a < 1$). This is sometimes referred to as ambipolar diffusion where both the ions and electrons will diffuse at the ion speed of sound, known as the Bohm velocity, v_B. The time between collisions, t_{ie}, is simply the inverse of the ionization collision frequency, ν_{ei} (Equation 2.13). The axial mean free path can therefore be expressed as,

$$\Lambda_{ei} = \frac{v_B}{\nu_{ei}} = \frac{v_B}{n_n c_e \sigma_i}.\tag{5.7}$$

This can be further simplified using the definition of the Bohm velocity in Equation 2.27, and the mean electron thermal speed which is defined as,

$$\bar{c}_e = \sqrt{\frac{8kT_e}{\pi m_e}}. \tag{5.8}$$

If the definition of the mean free path along the electron trajectory in Equation 5.5 is also used, then the electron axial mean free path for ionization becomes,

$$\Lambda_{ei} = \frac{v_B}{n_n c_e \sigma_i} = \lambda_{ei}\sqrt{\frac{\pi m_e}{8m_i}}. \tag{5.9}$$

The Knudsen number can be rewritten using this definition of the mean free path. Thus, Equation 5.4 becomes,

$$Kn = \frac{\lambda}{L} = \frac{\Lambda_{ei}}{L} = \frac{\lambda_{ei}}{L}\sqrt{\frac{\pi m_e}{8m_i}} = \frac{1}{Ln_n\sigma_i}\sqrt{\frac{\pi m_e}{8m_i}}. \tag{5.10}$$

The neutral density just upstream of the ionization layer can be expressed using flow rate continuity,

$$\dot{m}_a = m_n n_n v_n A, \tag{5.11}$$

where the neutral velocity is determined by the thruster wall temperature, T_w, and the Mach number,

$$v_n = M_n\sqrt{\gamma R T_w}. \tag{5.12}$$

The neutrals interact with thruster surfaces such as the anode and discharge chamber walls, and through collisions with these surfaces they take on the wall temperature. The scaling analysis assumed that the neutral temperature and velocity were constant with scaling, but experimental measurements (in combination with the finite element thermal model) have shown that the miniaturized thruster likely operated at higher temperatures than the baseline thruster. It is therefore important to include this effect in the Knudsen

number evaluation. Because the area scales as the characteristic length squared ($A \approx L^2$), the equations above can be combined to express the Knudsen number as,

$$Kn = \frac{m_n L M_n \sqrt{\gamma R T_w}}{\dot{m}_a \sigma_i} \sqrt{\frac{\pi m_e}{8 m_i}}. \tag{5.13}$$

The characteristic length for the Knudsen number should be representative of the overall thruster size. Thus, an estimate of $L \approx \pi D$ was made for this analysis. This ties the Knudsen number to concrete characteristics of the thruster's physical geometry and makes for an interesting comparison of different size thrusters.

5.3.2 Estimating the Thruster Wall Temperature

In order to use the Knudsen number expression in Equation 5.13, the thruster wall temperature must be known. The MHT-9 wall temperature was estimated using a combination of the thermal model described in Chapter 3 and the thermocouple measurements taken on the permanent magnet during performance testing. The majority of the neutrals that enter the channel are likely to have some contact with the anode surface as they encounter the plenum and baffles, and then flow out through the anode channel. The neutrals will take on the anode temperature through these surface collisions. The thermal model was used to estimate the difference between the average permanent magnet temperature and the average anode temperature. The different cases presented in Table 3.8 show that this temperature difference ranges between 602-907°C, with an average difference of 750°C. This temperature difference was added to the permanent magnet temperature taken at each operating condition to estimate the thruster wall temperature, or what is effectively the temperature of the neutral flow. Thus, the formula used for MHT-9 wall temperature was simply,

$$T_w = T_m + 750°C. \tag{5.14}$$

The wall temperatures of the various TAL thrusters used for comparison were estimated with a simple conduction model. The amount of energy that goes into heating a thruster,

P_w, is some fraction, f, of the total discharge power. This fraction is estimated to be between 0.25-0.5 since the mature thruster technology is roughly 50% efficient, leaving half of the discharge power available for thruster heating and other loss mechanisms.

$$P_w = fP_d = fV_dI_d \tag{5.15}$$

The thruster is assumed to have high utilization efficiency ($\eta_u > 0.9$) so that the discharge current can be approximated using the propellant flow rate. The heating power dumped into the walls will cause a temperature difference between the walls and some reference temperature that the thruster conducts (and radiates) to which is inversely proportional to the conductivity of the guard ring material. The heating power can thus be rewritten as,

$$P_w = f\frac{V_d\dot{m}_a e}{m_i} = k_w L(T_w - T_0). \tag{5.16}$$

The characteristic length, L, was chosen to be the diameter since this closely reflects the relative differences in overall size between different thrusters. The reference temperature, T_0, was assumed to be near room temperature, or the approximate temperature of a vacuum tank. The guard ring material used in TAL thrusters is typically graphite, which has a wide range of thermal conductivity ($k_w = 24\text{-}470$W/m-K) depending on the type and grade. The actual graphite type used in the D-55 or other TAL thrusters is unknown, however the conduction pathway is likely dominated by the thermal contact resistance. Therefore the bottom of this conductivity range was used to model the wall temperature. Equation 5.16 can be rearranged to express the wall temperature as,

$$T_w = T_0 + \frac{f}{k_w D}\frac{V_d\dot{m}_a e}{m_i}, \tag{5.17}$$

which is simply a function of the thruster diameter and operating conditions. Figure 5.8 shows a plot of the predicted wall temperature inside the D-55 for various propellant flow rates and discharge voltages. The predicted wall temperature was 283°C at the nominal operating conditions of 300V and 4.52mg/s.

5.3.3 Knudsen Number Comparison

Data on various other TAL thrusters built by TsNIIMASH with geometries that are similar to the D-55 were pulled from the literature in order to make a dimensionless performance comparison. The thrusters range in size from the 27mm diameter T-27 laboratory model to the 100mm diameter D-100, a thruster capable of operating at a maximum discharge power level of 7.5kW. All of the thrusters used in this comparison have metallic discharge chamber walls. Using the Knudsen number as the independent variable allows thrusters of vastly different scale to be closely compared in such a way as to remove their scale dependencies. The thrust efficiency was chosen as the dependent variable to keep the performance criterion dimensionless as well. The thrusters included in this comparison are (in order of increasing size, with numbers indicating midchannel diameter):

1. MHT-9: Laboratory thruster built for this research.

2. T-27: Laboratory version of a low power thruster designed to operate from 300-1000W [19].

3. D-38: Prototype thruster built for the Module-M flight experiment [19].

4. D-55: Flight proven technology that served as the baseline thruster for scaled down design of the MHT-9 [39].

5. D-80: Originally designed to operate at high voltage and in a two-stage configuration [80].

6. D-100: Nominally 4.5kW thruster with a 100mm diameter [76].

For the comparison, the effective ionization cross section of Xe was estimated using the electron temperature model discussed in Section 5.4 and the ionization rate calculations in Section 5.5. The neutral flow Mach number was estimated to be near unity, and the Mach number profiles amongst the differently sized thrusters were assumed to be similar. In order to make the interpretation of the results more intuitive, the thrust efficiency has been plotted against the inverse Knudsen number,

$$\frac{1}{Kn} = \frac{\dot{m}_a \sigma_i}{m_n \pi D M_n \sqrt{\gamma R T_w}} \sqrt{\frac{8 m_i}{\pi m_e}}. \tag{5.18}$$
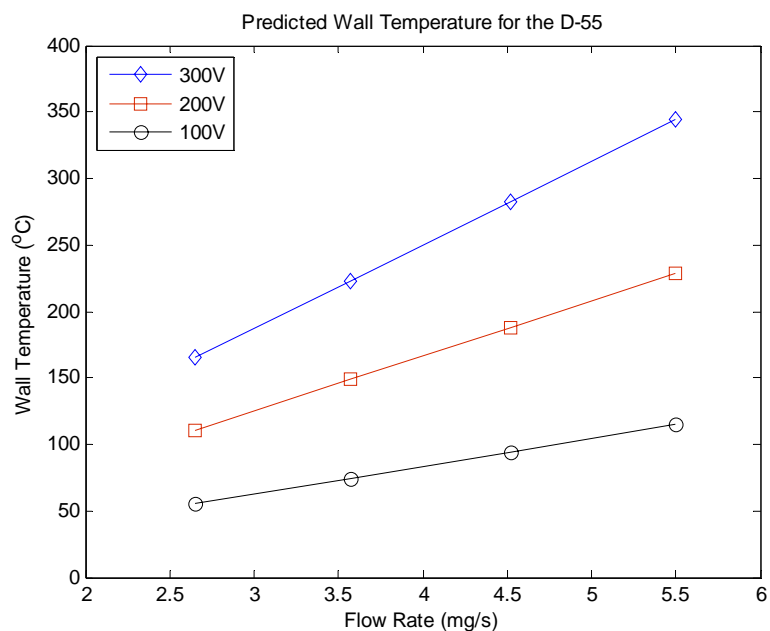
Figure 5.8   Predicted wall temperature inside the D-55 using the simple conduction model.
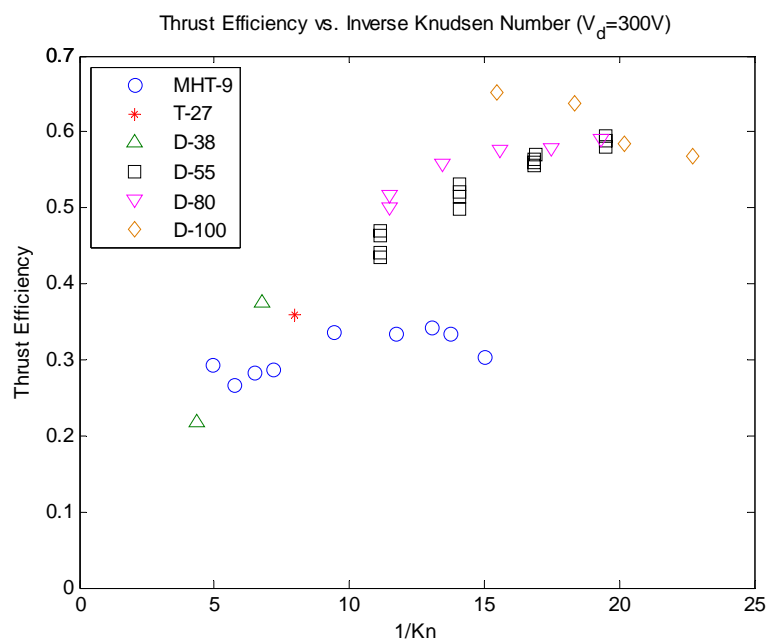
Figure 5.9   Thrust (anode) efficiency versus the inverse Knudsen number ($1/Kn$) at a discharge voltage of 300V, plotted for six different TAL thrusters with similar geometries.
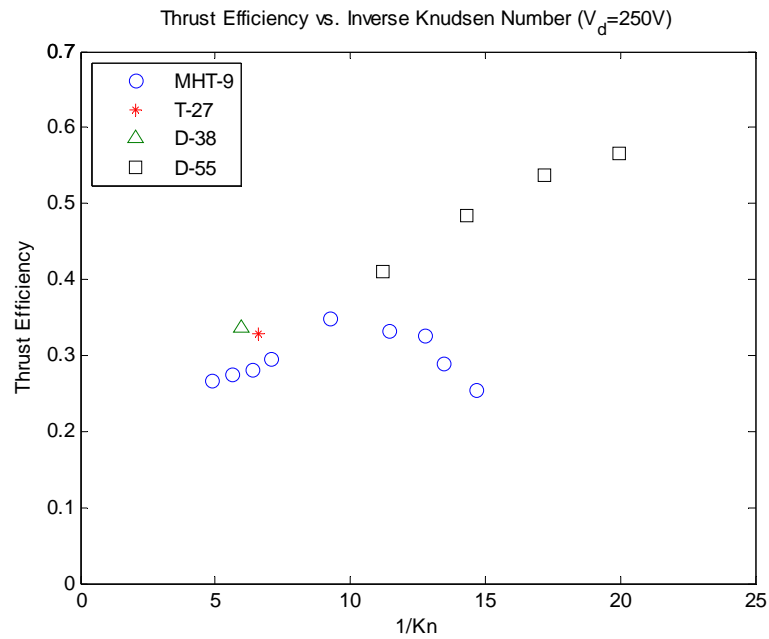
Figure 5.10 Thrust (anode) efficiency versus the inverse Knudsen number ($1/Kn$) at a discharge voltage of 250V, plotted for four different TAL thrusters with similar geometries.
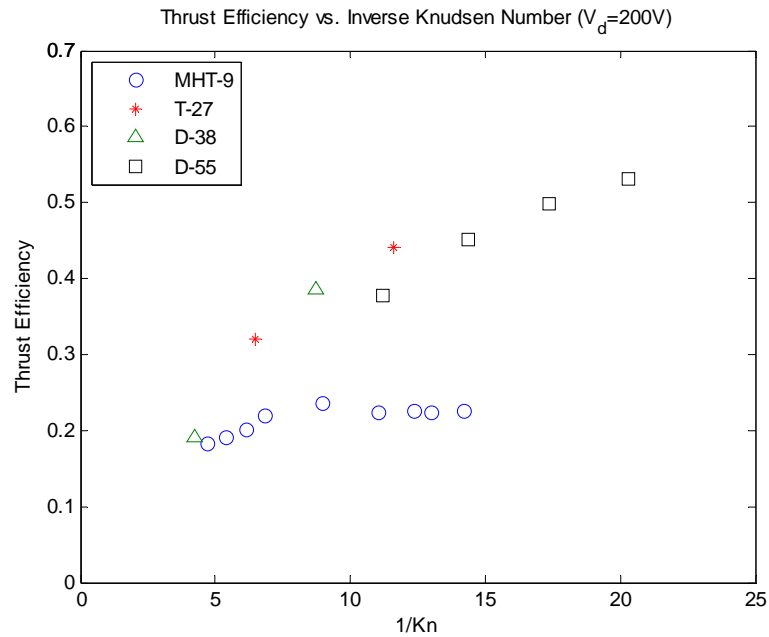
Figure 5.11 Thrust (anode) efficiency versus the inverse Knudsen number ($1/Kn$) at a discharge voltage of 200V, plotted for four different TAL thrusters with similar geometries.

Using the inverse Knudsen number allows the reader to look at the trends in a similar way as a flow rate trend, with wall temperature in the denominator acting to reduce the effective mass flow rate. Figures 5.9-5.11 show the results for discharge voltages in the range of 200-300V. Each plot is for a separate discharge voltage and shows anode thrust efficiency which excludes cathode mass flow, cathode power and magnet power. Data were available for all of the thrusters mentioned at 300V, but data were not available for the two largest thrusters at lower voltages. All three plots show that there is a correlation between the Knudsen number and the thrust efficiency. As the Knudsen number decreases (increasing inverse Knudsen number), the efficiency increases. The larger thrusters have lower Knudsen numbers which imply better ionization collisionality and this likely leads to higher thrust efficiencies through increased propellant utilization.

An interesting observation can be made about the MHT-9 data in all three plots presented. The highest flow rate data (or highest inverse Knudsen number) show a downturn in efficiency, moving the MHT-9 off the general trend amongst the different thrusters. One possible cause of this behavior is the heating of the permanent magnets. The other thrusters all use electromagnets that are tuned to give optimal thrust efficiency at each operational condition. However, the MHT-9 data shown are for one magnetic shunt condition (S=5.6mm) and the measured magnet temperature increased as the flow rate was increased. Because of the increased magnet temperature, the magnetic field strength decreased as flow rate increased whereas thrusters that utilize electromagnets typically increase the field with flow rate. By operating at a magnetic field strength that may have been less than optimal, this could have led to decreased efficiency in the MHT-9. This hypothesis is strengthened by the utilization estimates shown in Figure 4.31, that show decreases (or leveling off) in utilization at the highest flow rates.

The most important conclusion from these three plots is that the Knudsen number in the MHT-9 was consistently higher than that of the D-55. At the nominal operating point (V_d=300V, $\dot{m}_a$=0.74mg/s), the MHT-9 Knudsen number was almost 50% higher than that of the D-55. This appears to have been an important factor in the deficiency observed

between the ideal scaling predications and the actual MHT-9 performance. This was likely the result of a higher thruster wall temperature in the MHT-9, which may have been due to a difference in the cross sectional shape factor (ratio of channel length to width). The higher thruster temperature likely increased the neutral temperature and velocity, thus decreasing neutral density in the ionization layer. Because the cross sectional shape factor was not preserved in scaling, this may have led to an increased electron temperature in the MHT-9. The effects of channel geometry on electron temperature are discussed further in Section 5.4, but it is likely that the increased electron temperature in the MHT-9 was partly to blame for greater power losses due to ion-electron recombination at discharge chamber walls and the resulting increased thruster temperature as well.

5.3.4 Magnetic Confinement Parameter

The Knudsen number provided a method of comparison that accounted for the differences in flow rate, neutral temperature and scale for the various sized thrusters. The comparisons were made for a particular voltage in order to remove some of the variation in electron temperature that may come with various potential differences. However, the influence of the magnetic field is unaccounted for. The strength, and likely the shape as well, of the magnetic field is an important part of the ionization process. The magnetic equivalent of the Knudsen number would be the ratio of the Larmor radius to some characteristic thruster length,

$$\frac{R_L}{L} = \frac{m_e v_\perp}{eBL}. \tag{5.19}$$

If the electron population is sufficiently thermalized, then the perpendicular velocity can be substituted with the isotropic electron thermal velocity. As with the Knudsen number analysis, it is assumed that the characteristic length of the thruster is represented by the channel diameter. Thus, Equation 5.19 can be written as,

$$\frac{R_L}{L} = \frac{m_e \bar{c}_e}{eBD} = \frac{m_e}{eBD}\sqrt{\frac{8kT_e}{\pi m_e}}. \tag{5.20}$$

In order to make an estimate of this dimensionless magnetic confinement parameter, there must be some knowledge of the magnetic field strength and the electron temperature. Due to the competitive environment surrounding Hall thruster development, there are almost no data published that describe the magnetic field strengths and profiles of the various thrusters used in the comparisons made thus far. In order to make a magnetic comparison, a single magnetic field strength data point for the D-55 taken from one source, the same data point used for scaling, and was used in conjunction with magnet current data from a separate source [39-40]. A linear extrapolation of the field strength with current on the inner coil was used to make predictions of the field strength at other operating conditions. The inner coil current was selected instead of the outer coil current because there was more variation of the inner coil current during performance testing of the D-55, indicating it may have played a more important role in performance. Unfortunately, magnetic field data were not available on other thrusters.

The electron temperature was originally predicted to be constant with thruster scaling if the discharge voltage was kept constant (see Section 2.1.8). However, an analytical model has shown that this may not be correct if the geometric ratio of channel length to width is not preserved. This model is discussed in Section 5.4 and estimates of electron temperature are presented for the D-55 and the MHT-9. These results were used to make estimates of the R_L/L ratio.

5.3.5 Magnetic Confinement in the D-55

Figures 5.12-5.14 show the same plot of anode efficiency versus the R_L/L ratio for the D-55 with several different features highlighted. The data are organized into narrow ranges of Knudsen number that correspond to data taken at a particular flow rate. The initial hypothesis with this plot was that there would either be increased performance with decreasing R_L/L, indicating improved electron confinement, or there would be a value of the R_L/L ratio that showed a maximum in efficiency. This would be similar to the magnetic tuning of a Hall thruster where too little field strength does not confine electrons well

enough, and too much field strength results in excessive discharge current oscillations, which hurt performance. This initial hypothesis did turn out to have merit and the plot has proved to be full of interesting conclusions, but it requires some careful analysis.
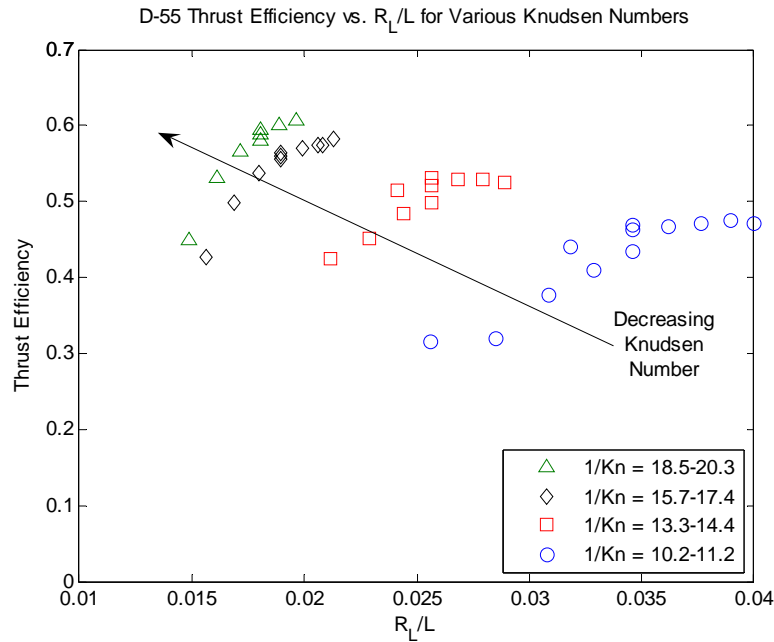
Figure 5.12   Thrust (anode) efficiency versus R_L/L for the D-55. Data are organized by Knudsen number. Thrust efficiency increases as the Knudsen number decreases (or $1/Kn$ increases).

Figure 5.12 shows that there are four distinct ranges of Knudsen number plotted for the D-55. As the Knudsen number decreases (increasing $1/Kn$), the efficiency of the thruster rises with each set of data. It also appears that R_L/L decreases with each decrease in the Knudsen number, indicating better electron confinement. This could be another possible cause of increased performance between lines of constant Knudsen number. The data for a particular Knudsen number range show increased performance with increasing R_L/L, which would signal worse confinement and contradict the previous conclusion. However, this might represent a magnetic tuning effect and could be the left hand side of a curve with a maximum at a particular value of R_L/L. A closer look at the magnetic field strength along each line can provide more insight.
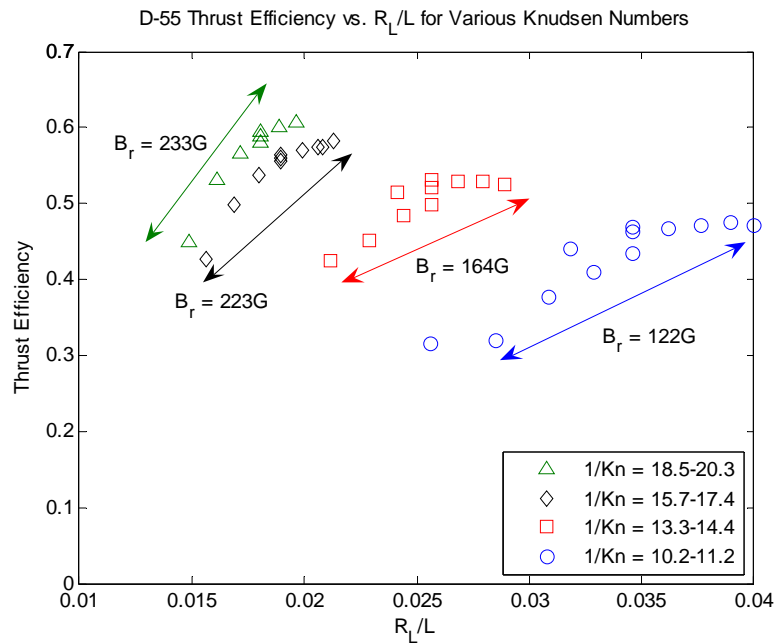
Figure 5.13 Thrust (anode) efficiency versus R_L/L for the D-55. Efficiency increases as B_r is increased, and the R_L/L ratio decreases. However, magnetic field changes are not responsible for efficiency increases within a particular $1/Kn$ range, since B_r is relatively constant.
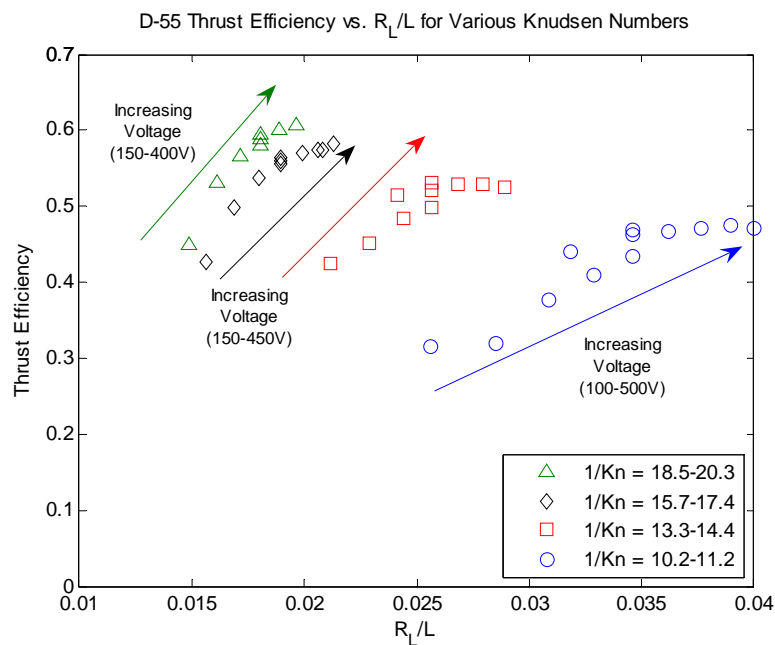
Figure 5.14 Thrust (anode) efficiency versus R_L/L for the D-55. Efficiency increases within a particular $1/Kn$ range are driven by T_e increases with discharge voltage.

Figure 5.13 shows that the radial magnetic field strength does not change along each line of relatively constant Knudsen number. The field strength was estimated using the simple extrapolation method described in Section 5.3.4, which relied on the magnet currents to determine the field strength from a known data point. It is likely that there were some minor temperature variations which changed the field strength at a particular coil current setting due to changes in core material permeability, but the changes were probably not significant. The relatively constant field strength along each Knudsen number line indicates that the R_L/L ratio was not varying because of changes in the magnetic field strength. The only adjustments in magnetic field occurred when the Knudsen number was changed as well, because magnet currents were increased with the flow rate. This indicates that the efficiency improvements between lines of different Knudsen number could have been due to either decreases in the Knudsen number or the R_L/L ratio (or both). The reason for performance changes along a line of constant Knudsen number still have not been explained, but a closer look a the discharge voltage may hold the answer.

Figure 5.14 indicates the range of voltages for the data points along each line of constant Knudsen number. The increases in voltage appear to be driving the increases in thrust efficiency along these lines. As will be shown in Section 5.4, the increases in discharge voltage are accompanied by increases in electron temperature. Increases in electron temperature increase the R_L/L ratio, but they also promote ionization through higher energy collisions between electrons and neutrals. Data taken with the MHT-9 and presented in Section 4.4, show that discharge voltage is an important factor in determining both propellant utilization and thrust efficiency. Higher voltages lead to higher utilization and thrust efficiencies. These data on the D-55 indicate that electron temperature is a very important factor in determining thrust efficiency. This is reflected in the dimensionless performance map because it influences both the R_L/L ratio and the Knudsen number (through changes in the ionization cross section).

5.3.6 Magnetic Confinement Comparison

After calculating the Knudsen number for each of the MHT-9 test conditions, only the Knudsen numbers for the four highest flow rates tested overlap with the D-55 data. These data are presented with the D-55 curves in Figure 5.15. The two data sets overlap within a $1/Kn$ range of roughly 10-15. Figure 5.15 shows that, similar to the D-55 data, the efficiency of the MHT-9 increases with discharge voltage. This increase in discharge voltage drives the electron temperature higher and moves the data to higher values of the R_L/L ratio. It was shown previously in Section 5.3.3 that the thrust efficiency of the MHT-9 increased with $1/Kn$, as the D-55 efficiency does, but only up until a point. At the highest values of $1/Kn$, the data show a leveling off or a decrease in performance. As mentioned previously, the magnetic field strength decreased as the $1/Kn$ increased in the MHT-9, due to heating of the permanent magnet. The D-55 has shown that increases in $1/Kn$ were accompanied by a strengthening of the magnetic field through increases in the coil currents, resulting in an improved thrust efficiency. This leads to the conclusion that the MHT-9 would benefit from a magnetic field that could be increased with flow rate ($1/Kn$).

Figure 5.16 shows the same plot but includes dashed lines to indicate that there does seem to be a good correlation between the two thrusters along the $1/Kn$ lines. The intent of this dimensionless analysis was to allow the relative size of the thrusters to be ignored, and the performance to be compared despite variations in several different, and sometimes uncontrollable, test variables. The agreement along the $1/Kn$ lines indicates that the comparison performed here is approaching that goal. The design of the MHT-9 was intended to match the performance of the D-55 line with a $1/Kn$ value of 15.7-17.4, indicated by diamond shaped markers. It can be seen that the MHT-9 data nearly met the goal set forth in magnetic confinement, as the R_L/L ratios are similar. The 300V point of the MHT-9 has a slightly higher R_L/L value than the D-55 due to its higher electron temperature. However, the major difference between these two lines is that Kn values are much lower for the D-55 (higher $1/Kn$), which led to better performance.
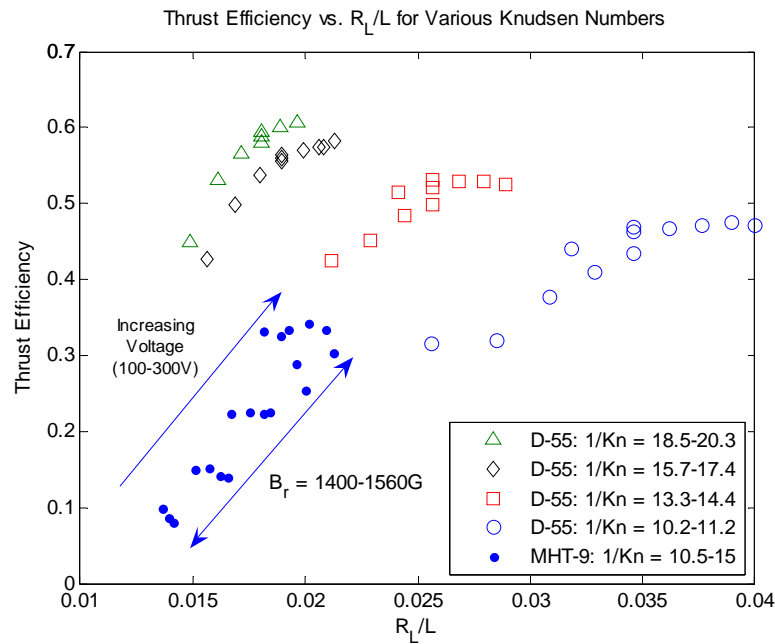
Figure 5.15   Thrust (anode) efficiency versus R_L/L for the D-55 and the MHT-9. The MHT-9 data show increasing efficiency with discharge voltage. The radial magnetic field strength spans 160G with the actual field strength depending on the magnet temperature.
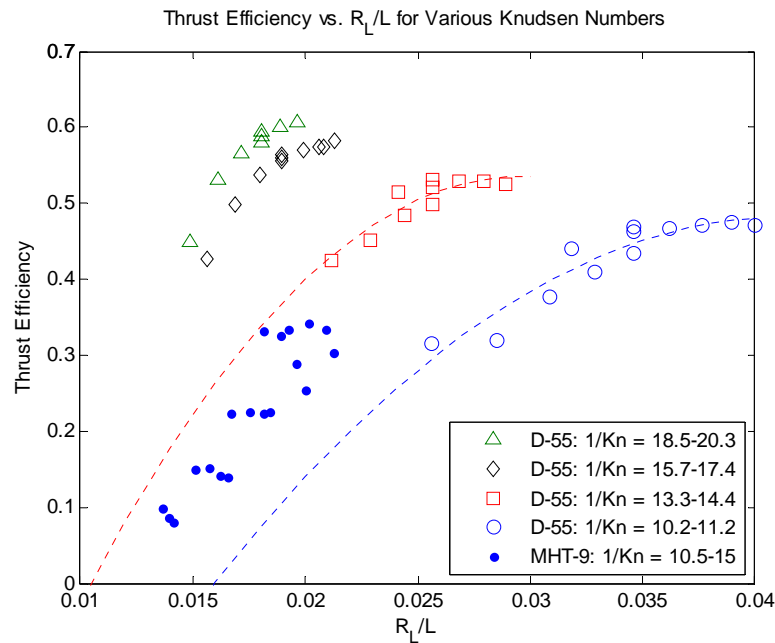
Figure 5.16   Thrust (anode) efficiency versus R_L/L for the D-55 and the MHT-9. The MHT-9 data overlap two sets of D-55 data in Knudsen number, and appear to fit amongst the trend lines.

5.4 Electron Temperature Modeling

The ideal scaling arguments made in Chapter 2 relied on the assumption that electron temperature would not change with thruster size so long as the discharge voltage was kept constant. During the dimensionless analysis and comparison of the MHT-9 to the D-55, it was decided to take a more careful look at this assumption. A simple model was created as an attempt to predict the electron temperature within the Hall thruster discharge and its variation with operating conditions as well as thruster geometry.
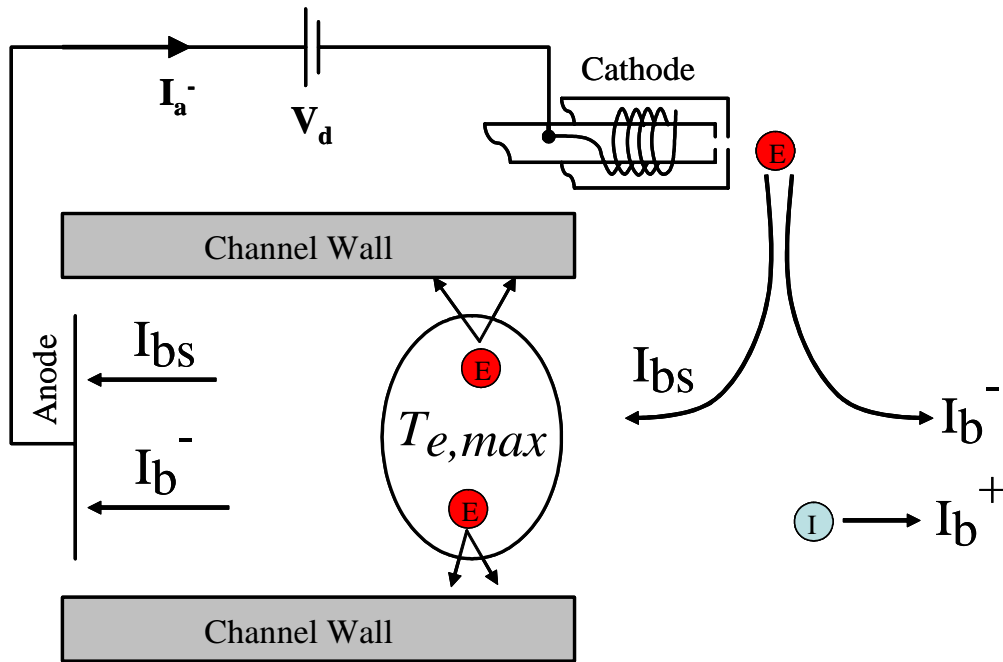
Figure 5.17   Drawing of the electron power balance used to estimate the peak electron temperature inside of a Hall thruster.

5.4.1 Model Formulation

The electron flow within the Hall thruster plasma is modeled using a power balance. This power balance is performed twice: once between the cathode and the anode, and once between the cathode and the point of maximum electron temperature. Figure 5.17 shows a simple diagram of the electron flow inside a Hall thruster. Electrons are emitted by the

cathode and used either for neutralization of the beam current or they backstream towards the anode to promote ionization. Near the point of maximum electron temperature, some electrons are lost to channel walls and recombine with arriving ions. The anode collects both the backstreaming current and the beam current of electrons produced by ionization.

The power balance is first conducted between the cathode and the anode. The total power in this electron flow is the product of the backstreaming current, I_{bs}, and the discharge voltage, V_d. This is the left hand side of Equation 5.21. The first term on the right hand side represents the thermal energy of the backstreaming electrons that arrive at the anode. The thermal energy they arrive with is calculated using the difference between the electron temperature near the anode, T_{ea}, and the temperature near the cathode, T_{ec}. The second term is the energy of the electrons produced through ionization that arrive at the anode with thermal energy and the energy spent in their creation, V_i. The final term on the right hand side is the energy lost due to recombination of electrons at the channel wall surfaces. The fraction of electrons lost is the same as that of ions attracted to the wall, and is determined by the ratio of wall area to exit area, A_w/A_e. These electrons carry the energy spent in their creation, thermal energy and enough kinetic energy to overcome the sheath potential near the wall. It is assumed that the electrons lost to the wall have a temperature near the maximum electron temperature, T_{em}.

$$I_{bs}V_d = I_{bs}\frac{5}{2}\frac{k(T_{ea}-T_{ec})}{e} + I_b\left(V_i + \frac{5}{2}\frac{kT_{ea}}{e}\right) + \frac{A_w}{A_e}I_b\left[V_i + \left(\phi_w + \frac{2kT_{em}}{e}\right)\right] \qquad (5.21)$$

The second power balance is conducted between the cathode and the point of maximum electron temperature. The structure of Equation 5.22 is the same as Equation 5.21 with some notable differences in each of the terms on the right hand side. In the first term, the thermal energy of the primary electrons is now the difference between the maximum electron temperature, T_{em}, and the cathode temperature, T_{ec}. The second term in the equation shows that the thermal energy of the electrons produced through ionization is T_{em} at this point in the channel, and the amount of electrons produced through ionization has been reduced by a factor of α. Ionization takes place both upstream and downstream of the

point where T_{em} occurs. The fraction of ionization that occurs downstream of the T_{em} location is represented by the factor α. The initial estimate of α was 0.5, but the factor was allowed to vary during the analysis to check this assumption. The final term on the right hand side of Equation 5.22 shows that the power lost through recombination has been adjusted by the factor α as well since recombination will take place to either side of the T_{em} point.

$$I_{bs}V_d = I_{bs}\frac{5}{2}\frac{k(T_{em}-T_{ec})}{e} + \alpha I_b\left(V_i + \frac{5}{2}\frac{kT_{em}}{e}\right) + \frac{A_w}{A_e}\alpha I_b\left[V_i + \left(\phi_w + \frac{2kT_{em}}{e}\right)\right] \quad (5.22)$$

These two simultaneous power balance equations can be reduced to a system of two equations with two unknowns. The electron temperature near the anode and the cathode must first be estimated. The cathode temperature was assumed to be 10eV and the temperature near the anode was assumed to be 5eV. These estimates are conservative considering previous probe measurements taken inside of a Hall thruster [55]. The actual temperatures are likely to be slightly lower at a discharge voltage of 300V. The area ratio, discharge voltage, ionization energy and α are inputs to the equations. Then by rearranging the equation, there are just two unknowns, the maximum electron temperature, T_{em}, and the ratio of backstreaming to beam current, I_{bs}/I_b. If the ratio of backstreaming to anode current is preferred, a substitution can be made by using,

$$I_b = I_a - I_{bs}. \quad (5.23)$$

The equations are then rearranged to solve for T_{em} and I_{bs}/I_a. The ionization energy, V_i, was set to be 3.2 times the actual first ionization potential of xenon because of the analysis presented in Section 3.4.1 regarding excitation. By using 38.7eV instead of 12.1eV, the energy spent in exciting neutral atoms before ionization occurs is accounted for.

5.4.2 Model Results

Figure 5.18 shows the solution for the maximum electron temperature versus the thruster area ratio for several different values of the beam current factor α. The estimated area ratio
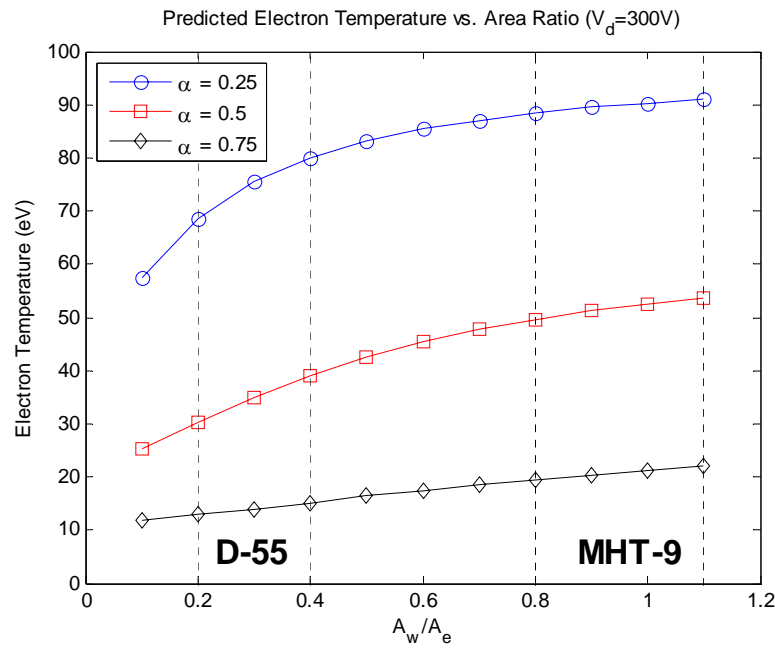
Figure 5.18 Plot of the predicted peak electron temperature versus the area ratio when operating at a discharge voltage of 300V. The factor α is a measure of the fraction of total beam current produced downstream of the peak electron temperature position. Estimated area ratio ranges for the D-55 and MHT-9 are indicated by dashed lines.
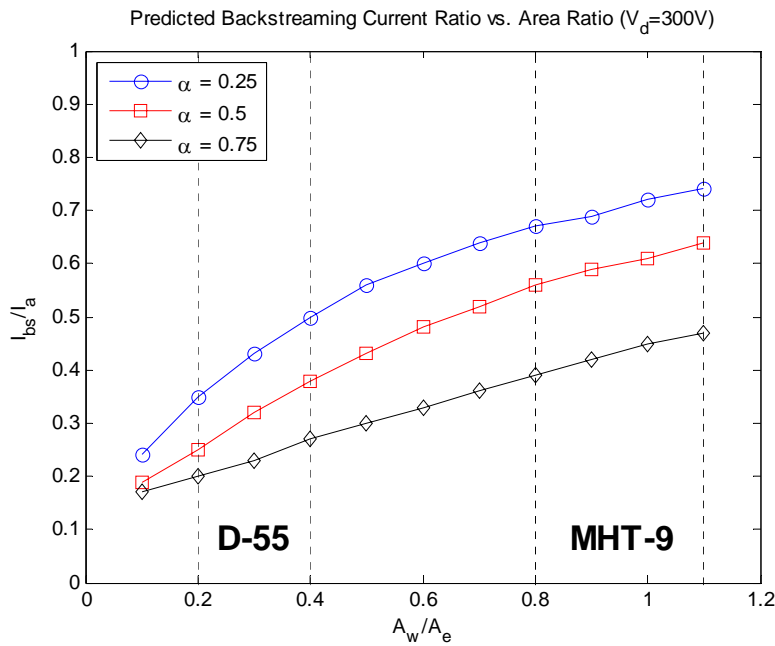
Figure 5.19 Plot of the predicted ratio of backstreaming to anode current versus the area ratio for different α values when operating at a discharge voltage of 300V. Estimated area ratio ranges for the D-55 and MHT-9 are indicated by bands of dashed lines.
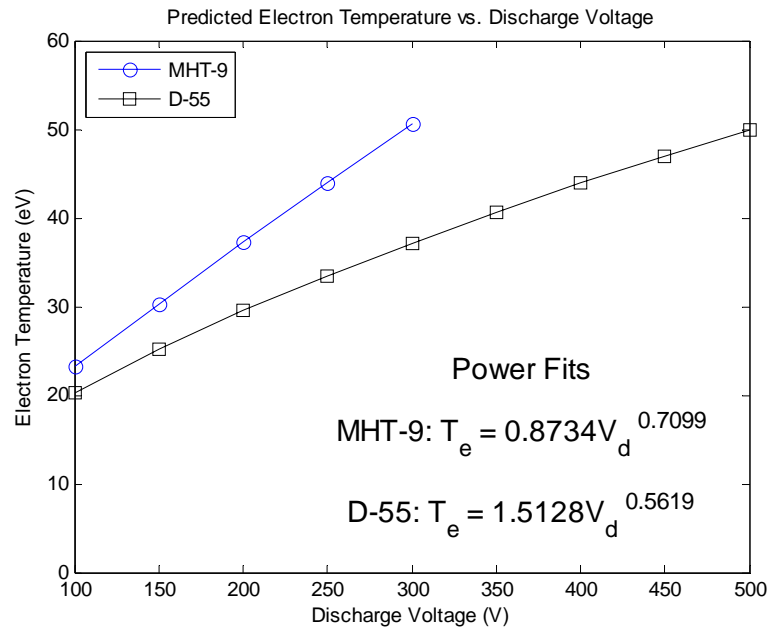
Figure 5.20 Plot of the predicted peak electron temperature versus discharge voltage for both the MHT-9 and the D-55. These results use area ratios of 0.86 and 0.35 for the MHT-9 and D-55, respectively (α=0.5).
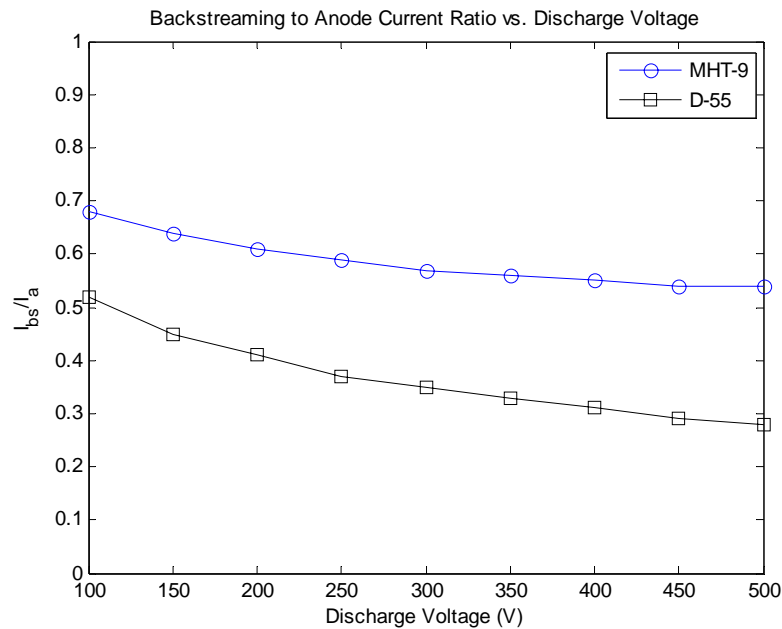
Figure 5.21 Plot of the predicted backstreaming to anode current ratio versus discharge voltage for both the MHT-9 and the D-55. These results use area ratios of 0.86 and 0.35 for the MHT-9 and D-55, respectively (α=0.5).

ranges for both the D-55 and the MHT-9 are indicated by bands of dashed lines. The exact geometry of the D-55 discharge chamber is unknown, and the amount of area on the tip of the center stem of the MHT-9 that experiences recombination is uncertain. The plot shows that the electron temperature is very sensitive to the α value, and increases monotonically with the area ratio but approaches a limit asymptotically. The α=0.5 line appears to be in the right range of electron temperatures. The D-55 shows a temperature of 30-39eV, which agrees well with temperature measurements made on a Busek built Hall thruster of a similar power level [55]. The BHT-1000 is a nominally 1kW thruster with a slightly larger diameter than the D-55, but a longer channel length as well, and therefore has a similar area ratio. Probe measurements indicated an electron temperature of 20eV at a discharge voltage of 300V in the BHT-1000, but because it is a ceramic walled thruster it is expected that this temperature would be lower than that of a metallic walled thruster. The increased secondary electron emission from the boron nitride ceramic cools the plasma and lowers the overall temperature.

The plot in Figure 5.18 also indicates that because geometric similarity to the D-55 was not perfectly maintained in scaling, the MHT-9 likely suffered from higher than intended wall losses. The channel length of the D-55 is not accurately known, and channel length was not seriously considered in the scaling method as applied to the design of the MHT-9. Additionally, the erosion observations of the MHT-9 indicated that the wetted area for wall losses likely included the front face of the center stem, and this must be to some extent also true for the D-55. This inadvertently lead to a higher effective wall area to exit area ratio, which appears to be an important factor for determining electron temperature and wall losses. This is because the higher electron temperature increases the strength of the wall sheath and therefore increases the ion flux to the wall. Spectroscopic measurements by Celik have confirmed that the electron temperature inside the MHT-9 was higher than temperatures observed in the D-55 [69].

The predicted backstreaming current ratio is shown in Figure 5.19. The ratio of I_{bs}/I_a is plotted versus the thruster area ratio for the same values of the factor α shown in

Figure 5.18. The graph shows that the relative amount of backstreaming current is significantly higher in the MHT-9 than in the D-55. This could be another possible source of thruster inefficiency. The backstreaming current ratio increases with the thruster area ratio, but declines as α is increased. In order to reduce the backstreaming current ratio in the MHT-9, it would be advantageous to reduce the wall area ratio and conduct an experimental cathode optimization process. The cathode flow rate and power were not adjusted during testing, but it is possible that the performance of the thruster could be improved by minimizing these operating parameters.

Figure 5.20 shows results of the electron temperature model for both the D-55 and the MHT-9 operating at various discharge voltages (for $\alpha=0.5$). These results used area ratios of 0.35 and 0.86 for the D-55 and the MHT-9, respectively. The predicted peak electron temperature inside the MHT-9 is higher due to its larger area ratio and higher backstreaming current ratio. The temperature inside both thrusters increases monotonically with discharge voltage. Power fits to both curves show that the peak electron temperature increases more slowly than discharge voltage. Again, this trend agrees well with measured electron temperatures within the BHT-1000 [55]. Figure 5.21 shows the corresponding backstreaming current ratio for the same thruster area ratios (and $\alpha=0.5$). The backstreaming current ratio is higher for the MHT-9 than the D-55, but it decreases in both thrusters with discharge voltage.

The electron temperature data from this model were used in the dimensionless performance mapping in Section 5.3. The electron temperature determined the ionization cross section in the Knudsen number, and was used directly in evaluating the magnetic confinement parameter, R_L/L. Further confirmation of the results of the electron temperature model are shown using a particle-in-cell computational simulation in Section 5.7.

5.4.3 Effect of Discharge Voltage on Electron Temperature

The general solution of the electron power balance can lend insight into the effect of discharge voltage on electron temperature, and help to explain why the relationship is not lin-

ear. It will be assumed that $\alpha=0.5$, which was shown to be a good estimate for the D-55, in order to simplify the form of the equation. If Equations 5.21-5.22 are solved simultaneously, the general power balance equation becomes,

$$3.1w\theta_m^2 + \left[(1+w)V_i + \left(\frac{1-3.1w}{2}\right)(V_d + \theta_c + \theta_a)\right]\theta_m - V_i\left(\frac{1+w}{2}\right)(V_d + \theta_c + \theta_a) - \theta_a(V_d + \theta_c) = 0, \quad (5.24)$$

where $w=A_w/A_e$ and $\theta=2.5kT/e$ (subscript indicates the location: anode, cathode, maximum). In order to assess the relative strength of each term and solve for the maximum electron temperature term, θ_m, assumptions must be made for the other temperatures. Assuming $\theta_a=12.5$, $\theta_c=25$, and $w\approx0.35$ in the case of the D-55, the electron power balance becomes approximately,

$$1.1\theta_m^2 + (1.4V_i - 0.04V_d - 1.6)\theta_m + 0.7V_dV_i + 12.5V_d + 337.8 = 0. \quad (5.25)$$

The first discharge voltage term is small and can be ignored for determining trends. Using an effective $V_i=38.7$ to account for the excitation of neutrals, the solution of this quadratic equation is,

$$\theta_m = \frac{-50.7 + \sqrt{50.7^2 + 4.3(38.8V_d + 337.8)}}{2.2}. \quad (5.26)$$

For discharge voltages of interest in a Hall thruster ($V_d>100$V), the discharge voltage term will dominate. Thus, it can be said that the model predicts a general relationship between electron temperature and discharge voltage that is not linear. For typical Hall thruster area ratios ($w\approx0.35$) this relationship is nearly square root,

$$T_m \propto \sqrt{V_d}. \quad (5.27)$$

The results in Figure 5.20 for the D-55 and the MHT-9 indicate that the exponent does depend on the thruster area ratio, with higher area ratios having a relationship closer to linear.

Further confirmation of the relationship in Equation 5.27 was made through experimental plume measurements by Azziz [81]. The ceramic walled, nominally 1500W, Busek built BHT-1500 Hall thruster was characterized at discharge voltages between 300-1000V. A simple model was used to relate the measured plume divergence angle, θ_d, to electron temperature and discharge voltage as,

$$\sin\theta_d \propto \sqrt{\frac{T_e}{V_d}}. \tag{5.28}$$

Plume divergence angles over the voltage range of 300-1000V indicated that the relationship between electron temperature and discharge voltage was approximately,

$$T_e \propto (V_d)^{0.567}. \tag{5.29}$$

Azziz estimates that the BHT-1500 has an effective area ratio of approximately 0.3, which is similar to that of the D-55. This result matches that of the D-55 shown in Figure 5.20 quite well. Although it is tempting to attribute the less than linear relationship between electron temperature and discharge voltage in the BHT-1500 to increased secondary electron emission at high discharge voltage, secondary electron emission was not included in the analytical model so it cannot be the only relevant effect. The consistency of these results may warrant further study beyond this work.

5.5 Effect of Electron Temperature on Ionization Rate

The higher electron temperature predicted in the MHT-9 compared to the D-55 will result in a different ionization cross section. Figure 5.22 shows a plot from the text by Mitchner and Kruger of the ionization cross section versus energy of an impacting electron for various noble gases [82]. The xenon cross section peaks at an electron energy of approximately 100eV, indicating that the higher electron temperature inside the MHT-9 would be better for ionization.
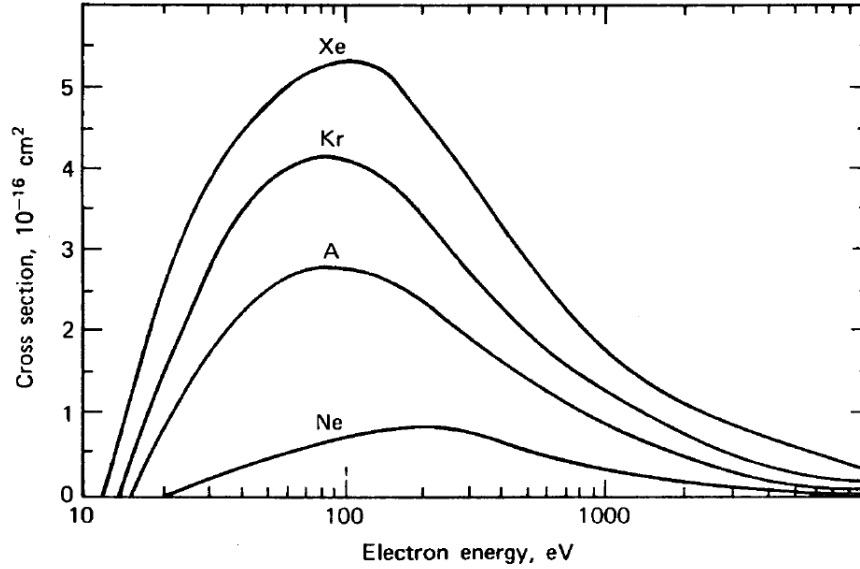
Figure 5.22 Plot of the total ionization cross section for the noble gases by electron impact. This plot is from the text by Mitchner and Kruger [82]. The ionization cross section for xenon peaks at approximately 100eV.

Although the cross section gives a good indication of the probability for ionization, a clearer way to look at the relationship between ion production and electron energy is directly through the ionization rate. The volumetric ionization rate, R_i, is simply the product of the electron thermal velocity and the ionization cross section, averaged over the distribution function,

$$R_i = \overline{c_e \sigma_i}. \tag{5.30}$$

The average of this rate over a Maxwellian electron distribution is written as,

$$R_i = \frac{1}{n_e} \int_{c_i}^{\infty} f_n c_e \sigma_i 4\pi c_e^2 dc_e, \tag{5.31}$$

where the limits of integration are from the minimum electron thermal velocity required for ionization, c_i, to infinity. The Maxwellian distribution is defined as,

$$f_n = n_e \left(\frac{m_e}{2\pi kT_e}\right)^{\frac{3}{2}} e^{-\frac{m_e c_e^2}{2kT_e}}. \tag{5.32}$$

A change of variables from electron thermal velocity to energy can be used to help compare the ionization rate directly to the cross section, and to facilitate the numerical integration. The change of variables is performed using the definition of electron thermal velocity in Equation 2.32. The ionization rate integral can thus be rewritten as,

$$R_i = \frac{8\pi}{(2\pi kT_e)^{3/2} m_e^{1/2}} \int_{E_i}^{\infty} E_e \sigma_i e^{-\frac{E_e}{kT_e}} dE_e, \tag{5.33}$$

where it is important to note that the ionization cross section, σ_i, is a function of the electron energy as well. In order to numerically compute this integral, a fit of the Xe cross section must be performed using Figure 5.22. The integral can then be computed for various values of the electron temperature to obtain the results plotted in Figure 5.23. This graph shows that the ionization rate peaks at a higher electron temperature than the cross section, indicating that utilization efficiency should increase with electron temperature up to approximately 300eV. Despite the ion loss and beam divergence penalties associated with high electron temperature, it is likely that the ionization rate in the MHT-9 is higher than the rate in the D-55. This may offset some of the inefficiencies due to other factors such as poor magnetic field topology or high Knudsen number.

The ionization rate results were used to calculate the effective cross section for ionization as a function of electron temperature, which was used in the calculations of Knudsen number in Section 5.3. This effective cross section is defined as,

$$\sigma_i = \frac{\overline{c_e \sigma_i}}{\overline{c_e}}. \tag{5.34}$$

The electron temperature used in this calculation was taken from results of the analytical model described in Section 5.4.
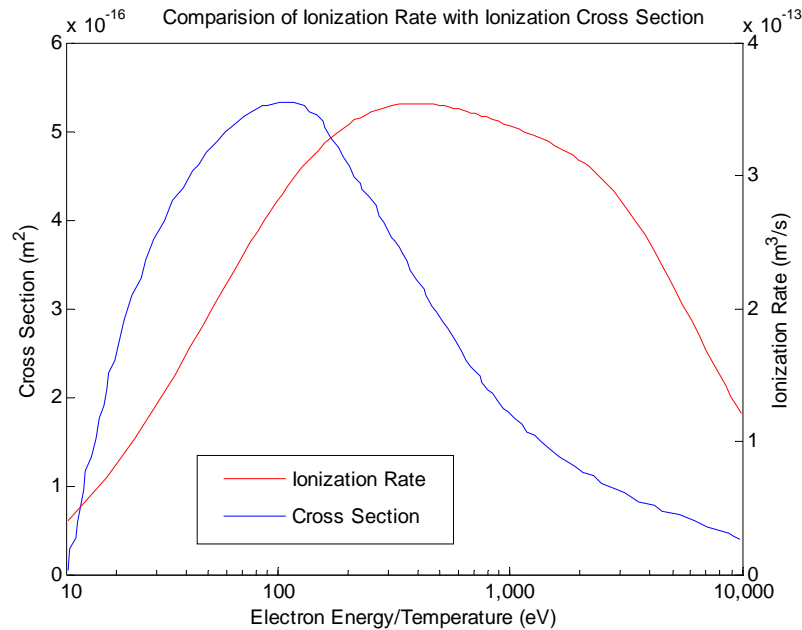
Figure 5.23 Comparison of the ionization cross section versus electron energy and the ionization rate versus electron temperature. This plot shows that the ionization rate peaks at a higher temperature than the energy for peak ionization cross section.

5.6 The Miniaturization Penalty

Given the many factors that have proven to be important in determining the performance of a Hall thruster at a particular size, it seems difficult to make a broad sweeping assessment of the penalty for miniaturization. However, an attempt at such a generalization is still warranted given that the motivation of this research was to understand the effects of miniaturization on thruster performance. It is recognized that at best this method yields a rough estimate of the ability to maintain efficiency at small scale.

An estimate of the miniaturization penalty can be made using the Knudsen number analysis summarized by Figure 5.9. A curve can be fit to these data that relates thrust efficiency to the inverse Knudsen number, D/Λ_{ie}. The trend shown in Figure 5.9 is clear but there are a few data points that appear to be outliers. These points may be for off-design operating conditions or where scaling relationships were not properly maintained. If these few

points are removed, the remaining data make for a more consistent curve fit. The data used and the resulting fit of a power law are shown in Figure 5.24.

An ideally scaled thruster would maintain both the Knudsen number and the magnetic confinement ratio. However, it has been shown that alterations of the cross sectional shape factor and poor magnetic field topology can lead to an increased Knudsen number and reduced performance at small scale. A general assessment of the challenges in building a thruster at small size can be made using the empirical data gathered in Figure 5.24. If it is assumed for a moment that a scaled down thruster were built and operated such that the electron axial mean free path for ionization, Λ_{ie}, was held constant, then the performance penalty would be due purely to the change in scale of the thruster. The power fit of the Knudsen number data can then be used to make a plot of the variation of performance with scale. The ratio of the thrust efficiencies for two thrusters of different size can be written as (primes denote properties of the scaled down thruster),

$$\frac{\eta_t}{\eta_t{'}} = \frac{0.0991\left(\dfrac{D}{\Lambda_{ie}}\right)^{0.6189}}{0.0991\left(\dfrac{D'}{\Lambda_{ie}{'}}\right)^{0.6189}}.$$

(5.35)

This equation can be solved for the change in efficiency due purely to scaling down assuming that $\Lambda_{ie} \approx \Lambda_{ie}{'}$. Rearranging the above equation, the result is,

$$\eta_t{'} = \eta_t\left(\frac{D'}{D}\right)^{0.6189}.$$

(5.36)

This equation represents what ought to be regarded as a minimum performance from the perspective of collisional ionization since it is not typically the case that $\Lambda_{ie} \approx \Lambda_{ie}{'}$. If the design of the magnetics in a scaled down thruster have successfully held the ratio of R_L/L constant, but the axial electron mean free path for ionization was not scaled with the size of the thruster, the performance will be predicted by Equation 5.36. It is the goal of the
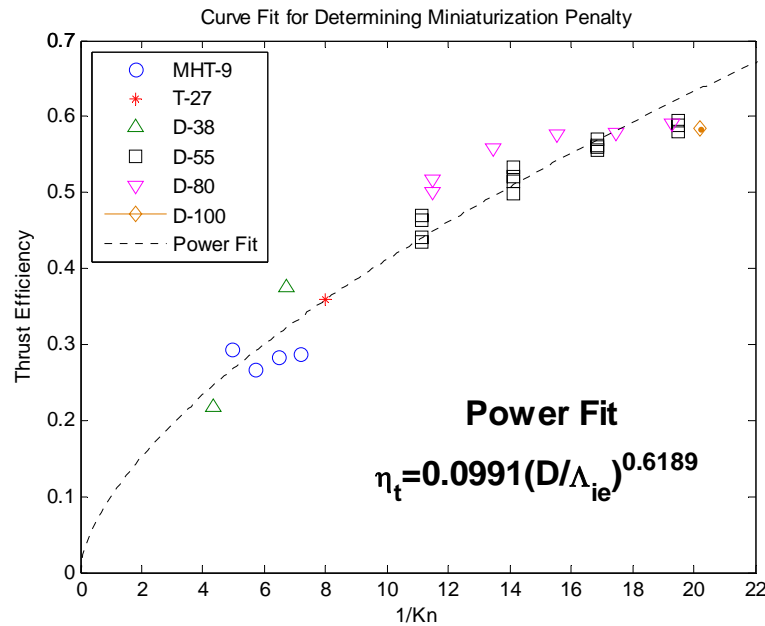
Figure 5.24 Power law fit of thruster data used to determine the general empirical penalty associated with miniaturization. This fit uses the same data shown in Figure 5.9, but a few outlying points have been eliminated to improve the fit quality.
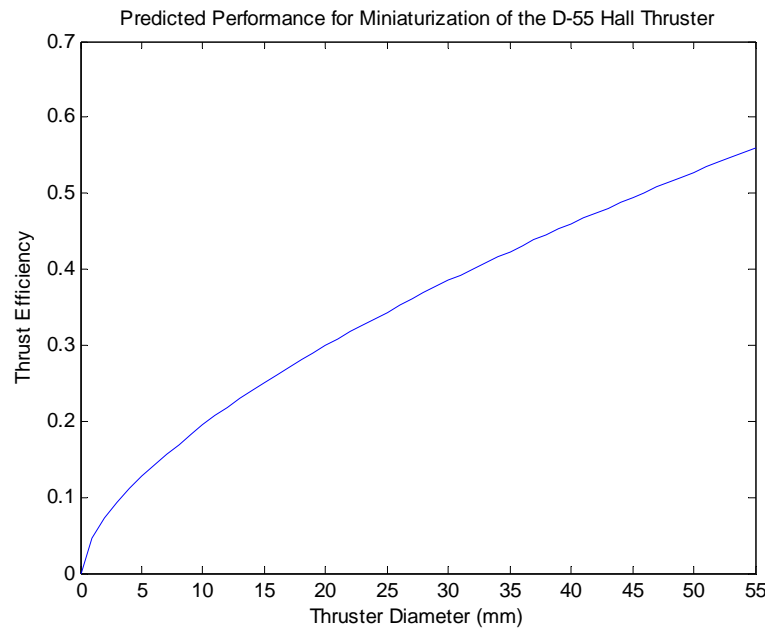
Figure 5.25 This plot shows the predicted thrust (anode) efficiency of a scaled down version of the D-55 Hall thruster. The analysis used in producing this plot assumes that both Λ_{ie} and R_L/L are constant with scaling.

designer to improve the thruster performance beyond this minimum by attempting to scale the mean free path with the characteristic length of the thruster, as well as preserving the channel length to width shape factor and the magnetic field topology. Figure 5.25 shows a plot of Equation 5.36 for the particular case of scaling down the D-55 thruster (D=55mm, η_t=0.56). The plot shows that the predicted thrust efficiency of the MHT-9 at a diameter of 9mm, is 18%. This is a 38% penalty from the efficiency of the D-55. However, the attempts to maintain the Knudsen number in the MHT-9 by scaling the mean free path helped, as the MHT-9 was able to perform better than this model predicts (MHT-9 maximum η_t=34%), despite imperfect scaling of the cross sectional shape factor and poor magnetic field topology.

5.7 Computational Modeling

A particle-in-cell (PIC) model originally developed at MIT by Szabo, and further refined at Busek, was adapted to the MHT-9 geometry to provide insight into the physics of the discharge and the performance trends [26]. The simulation determines plasma properties such as density, potential and temperature. Variations in the electron temperature profile with discharge voltage were compared to the analytical model presented in Section 5.4 and conclusions from the dimensionless performance analysis were tested. A simulated test matrix was executed where variations in the Knudsen number were made by adjusting the propellant flow rate, and the R_L/L ratio was changed by varying the magnetic field strength. A description of the simulation and the results are presented below.

5.7.1 Description of the Code

The plasma simulation developed by Szabo utilizes the particle-in-cell methodology for tracking and moving electrons, ions and neutrals. The Monte Carlo collision method is used to calculate particle interactions of various types including ionization, excitation, charge exchange, scattering and bulk recombination. Coulomb collisions were not used in this work but can be implemented in the simulation. The simulation is two dimensional and axisymmetric in space, and covers three dimensions in velocity. The charge distribu-

tion and boundary conditions are used to calculate the electric field with Gauss' Law. There is an anomalous diffusion mechanism that is imposed numerically on electrons in addition to the naturally occurring effects captured by classical diffusion and wall effects. In order to decrease convergence time of the simulation, several numerical techniques are employed. An artificial ion to electron mass ratio is used, as well as an artificial vacuum permittivity. Physically sensible results are produced by inverting these transformations. The simulation has been described in detail in several useful references [26, 83-84].

5.7.2 Simulation Setup

The MHT-9 simulation geometry is shown in Figure 5.26. The computational grid is non-orthogonal and conforms to the geometry of the thruster. The anode and center stem are embedded within the grid, and neutrals are injected at the left hand side of the simulation within the anode annulus. The anode and wall materials of the thruster are metallic, and are simulated to have zero secondary electron emission. The walls are held at a potential of 0V because they were grounded during the experimental testing, while the anode is at the discharge potential. The free space boundaries float at their calculated potentials, and electrons are injected along the right hand boundary. The simulation injects electrons into a cell at the right hand boundary whenever there are more ions than electrons within the cell, unless the calculated potential within the cell falls below the cathode potential (0V for the MHT-9). In the case of a temporarily negative potential within the boundary cell, electrons are not injected until the potential rises above the cathode potential again.

The code allows the user to specify the neutral injection temperature as well as the temperature of surfaces that neutrals interact with. The magnetic field must be supplied to the simulation on a regular grid that is then interpolated to the simulation coordinates. The anomalous electron diffusion is created in the simulation through an anomalous collision frequency, ν_a, that is applied to the electron velocity perpendicular to the magnetic field in addition to the collision frequency due to classical diffusion, ν_c. The sum of these two collision frequencies,
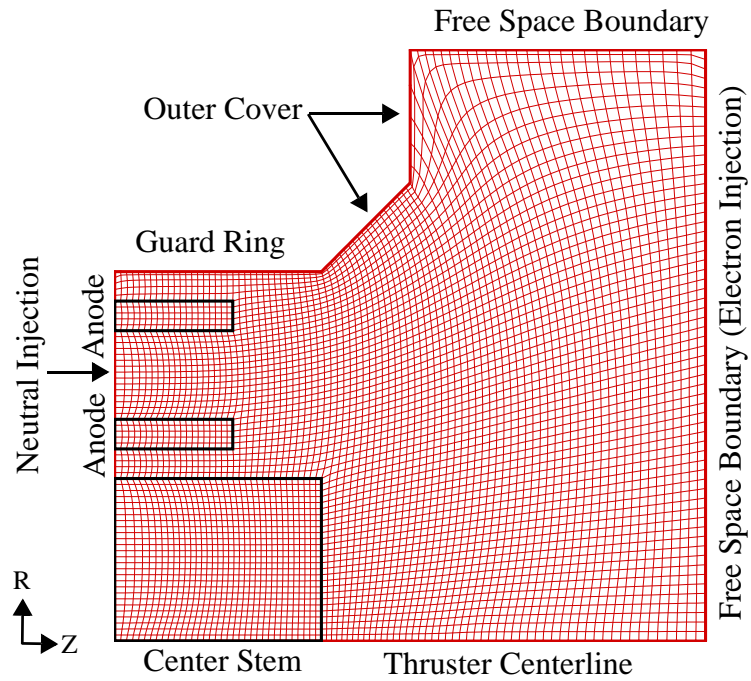
Figure 5.26 Simulation grid and geometry of the MHT-9. The anode and center stem are embedded within the grid (indicated by black lines). The grid extends 1cm in both the radial and axial directions.
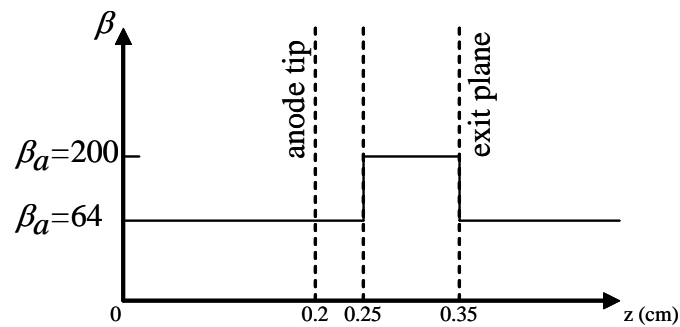
Figure 5.27 Diagram of the anomalous Hall parameter layer. The axial coordinates are in the simulation units.

$$\nu_s = \nu_c + \nu_a, \tag{5.37}$$

make up the total electron scattering frequency, ν_s, where the anomalous frequency is set by the user through an anomalous Hall parameter, β_a, such that,

$$\nu_a = \frac{\omega_c}{\beta_a} . \tag{5.38}$$

The anomalous Hall parameter is specified in the simulation through an axial layer system where different values of the parameter can be specified upstream, downstream and inside the layer. The axial location of the layer boundaries can be specified as well. The MHT-9 simulations used anomalous Hall parameters of 64 in the upstream and downstream regions and 200 inside the layer, meaning that nearly classical diffusion is used inside the layer. Figure 5.27 shows a diagram of the layer location relative to the anode tip and the exit plane, in the simulation coordinates. Anomalous diffusion continues to be an important area of ongoing research in Hall thruster modeling [85-87].

The simulation is started with a flow consisting of only neutrals injected between the anode pieces. After neutrals have been allowed to fill the channel, the simulation is seeded with an initial density of ions and electrons. The simulation is then allowed to run until it converges to a steady state, indicated by either a steady or regularly repeating anode current and plasma density. The results can then be averaged over a discharge oscillation to compute performance and particle moments.

5.7.3 Nominal Performance

The simulation seems to under predict the nominal MHT-9 anode current, but the thrust and specific impulse values are in good agreement. The most important performance results for the dimensionless analysis are the efficiency numbers. It is likely that with more adjustment of the anomalous Hall parameter, better agreement for the discharge current could be achieved, and this could bring the efficiency numbers in closer agreement as well. However, it is the trends in thrust efficiency that are most important in verifying the

conclusions of the dimensionless performance analysis. Table 5.4 compares the thruster performance determined by the code to experimental results at the nominal operating condition (V_d=300V, $\dot{m}_a$=0.74mg/s).

TABLE 5.4   Comparison of Nominal Performance Between PIC and Experiment

Performance Metric	Simulation	Experiment
I_a (A)	0.63	0.94-1.38
T (mN)	11.0	11.3-14.4
I_{sp} (s)	1521	1567-1989
η_t	0.44	0.30-0.34
η_u	0.83	0.73-0.93

5.7.4 Plasma Moments

Figures 5.28-5.31 show plots of the important plasma moments as predicted by the PIC simulation for the nominal flow rate and voltage of the MHT-9 (V_d=300V, $\dot{m}_a$=0.74mg/s). The magnetic field used in this simulation was for the 5.6mm shunt length and a magnet temperature of 250°C. The results show that the electric potential decreases rapidly between the anode tip and the exit plane of the thruster. The contours of potential also show that ions may likely impact the guard rings near the exit plane because of the field line curvature towards the corners of the thruster. The plot of electron temperature shows two lobes of high temperature right in front of each anode fork. The plasma density profile shows that the bulk of the ions and electrons are located just inside the anode annulus, but the ionization profile shows that the ions are created right outside the anode. The location of the ionization layer could mean that electrons produced through ionization are quickly lost to the anode.
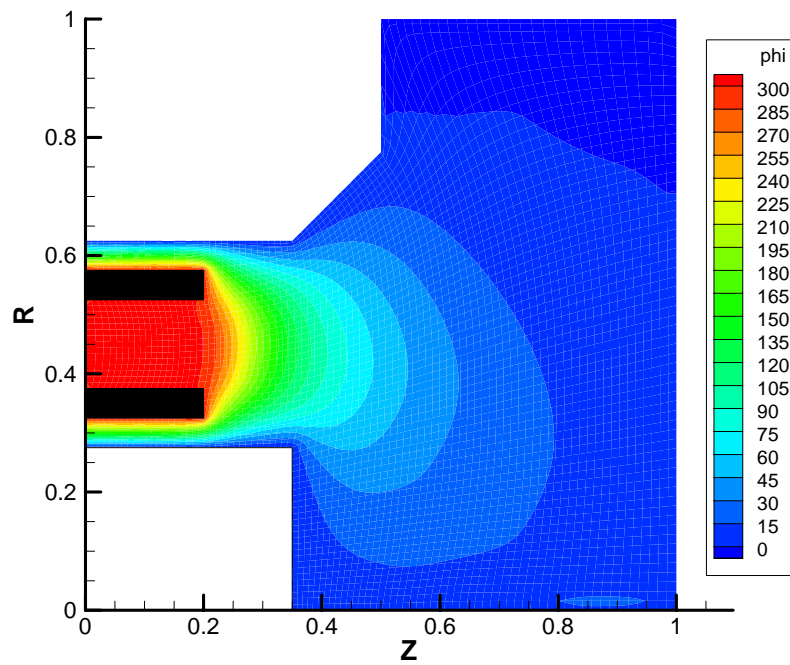
Figure 5.28   Plot of the electric potential in volts. (V_d=300V, $\dot{m}_a$=0.74mg/s)
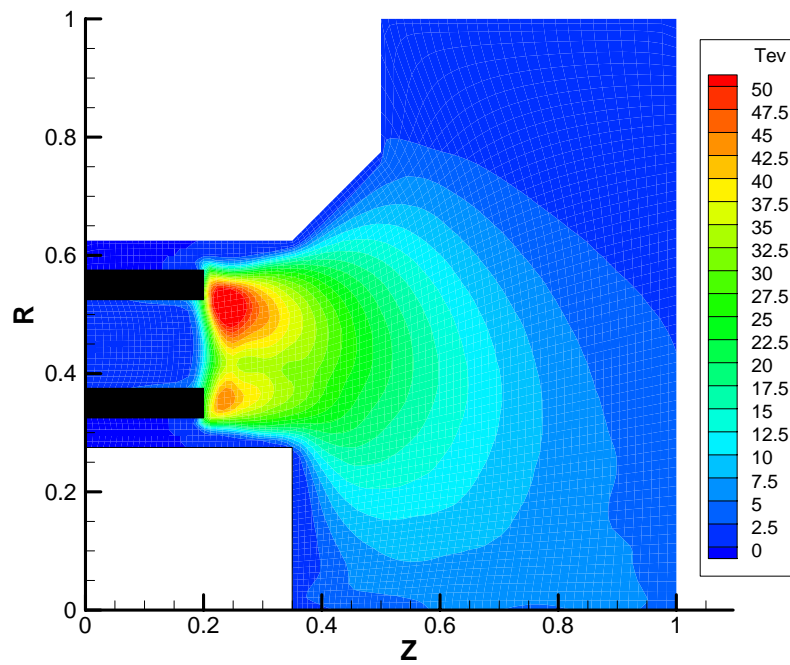
Figure 5.29   Plot of the electron temperature in electron-volts. (V_d=300V, $\dot{m}_a$=0.74mg/s)
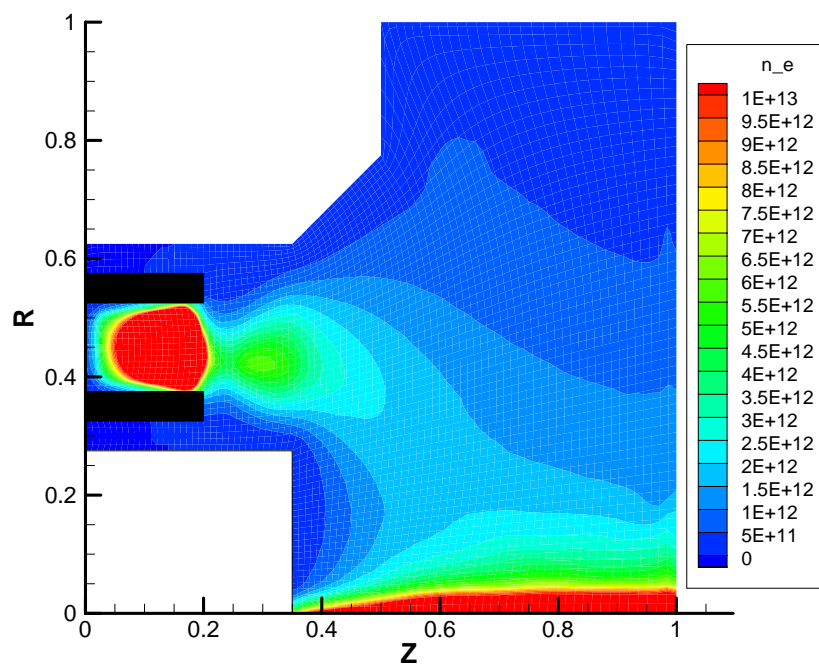
Figure 5.30   Plot of the plasma number density in cm^{-3}. (V_d=300V, $\dot{m}_a$=0.74mg/s)
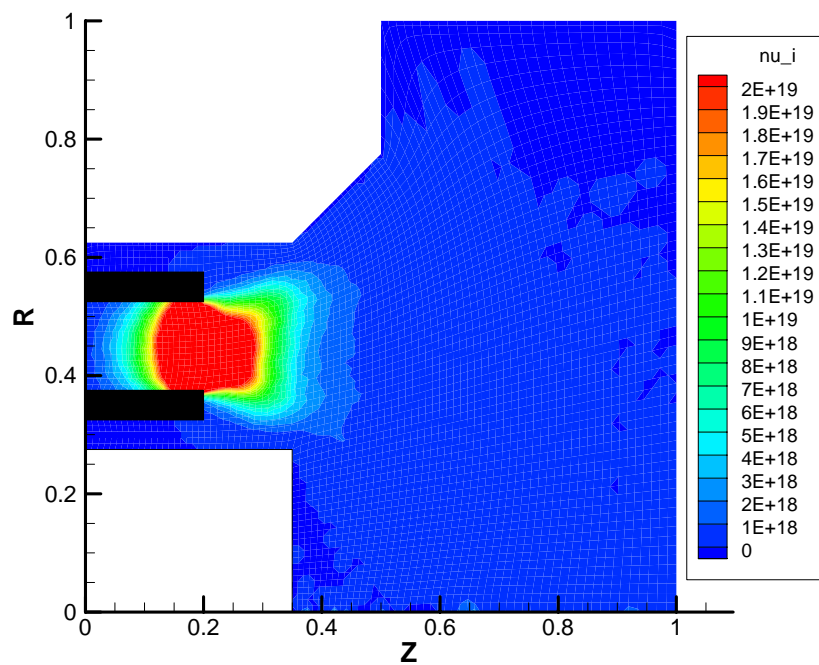
Figure 5.31   Plot of the ionization rate number density in cm^{-3}s^{-1}. (V_d=300V, $\dot{m}_a$=0.74mg/s)

5.7.5 Electron Temperature Comparison

The simulation was run at several voltages between 150-300V to determine the maximum electron temperature in the discharge. These results were then compared to the electron temperature model described in Section 5.4. Figure 5.32 shows plots of the electron temperature inside the MHT-9 operating at voltages between 150-250V, and the 300V case is shown in Figure 5.29. The simulation results were averaged along a radial line at the axial location of peak temperature. Table 5.5 shows that a comparison of the analytical model and the simulation yields good agreement at 300V, but the results do not match as well at lower discharge voltages.

TABLE 5.5   Comparison of Maximum Electron Temperature Results

Discharge Voltage (V)	Analytical Model T_e (eV)	Simulation T_e (eV)
150	30.3	16.8
200	37.2	26.6
250	44.0	36.2
300	50.6	45.6

5.7.6 Performance Trends

The dimensionless performance analysis described in Section 5.3 showed that the Knudsen number and the magnetic confinement ratio were good predictors of thrust efficiency. The analysis also indicated that the Knudsen number in the MHT-9 was 50% higher than anticipated because of neutral heating from the high temperature thruster walls. The confinement ratio was only slightly higher than the design intended, but data from the D-55 suggest that a lower value with increased magnetic field strength may increase performance. These trends were explored by running a simulated test matrix with the PIC code.

The simulation was used to test parameter variations that could not be easily reproduced in the laboratory. For example, the data shown in Figure 5.16 are for lines of nearly constant Knudsen number and magnetic field. The variation in R_L/L for a particular Knudsen number in the D-55 data is due only to changes in electron temperature through adjustments in
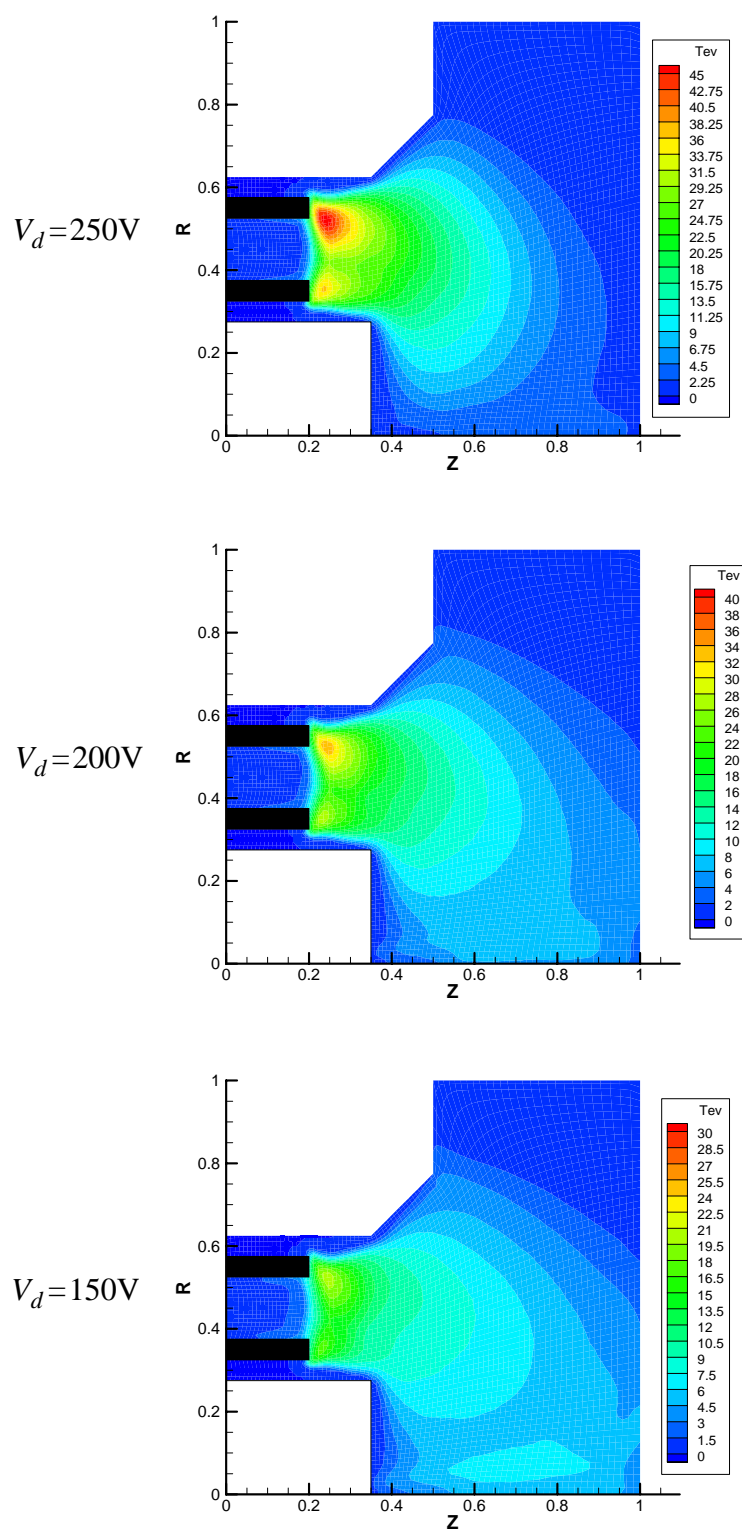
Figure 5.32   Plot of the electron temperature in eV for various discharge voltages. ($\dot{m}_a$ =0.74mg/s)

the discharge voltage. The MHT-9 data show variations in R_L/L along a Knudsen number line due to both magnetic field variations and electron temperature changes. However, the simulation has the advantage of being able to control most of the variables independently.

Figure 5.33 shows three lines of constant Knudsen number where the mass flow rate and wall temperature were held constant along each line. The wall (and neutral) temperature used in the simulation was 1000°C for all three lines, but the flow rate was varied between data sets from 0.43-0.74mg/s. Variations of R_L/L were accomplished by holding the voltage (and presumably the electron temperature as well) constant while varying only the magnetic field. The strength of the field was both increased and decreased by a factor of two from the nominal value in the MHT-9, which is much more variation than is achievable using the shunt system. The ionization cross section was assumed to be constant since voltage was not varied.

Several important conclusions from the dimensionless performance map are confirmed. First, as the Knudsen number is reduced the thrust efficiency increases, confirming the conclusion of the dimensionless performance analysis. Second, as R_L/L is reduced the efficiency increases, but there is an optimal value. If the field is increased too much, the performance declines again. This likely signals the point where oscillations begin to dominate the discharge. It is also interesting to note that at higher flow rates (higher $1/Kn$), the thruster seems to optimize performance at a lower value of R_L/L, indicating a higher magnetic field. This fits with the D-55 data shown in Figure 5.13 which show that the thruster performance is optimized by increasing the magnetic field strength with flow rate. Finally, increasing the magnetic field beyond the value observed at nominal operating conditions (R_L/L=0.019) shows increased efficiency for the nominal flow rate condition ($1/Kn$=11.7), indicating that the MHT-9 performance could be improved with a stronger magnetic field even if the Knudsen number cannot be practically reduced.
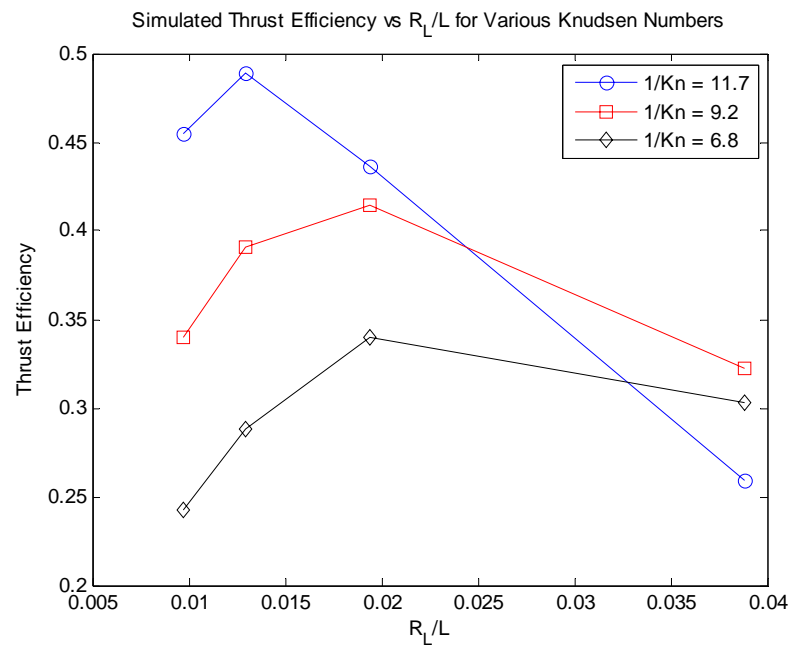
Figure 5.33 Simulated dimensionless performance map using magnetic field and flow rate variation only. All points use a discharge voltage of 300V and a wall/neutral temperature of 1000°C. The electron temperature was estimated analytically.

Chapter 6

CONCLUSIONS AND RECOMMENDATIONS

The objective of this research was to explore the possibility of miniaturizing a Hall thruster as a propulsion option for small satellite applications. Significant advancements were made through both theory and experiments that have helped to explain the critical challenges of building a small scale Hall thruster, as well as the fundamental limitations that govern performance and limit the effectiveness of miniaturization. This chapter summarizes the contributions of this research and presents recommendations for future work.

6.1 Summary of Results and Contributions

6.1.1 Hall Thruster Scaling Theory

The ideal scaling theory originally developed by Khayms and Martínez-Sánchez was extended and refined to be more specific to the Hall thruster geometry and discharge physics. Considerable progress was made in verifying the main principles of the ideal scaling theory, and identifying the key points that determine applicability. It was shown that in order to preserve the relevant plasma processes, the thruster power and flow rate should be scaled with the diameter. It was also shown that although the shape of the azimuthal channel cross section (specifically the ratio of channel width to length) must be preserved, the channel width and length can be scaled differently than the channel perimeter (or diameter for an axisymmetric configuration). Thus, once a target power level and perimeter are selected for scaling, the channel width and length become free parameters that can be

potentially optimized to reduce thruster erosion and improve lifetime, so long as the azimuthal shape is preserved. The optimal magnetic field was derived and shown to scale inversely with the channel length and width, meaning that the design of the magnetic circuit will also be a part of any cross sectional optimization process.

A version of the scaling theory that ignores the importance of channel length was used to determine the dimensions of a 200W device based on the TsNIIMASH D-55 anode layer Hall thruster as a baseline design. Channel width, diameter and flow rate were scaled together and inversely with the magnetic field strength. The resulting dimensions were used as the starting point for the design of a 9mm midchannel diameter miniaturized Hall thruster (MHT-9).

6.1.2 Development of a Miniature Hall Thruster

A nine millimeter diameter Hall thruster with a nominal power of 200W was developed using a detailed design process. Finite element magnetostatic modeling was utilized to design a magnetic circuit using a permanent magnet. The performance of the design was evaluated at various magnet temperatures to understand the effects of thruster heating on the magnetic field. A magnetic shunt system was designed and implemented to allow for coarse tuning of the field strength between different test runs of the thruster. The miniature anode was designed and built with a choked plenum and baffle system to ensure azimuthal uniformity of the propellant flow. Alignment of the anode with the thruster channel was accomplished through the use of a specially formed ceramic insulator and a plastic jig used during assembly. Steady-state thermal modeling was conducted using finite element techniques to predict the operating temperature of the thruster, and most importantly of the magnetic circuit. A detailed analysis was performed to estimate the heat transferred from the plasma to the thruster surfaces, and these estimates were used as inputs to the finite element thermal model.

The MHT-9 performance was tested over a wide range of input power, discharge voltage and flow rate. The peak measured thrust efficiency and specific impulse exceeded 34%

and 2000s, respectively. At the nominal design point of 0.74mg/s and 300V, the thruster operated at a thrust efficiency of 30% and a specific impulse of 1700s. The thrust efficiency was significantly lower than the baseline thruster, but much higher than previous subcentimeter Hall thrusters built at MIT and elsewhere.

Estimates of the gross guard ring erosion were made after two separate performance tests. The minimum thruster lifetime was estimated to be 20-50hrs if graphite guard rings were used. Further lifetime improvements could likely be achieved through small geometry changes that would not seriously affect performance, and could even improve efficiency.

Several important contributions were made during the experimental portion of this research. A simple to follow design process was laid out that could be replicated by others wishing to build a low power Hall thruster based on an existing design. It is hoped that this process will stimulate further work in the field and encourage greater disclosure of design techniques. The execution of this design process resulted in the best performing subcentimeter Hall thruster built to date. This is a significant achievement towards the goal of high performance, small scale Hall thruster propulsion. Further design improvements can be made, but a strong foundation has been established to continue to push the envelope in miniaturization. Finally, a comprehensive set of performance measurements were compiled for the MHT-9 that have aided in the understanding of the underlying physics of Hall thruster scaling.

6.1.3 Modeling and Analysis

The performance of the MHT-9 was compared to scaling predictions, various low power Hall thrusters and the D-55 baseline thruster. Although the MHT-9 compared favorably to other low power Hall thrusters given its small size, the performance targets set out in the scaling analysis were missed. The MHT-9 performance was further examined using dimensionless parameters that characterize the important processes governing the physics of the thruster. This facilitated a comparison to thrusters of various sizes so that the critical differences affecting performance could be identified. This dimensionless performance

map showed that the electron Knudsen number for ionization and the magnetic confinement ratio are important factors governing the efficiency of a Hall thruster at any scale. The Knudsen number in the MHT-9 was higher than expected because of the high thruster wall temperatures, resulting in longer than intended mean free paths for electrons between ionizing collisions. The magnetic confinement ratio, R_L/L, was slightly higher than expected, but more importantly the challenge of maintaining the magnetic field topology was identified as an inherent and fundamental problem for small scale Hall thrusters. Furthermore, it was shown that changes in the confinement ratio are largely driven by the electron temperature once the target range for the magnetic field has been selected.

The Knudsen number analysis was also used to make an empirical estimate of the performance penalty associated with scaling to small size, using data from published literature and the MHT-9. A curve fit of thrust efficiency versus Knudsen number was used to predict the performance of a thruster scaled down from a baseline design, assuming that the adverse effects associated with the challenges of miniaturization were built into the data. This technique yields a valuable estimate of the minimum performance expected when attempting to miniaturize a thruster.

An electron power balance model was created to estimate the peak electron temperature, as well as the backstreaming current ratio, inside a Hall thruster based on the operating voltage and the ratio of wall area to exit area. Because of the larger relative exposed wall area, the MHT-9 was predicted to operate at a higher electron temperature than the baseline thruster. This likely led to higher wall losses and beam divergence through a stronger wall sheath. The high electron temperature also reduced the magnetic confinement of electrons and this may have resulted in greater electron current leakage to the anode. Both of these effects led to lower thrust efficiency, however an analysis of the dependence of the ionization rate on electron temperature showed that the higher temperature in the MHT-9 actually benefits the ionization process because of an increased electron-neutral cross section for ionization. The electron temperature model also showed that the backstreaming

current ratio is likely higher in the MHT-9 than the D-55, and this is likely a further source of inefficiency.

A particle-in-cell computational simulation developed by Szabo was utilized to confirm the conclusions from analytical modeling and provide insight on the structure of the plasma discharge in the MHT-9. The correlation of Knudsen number and the magnetic confinement ratio with thrust efficiency were reproduced through a simulated test matrix. Simulation results showed that the optimal magnetic field strength for the MHT-9 was likely higher than that used in the experimental testing. The electron temperature model showed relatively good agreement with the simulation over a voltage range of 150-300V.

The modeling portion of this research has explained some of the inherent challenges in maintaining the important plasma processes inside the thruster as it is scaled to small size. The contributions of this research have helped to identify fundamental limitations in Hall thruster miniaturization, however there exists an important region in the design trade space that can be explored to find small size designs that provide acceptable levels of efficiency and specific impulse for small satellite applications. The MHT-9 showed that relatively high performance can be achieved at the expense of thruster lifetime, but further improvements can be made. Scaling analysis and modeling indicate that by reducing the channel length and wall area ratio, the power lost to ion-electron recombination can be reduced and thruster performance improved. Furthermore, there may be an optimal design where the cross sectional shape is preserved but scaled less strongly than thruster diameter, resulting in improved magnetic field topology and increased thruster lifetime without sacrificing performance.

6.2 Recommendations for Future Work

6.2.1 Further Development of the MHT-9

Several useful recommendations specific to the design and operation of the MHT-9 can be made at the conclusion of this research. In order to reduce the power lost to ion-electron

recombination at walls and extend the lifetime of the thruster, two simple geometry adjustments could be made. The anode tip could be moved further downstream with no redesign of the thruster. This would only require building a new, thicker anode insulating ceramic (or adding a spacer underneath the old insulator) and reassembling the thruster. Another potential adjustment would be to reduce the length of the center stem, but this would require a new Hiperco piece to be manufactured and heat treated. Both of these changes are aimed at reducing the area ratio of the discharge chamber, which should reduce erosion and improve performance.

Cathode optimization could be a useful investigation, particularly if it was explored simultaneously with an increase in the magnetic field strength. The field strength could be increased without building a new permanent magnet by simply reducing the cross sectional area of the focusing pole. It was originally made relatively thick to prevent saturation at high temperature and to allow for adjustment of the anode position while still maintaining the radial direction of field lines. However, measured thruster temperatures were lower than predicted, meaning that a thinner focusing pole would likely yield a stronger gap field strength and gradient without saturating. This magnetic change, coupled with a process to minimize the cathode flow and current, could help to reduce the backstreaming current ratio and increase thrust efficiency.

The Knudsen number analysis indicates that cooling the thruster with additional heat sinks or a fluid flow will also likely increase thrust efficiency. A fluid flow approach would be most effective but also the least practical from the standpoint of spacecraft integration.

6.2.2 Hall Thruster Miniaturization

The area of small scale plasma propulsion provides many opportunities for further exploration. Within conventional annular Hall thrusters, the most important progression of this research would be to further explore the design space identified in the scaling analysis of Chapter 2 where the geometry of the azimuthal cross section can be scaled independently from the diameter (or more generally, the perimeter). If the channel width and length were

scaled down by the same proportion but a factor less than the diameter, this would require a lower magnetic field strength and result in a lower plasma density (compared to purely photographic scaling). The reduction in required magnetic field strength would allow for improved field topology because the pole shapes of larger thrusters could be recreated more accurately. A lower plasma density would reduce thruster erosion and improve lifetime. This more open channel geometry will have a reduced power per unit of flow area, and should result in improved overall performance. The fundamental limitation of this strategy will occur where the channel width is expanded too far and the center pole overheats and begins to saturate magnetically.

Unconventional magnetic field geometries are another important area of research. The conventional annular circuit geometries are inherently limited by the small dimensions and associated saturation of the center pole, particularly at high temperature. However, research at Princeton has shown success with a single cusped field geometry, and work at Thales Electron Devices in Germany and at MIT by Courtney is exploring the use of multiple cusps to reduce wall erosion [17, 88-89].

REFERENCES

[1] Blackwood, G., Henry, C., Serabyn, E., Dubovitsky, S., Aung, M. and Gunter, S.M., "Technology and Design of an Infrared Interferometer for the Terrestrial Planet Finder," AIAA-2003-6329, AIAA Space 2003 Conference and Exposition, Long Beach, California, Sep. 23-25, 2003 .

[2] Polzin, K.A., Choueiri, E.Y., Gurfil, P. and Kasdin, N.J., "Plasma Propulsion for Three Terrestrial Planet Finder Architectures: Free-Flying, Monolithic and Tethered," AIAA-2001-3645, 37th Joint Propulsion Conference, Salt Lake City, UT, July 8-11, 2001.

[3] Pote, B. and Tedrake, R., "Performance of a High Specific Impulse Hall Thruster," IEPC-2001-035, 27th International Electric Propulsion Conference, Pasadena, CA, October 14-19, 2001.

[4] Manzella, D.H., Jacobson, D.T. and Jankovsky, R.S., "High Voltage SPT Performance," AIAA-2001-3774, 37th Joint Propulsion Conference, Salt Lake City, UT, July 8-11, 2001.

[5] Butler, G.W., Yuen, J.L., Tverdokhlebov, S.O., Semenkin, A.V., and Jankovsky, R.S., "Multimode, High Specific Impulse Hall Thruster Technology," AIAA-2000-3254, 36th Joint Propulsion Conference, Huntsville, AL, July 16-19, 2000.

[6] Oleson, S.R., "Mission Advantages of Constant Power, Variable Isp Electrostatic Thrusters," AIAA-2000-3413, 36th Joint Propulsion Conference, Huntsville, AL, July 16-19, 2000.

[7] Manzella, D., Jankovsky, R. and Hofer, R., "Laboratory Model 50kW Hall Thruster," AIAA-2002-3676, 38th Joint Propulsion Conference, Indianapolis, IN, July 7-10, 2002.

[8] Garkusha, V.I., Grishin, S.D., Mironov, S.G., Savitsev, V.V. and Semenkin, A.V, "Electric Propulsion Activity in TsNIIMASH," IEPC-1995-009, 24th International Electric Propulsion Conference, Moscow, Russia, September, 1995.

[9] Kim, V., Popov, G., Arkhipov, B., Murashko, V., Gorshkov, O., Koroteyev, A., Garkusha, V., Semenkin, A. and Tverdokhlebov, S., "Electric Propulsion Activity in Russia," IEPC-2001-005, 27th International Electric Propulsion Conference, Pasadena, CA, October 14-19, 2001.

[10] Hruby, V., *Hall Field Plasma Accelerator with an Inner and Outer Anode*, U.S. Patent # 6,075,321, June 13, 2000.

[11] Hruby, V., Monheiser, J., and Pote, B., *Tandem Hall Field Plasma Accelerator*, U.S. Patent # 6,150,764, November 21, 2000.

[12] Choueiri, E.Y., "Fundamental Difference Between the Two Hall Thruster Variants," *Physics of Plasmas*, Vol. 8, No. 11, November, 2001.

[13] Khayms, V. and Martinez-Sanchez, M., "Fifty-Watt Hall Thruster for Microsatellites," Micropropulsion for Small Spacecraft, Progress in Aeronautics and Astronautics, Vol. 187, AIAA, 2000, pp. 233-254.

[14] Khayms, V., "Design of a Miniaturized Hall Thruster for Microsatellites," Massachusetts Institute of Technology, S.M. Thesis, May, 1997.

[15] Khayms, V., "Advanced Propulsion for Microsatellites," Massachusetts Institute of Technology, Ph.D. Thesis, June, 2000.

[16] Monheiser, J., Hruby, V., Freeman, C., Connolly, W., and Pote, B., "Development and Testing of a Low-Power Hall Thruster System," Micropropulsion for Small Spacecraft, Progress in Aeronautics and Astronautics, Vol. 187, AIAA, 2000, pp. 255-270.

[17] Smirnov, A., Raitses, Y., and Fisch, N.J., "Performance Studies of Miniaturized Cylindrical and Annular Hall Thrusters," AIAA-2002-3823, 38th Joint Propulsion Conference, Indianapolis, IN, July 7-10, 2002.

[18] Biagioni, L., Cesari, U., Saverdi, M. and Andrenucci, M., "Development Status of the HT-100 Miniaturized Hall Effect Thruster System," AIAA-2005-3875, 41st Joint Propulsion Conference, Tucson, AZ, July 10-13, 2005.

[19] Zakharenkov, L., Chislov, G., Semenkin, A. and Lawrence, T., "Study of Low Power TAL Characteristics," IEPC-2001-041, 27th International Electric Propulsion Conference, Pasadena, CA, October 14-19, 2001.

[20] Bugrova, A.I., Desiatskov, A.D., Kaufman, H.R., Kharchevnikov, V.K., Morozov, A.I. and Zhurin, V.V., "Design and Experimental Investigation of a Small Closed Drift Thruster," IEPC-2001-344, 27th International Electric Propulsion Conference, Pasadena, CA, October 14-19, 2001.

[21] Jacobson, D.T. and Jankovsky, R.S., "Test Results of a 200W Class Hall Thruster," AIAA-1998-3792, 34th Joint Propulsion Conference, Cleveland, OH, July 13-15, 1998.

[22] Kim, V., Kozlov, V., Skrylnikov, A., Veselovzorov, A., Hilleret, N., Henrist, B., Locke, S. and Fife, J., "Investigation of Operation and Characteristics of Small SPT with Discharge Chamber Walls Made of Different Ceramics," AIAA-2003-5002, 39th Joint Propulsion Conference, Huntsville, AL, July 20-23, 2003.

[23] Guerrini, G., Vesselovzorov, A.N., and Bacal, M., "Investigation of Small, Closed Electron Drift, SPT," IEPC-1995-032, 24th International Electric Propulsion Conference, Moscow, Russia, September, 1995.

[24] Guerrini, G., Vesselovzorov, A.N., Bacal, M., and Pokrovsky, I.B., "Investigation of a Small, Closed Electron Drift, Stationary Plasma Thruster," *Review of Scientific Instruments*, Vol. 67, No. 3, March 1996.

[25] Ito, T., Gascon, N., Crawford, W.S. and Cappelli, M.A., "Further Development of a Micro Hall Thruster," AIAA-2006-4495, 42nd Joint Propulsion Conference, Sacramento, CA, July 9-12, 2006.

[26] Szabo, J.J., "Fully Kinetic Numerical Modeling of a Plasma Thruster," Massachusetts Institute of Technology, Ph.D. Thesis, January, 2001.

[27] Khayms, V. and Martinez-Sanchez, M., "Design of a Miniaturized Hall Thruster for Microsatellites," AIAA-96-3291, 32nd Joint Propulsion Conference, Lake Buena Vista, FL, July 1-3, 1996.

[28] Kim, V., Kozlov, V., Lazurenko, A., Popov, G., Skrylnikov, A., Clauss, C., Day, M. and Sankovic, J., "Development and Characterization of Small SPT," AIAA-1998-3335, 34th Joint Propulsion Conference, Cleveland, OH, July 13-15, 1998.

[29] Ahedo, E. and Gallardo, J.M., "Scaling Down Hall Thrusters," IEPC-2003-104, 28th International Electric Propulsion Conference, Toulouse, France, March 17-21, 2003.

[30] Andrenucci, M., Biagioni, L., Marcuccio, S. and Paganucci, F., "Fundamental Scaling Laws for Electric Propulsion Concepts," IEPC-2003-259, 28th International Electric Propulsion Conference, Toulouse, France, March 17-21, 2003.

[31] Andrenucci, M., Battista, F. and Piliero, P., "Hall Thruster Scaling Methodology," IEPC-2005-187, 29th International Electric Propulsion Conference, Princeton, NJ, October 31 - November 4, 2005.

[32] Pote, B., Hruby, V., and Tedrake, R., "Performance of a Multi-Kilowatt Non-Circular Discharge Hall Thruster," AIAA-2000-3249, 36th Joint Propulsion Conference, Huntsville, AL, July 16-19, 2000.

[33] Komurasaki, K., Mikami, K., and Kusamoto, D., "Channel Length and Thruster Performance of Hall Thrusters," AIAA-1996-3194, 32nd Joint Propulsion Conference, Buena Vista, FL, July 1-3, 1996.

[34] Semenkin, A.V., "Investigation of Erosion in Anode Layer Thruster and Elaboration High Life Design Scheme," IEPC-1993-231, 23rd International Electric Propulsion Conference, Seattle, WA, September, 1993.

[35] Semenkin, A.V., Tverdokhlebov, S.O., Garkush, V.I., and Grishin, S., "TAL Thruster Technology for Advanced Electric Propulsion Systems," 96-a-3-26, 20th International Symposium on Space Technology and Science, Gifu, Japan, May, 1996.

[36] Sankovic, J., Caveny, L., and Lynn, P., "The BMDO Russian Hall Electric Thruster Technology (RHETT) Program: From Laboratory to Orbit," AIAA-1997-2917, 33rd Joint Propulsion Conference, Seattle, WA, July 6-9, 1997.

[37] Press release by Space Systems Loral, "International Space Technologies, Inc. Debuts its Stationary Plasma Thrusters on Loral-Built MBSat Satellite," Palo Alto, CA, June 28, 2004. (http://www.ssloral.com/html/pressreleases/pr20040628.html)

[38] Garner, C.E., Polk, J.E., Brophy, J.R., and Marrese, C., "Experimental Evaluation of Russian Anode Layer Thrusters," AIAA-1994-3010, 30th Joint Propulsion Conference, Indianapolis, IN, June 27-29, 1994.

[39] Sankovic, J.M., Haag, T.W. and Manzella, D.H., "Operating Characteristics of the Russian D-55 Thruster with Anode Layer," AIAA-1994-3011, 30th Joint Propulsion Conference, Indianapolis, IN, June 27-29, 1994.

[40] Marrese, C., Polk, J., King, L., Garner, C., Gallimore, A., Semenkin, S., Tverdoklebov, S., and Garkusha, V., "Analysis of Anode Layer Thruster Guard Ring Erosion," IEPC-1995-196, 24th International Electric Propulsion Conference, Moscow, Russia, 1995.

[41] Renaudin, P., Cagan, V., Guyot, M., Cadiou, A., Lasgorceix, P., Dudeck, M., Vial, V., Dumazert, P., "Magnetic Circuits for Hall Thrusters: Use of Permanent Magnets," IEPC-2003-284, 28th International Electric Propulsion Conference, Toulouse, France, March 17-21, 2003.

[42] Dexter Magnetic Technologies, "Reference and Design Manual," 2001.

[43] Personal communication with Michael Devine, Senior Applications Engineer, Dexter Magnetic Technologies, Inc.

[44] Personal communication with Dr. JinFang Liu, Director of Technology, Electron Energy Corporation.

[45] Reprinted with permission from the Electron Energy Corporation.

[46] Personal communication with Humberto Raposo, Regional Metallurgist, Carpenter Technology Company.

[47] Kueser, P.E., Pavlovic, D.M., Lane, D.H., Clark, J.J., and Spewock, M., "Properties of Magnetic Materials for use in High-Temperature Space Power Systems," NASA SP-3043, 1967.

[48] Australian Stainless Steel Development Association, "Magnetic Effects of Stainless Steels," Technical FAQs No. 3, ASSDA Technical Series (www.assda.asn.au), 2004.

[49] Schlichting, H., *Boundary-Layer Theory*, McGraw-Hill, Inc., New York, 1979, pp. 731-735.

[50] Sutton, G.P., *Rocket Propulsion Elements*, John Wiley & Sons, Inc., New York, 1992, pp. 302-304.

[51] Azziz, Y., "Instrument Development and Plasma Measurements on a 200-Watt Hall Thruster Plume," Massachusetts Institute of Technology, S.M. Thesis, September, 2003.

[52] Kruithof, A.A., "Townsend's Ionization Coefficients for Neon, Argon, Krypton and Xenon," *Physica*, Volume 7, p. 519, 1940.

[53] Schönhuber, M.J., "Breakdown of Gases Below Paschen Minimum: Basic Design Data of High-Voltage Equipment," *IEEE Transactions on Power Apparatus and Systems*, Vol. PAS-88, p. 100, 1969.

[54] Bhattacharya, A.K., "Measurement of Breakdown Potentials and Townsend ionization Coefficients for the Penning Mixtures of Neon and Xenon," *Physical Review A*, Vol. 13, No. 3, p. 1219, 1976.

[55] Warner, N.Z., "Performance Testing and Internal Probe Measurments of a High Specific Impulse Hall Thruster," Massachusetts Institute of Technology, S.M. Thesis, September, 2003.

[56] King, L.B. and Gallimore, A.D., "Ion-Energy Diagnostics in an SPT-100 Plume from Thrust Axis to Backflow," *AIAA Journal of Propulsion and Power*, Vol. 20, No. 2, March-April, 2004.

[57] Ahedo, E., Martínez-Cerezo, P. and Martínez-Sánchez, M., "One-Dimensional Model of the Plasma Flow in a Hall Thruster," *Physics of Plasmas*, Vol. 8, No. 6, June, 2001.

[58] Hofer, R.R., "Development and Characterization of High-Efficiency, High-Specific Impulse Xenon Hall Thrusters," University of Michigan, Ph.D. Thesis, 2004.

[59] Fife, J.M., "Hybrid-PIC Modeling and Electrostatic Probe Survey of Hall Thrusters," Massachusetts Institute of Technology, Ph.D. Thesis, September, 1998.

[60] Dugan, J.V., and Sovie, R.J., "Volume Ion Production Costs in Tenuous Plasmas: A General Atom Theory and Detailed Results for Helium, Argon and Cesium," NASA Technical Note D-4150, September, 1967.

[61] Raju, G.G., *Gaseous Electronics Theory and Practice*, CRC Press, Taylor & Francis Group, Boca Raton, FL, 2006.

[62] Khakoo, M.A. et al, "Differential Cross Sections for Electron Impact Excitation of Xe: I. Excitation of the Five Lowest Levels; Experiment and Theory," *Journal of Physics B: Atomic, Molecular and Optical Physics*, Vol. 29, No. 15, p. 3455, 1996.

[63] Khakoo, M.A. et al, "Differential Cross Sections for Electron Impact Excitation of Xe: II. Excitation of the Sixth to Twentieth Lowest Levels; Experiment and Theory," *Journal of Physics B: Atomic, Molecular and Optical Physics*, Vol. 29, No. 15, p. 3477, 1996.

[64] Lienhard, J.H. and Lienhard, J.H., *A Heat Transfer Textbook*, Phlogiston Press, Cambridge, MA, 2005.

[65] Walter, J. and Dickens, J., "Thermal Characterization and Modeling of a Low-Power Laboratory Model TAL," IEPC-2001-072, 27th International Electric Propulsion Conference, Pasadena, CA, October 14-19, 2001.

[66] Rohsenow, W.M. and Hartnett, J.P. (editors), *Handbook of Heat Transfer*, McGraw Hill, New York, 1973.

[67] Wheeler, R.F., "Thermal Conductance of Fuel Element Materials," USAEC Report HW-60343, April 1959.

[68] Madhusudana, C.V., *Thermal Contact Conductance*, Springer-Verlag, New York, 1996.

[69] Celik, M., "Experimental and Computational Studies of Electric Thruster Plasma Radiation Emission," Massachusetts Institute of Technology, Ph.D. Thesis, June, 2007.

[70] Hruby, V., Monheiser, J., Pote, B., Rostler, P., Kolencik, J. and Freeman, C., "Development of Low Power Hall Thrusters," AIAA-1999-3534, 30th Plasmadynamics and Lasers Conference, Norfolk, VA, June 28 - July 1, 1999.

[71] Haag, T., "Design of a Thrust Stand for High Power Electric Propulsion Devices," AIAA-1989-2829, 25th Joint Propulsion Conference, Monterey, CA, July 10-12, 1989.

[72] Haag, T., and Osborn, M., "RHETT/EPDM Performance Characterization," IEPC-1997-107, 25th International Electric Propulsion Conference, Cleveland, OH, August 24-28, 1997.

[73] Hruby, V., Monheiser, J., Pote, B., Freeman, C. and Connolly, W., "Low Power Hall Thruster Propulsion System," IEPC-1999-092, 26th International Electric Propulsion Conference, Kitakyushu, Japan, October 17-21, 1999.

[74] Gorshkov, O.A., Shagayda, A.A., and Irishkov, S.V., "The Influence of the Magnetic Field Topology on Hall Thruster Performance," AIAA-2006-4472, 42nd Joint Propulsion Conference, Sacramento, CA, July 9-12, 2006.

[75] Blinov, N.V., Gorshkov, O.A. and Shagayda, A.A., "Experimental Investigation of Magnetic Field Topology Influence on Structure of Accelerating Layer and Performance of Hall Thruster," IEPC-2005-033, 29th International Electric Propulsion Conference, Princeton, NJ, October 31 - November 4, 2005.

[76] Garner, C.E., Tverdokhlebov, S.O., Semenkin, A.V. and Garkusha, V.I., "Evaluation of a 4.5-kW D-100 Thruster with Anode Layer," AIAA-1996-2967, 32nd Joint Propulsion Conference, Lake Buena Vista, FL, July 1-3, 1996.

[77] Wilson, R.G. and Brewer, G.R., *Ion Beams*, John Wiley & Sons, New York, 1973.

[78] Smirnov, A., Raitses, Y. and Fisch, N.J., "Parametric Investigation of Miniaturized Cylindrical and Annular Hall Thrusters," *Journal of Applied Physics*, Vol. 92, No. 10, p. 5673, 2002.

[79] Bird, G.A., *Molecular Gas Dynamics and the Direct Simulation of Gas Flows*, Clarendon Press, Oxford, 1994.

[80] Jacobson, D.T., Jankovsky, R.S., Rawlin, V.K. and Manzella, D.H., "High Voltage TAL Performance," AIAA-2001-3777, 37th Joint Propulsion Conference, Salt Lake City, UT, July 8-11, 2001.

[81] Azziz, Y., "Experimental and Theoretical Characterization of a Hall Thruster Plume," Massachusetts Institute of Technology, Ph.D. Thesis, June, 2007.

[82] Mitchner, M. and Kruger, C.H., *Partially Ionized Gases*, John Wiley & Sons, New York, 1973.

[83] Szabo, J., Martinez-Sanchez, M. and Batishchev, O., "Fully Kinetic Hall Thruster Modeling," IEPC-2001-341, 27th International Electric Propulsion Conference, Pasadena, CA, October 14-19, 2001.

[84] Szabo, J., Warner, N., Martinez-Sanchez, M. and Batishchev, O., "A Full Particle-In-Cell Simulation Methodology for Axisymmetric Hall Effect Thruster Discharges," submitted to the AIAA Journal of Propulsion and Power, March, 2007.

[85] Cappelli, M.A., Meezan, N.B. and Gascon, N., "Transport Physics in Hall Plasma Thrusters," AIAA-2002-0485, 40th AIAA Aerospace Sciences Meeting and Exhibit, Reno, NV, January, 2002.

[86] Blateau, V., "PIC Simulation of a Ceramic-Lined Hall-Effect Thruster," Massachusetts Institute of Technology, S.M. Thesis, September, 2002.

[87] Fox, J., "Advances in Fully-Kinetic PIC Simulations of a Near-Vacuum Hall Thruster and Other Plasma Systems," Massachusetts Institute of Technology, Ph.D. Thesis, September, 2007.

[88] Kornfeld, G., Koch, N. and Coustou, G., "First Test Results of the HEMP Thruster Concept," IEPC-2003-212, 28th International Electric Propulsion Conference, Toulouse, France, March 17-21, 2003.

[89] Courtney, D. and Martínez-Sánchez, M., "Diverging Cusped-field Hall Thruster," 30th International Electric Propulsion Conference, Florence, Italy, September 17-20, 2007.

Appendix A

MHT-9 PERFORMANCE DATA

The following three tables list the performance data taken with the MHT-9 during testing at the Busek Company, Inc. The temperatures shown are for the permanent magnet, T_m, and the Hiperco core, T_H, that were measured at the locations indicated in Figure 4.4. The magnetic field estimation, B_r, is corrected for the temperature of the permanent magnet and represents the average radial field strength at the tip of the anode. The specific impulse, I_{sp}, and the thrust efficiency, η_t, do not include the cathode flow or the cathode power. The cathode flow rate was held constant at 0.1mg/s for all test conditions, and the cathode keeper current was kept at 0.5A. The Busek T6 vacuum tank facility was operated with only the diffusion pump; the cryopumps were not utilized during testing. The tank pressure varied from 7×10^{-6}torr to 3×10^{-5}torr during testing.

TABLE A.1   Data From Test #3 Without a Magnetic Shunt ($S=0$mm)

V_d (V)	I_d (A)	P_d (W)	$\dot{m}_a$ (mg/s)	T_m (°C)	T_H (°C)	B_r (G)	T (mN)	I_{sp} (s)	η_t
303	0.33	99.1	0.30	90.9	89.6	1846	3.5	1201	0.208
253	0.32	79.6	0.30	93.7	92.5	1843	3.4	1174	0.247
202	0.41	83.8	0.30	98.4	96.2	1839	3.1	1070	0.195
151	0.34	51.9	0.30	101.6	99.0	1835	1.9	665	0.121
101	0.20	20.6	0.30	98.0	96.6	1839	0.8	279	0.054
303	0.38	114.2	0.34	105.7	104.6	1831	4.5	1321	0.254
253	0.38	96.1	0.34	111.6	110.4	1825	4.0	1180	0.241
202	0.53	106.7	0.34	122.9	119.3	1814	3.5	1048	0.171
151	0.43	64.7	0.34	124.3	121.0	1813	2.3	674	0.117
101	0.27	27.0	0.34	119.5	117.7	1817	1.0	287	0.051
303	0.44	134.8	0.39	131.8	130.5	1806	5.4	1392	0.274
253	0.45	114.0	0.40	136.3	135.0	1802	4.9	1275	0.272
202	0.64	128.7	0.39	144.8	141.3	1795	4.2	1085	0.174
151	0.50	76.0	0.40	147.8	144.1	1793	2.6	662	0.110
101	0.33	33.0	0.39	142.0	140.0	1797	1.1	297	0.051
303	0.49	148.9	0.43	152.5	151.1	1790	5.9	1392	0.270
253	0.50	126.6	0.43	156.7	155.3	1787	5.3	1258	0.260
202	0.69	140.2	0.43	166.2	162.0	1781	4.3	1013	0.152
151	0.54	81.6	0.43	166.4	162.7	1781	2.6	608	0.094
101	0.36	36.4	0.43	160.0	158.0	1785	1.1	262	0.039
303	0.70	212.6	0.58	175.7	173.9	1776	8.0	1398	0.258
253	0.72	183.0	0.58	181.6	179.6	1772	7.2	1268	0.246
202	0.95	192.5	0.58	199.1	193.9	1760	5.6	984	0.141
151	0.76	114.9	0.58	199.6	194.1	1759	3.9	683	0.114
101	0.54	55.0	0.58	189.9	187.1	1767	2.2	384	0.075
303	0.94	283.7	0.74	211.9	209.7	1748	11.3	1567	0.307
253	0.97	245.7	0.74	220.2	217.5	1738	10.4	1442	0.300
202	1.53	308.3	0.74	238.3	233.1	1716	10.0	1389	0.222
151	1.32	199.6	0.74	243.6	238.2	1709	6.8	935	0.155
101	0.89	90.1	0.74	232.7	228.8	1723	3.8	522	0.107

TABLE A.2 Data From Test #4 With a 6.6mm Magnetic Shunt (*S*=6.6mm)

V_d (V)	I_d (A)	P_d (W)	$\dot{m}_a$ (mg/s)	T_m (°C)	T_H (°C)	B_r (G)	T (mN)	I_{sp} (s)	η_t
303	0.33	99.1	0.30	79.1	76.3	1569	3.8	1320	0.251
253	0.31	78.1	0.30	87.7	85.4	1561	3.3	1133	0.234
202	0.32	65.6	0.30	90.3	87.7	1559	2.8	967	0.203
151	0.36	54.2	0.30	93.7	89.5	1556	1.7	582	0.089
101	0.22	22.6	0.30	91.5	88.4	1558	0.5	186	0.022
303	0.37	111.5	0.34	104.1	101.5	1546	4.4	1314	0.257
253	0.38	95.4	0.34	108.7	106.0	1542	4.2	1230	0.263
202	0.45	91.8	0.34	115.7	110.8	1536	3.7	1095	0.217
151	0.44	66.8	0.34	118.2	112.7	1534	2.3	683	0.116
101	0.29	29.0	0.34	114.6	110.7	1537	1.0	287	0.047
303	0.43	130.4	0.39	126.0	122.9	1527	5.1	1331	0.258
253	0.44	112.0	0.39	131.2	128.0	1523	4.8	1230	0.256
202	0.64	128.9	0.39	141.3	134.5	1514	4.4	1126	0.187
151	0.53	80.0	0.39	144.0	137.2	1513	2.6	676	0.108
101	0.35	35.4	0.39	137.9	133.5	1517	1.1	295	0.047
303	0.48	146.1	0.43	150.1	146.4	1509	5.7	1347	0.258
253	0.50	125.1	0.43	156.7	152.9	1505	5.1	1216	0.246
202	0.73	148.2	0.43	166.2	158.9	1500	4.7	1106	0.172
151	0.59	89.3	0.43	168.5	161.1	1499	2.7	628	0.092
101	0.40	40.1	0.43	161.5	156.8	1503	1.0	243	0.031
303	0.69	209.2	0.58	206.0	200.3	1476	8.2	1442	0.278
253	0.71	179.7	0.58	186.9	181.4	1489	7.8	1360	0.288
202	1.10	222.6	0.58	202.1	192.1	1479	7.3	1278	0.205
151	0.88	132.6	0.58	204.9	195.7	1477	4.6	808	0.138
101	0.60	60.5	0.58	195.0	189.5	1484	2.4	413	0.079
303	1.14	346.8	0.73	241.1	231.0	1442	12.3	1706	0.297
252	1.34	338.0	0.73	262.5	253.7	1418	11.9	1645	0.284
202	1.49	301.7	0.73	272.5	263.4	1407	9.1	1255	0.185
151	1.20	181.1	0.73	268.6	261.2	1412	5.8	801	0.125
101	0.87	87.5	0.73	255.8	250.2	1426	3.1	432	0.076

TABLE A.3 Data From Test #5-6 With a 5.6mm Magnetic Shunt ($S=5.6$mm)

V_d (V)	I_d (A)	P_d (W)	$\dot{m}_a$ (mg/s)	T_m (°C)	T_H (°C)	B_r (G)	T (mN)	I_{sp} (s)	η_t
303	0.37	113.1	0.30	127.3	124.7	1649	4.4	1525	0.294
253	0.36	90.0	0.30	128.5	126.1	1648	3.8	1297	0.267
202	0.43	86.3	0.30	130.9	128.2	1646	3.1	1051	0.183
151	0.35	52.7	0.30	130.3	127.8	1646	1.8	626	0.106
101	0.20	20.3	0.30	125.4	123.8	1651	0.7	236	0.039
303	0.43	130.9	0.34	135.5	133.2	1642	4.9	1452	0.267
253	0.45	114.3	0.34	142.9	140.3	1636	4.7	1380	0.276
202	0.53	107.3	0.34	147.4	144.3	1633	3.8	1112	0.191
151	0.43	65.5	0.34	147.2	144.4	1633	2.3	666	0.112
101	0.27	26.9	0.34	142.2	140.3	1637	1.0	294	0.053
303	0.54	163.9	0.39	164.3	161.0	1622	6.0	1560	0.283
253	0.56	142.5	0.39	170.7	167.3	1619	5.6	1452	0.282
202	0.64	129.4	0.39	174.6	170.8	1617	4.5	1170	0.201
151	0.52	78.9	0.39	173.1	169.8	1618	2.7	697	0.117
101	0.33	33.3	0.39	166.8	164.6	1621	1.2	301	0.052
303	0.67	202.9	0.43	118.3	114.0	1657	7.1	1676	0.287
253	0.66	166.3	0.43	124.8	120.6	1651	6.5	1538	0.295
202	0.69	140.3	0.43	128.1	123.5	1648	5.2	1220	0.220
151	0.57	86.4	0.43	127.2	123.4	1649	2.9	697	0.117
101	0.38	38.0	0.43	121.7	119.7	1654	1.4	325	0.058
303	1.02	308.4	0.58	184.9	178.2	1611	11.0	1928	0.337
252	1.00	251.9	0.58	193.8	187.4	1606	10.1	1772	0.349
202	1.02	206.1	0.58	192.8	186.7	1606	7.5	1321	0.237
151	0.85	129.2	0.58	193.0	187.6	1606	4.9	850	0.157
101	0.58	58.6	0.58	184.4	181.9	1611	2.7	469	0.105
303	1.38	417.8	0.74	238.2	229.0	1563	14.4	1989	0.335
252	1.35	340.7	0.74	252.0	243.3	1547	12.9	1791	0.333
202	1.43	288.3	0.74	256.8	248.0	1541	9.8	1353	0.225
151	1.21	183.2	0.74	253.8	246.6	1545	6.4	884	0.151
101	0.86	86.7	0.74	240.5	237.1	1560	3.5	491	0.098

TABLE A.3 Data From Test #5-6 With a 5.6mm Magnetic Shunt ($S=5.6$mm)

V_d (V)	I_d (A)	P_d (W)	$\dot{m}_a$ (mg/s)	T_m (°C)	T_H (°C)	B_r (G)	T (mN)	I_{sp} (s)	η_t
303	1.59	480.9	0.84	294.3	282.9	1495	16.6	2022	0.343
252	1.59	402.0	0.84	305.7	294.5	1481	14.8	1807	0.327
202	1.68	338.3	0.84	309.1	297.8	1476	11.3	1379	0.226
151	1.48	223.9	0.84	303.5	294.5	1483	7.5	918	0.152
101	1.06	107.3	0.84	288.9	284.0	1502	4.2	514	0.099
303	1.61	488.7	0.89	333.8	322.3	1442	17.1	1950	0.335
252	1.81	456.2	0.89	343.9	331.6	1428	15.4	1751	0.289
202	1.81	365.9	0.89	345.4	332.9	1425	12.1	1379	0.224
151	1.62	245.9	0.89	335.8	326.1	1439	7.9	902	0.142
101	1.20	121.0	0.89	320.8	314.7	1460	4.4	498	0.088
303	1.71	516.5	0.98	348.9	337.7	1420	17.6	1820	0.304
252	1.96	495.5	0.98	362.5	351.0	1401	15.8	1634	0.255
202	1.97	396.9	0.98	364.0	352.3	1399	13.3	1375	0.226
151	1.83	277.7	0.98	355.3	344.2	1412	8.7	906	0.140
101	1.38	139.3	0.98	333.3	326.7	1443	4.7	488	0.081